

ISTANBUL TECHNICAL UNIVERSITY ★ EURASIA INSTITUTE OF EARTH SCIENCES

**PRE-COLLISIONAL ACCRETION AND EXHUMATION ALONG THE
SOUTHERN LAURASIAN ACTIVE MARGIN, CENTRAL PONTIDES,
TURKEY**

Ph.D. THESIS

Mesut AYGÜL

Department of Climate and Sea Sciences

Earth System Sciences

NOVEMBER 2015

ISTANBUL TECHNICAL UNIVERSITY ★ EURASIA INSTITUTE OF EARTH SCIENCES

**PRE-COLLISIONAL ACCRETION AND EXHUMATION ALONG THE
SOUTHERN LAURASIAN ACTIVE MARGIN, CENTRAL PONTIDES,
TURKEY**

Ph.D. THESIS

**Mesut AYGÜL
(601092002)**

Department of Climate and Sea Sciences

Earth System Sciences

**Thesis Advisor: Prof. Dr. Aral OKAY
Co-advisor: Prof. em. Dr. Roland OBERHÄNSLI**

NOVEMBER 2015

İSTANBUL TEKNİK ÜNİVERSİTESİ ★ AVRASYA YER BİLİMLERİ ENSTİTÜSÜ

**LAVRASYA’NIN GÜNEY AKTİF KENARI BOYUNCA ÇARPIŞMA ÖCESİ
EKLEMLENME VE YÜZEYLENME, ORTA PONTİDLER, TÜRKİYE**

DOKTORA TEZİ

**Mesut AYGÜL
(601092002)**

İklim ve Deniz Bilimleri Anabilim Dalı

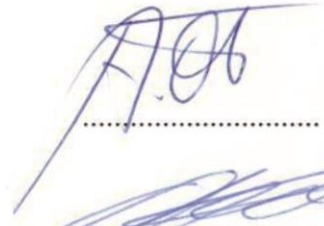
Yer Sistemi Bilimleri

**Tez Danışmanı: Prof. Dr. Aral OKAY
Ortak Danışman: Prof. em. Dr. Roland OBERHÄNSLI**

KASIM 2015

Mesut Aygöl, a **Ph.D.** student of **ITU Eurasia Institute of Earth Sciences** student ID **601092002**, successfully defended the **thesis/dissertation** entitled “**PRE-COLLISIONAL ACCRETION AND EXHUMATION ALONG THE SOUTHERN LAURASIAN ACTIVE MARGIN, CENTRAL PONTIDES, TURKEY**”, which he prepared after fulfilling the requirements specified in the associated legislations, before the jury whose signatures are below.

Thesis Advisor : **Prof. Dr. Aral OKAY**
İstanbul Technical University



Co-advisor : **Prof. em. Dr. Roland OBERHÄNSLI**
University of Potsdam



Jury Members : **Prof. Dr. Boris NATAL'IN**
İstanbul Technical University



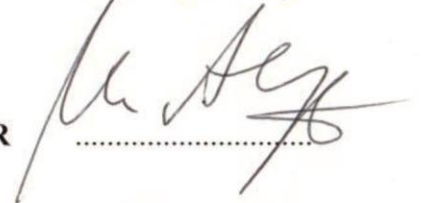
Prof. Dr. Okan TÜYSÜZ
İstanbul Technical University



Prof. Dr. Timur USTAÖMER
İstanbul University



apl. Prof. Dr. Uwe ALTENBERGER
University of Potsdam



apl. Prof. Dr. Helmut ECHTLER
GFZ and University of Potsdam



Date of Submission : 03 August 2015

Date of Defense : 24 November 2015

To my family,

FOREWORD

Well, this thesis took more time than I expected. However, I feel satisfied and comfortable because I enjoyed almost every moment of this passage of time by learning new things and improving my knowledge. In fact, I realized that the point is not about simply knowing things but rather how did you get that information. I think, that is the essence of science or scientific research. Beyond satisfying my personal curiosity, however, I also hope that this thesis will be useful for other researchers and make some contribution to the geology of Turkey and some similar geological settings.

I am very happy that this PhD thesis is done under the supervision of Prof. Aral Okay. Without his huge motivating, improving and constructive efforts, I wouldn't be able to finish this thesis. I am grateful to Prof. Aral Okay for his supervision, from field work to petrographic microscope studies. The submitted manuscripts and the thesis itself have largely benefited from his comments, suggestions and corrections. I am also grateful to my co-advisor Prof. em. Dr. Roland Oberhänsli. He kindly provided me opportunity to work in University of Potsdam. During my stay in Potsdam, I used many of the laboratory facilities and without these analytical data this thesis definitely wouldn't have finished. But more importantly, I discussed and learned a lot during my stay in Potsdam! Mostly with Prof. Oberhänsli (sometimes half a day!) but also with almost all of the other members of Mineralogy and Petrology groups. I am particularly grateful to Dr. Matthias Konrad-Schmolke for discussions on thermodynamics and Theriak-Domino software.

Special thanks to Dr. Masafumi Sudo, Dr. Alexander Schmidt and Dr. Martin A. Ziemann. Dr. Sudo is responsible for the $^{40}\text{Ar}/^{39}\text{Ar}$ Geochronology Lab at Potsdam University. I am grateful to him for dating of metapelitic samples by $^{40}\text{Ar}/^{39}\text{Ar}$ phengite method and critical discussions on the results. Dr. Schmidt is thanked for performing the LA-ICP-MS and U/Pb zircon dating. I also want to thank him for his contribution on the interpretation of the geochemical data. Dr. Ziemann is responsible for the Raman Spectroscopy Lab in the University of Potsdam. I am grateful to him for his help in performing Raman spectroscopy on carbonaceous material and improving discussion and comments on the topic.

Prof. Boris Natalin and Prof. Timur Ustaömer were the members of the thesis monitoring committee. I would like to thank them for their comments. Prof. Ercan Özcan is thanked for the paleontological dating of the Maastrichtian limestone based on the benthic foraminifera. I am indebted to Dr. Christina Günter for her help during electron microprobe analysis. Anja Städtke is kindly acknowledged for the XRF and REE analysis. Mehmet Ali Oral and Christine Fischer are thanked for preparing the thin sections. I was supported by the İTU and TÜBİTAK grants during my stay in the Potsdam University. During geological mapping in the field, my expenses were financed by İTU Division of Scientific Research Projects for PhD students and by the TÜBİTAK grant 109Y049.

July, 2015

Mesut AYGÜL

TABLE OF CONTENTS

	<u>Page</u>
FOREWORD	ix
TABLE OF CONTENTS	xi
ABBREVIATIONS	xv
LIST OF TABLES	xvii
LIST OF FIGURES	xix
SUMMARY	xxvii
ÖZET	xxxii
1. INTRODUCTION	1
1.1 Regional Geology.....	3
1.2 Geology of the Central Pontides.....	5
1.3 Purpose of Thesis.....	9
1.4 Methodology.....	9
1.4.1 PT calculations.....	10
1.4.1.1 THERMOCALC.....	10
1.4.1.2 Theriak-Domino.....	10
1.4.1.3 Raman spectra of carbonaceous material (RSCM) thermometers.....	10
1.4.2 Geochemistry.....	12
1.4.3 Geochronology.....	12
1.4.3.1 ⁴⁰ Ar/ ³⁹ Ar white mica geochronology.....	12
1.4.3.2 U/Pb zircon geochronology.....	14
2. GEOLOGY	15
2.1 Mesozoic Subduction-Accretionary Complexes.....	15
2.1.1 Esenler Unit: Accreted distal turbidites.....	17
2.1.2 Domuzdağ Complex: Oceanic metabasalts and metasediments.....	18
2.1.2.1 Extensional shear zone.....	20
2.1.3 Kunduz Metamorphics.....	21
2.1.4 Kirazbaşı Complex: Forearc basin and mélanges.....	22
2.1.5 İkiçam Formation: Alkaline volcanic rocks and turbidites.....	23
2.2 Accreted Arc Sequence.....	24
2.2.1 Köşdağ Formation.....	25
2.2.2 Dikmen Formation.....	27
2.2.3 Ophiolitic mélange (İAES).....	29
2.3 Cover Units.....	30
2.4. Structural Analysis of the Wedge.....	32
3. PETROGRAPHY AND MINERAL CHEMISTRY	35
3.1 Esenler Unit.....	35
3.2 Domuzdağ Complex.....	40
3.2.1 Metabasites.....	40
3.2.1.1 Lawsonite-blueschist (sample 128).....	41
3.2.1.2 Garnet-epidote-blueschist (sample 702A).....	42

3.2.2 Micaschists.....	44
3.2.2.1 Garnet-chloritoid-micaschist (sample 775).....	46
3.2.2.2 Chloritoid-micaschist (sample 753A).....	48
3.2.2.3 Chloritoid-micaschist (sample 178).....	49
3.2.2.4 Micaschist with albite porphyroblasts(sample 392).....	52
3.3 Kunduz Metamorphics.....	52
3.4 Köşdağ Formation.....	54
3.4.1 Felsic volcanic rocks.....	54
3.4.2 Basaltic andesite/andsesite.....	56
4. RAMAN MICROSPECTROSCOPY OF CARBONACEOUS MATERIAL.....	59
4.1 Esenler Unit.....	59
4.2 Domuzdağ Complex.....	62
4.3 Concluding Remarks.....	63
5. METAMORPHIC CONDITIONS.....	65
5.1 Esenler Unit.....	65
5.1.1 Metabasite within the Esenler Unit.....	66
5.1.2 Peak metamorphic temperatures of the slate/phyllites.....	67
5.2 Domuzdağ Complex.....	68
5.2.1 Lawsonite-blueschist.....	69
5.2.2 Garnet-blueschist.....	70
5.2.3 Chloritoid-micaschists.....	71
5.2.3.1 Sample 775.....	71
5.2.3.2 Sample 753A.....	73
5.2.3.3 Sample 178.....	74
5.3 Concluding Remarks.....	76
5.3.1 Esenler Unit.....	76
5.3.2 Domuzdağ Complex.....	77
6. GEOCHRONOLOGY.....	81
6.1 ⁴⁰ Ar/ ³⁹ Ar Geochronology.....	81
6.1.1 Esenler Unit.....	81
6.1.2 Domuzdağ Complex.....	83
6.1.3 Kunduz Metamorphics.....	84
6.1.4 Metamorphic age of the Köşdağ Formation.....	86
6.2 U/Pb Zircon Geochronology.....	87
6.2.1 Crystallization age of the Köşdağ Formation.....	87
6.3 Concluding Remarks.....	89
6.3.1 Accretionary wedge.....	89
6.3.2 Arc sequence.....	90
7. GEOCHEMISTRY.....	91
7.1 Geochemistry of the Köşdağ Formation.....	91
7.1.1 Major element compositions.....	91
7.1.2 Trace and rare earth element compositions.....	93
7.2 Interpretation of the Analytical Data.....	95
7.3 Concluding Remarks.....	95
8. GEODYNAMICS.....	99
8.1 Tectonic Thickening of the Albian-Turonian Accretionary Wedge.....	100
8.2 Exhumation of HP/LT Metamorphic Rocks.....	105
8.3 Comparative Regional Geology.....	108
8.3.1 Late Cretaceous intra-oceanic Köşdağ arc and supra-subduction ophiolites.....	109

9. CONCLUSIONS	113
REFERENCES.....	117
APPENDICES	141
CURRICULUM VITAE.....	205

ABBREVIATIONS

Al	: Aluminium
Appx	: Appendix
Ar	: Argon
B	: Boron
BA1	: Basaltic andesite 1
BA2	: Basaltic andesite 2
ca.	: circa
Ca	: Calcium
CaF₂	: Calcium fluoride
cm	: centimeter
CO₂	: Carbon dioxide
c.p.f.u	: cation per formula unit
CPS	: Central Pontide Supercomplex
e.g.	: for example
EMPA	: Electron microprobe analysis
et al.	: and others
GPS	: Global Positioning System
HFSE	: High Field Strength Elements
Hg	: mercury
HP/LT	: high pressure/low temperature
HREE	: Heavy Rare Earth Elements
ICP-AES	: Inductively Coupled Plasma Atomic Emission Spectrometry
İAES	: İzmir-Ankara-Erzincan Suture
Kbar	: kilobar
keV	: kilo-electronvolt
K	: Potassium
K₂SO₄	: Potassium sulfate
LA-ICP-MS	: Laser ablation inductively coupled plasma mass spectrometry
LILE	: Large Ion Lithophile Elements
LREE	: Light Rare Earth Elements
m	: meter
Ma	: megaannus
Mg	: magnesium
MORB	: Mid-Ocean Ridge Basalt
mm	: millimeter
µm	: micrometer
nA	: nanoampere
NAF	: North Anatolian Fault
nm	: nanometer
Pb	: lead
REE	: Rare Earth Elements
RSCM	: Raman spectra of carbonaceous material

s : second
SPT : Sodium polytungstate
U : uranium
W : watt
XRF : X-ray fluorescence
°C : degree Celsius

LIST OF TABLES

	<u>Page</u>
Table 4.1 : Parameters of decomposed Raman spectra of carbonaceous material from the Esenler Unit.	61
Table 4.2 : Parameters of decomposed Raman spectra of carbonaceous material from the Domuzdağ Complex.	62
Table 5.1 : Raman parameters and the calculated peak metamorphic temperatures for the Esenler Unit	67
Table 5.2 : Raman parameters and the calculated peak metamorphic temperatures for the chloritoid micaschists.	73
Table 6.1 : LA-ICP-MS U-Pb data of the measured zircons from the metarhyolites.	89
Table 7.1 : Major, trace and rare earth element analysis of the metavolcanic rocks.	92
Table A.1 : Mineral chemistry of the measured amphiboles. Mineral formula calculations are based on 23 oxygens.	147
Table A.2 : Mineral chemistry of the measured phengitic white micas. Mineral formula calculations are based on 11 oxygens.	154
Table A.3 : Mineral chemistry of the measured paragonites. Mineral formula calculations are based on 11 oxygens.	163
Table A.4 : Mineral chemistry of the measured garnets. Mineral formula calculations are based on 12 oxygens.	165
Table A.5 : Mineral chemistry of the measured chloritoids. Mineral formula calculations are based on 12 oxygens.	169
Table A.6 : Mineral chemistry of the measured lawsonites. Mineral formula calculations are based on eight oxygens.	179
Table A.7 : Mineral chemistry of the measured sodic-pyroxenes. Mineral formula calculations are based on four cations.	180
Table A.8 : Mineral chemistry of the measured epidotes. Mineral formula calculations are based on 12.5 oxygens.	181
Table A.9 : Mineral chemistry of the measured chlorites. Mineral formula calculations are based on 14 oxygens.	186
Table A.10 : Mineral chemistry of the measured plagioclases. Mineral formula calculations are based on eight oxygens.	192
Table A.11 : Bulk rock compositions and calculated element mol percentages used in the pseudosection calculations.	195
Table A.12 : UTM coordinates (European 1979 datum) of the metapelitic samples of the Esenler Unit that were analyzed by Raman Spectroscopy.	196
Table A.13 : $^{40}\text{Ar}/^{39}\text{Ar}$ analytical data of the dated samples.	197

LIST OF FIGURES

	<u>Page</u>
Figure 1.1 : Main components of an accretionary-type orogeny including oceanward tectonic growth of subduction-accretionary wedge and addition of juvenile material to the crust. Modified from Barr et al. (1999)	2
Figure 1.2 : Tectonic map of Turkey and surrounding regions (modified from Okay and Tüysüz, 1999). Green and pale blue colors highlight the Laurasia and Gondawana-derived terranes, respectively. CPS: Central Pontide Supercomplex, CTF: Lower Cretaceous submarine turbidite fan. North of the Black Sea, “V” marks the Albian volcanic arc modified from Nikishin et al. (2015)	4
Figure 1.3 : Geological map of the Central Pontides modified from Tüysüz (1990), Uğuz et al. (2002), Okay et al. (2013, 2014) and this study	6
Figure 1.4 : A photomicrograph in plane polarized light showing carbonaceous material (CM) within albite and quartz. Ab=albite, Qtz=quartz, Phe=phengite	11
Figure 2.1 : Geological map of the area studied across the Central Pontide Supercomplex between Kastamonu-Tosya. For the location see Figure 1.3.	16
Figure 2.2 : Geological cross sections. See Fig. 2.1 for their locations. a) A-A’ section shows the initial structural relations between the Çangaldağ Complex, the Esenler Unit and the Domuzdağ Complex. b) B-B’ section shows the post-metamorphic faulting and folding between the Esenler Unit, Domuzdağ Complex and the Kunduz Metamorphics.....	17
Figure 2.3 : Field photos of the Esenler Unit. a) Sheared and deformed slate and metasandstone intercalation. b) Phyllite exposed close to the contact c) A debris flow level consisting of various sized marble olistoliths. d) A serpentinite slice within the phyllite along the main Kastamonu-Tosya road.	18
Figure 2.4 : Field photos of the Domuzdağ Complex. a) Micaschist with its typical dark grey outcrop color. b) Well-foliated epidote-blueschist	19
Figure 2.5 : Field photos of the extensional shear zone. a) General view of the shear zone with blocks of (from S to N) marbles and a retrogressed metabasite within a grey cataclasite. b) A micaschist block within the cataclasite with NW sense of shear (pencil // lineation)	20
Figure 2.6 : Field photos of the Kunduz Metamorphics. a) General view of the multicolored exposures of marble and metabasite/metatuff intercalation. b) A closer view of the same outcrop. Marbles form strained pods within the metatuff. c) Thinly bedded sodic-amphibole-bearing metatuff and marble intercalation. d) Light colored metatuff, metachert and metabasite interbeds.....	21

Figure 2.7 :	Field photos of the Kirazbaşı Complex. a) Sheared slate-greywacke type mélangé. b) Hemipelagic volcanoclastic sedimentary rocks. c) Discoidal shape pillow lavas. d) Sheared sedimentary mélangé/debris flow with blocks of sandstone, siltstone, limestone and serpentinite.....	23
Figure 2.8 :	Field photos of the İkiçam Formation. (a) & (b) Pyroclastic rocks of andesitic composition. c) Leucite-bearing basalt. d) Volcanoclastic dark grey turbidites. This part mainly consists of sandstone and siltstone	24
Figure 2.9 :	Geological map of the studied section south of Tosya, along the İzmir-Ankara-Erzincan suture with a cross section between A and A'. For location see Fig. 1.3	25
Figure 2.10 :	Field photos of the Köşdağ Formation. All rocks have undergone a low-grade metamorphism but are referred here with their protolith names. a) Basaltic andesite and rhyolite. b) Thin chert interbeds within the acidic and basic rocks. Pyroclastic rocks of acidic (c) and andesitic (d) compositions. e) Red pelagic limestone/chert interbeds with basaltic andesitic rocks. f) A close look to the same outcrop in (e). Folded bright cherts occur within the red pelagic limestone.....	26
Figure 2.11 :	Field photos of the Dikmen Formation. a) Contact between rhyolite and overlying recrystallized reddish micritic limestone of Dikmen Formation in the upper limb of the overturned anticline. b) Yellowish and reddish slate and recrystallized limestone exposed along the transitional section between Köşdağ and Dikmen formations. c&d) Recrystallized calciturbidite consisting intercalation of moderately bedded dark levels consisting of transported coarse grains and thinly bedded pinkish pelagic levels	27
Figure 2.12 :	Measured stratigraphic section illustrating the transitional character between the Köşdağ Formation and the overlying Dikmen Formation. The section is about 250m and is measured along the main road to Yukarıdikmen village. For location, see Fig. 2.9.....	28
Figure 2.13 :	Field photos of the ophiolitic mélangé. a) Serpentinite (green) that is overthrust by recrystallized limestone (pinkish) of Dikmen Formation. b) Pillow basalts.....	29
Figure 2.14 :	Maastrichtian limestone with Orbitoides (a) and Helonocyclina (b) type foraminifera.....	30
Figure 2.15 :	Field photos of the Lower-Middle Eocene limestone (a) and turbidite (b). c) Eocene limestone and overlaying basalt cover. d) Vesicular basalts of probable Eocene age.	31
Figure 2.16 :	a) A general view of the Tosya Basin between the Kunduz Metamorphics to the north and hills made up from the metavolcanic rocks of the Köşdağ Formation to the south. b & c) Field photos of the NAF-related unconsolidated Neogene gravelstone and sandstone of the Tosya Basin.....	32
Figure 2.17 :	Lower hemisphere, equal area projections of the foliations and the lineations. a) Foliation and b) lineation data from the Esenler Unit. c) Foliation and d) lineation measurements of the northern part of the Domuzdağ Complex. Lineations are mostly orthogonal to the NW dipping foliation planes and plunge to the NW related exhumation. e) Foliation data from the southern part of the Domuzdağ Complex and f) the Kunduz Metamorphics. Contour interval is 10.....	33

- Figure 2.18** : Lower hemisphere, equal area projections of the foliations of the Kösdag Formation. Contour interval is 10..... 34
- Figure 3.1** : Representative photomicrographs of the metapelitic rocks from the Esenler Unit (plane polarized light). a & b) Fine-grained slates (samples 847 and 853). Foliation is defined by white mica and partly recrystallized detrital quartz. c & d) Coarser grained phyllites with spaced foliation (samples 31 and 879). Ab=albite, Qtz=quartz, Phe=phengite, Cc=calcite. 36
- Figure 3.2** : Photomicrographs of a greywacke-type metasandstone from the Esenler Unit under plane (left) and cross (right) polarized light. Majority of the clasts are quartz (Qtz) with minor feldspar (Pl) and white mica (Ms).. 36
- Figure 3.3** : A marble with elongated fibrous calcite..... 37
- Figure 3.4** : Plane-polarized photomicrographs of incipient blueschist facies metabasites from the Esenler Unit. a) A foliated blueschist. Foliation is defined by sodic-amphibole (Na-amph). b) An unfoliated metabasite with randomly distributed sodic-amphiboles (sample 211B). Cpx= augite relicts; Ep= epidote; Chl= chlorite; Ab= albite..... 37
- Figure 3.5** : Compositional range of amphibole. Act= actinolite, Gln= glaucophane. 38
- Figure 3.6** : Compositional range of sodic-pyroxene..... 39
- Figure 3.7** : Compositional range of epidotes..... 39
- Figure 3.8** : Compositional range of chlorites..... 39
- Figure 3.9** : Plane-polarized photomicrographs from the Domuzdağ Complex of a) epidote-blueschist and b) albite-chlorite fels that represents a strongly retrogressed blueschist. Na-amph= sodic-amphibole, Chl= chlorite, Ab= albite, Ep= epidote, Cc= calcite 40
- Figure 3.10** : Microphotograph of a lawsonite blueschist (sample 128) from the Domuzdağ Complex. Na-amph= sodic-amphibole, Na-cpx=sodic-pyroxene, Lws= lawsonite, Ttn= titanite. 41
- Figure 3.11** : Compositional range of phengites. Al vs Si diagram showing the celadonite exchange. Decreasing Si content mainly depicts the effect of the retrogression..... 42
- Figure 3.12** : a) BSE image of the garnet-blueschist (702A). Garnet (Grt) exhibit pressure shadow consisting of glaucophane (Gln) + phengite (Phe) +epidote (Ep). Calcic-amphibole (Ca-amph), chlorite (Chl) and albite (Ab) are secondary and replace glaucophane. b) Element mapping of the garnet in Fig. 3.9a with typical growth zoning. Ca and Mg are almost stable. Mn decreases rimward while Fe increases. Ttn=titanite, Aug=augite. 43
- Figure 3.13** : Compositional range of garnets..... 44
- Figure 3.14** : Microphotograph of a retrogressed micaschists from the Domuzdağ Complex with syn-kinematic albite porphyroblasts under plane (left) and cross (right) polarized light. Qtz= quartz, Phe= phengite, Chl= chlorite, Ab= albite. 44
- Figure 3.15** : Photomicrographs of the chloritoid-micaschists from the Domuzdağ Complex (plane polarized light). a) Sample 775, a garnet-chloritoid micaschist. b) Sample 753A, a chloritoid-micaschist. c) Syn-kinematic pseudomorphs after lawsonite (sample 775). Former lawsonite was replaced by epidote (Ep), paragonite (Pa) and quartz (Qtz). The syn-kinematic character of the pseudomorphs suggests that they were stable

- during the peak metamorphic conditions. d) Pseudomorphs after glaucophane (sample 753A). They are replaced by chlorite (Chl), phengite (Phe), and quartz (Qtz). Cld=chloritoid, Grt= garnet. 45
- Figure 3.16** : BSE images of the sample 775. Epidote (Ep) + paragonite (Pa) + quartz (Qtz) replaced former lawsonite and chlorite (Chl) + phengite (Phe) + quartz (Qtz) replaced former glaucophane. Albite (Ab) is secondary. Quartz (Qtz) inclusions in garnet (Grt) do not show any rotational fabric. Cld=chloritoid. 46
- Figure 3.17** : A photomicrograph showing the partly preserved glaucophane (Gln) relicts in the sample 775. The majority of the glaucophanes are replaced by chlorite, phengite and quartz (see Fig 3.16) Qtz= quartz, Phe= phengite..... 47
- Figure 3.18** : Element mapping of the post-kinematic garnet in sample 775. Dark areas within the garnet are quartz inclusions. Notice the Ca-rich outermost rim possibly depicting increasing rate of lawsonite breakdown 47
- Figure 3.19** : Compositional range of the chloritoids. (a) Ternary compositional diagram. While in sample 178, main exchange occur between Fe and Mg, in the samples 775 and 753A Mg mainly substitute with Mn. (b) XMg vs XFe diagram..... 48
- Figure 3.20** : BSE images of the sample 753A. Chlorite(Chl) + phengite (Phe) + quartz (Qtz) replaced former glaucophane. The matrix chlorite penetrates into former glaucophane as secondary thin stripes. Paragonite also possibly replaced former glaucophane along its rims. Apa= apatite. 49
- Figure 3.21** : BSE images of the sample 178. a). Chloritoid (Cld) aggregates together with a rectangular pseudomorph at the center of image composed of albite (Ab). Tiny inclusions of phengites within the pseudomorph exhibit rotational fabrics. Foliation also slightly bends around the pseudomorphs indicating its syn-kinematic origin. It is interpreted as former jadeite. b) A pseudomorph after chloritoid (Cld) within the quartz rich domain. It is replaced by chlorite (Chl) + quartz (Qtz) + phengite (Phe). c) The same pseudomorph in “b” under microscope (plane polarized light). Pa= paragonite. 51
- Figure 3.22** : Microphotographs from the Kunduz Metamorphics. a) A greenschist consisting of calcic-amphibole (Ca-amph), chlorite (Chl), albite (Ab) and titanite (Ttn). b) A blueschist consisting of sodic amphibole (Na-amph), epidote (Ep), albite (Ab) and chlorite (Chl). c) a phyllitic metatuff consisting of phengite (Phe), quartz (Qtz), calcic-amphibole (Ca-amph), chlorite (Chl), stilpnomelane (Stp) with relict clinopyroxene (Cpx). d) A weakly metamorphosed metabasite from the lower part of the Kunduz Metmorphics. Cpx= magmatic pyroxene, Chl= chlorite, Al=albite. 53
- Figure 3.23** : Microphotographs (plane polarized in the left side and cross polarized in the right) of the acidic rocks of the Köşdağ Formation. a & b) SiO₂ saturated metarhyolite with quartz (Qtz) and feldspar (Pl) phenocrysts. c & d) A cognate mafic xenolith within a metarhyolite (1213). It consists of plagioclase (Pl), clinopyroxene, Fe-Ti oxide (Ilm), and apatite. e & f) A cognate xenolith with cumulate-like plagioclases (Pl) with interstitial clinopyroxene (Cpx) in a metarhyolite. Apatite (Apa) and Fe-Ti oxides

- also occur in the xenolith. g & h) A cumulate-like plagioclase cluster without mafic minerals within a metarhyolite (1304B). 55
- Figure 3.24** : Microphotographs (plane polarized in the left side and cross polarized in the right) of the basaltic andesite/andesite of the Kösdag Formation. a & b) Glomeroporphyritic cluster within basaltic andesites, sample 1287 (a&b) and sample 1288 (c&d). e & f) A cognate xenolith consisting of clinopyroxene, plagioclase and apatite in an andesite (1286). Apatite is also found as inclusion within the clinopyroxene. g & h) Metabasite with augite relicts. Ca-amphibole replaces the augite along their rims. 56
- Figure 4.1** : Representative Raman spectra of carbonaceous material of the measured samples from the Esenler Unit. The RSCM forms two clusters corresponding texturally to the slates and phyllites. The sample numbers are given at the right side of the each spectrum..... 60
- Figure 4.2** : Representative examples of fitting of the measured Raman spectra. a) Low-temperature slates that are characterized by undifferentiating of graphite (G) and D2 defect bands and occurrence of broad D3 and D4 defect bands (sample 847). b) Phyllite showing slightly pronounced G band with D2 occurring on its shoulder (sample 230)..... 61
- Figure 4.3** : Representative RSCM of the metapelitic rocks of the Domuzdag Complex..... 63
- Figure 5.1** : PT conditions of an incipient blueschist facies metabasite within the Esenler Unit. Stabilities of the amphiboles are from Otsuki and Banno (1990) and a petrogenetic grid in NCMASH system for low-grade metabasite is from Schiffman and Day (1999) 66
- Figure 5.2** : Diagram showing RSCM temperatures of the metapelitic rocks of the Esenler Unit. The temperatures are obtained using calibrations of Beyssac et al. (2002a) and Rahl et al. (2005). 68
- Figure 5.3** : Pseudosection produced by the Theriak-Domino for the sample 128. Thick blue line limits the stability field of lawsonite, thick dashed line garnet and thin dashed line of paragonite in this specific rock composition. According to XJd (red) of sodic-pyroxene and Si isopleths (grey) of phengite metamorphic conditions of the sample are constrained to 14 ± 2 kbar and $370\text{--}440$ °C (the shaded area)..... 69
- Figure 5.4** : Pseudosection produced by the Theriak-Domino for the sample 702A. For this specific rock composition, thick black line limits stability field of epidote and dashed line of garnet. Stability field of lawsonite is marked by thick blue line. Isopleths; grey, Si content of phengite; green and red, XGrs and XAlm, respectively; dashed isopleth, XJd. Metamorphic conditions constrained as 17 ± 1 kbar and 500 ± 40 °C (the shaded area). 70
- Figure 5.5** : a) Pseudosection modelling for the sample 775. Stability field of garnet is limited by thick black dashed line, of lawsonite by thick red line, of chloritoid by thick green dashed line, of glaucophane by blue line, of paragonite by thin black dashed line for this specific bulk rock composition. b) A detailed part of the pseudosection. Isopleths; grey= Si content of phengite; black and orange are XAlm and XGrs of garnet, respectively, green= XMg of chloritoid. Vertical grey strip indicates temperature values obtained by the RSCM thermometer based on Rahl et al. (2005) calibration. Metamorphic conditions constrained to 17.5 ± 1 kbar and $390\text{--}450$ °C (the shaded area in orange)..... 72

- Figure 5.6 :** Pseudosection produced by the Theriak-Domino for the sample 753A. Stability field of garnet is limited by thick black dashed line, of chloritoid by thick green dashed line, of glaucophane by blue line, of paragonite by thin black dashed line for this specific bulk rock composition. Isopleths; grey= Si content of phengite, green= XMg of chloritoid. Vertical grey strip indicates temperature values obtained by the RSCM thermometer based on Rahl et al. (2005) calibration. Metamorphic conditions constrained to 16-18 kbar and 475 ± 40 °C (the shaded area in orange).. 74
- Figure 5.7 :** Pseudosection modelling for the sample 178. Stability field of garnet is limited by thick black dashed line, of chloritoid by thick green dashed line, of glaucophane by blue lines, of paragonite by red dashed line for the specific bulk rock composition. Isopleths; grey= Si content of phengite, green= XMg of chloritoid. Vertical grey strip indicates temperature values obtained by the RSCM thermometer based on Rahl et al. (2005) calibration. Metamorphic conditions constrained to 22-25 kbar and 440 ± 30 °C (the shaded area in orange). 75
- Figure 5.8 :** Thermal structure of the accreted distal turbidites. The temperature values are from the calibration of Rahl et al. (2005) due to the fact that it is essentially calibrated for low-grade metamorphic rocks. Relatively high temperature phyllites form a sliver within the low temperature slates. A sliver of Na-amphibole-bearing metabasite is possibly associated with the phyllites. 76
- Figure 5.9 :** Compilation of the estimated PT data from the Domuzdağ Complex including chloritoid-micaschists, a lawsonite- and a garnet-blueschist. PT conditions of the Elekdağ eclogites are from Okay et al. (2006a). Possible PT paths for the sample 178 and 775 are indicated by thick grey lines. The dashed parts stand for zero strain decompressional exhumation. Metamorphic facies are modified from Evans (1990). Facies: LBS: lawsonite-blueschist, EBS: epidote-blueschist, EC: eclogite, AEA: albite-epidote amphibolite, GS: greenschist facies. The compilation suggest that Domuzdağ Complex consists of metamorphic rocks that were metamorphosed under distinct PT conditions 79
- Figure 6.1 :** Microphotographs of the samples from the Esenler Unit dated by $^{40}\text{Ar}/^{39}\text{Ar}$ phengite method. a&b) Sample 31 and c&d) sample 230 are phyllites that consist of quartz (Qtz), phengite (Phe), albite (Ab), chlorite (Chl). 82
- Figure 6.2 :** $^{40}\text{Ar}/^{39}\text{Ar}$ age spectra of the analyzed phengites from the (a) sample 31 and (b) sample 230 from the Esenler Unit. 82
- Figure 6.3 :** Microphotographs of the samples from the Domuzdağ Complex dated by $^{40}\text{Ar}/^{39}\text{Ar}$ phengite method. a&b) Sample 392 consists of quartz (Qtz), phengite (Phe), albite (Ab), chlorite (Chl). c&d) Sample 753A consists of chloritoid (Cld), quartz (Qtz), phengite (Phe), chlorite (Chl). 83
- Figure 6.4 :** $^{40}\text{Ar}/^{39}\text{Ar}$ age spectra of the analyzed phengites from the Domuzdağ Complex. a) Sample 392, a micaschist. b) Sample 753A, a chloritoid-micaschist. 84
- Figure 6.5 :** Microphotographs of the samples from the Kunduz Metamorphics dated by $^{40}\text{Ar}/^{39}\text{Ar}$ phengite method. a & b) Sample 626A is a quartz-micaschist consisting of quartz (Qtz), phengite (Phe), hematite (Hem),

- epidote (Ep). c & d) Sample 1290 is a phyllite consisting of quartz (Qtz), phengite (Phe), chlorite (Chl), calcic-amphibole (Amph)..... 85
- Figure 6.6** : $^{40}\text{Ar}/^{39}\text{Ar}$ age spectra of the analyzed phengites from the Kunduz Metamorphics. a) sample 626, a quartz-micaschist. b) Sample 1290, a phyllitic metatuff..... 86
- Figure 6.7** : a) Microphotograph of the dated sample 1214 from the Kösdag Formation. The rock consists of quartz (Qtz), plagioclase (Pl), epidote (Ep) and muscovite (Ms). b) $^{40}\text{Ar}/^{39}\text{Ar}$ age spectrum diagram obtained from the muscovites of this sample by stepwise heating method..... 87
- Figure 6.8** : Cathodoluminescence images of the dated zircons from the sample 1214 (a) and 1215 (b)..... 88
- Figure 6.9** : Zircon U/Pb concordia diagram for the sample 1214 (a) and 1215 (b) and their weighted mean age values (c and d). 88
- Figure 7.1** : Total alkali vs silica classification diagram (Le Bas et al., 1986) of the metavolcanic rocks. Symbols are in accordance with REE diagram in Fig. 7.3a. 93
- Figure 7.2** : a) AFM (Irvine and Barager, 1971) and b) SiO_2 vs FeO/MgO (Miyashiro, 1974) diagrams for the basaltic andesite/andesite of the Kösdag Formation..... 93
- Figure 7.3** : a) Chondrite normalized REE diagram for the metavolcanic rocks according to normalization values of Boynton (1984). b) NMORB normalized multi-element spider diagram of the metavolcanic rocks normalized to Sun and McDonough (1989) values. 94
- Figure 7.4** : a) Cartoon model showing the Late Cretaceous tectonic configuration of the Central Pontides. a) The Kösdag Arc formed at ca. 95 Ma in an intra-oceanic setting located south of the Laurasian active margin. b) Slab rollback controlled arc migration leading to the termination of volcanism in the Kösdag Arc..... 97
- Figure 8.1** : A model showing a possible initial situation of the phyllites and the slates within the Albian accretionary wedge. While the slates represent the offscraped distal turbidites, the phyllite possibly represent underplated metasediments of the turbidite fan. Out-of-sequence thrusting (dashed thick lines) is proposed for uplift and tectonic emplacement of the phyllites. The model is modified after Moore et al. (2001)..... 101
- Figure 8.2** : Model for the tectonic evolution of the Albian-Turonian wedge with a possible tectonic thickening and subsequent exhumation mechanism of the deep seated subduction-accretion complexes. During Albian, the wedge was dominated by accretion of clastic detritus. Lawsonite blueschists possibly formed during initial low shear stress Albian subduction. Late Albian to Turonian evolution of the wedge was mainly controlled by slab rollback, which creates the necessary space for deep level underplating by décollement propagation. Synchronous extension of the wedge by slab rollback, subsequently exhumes the deep-seated metamorphic sequence..... 104
- Figure 8.3** : An exhumation model for the deeply underplated oceanic HP/LT metamorphic sequence by decompression of the wedge along a retreating slab. Zero strain domains are characterized by partly preservation of the peak metamorphic assemblages. Retrogression is manifested by pseudomorphs formed through trapped fluids. B-rich

fluids are generated from the newly underplating oceanic metabasalts and metasediments through dehydration reactions. The fluids then were channelized and migrated upward along the high-strain shear zones.. 107

- Figure 8.4 :** Paleogeographic sketch map at ca. 95 Ma showing the dual subduction during Tethyan consumption (modified from Van der Voo et al. (1999)). Dashed line indicates location of the N-S section along the Central Pontides in Figure 7.4. ATB: Anatolide-Tauride Block..... 112
- Figure A.1 :** Geological map of the area studied across the Central Pontide Supercomplex between Kastamonu-Tosya..... 143
- Figure A.2 :** Geological map of the studied section south of Tosya, along the İzmir-Ankara-Erzincan suture with a cross section between A and A' 145

PRE-COLLISIONAL ACCRETION AND EXHUMATION ALONG THE SOUTHERN LAURASIAN ACTIVE MARGIN, CENTRAL PONTIDES, TURKEY

SUMMARY

The Central Pontides is an accretionary-type orogenic area within the Alpine-Himalayan orogenic belt characterized by pre-collisional tectonic continental growth. The region comprises Mesozoic subduction-accretionary complexes and an accreted intra-oceanic arc that are sandwiched between the Laurasian active continental margin and Gondwana-derived the Kırşehir Block. The subduction-accretion complexes mainly consist of an Albian-Turonian accretionary wedge representing the Laurasian active continental margin. To the north, the wedge consists of slate/phyllite and metasandstone intercalation with recrystallized limestone, Na-amphibole-bearing metabasite (PT= 7–12 kbar and 400 ± 70 °C) and tectonic slices of serpentinite representing accreted distal part of a large Lower Cretaceous submarine turbidite fan deposited on the Laurasian active continental margin that was subsequently accreted and metamorphosed. Raman spectra of carbonaceous material (RSCM) of the metapelitic rocks revealed that the metaflysch sequence consists of metamorphic packets with distinct peak metamorphic temperatures. The majority of the metapelites are low-temperature (ca. 330 °C) slates characterized by lack of differentiation of the graphite (G) and D2 defect bands. They possibly represent offscraped distal turbidites along the toe of the Albian accretionary wedge. The rest are phyllites that are characterized by slightly pronounced G band with D2 defect band occurring on its shoulder. Peak metamorphic temperatures of these phyllites are constrained to 370–385 °C. The phyllites are associated with a strip of incipient blueschist facies metabasites which are found as slivers within the offscraped distal turbidites. They possibly represent underplated continental metasediments together with oceanic crustal basalt along the basal décollement. Tectonic emplacement of the underplated rocks into the offscraped distal turbidites was possibly achieved by out-of-sequence thrusting causing tectonic thickening and uplift of the wedge. $^{40}\text{Ar}/^{39}\text{Ar}$ phengite ages from the phyllites are ca. 100 Ma, indicating Albian subduction and regional HP metamorphism.

The accreted continental metasediments are underlain by HP/LT metamorphic rocks of oceanic origin along an extensional shear zone. The oceanic metamorphic sequence mainly comprises tectonically thickened deep-seated eclogite to blueschist facies metabasites and micaschists. In the studied area, metabasites are epidote-blueschists locally with garnet (PT= 17 ± 1 kbar and 500 ± 40 °C). Lawsonite-blueschists are exposed as blocks along the extensional shear zone (PT= 14 ± 2 kbar and 370–440 °C). They are possibly associated with low shear stress regime of the initial stage of convergence. Close to the shear zone, the footwall micaschists consist of quartz, phengite, paragonite, chlorite, rutile with syn-kinematic albite porphyroblast formed by pervasive shearing during exhumation. These types of

micaschists are tourmaline-bearing and their retrograde nature suggests high-fluid flux along shear zones. Peak metamorphic mineral assemblages are partly preserved in the chloritoid-micaschist farther away from the shear zone representing the zero strain domains during exhumation. Three peak metamorphic assemblages are identified and their PT conditions are constrained by pseudosections produced by Theriak-Domino and by Raman spectra of carbonaceous material: 1) garnet-chloritoid-glaucophane with lawsonite pseudomorphs ($P= 17.5 \pm 1$ kbar, $T: 390-450$ °C) 2) chloritoid with glaucophane pseudomorphs ($P= 16-18$ kbar, $T: 475 \pm 40$ °C) and 3) relatively high-Mg chloritoid (17%) with jadeite pseudomorphs ($P= 22-25$ kbar; $T: 440 \pm 30$ °C) in addition to phengite, paragonite, quartz, chlorite, rutile and apatite. The last mineral assemblage is interpreted as transformation of the chloritoid + glaucophane assemblage to chloritoid + jadeite paragenesis with increasing pressure. Absence of tourmaline suggests that the chloritoid-micaschist did not interact with B-rich fluids during zero strain exhumation. $^{40}\text{Ar}/^{39}\text{Ar}$ phengite age of a pervasively sheared footwall micaschist is constrained to 100.6 ± 1.3 Ma and that of a chloritoid-micaschist is constrained to 91.8 ± 1.8 Ma suggesting exhumation during on-going subduction with a southward younging of the basal accretion and the regional metamorphism. To the south, accretionary wedge consists of blueschist and greenschist facies metabasite, marble and volcanogenic metasediment intercalation. $^{40}\text{Ar}/^{39}\text{Ar}$ phengite dating reveals that this part of the wedge is of Middle Jurassic age partly overprinted during the Albian. Emplacement of the Middle Jurassic subduction-accretion complexes is possibly associated with obliquity of the Albian convergence.

Peak metamorphic assemblages and PT estimates of the deep-seated oceanic metamorphic sequence suggest tectonic stacking within wedge with different depths of burial. Coupling and exhumation of the distinct metamorphic slices are controlled by decompression of the wedge possibly along a retreating slab. Structurally, decompression of the wedge is evident by an extensional shear zone and the footwall micaschists with syn-kinematic albite porphyroblasts. Post-kinematic garnets with increasing grossular content and pseudomorphing minerals within the chloritoid-micaschists also support decompression model without an extra heating.

Thickening of subduction-accretionary complexes is attributed to i) significant amount of clastic sediment supply from the overriding continental domain and ii) deep level basal underplating by propagation of the décollement along a retreating slab. Underplating by basal décollement propagation and subsequent exhumation of the deep-seated subduction-accretion complexes are connected and controlled by slab rollback creating a necessary space for progressive basal accretion along the plate interface and extension of the wedge above for exhumation of the tectonically thickened metamorphic sequences. This might be the most common mechanism of the tectonic thickening and subsequent exhumation of deep-seated HP/LT subduction-accretion complexes.

To the south, the Albian-Turonian accretionary wedge structurally overlies a low-grade volcanic arc sequence consisting of low-grade metavolcanic rocks and overlying metasedimentary succession is exposed north of the İzmir-Ankara-Erzincan suture (İAES), separating Laurasia from Gondwana-derived terranes. The metavolcanic rocks mainly consist of basaltic andesite/andesite and mafic cognate xenolith-bearing rhyolite with their pyroclastic equivalents, which are interbedded with recrystallized pelagic limestone and chert. The metavolcanic rocks are stratigraphically overlain by recrystallized micritic limestone with rare volcanogenic

metaclastic rocks. Two groups can be identified based on trace and rare earth element characteristics. The first group consists of basaltic andesite/andesite (BA1) and rhyolite with abundant cognate gabbroic xenoliths. It is characterized by relative enrichment of LREE with respect to HREE. The rocks are enriched in fluid mobile LILE, and strongly depleted in Ti and P reflecting fractionation of Fe-Ti oxides and apatite, which are found in the mafic cognate xenoliths. Abundant cognate gabbroic xenoliths and identical trace and rare earth elements compositions suggest that rhyolites and basaltic andesites/andesites (BA1) are cogenetic and felsic rocks were derived from a common mafic parental magma by fractional crystallization and accumulation processes. The second group consists only of basaltic andesites (BA2) with flat REE pattern resembling island arc tholeiites. Although enriched in LILE, this group is not depleted in Ti or P.

Geochemistry of the metavolcanic rocks indicates supra-subduction volcanism evidenced by depletion of HFSE and enrichment of LILE. The arc sequence is sandwiched between an Albian-Turonian subduction-accretionary complex representing the Laurasian active margin and an ophiolitic mélange. Absence of continent derived detritus in the arc sequence and its tectonic setting in a wide Cretaceous accretionary complex suggest that the Köşdağ Arc was intra-oceanic. This is in accordance with basaltic andesites (BA2) with island arc tholeiite REE pattern.

Zircons from two metarhyolite samples give Late Cretaceous (93.8 ± 1.9 and 94.4 ± 1.9 Ma) U/Pb ages. Low-grade regional metamorphism of the intra-oceanic arc sequence is constrained 69.9 ± 0.4 Ma by $^{40}\text{Ar}/^{39}\text{Ar}$ dating on metamorphic muscovite from a metarhyolite indicating that the arc sequence became part of a wide Tethyan Cretaceous accretionary complex by the latest Cretaceous. The youngest $^{40}\text{Ar}/^{39}\text{Ar}$ phengite age from the overlying subduction-accretion complexes is 92 Ma confirming southward younging of an accretionary-type orogenic belt. Hence, the arc sequence represents an intra-oceanic paleo-arc that formed above the sinking Tethyan slab and finally accreted to Laurasian active continental margin. Abrupt non-collisional termination of arc volcanism was possibly associated with southward migration of the arc volcanism similar to the Izu-Bonin-Mariana arc system.

The intra-oceanic Köşdağ Arc is coeval with the obducted supra-subduction ophiolites in NW Turkey suggesting that it represents part of the presumed but missing incipient intra-oceanic arc associated with the generation of the regional supra-subduction ophiolites. Remnants of a Late Cretaceous intra-oceanic paleo-arc and supra-subduction ophiolites can be traced eastward within the Alp-Himalayan orogenic belt. This reveals that Late Cretaceous intra-oceanic subduction occurred as connected event above the sinking Tethyan slab. It resulted as arc accretion to Laurasian active margin and supra-subduction ophiolite obduction on Gondwana-derived terranes.

LAVRASYA'NIN GÜNEY AKTİF KENARI BOYUNCA ÇARPIŞMA ÖCESİ EKLEMLENME VE YÜZEYLENME, ORTA PONTİDLER, TÜRKİYE

ÖZET

Orta Pontidler Alp-Himalaya orojenik kuşağı içindeki çarpışma öncesi tektonik kıtasal büyüme ile karakterize olan eklemlemeli-tipteki bir orojenik alanı temsil eder. Bölge, Lavrasya aktif kıta kenarı ile Gondwana kökenli Kırşehir bloğu arasında sıkıştırılmış Mesozoik yaşlı dalma-batma ve eklemleme karmaşıkları ile okyanus-içi bir yayı içerir. Dalma-batma ve eklemleme karmaşıkları temel olarak Lavrasya aktif kıta kenarını temsil eden Albiyen-Turoniyen eklemleme kamasından oluşur. Kuzey kesimlerde, bu kama Lavrasya aktif kıta kenarında çökelmiş ve takiben eklenerek başkalaşıma uğramış Alt Kretase yaşlı geniş bir denizaltı türbidit yelpazesinin iraksak kesimlerini temsil eden sleyt/fillat ve metakumtaşı aralanması ile rekristallize kireçtaşı, sodik amfibollü metabazit (PT= 7–12 kbar and 400 ± 70 °C) ve serpantin tektonik dilimlerini içerir. Bu istife ait metapelitik kayaçların organik malzeme Raman spektrumları (RSCM), istifin farklı metamorfik sıcaklıklara sahip metamorfik paketler içerdiğini göstermektedir. Metapelitik kayaçların çoğunluğu düşük sıcaklıklarda (ca. 330 °C) oluşmuş sleytler olup grafit (G) ve D2 kusur bantlarının ayrışmaması ile karakterize olur. Bu kayaçlar muhtemelen Albiyen eklemleme kamasının ucu boyunca kazanmış iraksak türbiditleri temsil etmektedir. Geri kalan metapelitik kayaçlar ise omuz kesiminde D2 bandı yer alan hafifçe belirginleşmiş G bantları ile karakterize olan fillatlardır. Bu fillatların metamorfizma sıcaklıkları 370-385 °C olarak sınırlandırıldı. Fillitik kayaçlar başlangıç mavişist fasiyesli metabazit şeridi ile ilişkilidir ve kazanmış iraksak türbiditler içinde kıymık halinde bulunmaktadır. Bu kayaçlar muhtemelen bazal sıyrılmaya boyunca kama-altı-sıvanmış kıtasal metasedimentleri ile okyanus kabuğu basaltlarını temsil eder. Bu kama-altı-sıvanmış kayaçların, kazanmış iraksak türbiditler içine tektonik olarak yerleşmesi muhtemelen kamanın tektonik olarak kalınlaşmasına ve yükselmesine neden olan dizi-dışı bindirmelerce sağlanmıştır. Fillatların $^{40}\text{Ar}/^{39}\text{Ar}$ fengit yaşları yaklaşık 100 Ma olup Albiyen yaşlı bir dalma-batmaya ve bölgesel yüksek basınç başkalaşımına işaret eder.

Eklenmiş kıtasal metasedimentler genişlemeli bir makaslama zonu boyunca okyanusal yüksek basınç/düşük sıcaklık metamorfik kayaçlarının üzerine gelir. Okyanusal metamorfik dizi baskın olarak tektonik olarak kalınlaşmış derin-oluşumlu eklojit ve mavişist fasiyesli metabazitleri ve mikaşistleri kapsar. Çalışma alanında, metabazitler yersel olarak granatlı epidot-mavişistlerdir (PT= 17 ± 1 kbar and 500 ± 40 °C). Lavsonit-mavişistler makaslama zonu boyunca bloklar halinde yüzeyler (PT= 14 ± 2 kbar and 370–440 °C). Bu kayaçlar muhtemelen yitimin başlangıç aşamasındaki zayıf makaslama stres rejimi ile ilişkilidir. Makaslama zonu yakınında, yüzeyleme boyunca yaygın bir biçimde makaslanan taban mikaşistleri kuvars, fengit, paragonit, klorit, rutil, ile kinematik ile eş anlı gelişen albit porfiroblastı içerir. Bu tip mikaşistler turmalinli olup, bunların gerileme tabiatları makaslama zonları boyunca yüksek akışkan akısı olduğunu akla getirir. Başkalaşımın doruk koşullarına ait mineral toplulukları, makaslama zonunun uzağındaki, yüzeyleme esnasında

yamulmaya maruz kalmamış alanları temsil eden kloritoyid-mikaşistlerde kısmen korunmuştur. Kloritoyid-mikaşistlerde üç farklı metamorfik birliktelik tanımlandı ve bunların sıcaklık-basınç koşulları Theriak-Domino tarafından hesaplanan yalancı kesitler ile içerdikleri organik malzemenin Raman spektrumları kullanılarak sınırlandırıldı: Fengit-paragonit-kuvars-klorit-rutil ve apatite ek olarak 1) granat-kloritoyid-glokofan ile lavsonit psödomorfları ($P= 17.5 \pm 1$ kbar, $T: 390-450$ °C), 2) kloritoyid ile glokofan psödomorfları ($P= 16-18$ kbar, $T: 475 \pm 40$ °C) ve 3) görece yüksek Mg'lu kloritoyid (%17) ile jadeyit psödomorfları ($P= 22-25$ kbar; $T: 440 \pm 30$ °C). Üçüncü mineral topluluğu kloritoyid-glokofan birlikteliğinin yükselen basınca bağlı olarak kloritoyid-jadeyit parajenezine dönüşümü olarak yorumlandı. Turmalinin bulunmaması, kloritoyid-mikaşistlerin yamulma olmadan yüzeylerken B'ca zengin akışkanlarla etkileşmediğini işaret eder. Yaygın olarak makaslanmış bir taban mikaşistin $^{40}\text{Ar}/^{39}\text{Ar}$ fengit yaşı 100.6 ± 1.3 Ma ve bir kloritoyid-mikaşistin ki ise 91.8 ± 1.8 Ma olarak sınırlandırıldı. Bu yaşlar yüzeylemenin yitim devam ederken gerçekleştiğini ve bazal eklemleme ile bölgesel metamorfizmanın güneye doğru gençleştiğini gösterir. Güney kesimlerde eklemleme kaması mavişist ve yeşilşist fasiyesli metabazit, mermer ve volkanojenik metasediment araldanmasından oluşur. $^{40}\text{Ar}/^{39}\text{Ar}$ fengit yaşları eklemleme kamasının bu kesimlerinin Orta Jura yaşlı olduğunu ve Albiyen döneminde kısmen tekrar metamorfizmaya uğradığını göstermektedir. Orta Jura yaşlı dalma-batma ve eklemleme karmaşıklarının tektonik yerleşmesi muhtemelen Albiyen yitiminin verev olmasıyla ilintilidir.

Derin-oluşumlu okyanusal metamorfik diziyeye ait metamorfizmanın doruk koşulları temsil eden mineral toplulukları ve sıcaklık-basınç hesapları, kama içerisinde farklı derinliklerde gelişen bir tektonik istiflenmeye işaret eder. Farklı metamorfik dilimlerin yüzeylenmesi ve yan yana gelmesi, muhtemelen yiten okyanusal levhanın geriye göçü neticesinde kamayı dekomprese etmesi tarafından denetlenmektedir. Yapısal olarak, kamanın dekomprese olması genişlemeli makaslama zonu ve kinematik ile eş anlı albit porfiroblastlı taban mikaşistleri ile belirgindir. Kloritoyid-mikaşistler içindeki kinematik sonrası granatların grosular bileşimindeki artış ve psödomorf içindeki mineraller de ilave ısı artışı olmadan, dekompresyon nedeni ile yüzeyleme modelini destekler.

Dalma-batma ve eklemleme karmaşıklarının kalınlaşması aşağıdaki iki hususa yoruldu: 1) üzerleyen kıtasal alandan önemli miktarda sediment akışının olması ve 2) geriye göç eden yiten okyanusal levha boyunca bazal sıyrılanın yayılarak derin seviyelerde gerçekleşen bazal kama-altı-sıvanması. Derin-oluşumlu eklemleme karmaşıklarının bazal sıyrılanın yayılmasına bağlı kama-altı-sıvanması ve takibeden yüzeylenmesi birbiriyle bağlantılı olup, levha gerilemesi tarafından kontrol edilmektedir. Levha gerilemesi, plaka arayüzeyi boyunca gelişen bazal eklemleme için gerekli mekânı yaratırken, kama üzerinde genişlemeye neden olarak tektonik olarak kalınlaşan bu eklemleme karmaşıklarının yüzeylenmesine olanak sağlar. Bu derin-oluşumlu dalma-batma ve eklemleme karmaşıklarının tektonik kalınlaşmasının ve takibeden yüzeylenmesinin en genel mekanizması olabilir.

Albiyen-Turoniyen eklemleme kaması, güneyde, Lavrasya'yı Gondwana-türevli kıtasal bloklardan ayıran İzmir-Ankara-Erzincan kenedinin boyunca yüzeyleyen ve düşük-dereceli metavolkantiler ile bunları stratigrafik olarak üzerleyen metasedimenter kayaçlardan oluşan bir volkanik yay istifini yapısal olarak üzerler. Metavolkanik kayaçlar baskın olarak bazaltik andezit/andezit ve mafik ksenolit içeren riyolit ile pelajik kireçtaşı ve çört arakatlı piroklastik eşleniklerini içerir. Metavolkanitler stratigrafik olarak volkanojenik metasedimenter arakatlı rekristalize

mikritik kireçtaşları tarafından üzerlenir. Volkanik kayalar nadir toprak ve iz elementlerinin özelliklerine göre iki gruba ayrılır. Birinci grup bazaltik andezit/andezit (BA1) ile jenetik olarak ilintili yaygın gabroyik ksenolitler barındıran riyolitleri kapsar. Bu grup hafif nadir toprak elementlerinin ağır olanlara göre zenginleşmesiyle karakterize olur. Bu gruba ait kayalar akışkanlarca kolayca taşınan geniş iyonlu elementlerce (LILE) zenginken, Fe-Ti oksitlerin ve apatit fraksiyonlaşmasını yansıtan Ti ve P'ca fakirleşmiştir ki bu mineraller jenetik olarak ilintili gabroik ksenolitler içinde de bulunurlar. Riyolitlerde ve andezitlerde yaygın gabroyik ksenolitlerin oluşu ve benzer nadir toprak ve iz element içerikleri, riyolitler ile bazaltik andezit/andezitlerin (BA1) jenetik olarak ilintili olduğunu ve felsik kayaların fraksiyonel kristallenme ve birikme süreçleriyle ortak bir mafik mağmadan tüvelendiğini işaret eder. İkinci grup ise sadece bazaltik andezitleri içerir (BA2). Bu kayaların nadir toprak element desenleri düz olup ada-yayı toleyitlerine benzemektedir. LILE'lerce zenginleşmesine rağmen, bu grup Ti ve P'ca fakirleşmemiştir.

Metavolkanik kayaların jeokimyası, HFSE fakirleşmesi ve LILE zenginleşmesi ile belirginleşen yitim-üstü volkanizmasını işaret eder. Yay dizisi Lavrasya aktif kıta kenarını temsil eden Albiyen-Turoniyen yaşlı dalma-batma/eklemlenme karmaşığı ile ofiyolitik melanj arasında sıkıştırılmıştır. Yay dizisi içerisinde kıta türevli kırınların bulunmayışı ve geniş bir eklemlenme karmaşığı içerisindeki tektonik konumu, bu Kösdag Yayının okyanus-ıci bir yay olduğuna işaret eder. Bu ada yayı toleyitlerine benzer düz nadir toprak element desenli bazaltik andezitlerin (BA2) varlığıyla uyumludur.

Metariyolitlerden ayrılan zirkonlar Geç Kretase (93.8 ± 1.9 and 94.4 ± 1.9 Ma) U/Pb yaşı vermektedir. Okyanus-ıci yay dizisinin düşük dereceli bölgesel metamorfizması bir metariyolit örneğindeki metamorfik muskovitler üzerinde yapılan $^{40}\text{Ar}/^{39}\text{Ar}$ yaşlandırmasıyla 69.9 ± 0.4 Ma olarak sınırlandırıldı. Bu yaş, yay dizisinin en geç Kretase'de geniş bir Kretase yaşlı Tetis eklemlenme karmaşığının parçası haline geldiğine işaret eder. Üzerleyen dalma-batma ve eklemlenme karmaşıklarına ait en genç $^{40}\text{Ar}/^{39}\text{Ar}$ fengit yaşı 92 Ma olup, eklemlenmeli orojenezin güneye doğru gençleştiğini doğrulamaktadır. Bu durumda, Geç Kretase yaşlı yay dizisi yiten Tetis okyanusal levhasının üzerinde gelişmiş ve en sonunda Lavrasya aktif kıta kenarına yamanmış bir okyanus-ıci eski volkanik yayı temsil etmektedir. Mağmatizmanın çarpışma öncesi ani bir şekilde kesilmesi yay volkanizmasının Izu-Bonin-Mariana yay sistemine benzer şekilde muhtemelen güneye doğru göç etmesi ile ilintilidir.

Okyanus-ıci Kösdag Yayının, KB Türkiye'de yüzeleyen yitim-üstü ofiyolitleri ile eş yaşlı olması, onun bölgesel yitim-üstü ofiyolit oluşumuyla ilintili varolduğu tahmin edilen fakat tanımlanamayan okyanus-ıci yayın bir parçasını temsil ettiğini akla getirmektedir. Geç Kretase yaşlı okyanus-ıci eski yay kalıntıları ve bunlarla ilintili yitim-üstü ofiyolitler doğuya doğru Alp-Himlaya dağkuşığı boyunca izlenebilir. Bu durum Geç Kretase okyanus-ıci yitiminin yiten Tetis okyanusal levhası üzerinde birbiriyle bağlantılı olarak gerçekleştiğini gösterir. Bu yitim, Lavrasya aktif kıta kenarına yay eklemlenmesi ve Gondwana-türevli kıtasal blokların üzerine ise yitim-üstü ofiyolitlerinin bindirmesi şeklinde sonuç vermiştir.

1. INTRODUCTION

The term of accretionary, Pacific- or Turkeic-type orogeny has been used to emphasize the pre-collisional growth of continental crust by subduction and accretion processes (Şengör et al., 1993; Şengör and Natal'in, 1996; Maruyama, 1997; Dickinson, 2008; Cawood et al., 2009). This includes addition of juvenile material to the crust in the magmatic arcs and ocean-ward tectonic growth of the associated accretionary prism (Fig. 1.1). Additionally, oceanic crustal edifices like seamounts, oceanic plateaus and intra-oceanic arcs are favored to accrete rather than recycling into the mantle due to their relatively high buoyancy (Cloos, 1993). An accretionary orogeny is best recognized by tectonically thickened subduction-accretionary complexes composed of trench turbidites, high pressure/low temperature (HP/LT) metamorphic rocks, ophiolitic fragments and mélanges. There are two modes of accretion proposed: i) frontal accretion through offscraping mainly of trench-fill turbidites and oceanic pelagic sediments as wedge shape packages (e.g. Seely et al., 1974; Karig and Sharman, 1975; Moore et al., 1982; Ujiie 1997) and ii) underplating as duplexes beneath the offscraped part of the prism (Fig. 1.1, e.g. Platt et al., 1985; Sample and Fischer, 1986; Kimura et al., 1996). These two types of accretions were also simulated by analog sandbox experiments (e.g. Gutscher et al., 1998; Malavieille, 2010). A significant portion of accretion occurs at deeper part of the accretionary wedge (>30 km) as revealed by seismic studies on modern subduction zones (Moore et al., 1991; Ye et al., 1997; Calvert, 2004; Kimura et al., 2010). This type of deep-level underplating is evidenced by eclogite and blueschist facies metamorphic rocks of the exhumed subduction-accretionary complexes (e.g. Takasu et al., 1994; Barr et al., 1999; Agard et al., 2001; Okay et al., 2002, 2006a; Tsujimori et al., 2006a). Tectonic thickening of these deep-seated HP/LT metamorphic rocks, however, remains ambiguous due to the necessary space problem for basal accretion along the plate interface.

Accretionary orogenies have been defined in many regions including the Altaiids (Şengör et al., 1993; Şengör and Natal'in, 1996), the Circum-Pacific realm (e.g.

Isozaki, 1996; Maruyama, 1997; Dickinson, 2008; Fuis et al., 2008), and the Lachlan orogeny of eastern Australia (Foster and Gray, 2000; Spaggiari et al., 2002). Their geographical distribution and age ranges suggest that they play a major role for continental crustal growth (Cawood et al., 2009). In the Alpine-Himalayan orogenic belt, however, accretionary-type continental growth is apparently rare. Accretionary complexes or mélanges in the Tethyan belt are generally regarded as suture zones separating the main continental domains (Şengör and Natal'in, 1996) and the Alpine-Himalayan orogeny is interpreted as a collisional rather than accretional mountain belt.

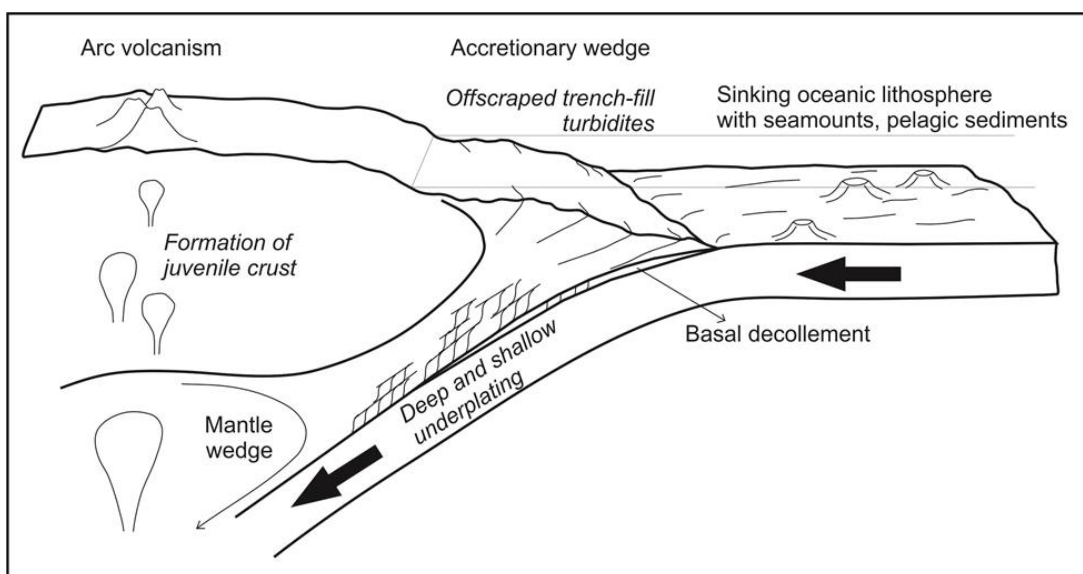


Figure 1.1 : Main components of an accretionary-type orogeny including oceanward tectonic growth of subduction-accretionary wedge and addition of juvenile material to the crust. Modified from Barr et al. (1999).

However, in the central part of the Pontides, an Alpine-Himalayan mountain chain along northern Turkey, Mesozoic subduction-accretionary complexes crop out over large areas suggesting a major contribution of pre-collisional accretionary processes along the southern Eurasian active continental margin. Accretionary units comprise Middle Jurassic and Cretaceous subduction-accretionary complexes called as Central Pontide Supercomplex (CPS) (Okay et al., 2013). In the CPS, Cretaceous accretionary units consist of HP/LT metamorphic units of continental and oceanic origin, forearc deposits and mélanges accreted to the Eurasian active continental margin. The Cretaceous accretionary complexes include low-grade distal turbidites exposed to the north. They are underlain by oceanic crust derived deep-seated HP/LT metamorphic rocks along an extensional shear zone. Furthermore, Middle Jurassic

subduction-accretionary complexes are found within the Cretaceous accretionary wedge as tectonic slices. To the south, the CPS structurally overlies arc-related metavolcanic rocks which are thrust over the ophiolitic rocks of the İzmir-Ankara-Erzincan Suture (İAES), separating the Laurasia from Gondwana-derived continental blocks.

Without an understanding of this accretionary-type orogenic period in the Central Pontides, attempts of tectonic reconstructions within the Tethyan realm will inevitably be incomplete. Moreover, the accretionary units that are sourced from both continental and oceanic crusts provide a natural laboratory for a better understanding of accretionary wedge tectonics worldwide.

1.1 Regional Geology

The Pontides are a mountain chain between the Black Sea and the İzmir-Ankara-Erzincan suture, which separates Laurasia from Gondwana-derived terranes, Anatolide-Taurides and Kırşehir Massif (Fig. 1.2). It represents part of the Mesozoic active continental margin of Laurasia (Okay and Nikishin, 2015; Meijers et al., 2010a) and was rifted from the Eurasian mainland by opening of the Black Sea as back-arc basin during Late Cretaceous (Okay et al., 1994; Okay and Tüysüz, 1999). The Pontides comprise three tectonic units: the Strandja Massif, the İstanbul and Sakarya zones (Okay, 1989; Fig. 1.2). Contact relations between these tectonic units are still controversial. However, the most prominent structure is the east-west striking Intra-Pontide suture zone, separating the İstanbul Zone from the Sakarya Zone (Okay and Tüysüz, 1999; Robertson and Ustaömer, 2004; Akbayram et al., 2013; Göncüoğlu et al., 2014).

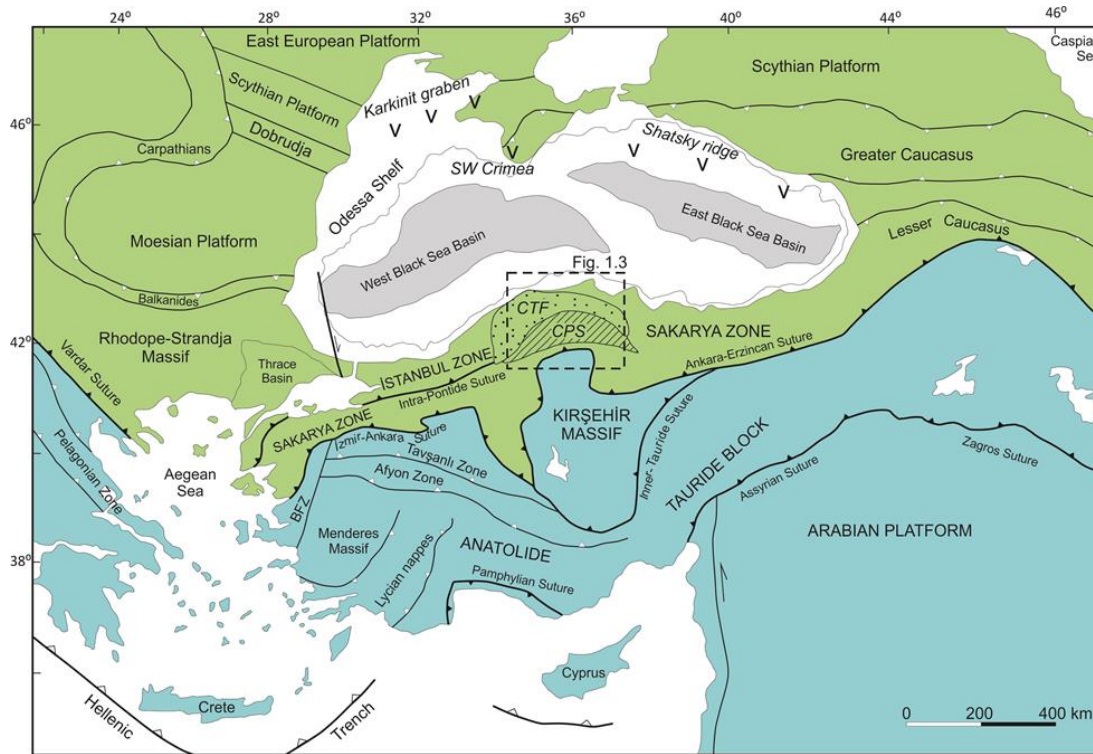


Figure 1.2 : Tectonic map of Turkey and surrounding regions (modified from Okay and Tüysüz, 1999). Green and pale blue colors highlight the Laurasia and Gondwana-derived terranes, respectively. CPS: Central Pontide Supercomplex, CTF: Lower Cretaceous submarine turbidite fan. North of the Black Sea, “V” marks the Albian volcanic arc modified from Nikishin et al. (2015).

İstanbul Zone is a continental fragment in the western part of the Pontides. It has a crystalline basement consisting of gneiss, amphibolite and metavolcanic rocks that were intruded by Neo-Proterozoic granitoids (Ustaömer and Rogers, 1999; Yiğitbaş et al., 2004; Ustaömer et al., 2005). The crystalline basement is unconformably overlain by an Ordovician-Carboniferous sedimentary sequence (Görür et al., 1997; Özgül, 2012). The Paleozoic sequence is unconformably covered by Triassic red beds passing into shallow and deep marine limestones. Upper Cretaceous arc related volcanic and volcanoclastic rocks are exposed in the northern part of the İstanbul Zone along the SW shores of the Black Sea. In terms of lithology, İstanbul Zone is similar to the Moesian platform to the north and Okay et al. (1994) suggested that İstanbul Zone was rifted from the Moesian Platform during opening of the Black Sea.

The Sakarya Zone forms a ribbon along the northern Turkey and consists of slivers of Devonian granitoids (Okay et al., 1996; Aysal et al., 2012; Sunal, 2012), Permo-Carboniferous high-grade metamorphic and related intrusive rocks (Okay et al., 1996, 2006b; Topuz et al., 2004, 2007), and Late Triassic subduction-accretionary

complexes with eclogite and blueschist slices (Okay and Monié, 1997; Okay, 2000; Okay et al., 2002; Okay and Göncüoğlu, 2004; Pickett and Robertson, 2004; Topuz et al., 2014). Recently, Middle Jurassic subduction-accretion complexes were also reported in the Eastern Pontides suggesting episodic accretionary construction of the Pontides (Topuz et al., 2013a). This basement is unconformably overlain by a Jurassic to Lower Cretaceous transgressive sedimentary sequence (Okay, 2008).

To the South, the Pontides are separated from the Gondwana-derived terranes, the Anatolide-Taurides and the Kırşehir Massif, along the İAES. The Anatolide-Taurides is represented by HP/LT metamorphic rocks that were metamorphosed by continental subduction in Late Cretaceous (80-60 Ma, Sherlock et al., 1999; Okay, 2002; Plunder et al., 2013; Pourteau et al., 2010, 2013). The HP/LT metamorphic rocks are widely overlain by ophiolite and accretionary complexes. Metamorphic sole ages of the ophiolites concentrate between 90-93 Ma (Dilek et al., 1999; Parlak & Delaloye, 1999; Önen & Hall, 2000; Önen, 2003; Çelik et al., 2006). In the central Turkey, there is a large area of Upper Cretaceous metamorphic and granitic rocks, known as the Kırşehir Massif. It is composed of Late Cretaceous LP/HT metamorphic rocks and associated widespread granitoids representing an ensiallic arc (Seymen, 1981; Whitney et al., 2003; Whitney & Hamilton, 2004; İlbeyli et al., 2004; Köksal et al., 2004; Boztuğ et al., 2009; Lefebvre et al., 2013).

1.2 Geology of the Central Pontides

In the Central Pontides, the İstanbul Zone is represented by a Neo-Proterozoic crystalline basement consisting of tonalitic and granitic metagranitoids with 590-560 Ma zircon crystallization ages exposed northwest of Araç (Fig. 1.3, Chen et al., 2002). The basement rocks are stratigraphically overlain by Early Ordovician to Devonian sedimentary rocks of the İstanbul Paleozoic sequence (Boztuğ, 1992; Dean et al., 2000). The Sakarya Zone consists of Permo-Carboniferous granitic rocks (Nzegge et al., 2006; Okay et al., 2015) and Upper Triassic distal turbidites with dismembered ophiolites, known as the Küre Complex, (Ustaömer and Robertson, 1993, 1994, 1997; Okay et al., 2015).

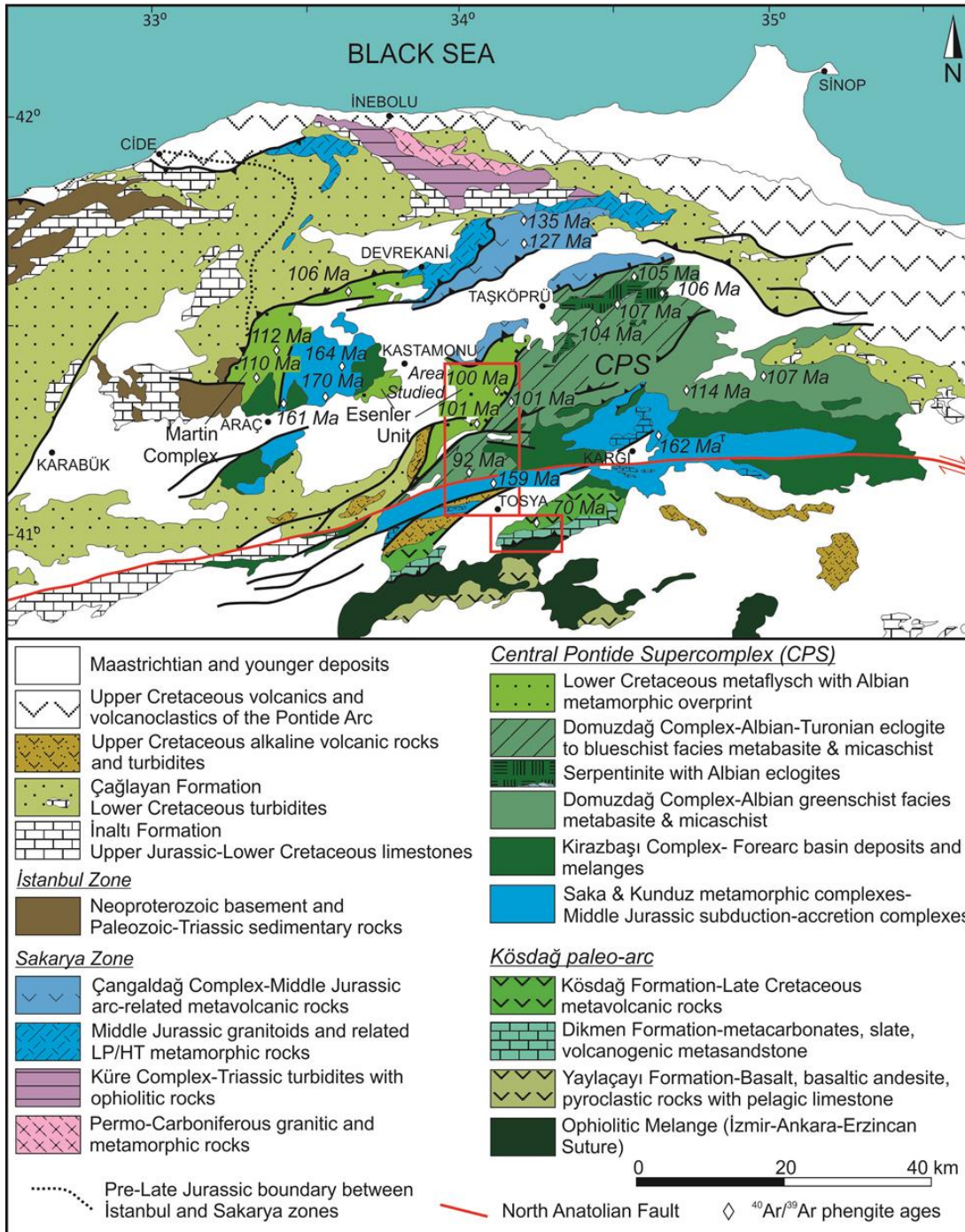


Figure 1.3 : Geological map of the Central Pontides modified from Tüysüz (1990), Uğuz et al. (2002), Okay et al. (2013, 2014) and this study.

The Küre Complex is intruded by Middle Jurassic granitoids representing part of a major magmatic arc (Yılmaz and Boztuğ, 1986; Okay et al., 2014). The granitoids are associated with Middle Jurassic low pressure and high temperature metamorphic rocks constituting deeper levels of the magmatic arc (Okay et al., 2014).

Upper Jurassic limestones, named as the İnaltı Formation unconformably cover the basement rocks of İstanbul and Sakarya zones indicating that these tectonic zones

were juxtaposed before the Late Jurassic (Tüysüz 1999; Okay et al., 2013). The limestones of the İnaltı Formation are unconformably overlain by the Lower Cretaceous turbidites, known as the Çağlayan Formation, which forms an arc shaped sub-marine fan (Fig. 1.3). The Çağlayan Formation consists of sandstone and dark shale and comprises a large number of blocks of Upper Jurassic-Lower Cretaceous shallow marine limestone and lesser amounts of Paleozoic sandstone derived from the underlying sequences of the İstanbul Zone. Based on its nannofossil contents, the Çağlayan Formation is assigned a Barremian to Aptian age (Hippolyte et al., 2010). A Lower Cretaceous depositional age is further supported by detrital zircons (Okay et al., 2013). The Çağlayan Formation is interpreted as syn-rift deposits related to opening of the Black Sea basin (Görür, 1988; Hippolyte et al., 2010). Detrital zircons from the turbidites, however, indicate a major source area in the East European Craton and Scythian Platform north of the Black Sea implying that the Black Sea basin opened after Early Cretaceous time (Okay et al., 2013).

South of the Lower Cretaceous turbidites, metamorphic rocks crop out over a large area. These rocks were previously considered as the pre-Jurassic basement of the Central Pontides (e.g., Yılmaz and Şengör, 1985; Tüysüz, 1990; Ustaömer and Robertson, 1994, 1999; Yılmaz et al., 1997; Uğuz et al., 2002). However, recent studies have shown that this area consists of Middle Jurassic and Early Cretaceous subduction-accretionary complexes and was collectively named as Central Pontide Supercomplex (CPS, Fig. 1.3; Okay et al., 2013). Within the CPS, Cretaceous accretionary complexes comprise Albian HP/LT metamorphic rocks of both continental and oceanic origin, forearc deposits and mélanges representing the Laurasian active continental margin. An associated Albian arc is reported north of the Black Sea (Fig. 1.2, Nikishin et al., 2015). Middle Jurassic subduction-accretionary complexes are exposed as tectonically emplaced slices within the Cretaceous wedge (Okay et al., 2013; Marroni et al., 2014; this study). They form part of a Middle Jurassic subduction system along the Laurasian margin (Çelik et al., 2011; Dilek and Thy, 2006; Okay et al., 2014; Robertson et al., 2013; Topuz et al., 2013a, 2013b). The CPS is unconformably overlain by an Upper Cretaceous volcano-sedimentary sequence representing fore-arc deposits (Okay et al., 2006a, 2013; Tüysüz and Tekin, 2007). The Central Pontides have been subjected up to 40°

Late Cretaceous-Paleocene counter-clockwise rotation revealed by paleomagnetic studies (Meijers et al., 2010b).

The Cretaceous accretionary wedge is characterized by presence of voluminous accreted terrigenous metaclastic rocks in the north. The accreted metaclastic rocks consist of slate/phyllite and metasandstone with blocks of marble, metabasite and serpentinite, all representing the distal parts of the Lower Cretaceous turbidite fan deposited on Laurasian active continental margin and subsequently accreted (Okay et al., 2013; this study). There are two main exposures of the metaflysch units: i) the Martin Complex exposed north of Araç with a contact with Lower Cretaceous turbidites (Fig.1.3) ii) the Esenler Unit exposed further southeast of Kastamonu (area studied). While the Martin Complex is characterized by greenschist facies metamorphism, the Esenler Unit contains metabasites showing incipient blueschist facies metamorphism. $^{40}\text{Ar}/^{39}\text{Ar}$ phengite dating on the Martin Complex constrains the regional metamorphism to Albian (112-106 Ma) (Okay et al., 2013). Clastic zircon studies on the Martin Complex reveal that it represents metamorphosed equivalents of the Lower Cretaceous turbidite fan (Okay et al., 2013).

The metaclastic sequence is underlain by a metabasite-dominated HP/LT metamorphic sequence. This Domuzdağ Complex consists mainly of eclogite to blueschist facies metabasite and micaschist with serpentinites, metagabbro, metachert and marble representing deep levels of a subduction-accretionary complex (Tüysüz, 1990; Ustaömer and Robertson, 1993, 1994, 1999; Altherr et al., 2004; Okay et al., 2006a, 2013). $^{40}\text{Ar}/^{39}\text{Ar}$ phengite ages from the Domuzdağ Complex constrained HP/LT metamorphism to Albian (114-104 Ma; Okay et al., 2006a, 2013).

To the south of the CPS, arc-related metavolcanic rocks known as Köşdağ Formation exposes as a tectonic slice along the main Tethyan İzmir-Ankara-Erzincan suture (Tüysüz, 1990, 1993). The Köşdağ Formation consists of greenschist facies mafic and felsic lavas with pyroclastic rocks that are interbedded with Upper Cretaceous pelagic limestone without terrigenous input (Tüysüz 1990, 1993; Rice et al., 2006). Although initially described as an intra-oceanic arc sequence (Tüysüz, 1990), the Köşdağ Formation was later interpreted as an ensialic arc formed above the Laurasian active margin (Tüysüz, 1993; Tüysüz et al., 1995) or an island arc that was

separated from the Laurasian margin by a marginal sea formed as a back arc basin (Rice et al., 2006).

1.3 Purpose of Thesis

During this study, the geology of a north-south transect across the Central Pontides between Kastamonu and Tosya towns is mapped. The transect consists of two main sections (Fig. 1.3). The first section is made across the CPS between Kastamonu and Tosya towns. The aim of the section is to characterize continental and oceanic crust derived accretionary units and their contacts, determine the age and grade of the HP/LT metamorphism. The geological, petrologic and geochronological data are interpreted in terms of the tectonic growth of the wedge. A major portion of the accretionary wedge comprises deep-seated HP/LT metamorphic sequences. Another aim of the thesis is to unveil exhumation of these deep-seated HP/LT metamorphic sequences in connection with their tectonic thickening within the wedge.

The second section is located south of Tosya town, along the northern edge of the İAES where metavolcanic rocks are widely exposed. Main purpose of this section is to understand the petrogenesis of the metavolcanic rocks and unveiling transition between the CPS and the İAES with regional tectonic implications.

1.4 Methodology

The study based on field and laboratory data. The field studies include geological mapping, collecting structural data and sampling. During geological mapping, 1:25.000 scaled topographic maps were used. Planar and linear structural data were collected by Brunton-type compass and geographical positions by Navitech GPS. In the field studies, around 300 samples were collected along the two sections mapped between Kastamonu and Tosya. Thin sections of the samples were prepared in thin section laboratories of both İstanbul Technical University and University of Potsdam. After petrographical investigations of the thin sections, selected thin sections (~10) were polished for detailed mineral chemistry analysis. Polished thin sections were prepared at the University of Potsdam.

1.4.1 PT calculations

Metamorphic conditions were constrained through conventional geothermobarometric methods based on the single reactions calculated by THERMOCALC software, PT modelling through pseudosections calculated by Theriak-Domino and Raman spectra of carbonaceous material. Necessary analytical data were obtained by electron microprobe analysis (EMPA), X-ray fluorescence (XRF) and Raman microspectrometry on carbonaceous material.

Microprobe analyses of the selected samples were performed on polished thin sections by JEOL JXA8200 electron microprobe at the University of Potsdam using natural standards. Measurement conditions were 15 keV acceleration potential, 10 nA beam current and a beam diameter of 2-5 microns for counting times of 20 s. Beside the single spot analyses, element mapping of suitable minerals like garnet were also made.

1.4.1.1 THERMOCALC

Single reactions were calculated by THERMOCALC (3.33) software (Powell & Holland, 1988). The program uses the thermodynamic data set of Holland & Powell (1998). Activities of reaction were calculated by the AX program for a known mineral chemistry. Metamorphic conditions of an incipient blueschist facies metabasite are constrained by THERMOCALC software.

1.4.1.2 Theriak-Domino

Metamorphic conditions of two blueschists and three chloritoid-micaschists were constrained by pseudosections produced by Theriak-Domino software. It calculates equilibrium mineral assemblages of a given bulk rock composition by the Gibbs free energy minimization method (de Capitani & Brown, 1987; de Capitani & Petrakakis, 2010). Bulk rock chemistry was obtained by XRF analysis of the metamorphic rocks. During calculation of the pseudosections, Mn was excluded due to lack of thermodynamic data for Mn-endmembers.

1.4.1.3 Raman spectra of carbonaceous material (RSCM) thermometers

Raman microspectroscopy on carbonaceous material were performed at the Raman Laboratory of the Institute of Earth and Environmental Sciences at Potsdam

University using a confocal, edge filter-based spectrometer (LabRam HR 800, HORIBA Jobin–Yvon) with a Nd:YAG laser for excitation at a wavelength of 532 nm. Measurements were performed in situ on polished thin sections. Thin sections of the samples were cut orthogonal to the foliation and parallel to lineation. Carbonaceous particles below transparent minerals like quartz, albite and white mica were measured to exclude influences of polishing-related mechanical destruction of the carbonaceous material structure (Fig. 1.4; Pasteris, 1989; Beyssac et al., 2002a, 2002b; Scharf et al., 2013). 20 to 30 points were measured for each of all samples with an acquisition time of 120 s. However, some of the analyzed points were eliminated due to the contamination with the epoxy. Measured Raman spectra of the carbonaceous material were decomposed for all Raman peaks of carbon by the PeakFit (v4.12) software. A Voight function was used for fitting of the Raman bands. Fitting procedures applied to 1000-2000 cm^{-1} interval of the Raman range, which contains the first-order region of the Raman spectrum (Tuinstra and Koenig, 1970; Nemanich and Solin, 1979). The first-order region (1100-1800 cm^{-1}) hosts the main graphite band (G band, at 1580 cm^{-1}) with defects bands D1, at 1350 cm^{-1} and D2, at 1620 cm^{-1} . Broad defect bands of D3 (at 1500 cm^{-1}) and D4 (at 1200 cm^{-1}) occur in carbonaceous material at low temperatures with very poorly ordered atomic structure (Beyssac et al., 2002a, 2002b; Sadezky et al., 2005; Lahfid et al., 2010).

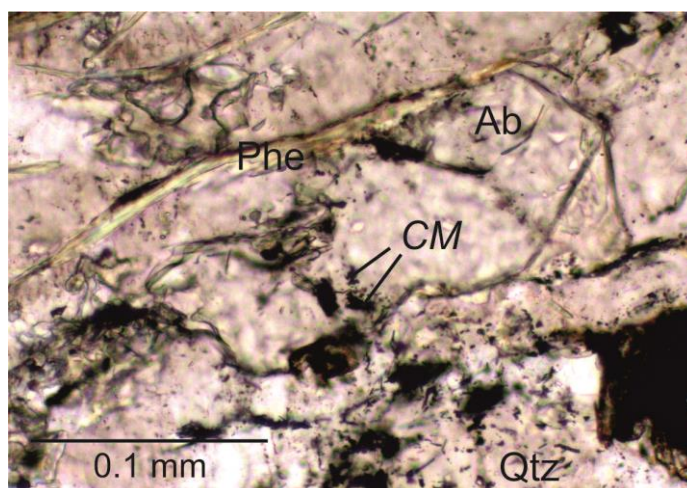


Figure 1.4 : A photomicrograph in plane polarized light showing carbonaceous material (CM) within albite and quartz. Ab=albite, Qtz=quartz, Phe=phengite.

Raman spectra of carbonaceous material (RSCM) is a relatively new, empirically calibrated thermometer based on the graphitization of the carbonaceous material with increasing metamorphic grade (Beyssac et al., 2002a; Rahl et al., 2005; Aoya et al.,

2010; Lahfid et al., 2010). For temperature calculations two empirical RSCM calibrations were used. Calibration of Beyssac et al. (2002a) uses R2 ratio of integral intensities of the bands $[(D1 / (G + D1 + D2)) A]$ and is applicable for a temperature range of 330–650 °C. Rahl et al. (2005) presented a modified calibration using both R1 $[(D1/G) H]$ and R2 ratios extending the temperature range between 100–700 °C. Both calibrations are reported to have ± 50 °C error range. Since graphitization is an irreversible process; RSCM thermometers give the peak metamorphic temperatures (Pasteris and Wopenka, 1991; Beyssac et al., 2002a).

1.4.2 Geochemistry

Major, trace and rare earth element composition were analyzed to investigate the petrogenesis of metavolcanic rocks of Kösdag Formation. Bulk rock compositions were obtained by XRF. Rocks powders were prepared at the Mineral Separation Laboratory of İTÜ by crushing and grinding. Glassy pellets were prepared in the University of Potsdam. XRF measurements on the prepared pellets were performed at GeoForschungsZentrum, Potsdam. Trace and rare earth elements analyses of the selected rhyolitic and basaltic volcanic rocks were made by Inductively Coupled Plasma Atomic Emission Spectrometry (ICP-AES) at the University of Potsdam. Detailed trace element analyses of three samples were made at the ACME Lab, Canada.

1.4.3 Geochronology

1.4.3.1 $^{40}\text{Ar}/^{39}\text{Ar}$ white mica geochronology

In order to constrain the age of regional metamorphism, phengite separates were dated by $^{40}\text{Ar}/^{39}\text{Ar}$ method. The dating has been conducted at the $^{40}\text{Ar}/^{39}\text{Ar}$ geochronology laboratory at the University of Potsdam. Phengite separates were prepared in the Mineral Separation Lab, İTÜ. After crushing and sieving the rocks, white mica of 125 to 250 μm across is enriched by the Frantz magnetic separator. Lastly, we used paper to remove the impurities within the separates.

The $^{40}\text{Ar}/^{39}\text{Ar}$ analytical system of University of Potsdam consists of (1) a New Wave Gantry Dual Wave laser ablation system with a 50W CO_2 laser (wavelength 10.6 micrometer) for heating samples, (2) an ultra-high vacuum purification line with SAES getters and a cold trap kept at freezing temperature of ethanol, and (3) a high-

sensitivity Micromass 5400 noble gas mass spectrometer with an electron multiplier to conduct pulse-counting analysis, which effectively works for very minor amounts of Ar gas.

Neutron activation of phengite separates was performed at the reactor of NRG Petten, Netherlands and at the OSTR, the TRIGA Reactor in the Oregon State University, Oregon, USA (samples 1214 and 1290). All the unknown samples were wrapped by commercial Al foils, then contained in 99.999% pure two Al containers with 22.7 mm diameter and 32.5 mm height. The neutron flux monitoring mineral Fish Canyon Tuff sanidine age standard, which was prepared by Geological Survey of Japan (27.5 Ma; Uto et al., 1997; Ishizuka, 1998), the crystals of K_2SO_4 and CaF_2 for correction of interference by the Ar isotopes produced by nuclear reaction on K and Ca in samples, and two biotite K-Ar age standards, SORI93 biotite (92.6 ± 0.6 Ma; Sudo et al., 1998) and HD-B1 biotite (24.21 ± 0.32 Ma; Hess and Lippolt, 1994) for checking accuracy of the system, were contained together for neutron irradiation. The Al container was finally wrapped by Cd foil with 1.0 mm thickness to cut off thermal neutron fluxes in order to reduce unnecessary nuclear reactions in samples. The neutron irradiation was performed for 10 hours with fast neutron flux of 1×10^{13} n/cm²/s (4 hours with fast neutron flux of 2.5×10^{13} n/cm²/s for the samples 1214 and 1290). Samples were cooled down for one or two month at the reactor, and then were brought back to Potsdam for $^{40}Ar/^{39}Ar$ analysis.

Stepwise heating of the phengite separates of around 0.1 mg has been conducted with a defocused continuous CO₂ laser beam for 1 minute. Then, the extracted gas has been exposed to the SAES getters and a cold trap for 10 minutes to gain a pure Ar-sample gas. Finally, the Ar gas was admitted to the mass spectrometer to determine the Ar-isotope ratios. The isotopic ratios of each analysis have finally been obtained after corrections of blank, mass discrimination by the analysis of atmospheric argon, interference of Ar isotopes derived from Ca and K, and the decay of the Ar isotopes (^{37}Ar and ^{39}Ar) produced by the irradiation. Age and error calculation followed descriptions in Uto et al. (1997). Except the samples 1214 and 1290, the $^{40}Ar/^{39}Ar$ analyses were performed 480-520 days after the neutron irradiation, thus, Ca-derived ^{37}Ar (half-life; 35.1 days) in phengite samples had almost decayed at the analysis because of its originally Ca poor chemical composition (typical Ca/K ratio is 0.01) of phengites. Therefore, in age calculation, ^{37}Ar amounts assumed as each Ca/K ratio in

the analytical result indicates around 0.01 were given to all Ar analytical results. The used ratio of production rate to convert from $^{37}\text{Ar}_{\text{Ca}}/^{39}\text{Ar}_{\text{K}}$ to Ca/K was 1.7 based on the Table 3-3 in McDougall and Harrison (1999). The $^{40}\text{Ar}/^{39}\text{Ar}$ ages from all the steps adopted for the plateau ages in this study do not vary beyond 0.03 Ma between the cases of zero or 0.1 for Ca/K ratios. Therefore, $^{37}\text{Ar}_{\text{Ca}}$ amounts adopted in this study gives enough accurate $^{40}\text{Ar}/^{39}\text{Ar}$ ages. The criterion for identifying plateau ages followed Fleck et al. (1977).

1.4.3.2 U/Pb zircon geochronology

Magmatic crystallization age of the metavolcanic rocks of the Köşdağ Formation was constrained by U/Pb zircon dating. The dating was performed by LA-ICP-MS (Thermo Scientific ELEMENT 2 single collector magnetic sector ICP-MS with CETAC LSX-213 G2 laser system) at the University of Potsdam.

Zircons were separated from two metarhyolite samples (1214 and 1215) by conventional methods in the Istanbul Technical University. After crushing, sieving and magnetic separation, zircons were enriched by using heavy liquid, sodium polytungstate (SPT). Finally, 63-125 μm sized zircon crystals were embedded in to epoxy and polished. Before the measurements, cathodoluminescence images of the zircon grains were taken.

The correction for laser-induced elemental fractionation and mass discrimination by the instrument was done by normalizing to the GJ1 zircon standard (Jackson et al., 2004). Data reduction was performed with the software PepiAGE (Dunkl et al., 2009) using a linear regression line fitting over time for the measured isotope ratios of the GJ1 zircon, and a t-zero intercept for the individual U/Pb ratios of standard and sample analysis. Spot analyses of sample zircons were also corrected for common Pb contributions using the Hg-corrected ^{204}Pb signal.

2. GEOLOGY

Along the Kastamonu-Tosya transect, there are two main lithological associations below the Eocene and younger sedimentary cover. The first one comprises Mesozoic subduction-accretionary complexes including HP/LT metamorphic rocks, mélanges and forearc deposits forming part of the Central Pontide Supercomplex (CPS). The HP/LT metamorphic units consist of Cretaceous low-grade HP metaflysch sequence, the Esenler Unit and a metabasite-dominated oceanic Domuzdağ Complex. Within the Cretaceous HP/LT metamorphic rocks, Middle Jurassic subduction-accretionary complexes, known as Kunduz Metamorphics, crop out as a tectonic slice. The HP/LT metamorphic rocks are unconformably overlain by a volcanoclastic unit. In the upper levels, this Kirazbaşı Complex passes into a debris flow and a mélange consisting predominately of ophiolitic blocks. In the southern part of the CPS, alkaline volcanic rocks and turbidites are exposed as a tectonic slice. This İkiçam Formation were possibly initially unconformably covering the HP/LT metamorphic rocks.

The second lithological association is an accreted arc sequence exposed north of the İzmir-Ankara-Erzincan Suture (IAES) south of Tosya. It consists predominately of metavolcanic rocks with their pyroclastic equivalents, the Köşdağ Formation and stratigraphically overlying metasedimentary rocks, the Dikmen Formation. To the south, the arc sequence overthrust an ophiolitic mélange. To the north, the arc sequence is structurally underlain the CPS. General geological features of the accretionary units and the arc sequence are given below.

2.1 Mesozoic Subduction-Accretionary Complexes

In the area studied, accretionary complexes comprise Middle Jurassic and Cretaceous subduction-accretion complexes forming part of the Central Pontide Supercomplex (CPS). The Cretaceous accretionary complexes consist of HP/LT metamorphic units derived from both continental and oceanic crust, forearc basin deposits and mélanges representing the Laurasian active continental margin. Three major metamorphic units are distinguished (Figs. 2.1, 2.2).

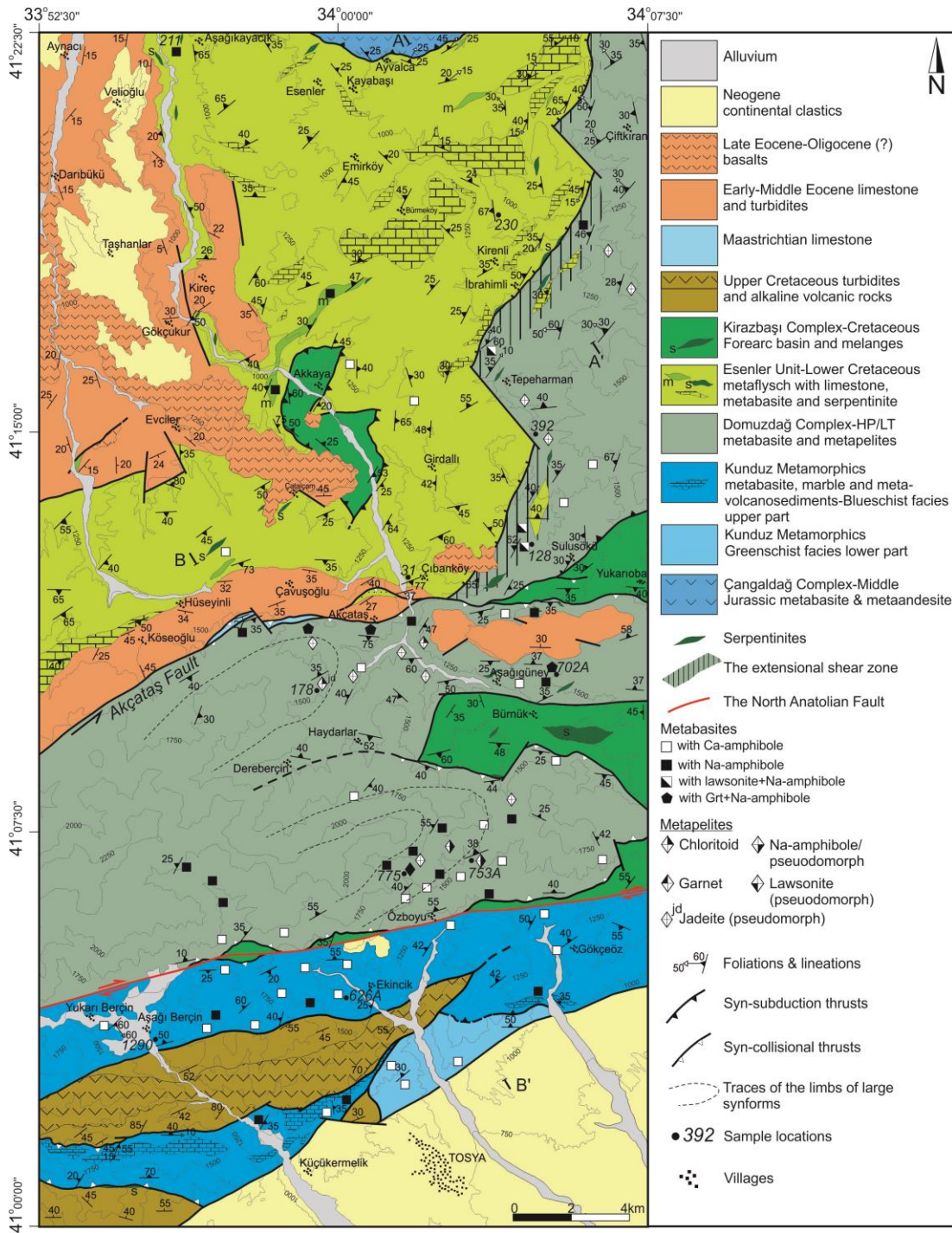


Figure 2.1 : Geological map of the area studied across the Central Pontide Supercomplex between Kastamonu-Tosya. For the location see Figure 1.3.

In the northwest, there is a thick metaclastic sequence, the Esenler Unit, showing incipient blueschist facies metamorphism. To the south, the Esenler Unit is underlain along an extensional shear zone by a tectonically thickened metamorphic sequence dominated by metabasic rocks. This Domuzdağ Complex has undergone a high-grade blueschist facies metamorphism. In the south of the Domuzdağ Complex, there is another metabasite-dominated unit, the Kunduz Metamorphics with low-grade

blueschist facies metamorphism of Middle Jurassic age. It is separated from the Domuzdağ Complex by the North Anatolian Fault.

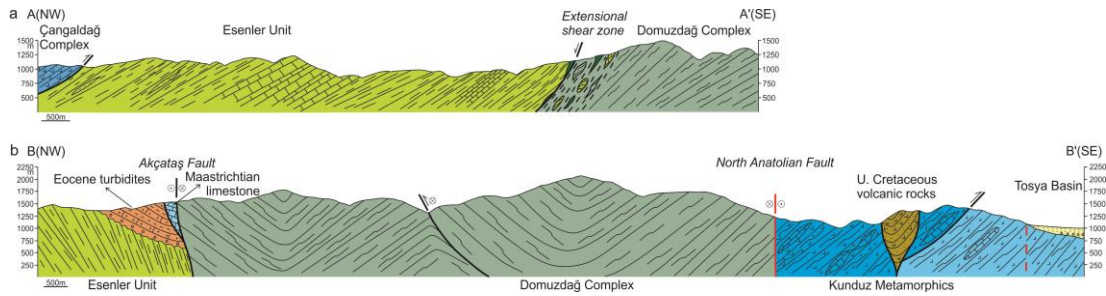


Figure 2.2 : Geological cross sections. See Fig. 2.1 for their locations. a) A-A' section shows the initial structural relations between the Çangaldağ Complex, the Esenler Unit and the Domuzdağ Complex. b) B-B' section shows the post-metamorphic faulting and folding between the Esenler Unit, Domuzdağ Complex and the Kunduz Metamorphics.

2.1.1 Esenler Unit: Accreted distal turbidites

In the NW part of the area studied, there is a thick metasedimentary sequence, named as the Esenler Unit (Fig. 2.1). The Esenler Unit is a metamorphosed flysch sequence composed predominantly of slate/phyllite and metasandstone intercalation with marble olistoliths and tectonic slices of Na-amphibole bearing metabasite and serpentinite. Metasandstones are mostly of greywacke type and occur as sheared pods within the slates (Fig. 2.3a). Close to the contacts, however, slates transform into phyllites (Fig. 2.3b). The nature of this slate to phyllite transition is not clear. Debris flow levels consisting of clast to boulder size recrystallized limestone blocks occur within the metaflysch sequence (Fig. 2.3c). These gravity-driven recrystallized limestone blocks can reach up to 200 m across. Barkurt et al. (1990) describe Lower Cretaceous fossils from these limestones. Some of the marble blocks show a fibrous fabric suggesting that aragonite was the stable phase (Brady et al., 2004; Seaton et al., 2009). Most of the metabasites show an incipient blueschist facies metamorphism and consist of sodic- and calcic-amphibole, sodic-pyroxene, epidote, chlorite, albite and titanite with augite relicts. Sheared serpentinite slices are found along shear zones together with phyllites (Fig. 2.3d).

North of the study area, the Esenler Unit is overthrust by low-grade metavolcanic rocks, which possibly form part of the Çangaldağ Complex, a Middle Jurassic volcanic arc (Okay et al., 2014). To the south, the Esenler Unit is separated from the

Domuzdağ Complex by an extensional shear zone, partly overprinted by a post-Eocene strike slip fault, called as Akçataş Fault (Figs. 2.1, 2.2).



Figure 2.3 : Field photos of the Esenler Unit. a) Sheared and deformed slate and metasandstone intercalation. b) Phyllite exposed close to the contact c) A debris flow level consisting of various sized marble olistoliths. d) A serpentinite slice within the phyllite along the main Kastamonu-Tosya road.

In terms of lithology, grade and metamorphic age, the Esenler Unit resembles the metamorphosed Lower Cretaceous turbidites, the Martin Complex, exposed NW of Araç (Fig. 1.2). However, while the metabasites of Esenler Unit show an incipient blueschist facies metamorphism, in the Martin Complex the metamorphism is in greenschist facies. The Esenler Unit possibly represents distal parts of the Lower Cretaceous turbidite fan deposited on Laurasian active continental margin that was subsequently accreted and metamorphosed.

2.1.2 Domuzdağ Complex: Oceanic metabasalt and metasediments

The Domuzdağ Complex consists of micaschist (about 40% of the sequence) metabasite (40%) and serpentinite (5%) with minor amounts of metachert, marble and metagabbro (Fig. 2.4). Metabasites are mostly well-foliated epidote-blueschists locally with garnet. The common mineral assemblage in the blueschist metabasites is

sodic amphibole + epidote + chlorite + titanite + albite ± garnet. Retrogression to albite-chlorite fels is common with relicts of sodic-amphibole.

In terms of geochemistry, metabasites of the Domuzdağ Complex predominantly exhibit MORB (Mid-Ocean Ridge Basalt) and within-plate basalt characteristics (Ustaömer and Robertson, 1999). Dominant oceanic crustal lithologies, geochemistry of the metabasites, and blueschist to eclogite facies HP/LT metamorphism indicate that the Domuzdağ Complex was formed along an active margin and represents a subduction-accretionary complex (Tüysüz, 1990; Ustaömer and Robertson, 1994, 1999; Okay et al., 2006a, 2013).

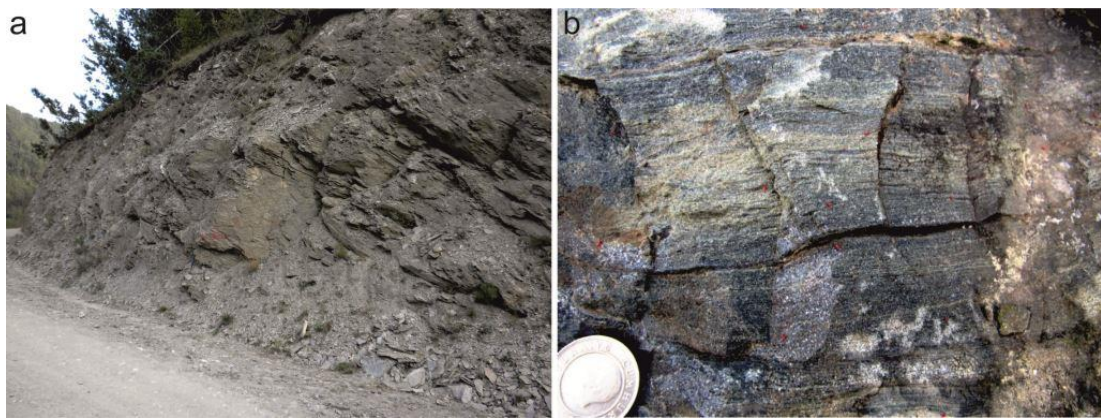


Figure 2.4 : Field photos of the Domuzdağ Complex. a) Micaschist with its typical dark grey outcrop color. b) Well-foliated epidote-blueschist.

In the area studied, Domuzdağ Complex is overlain by the Esenler Unit along an extensional shear zone. To the south of the extensional shear zone, the footwall micaschists consist of quartz, phengite, paragonite, chlorite, rutile, apatite, tourmaline and calcite with syn-kinematic albite porphyroblast with rotational inclusion fabrics. They are characterized by absence of peak metamorphic assemblages and occurrence of syn-kinematic albite porphyroblasts suggesting that they were formed by pervasive shearing during exhumation. Peak metamorphic assemblages are partly preserved in the chloritoid-micaschists farther away from the shear zone representing zero strain domains of exhumation. Three peak metamorphic assemblages are identified: 1) garnet + chloritoid + glaucophane with pseudomorphs after lawsonite 2) chloritoid with pseudomorphs after glaucophane 3) chloritoid with pseudomorphs after jadeite in addition to phengite, paragonite, quartz, chlorite, rutile and apatite.

2.1.2.1 Extensional shear zone

An extensional shear zone of ca. 600 m in thickness forms the main boundary between continental and oceanic accretionary units. It is characterized by mixing of blocks from the hanging- and foot-wall within a highly sheared brittle fault cataclasite (Fig. 2.5).

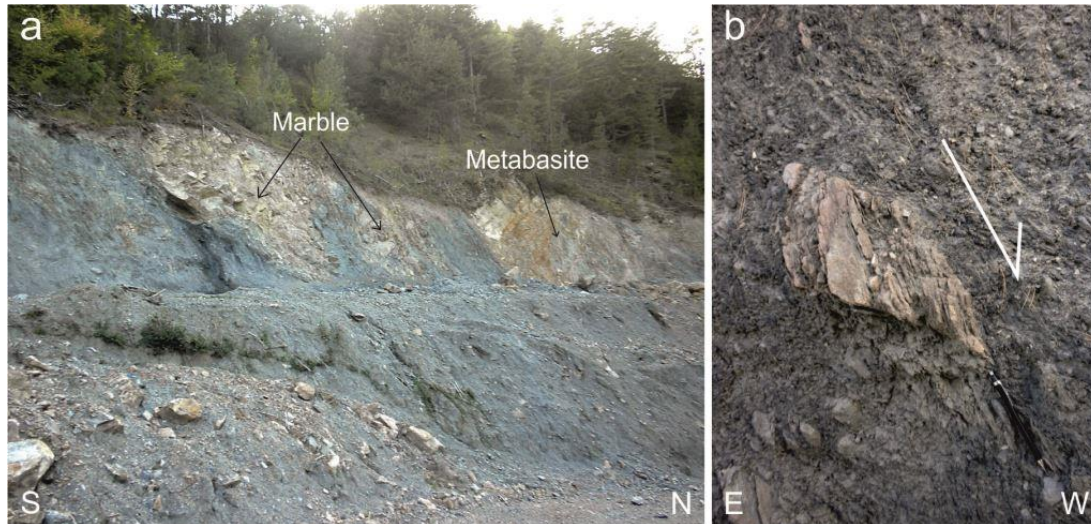


Figure 2.5 : Field photos of the extensional shear zone. a) General view of the shear zone with blocks of (from S to N) marbles and a retrogressed metabasite within a grey cataclasite. b) A micaschist block within the cataclasite with NW sense of shear (pencil // lineation).

Marble, serpentinite, metabasite, and micaschist blocks are found along the extensional shear zone. Metabasites consist of fresh lawsonite-blueschist and retrogressed albite-chlorite fels with relicts of aligned Na-amphibole, which resemble the metabasites of the Domuzdağ Complex. Lawsonite-blueschists predominantly consist of lawsonite and sodic-amphibole with additional sodic-pyroxene, chlorite, phengite, epidote, albite and titanite. Absence of lawsonite relicts in the albite-chlorite fels suggests that mixing of distinct metabasites occurred late in the exhumation. NW dipping stretching lineations are observed within or around the shear zone, especially in the footwall micaschists, which are characterized by the syn-kinematic albite porphyroblasts. Blocks within the fault gouge consistently indicate top to NW sense of shear (Fig. 2.5b). The shear zone was responsible for the final exhumation of deeply buried metabasites and micaschists of the Domuzdağ Complex to shallow levels.

2.1.3 Kunduz Metamorphics

To the south, the Domuzdağ Complex is in contact with a metabasite-marble dominated unit along the North Anatolian Fault. The unit, which forms the western extension of the Kunduz Metamorphics of Tüysüz (1990), consists of metabasite, volcanogenic metasediments and metatuff intercalated with pale marble horizons and minor metachert (Fig. 2.6). It is easily identified by its multicolored exposures in the field.

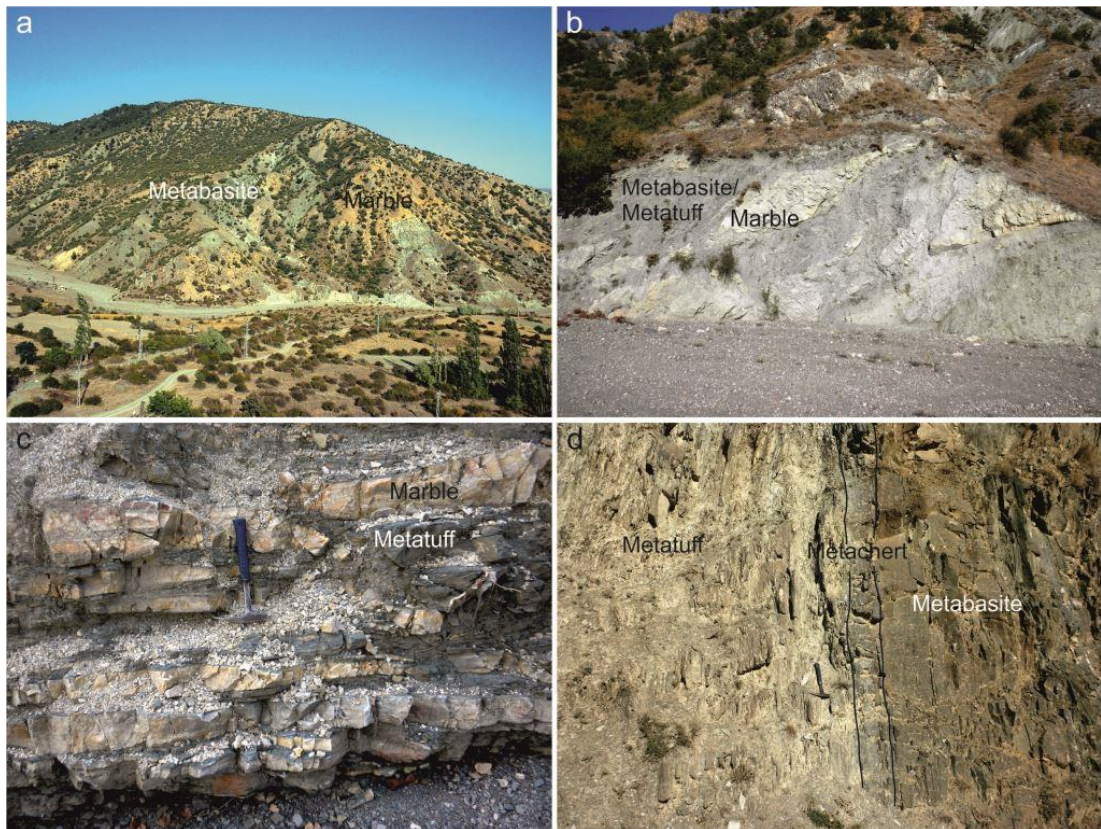


Figure 2.6 : Field photos of the Kunduz Metamorphics. a) General view of the multicolored exposures of marble and metabasite/metatuff intercalation. b) A closer view of the same outcrop. Marbles form strained pods within the metatuff. c) Thinly bedded sodic-amphibole-bearing metatuff and marble intercalation. d) Light colored metatuff, metachert and metabasite interbeds.

The common mineral paragenesis in the metabasites is calcic-amphibole, epidote, chlorite, albite and titanite locally with sodic-amphibole. Primary sedimentary structures of the volcanogenic metasediments like bedding are locally preserved. Marble forms sheared pods within relatively weak sodic-amphibole bearing metatuff. In the area studied, the Kunduz Metamorphics are structurally divided into two parts by a thrust fault (Figs. 2.1, 2.2). The structurally upper part shows higher degree of

metamorphism and deformation, which are evidenced by well-foliated metabasites locally with sodic amphibole. In the lower part, however, metabasites are weakly foliated and do not have any high-pressure index minerals, and magmatic textures and mafic minerals are mostly retained. In the lower part, metamorphism is characterized by growth of tiny calcic amphibole, epidote and chlorite.

2.1.4 Kirazbaşı Complex: Forearc basin and mélanges

The CPS is widely overlain by an Upper Cretaceous volcano-sedimentary sequence. Most of the contacts of the volcano-sedimentary unit, called the Kirazbaşı Complex, with the metamorphic rocks are faulted. However, at a few localities a stratigraphic contact is preserved (Yiğitbaş et al., 1990, Okay et al., 2006a). In these localities, the Kirazbaşı Complex starts with Turonian pelagic limestones, which pass up into siliciclastic turbidites overlain by mass flows and ophiolitic mélange, consisting of basalt, radiolarian chert, serpentinite, pelagic shale and limestone. Tüysüz and Tekin (2007) describe Cretaceous (Barremian to Cenomanian) radiolaria from the chert blocks within the Kirazbaşı Complex. In the area studied, there are two main exposures of this unit. Around Akkaya village, reddish hemipelagic siltstone-shale alternation is overlain by slightly sheared greywacke-shale alternation with pillow basalt and chert blocks (Fig. 2.7a, b and c). Around Bürnük, a clastic sedimentary sequence consisting of sandstone and siltstone is overlain by a mélange consisting of serpentinite, radiolarian chert, basalt, diabase and grey limestone blocks. There are also sheared debris flows consisting mainly of blocks of sandstone and siltstone with serpentinite and limestone (Fig. 2.7d). The Kirazbaşı Complex is interpreted as a forearc basin developed in front of southward verging thrust slices in the accretionary prism.

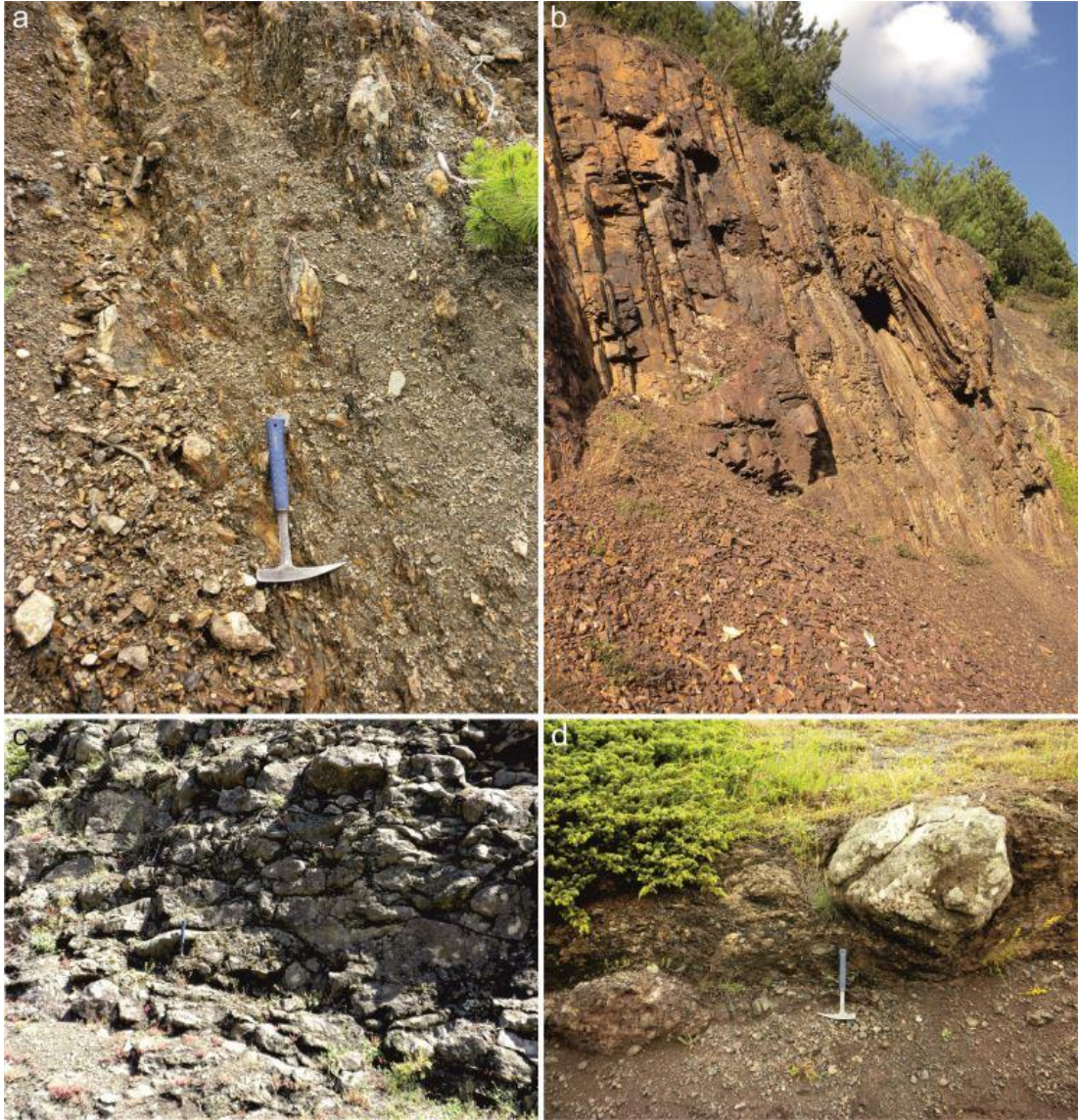


Figure 2.7 : Field photos of the Kirazbaşı Complex. a) Sheared slate-greywacke type mélange. b) Hemipelagic volcanoclastic sedimentary rocks. c) Discoidal shape pillow lavas. d) Sheared sedimentary mélange/debris flow with blocks of sandstone, siltstone, limestone and serpentinite.

2.1.5 İkiçam Formation: Alkaline volcanic rocks and turbidites

In the southern part of the area studied, alkaline volcanic rocks and volcanoclastic turbidites are widely exposed in tectonic contact with the Kunduz Metamorphics (Fig. 2.1). The volcanic sequence consists predominantly of pyroclastic rocks interbedded with volcanogenic sandstone and siltstone (Fig. 2.8a, b). Some of the basalts contains large leucite crystals characteristic of alkaline volcanism (Fig. 2.8c). The contact relation between the pyroclastic rocks and leucite-bearing basalts is not clear. Syenitic dykes, probably form part of the İkiçam Formation, are common and crosscut the metamorphic rocks of the Kunduz Metamorphics. The volcanic

sequence is associated with dark turbidites possibly representing distal and deeper of the basin (Fig. 2.8d).

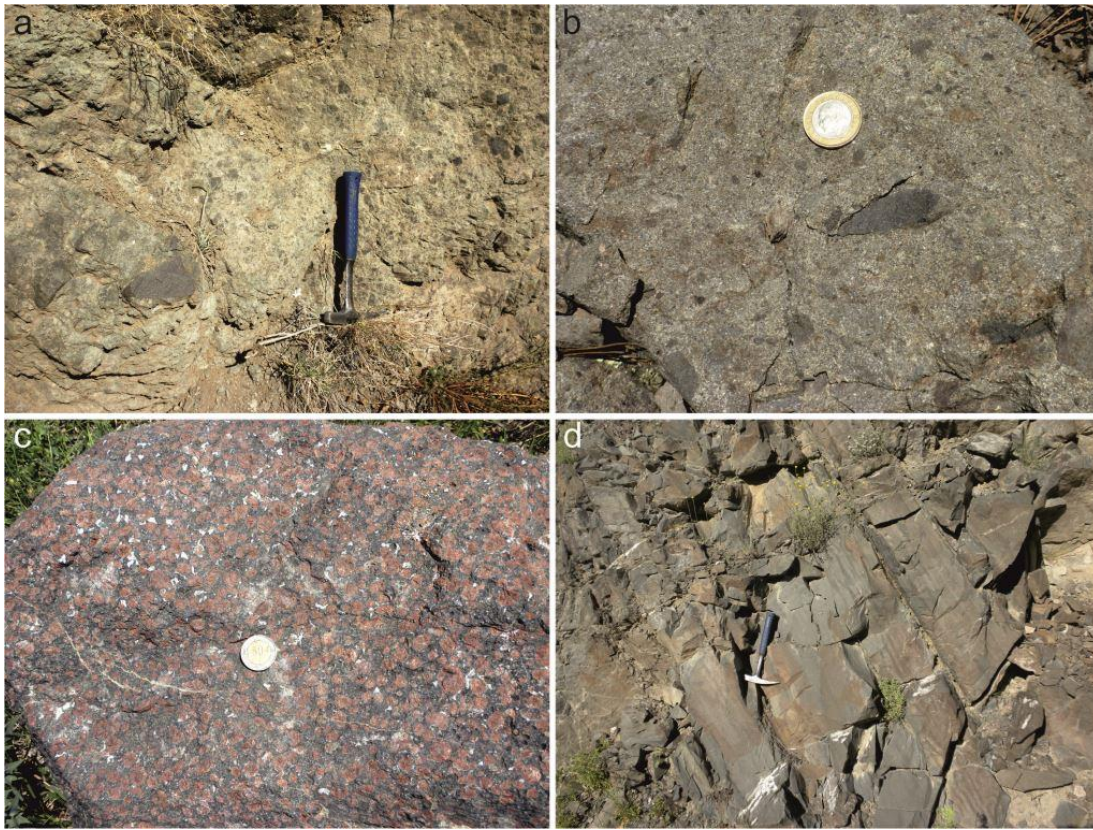


Figure 2.8 : Field photos of the İkiçam Formation. (a) & (b) Pyroclastic rocks of andesitic composition. c) Leucite-bearing basalt. d) Volcanoclastic dark grey turbidites. This part mainly consists of sandstone and siltstone.

The volcanic sequence is reported to be of Campanian-Maastrichtian age based on the planktonic foraminifera content (per. com. in Rice et al., 2006). This is supported by recent $^{40}\text{Ar}/^{39}\text{Ar}$ biotite age data on the alkaline volcanic rocks of 73.6 ± 0.18 and 76.78 ± 0.19 Ma (Genç et al., 2013, 2014). Although, the volcanoclastic rocks were probably initially deposited on the Kunduz Metamorphics, they now form a steeply dipping tectonic slice within the complex (Fig. 2.1, 2.2). Initial limited geochemical data from the volcanic rocks suggested a within-plate setting without any subduction influence (Rice et al., 2006), more recent data, however, indicate subduction-related volcanism (Genç et al., 2014; Gülmez et al., 2014).

2.2 Accreted Arc Sequence

In the Kastamonu-Tosya transect, a coherent arc sequence is exposed south of the Tosya Basin along the İAES (Figs. 1.3, 2.9). It is structurally overlain by the CPS to

the north and overthrusts an ophiolitic mélangé in the south. Two main units are identified in the arc sequence: 1) a low-grade metavolcanic unit, the Köşdağ Formation, consisting predominately of basaltic andesitic and felsic rocks together with the associated pyroclastic rocks and 2) an overlying low grade metasedimentary sequence consisting of micritic limestone and shale, the Dikmen Formation.

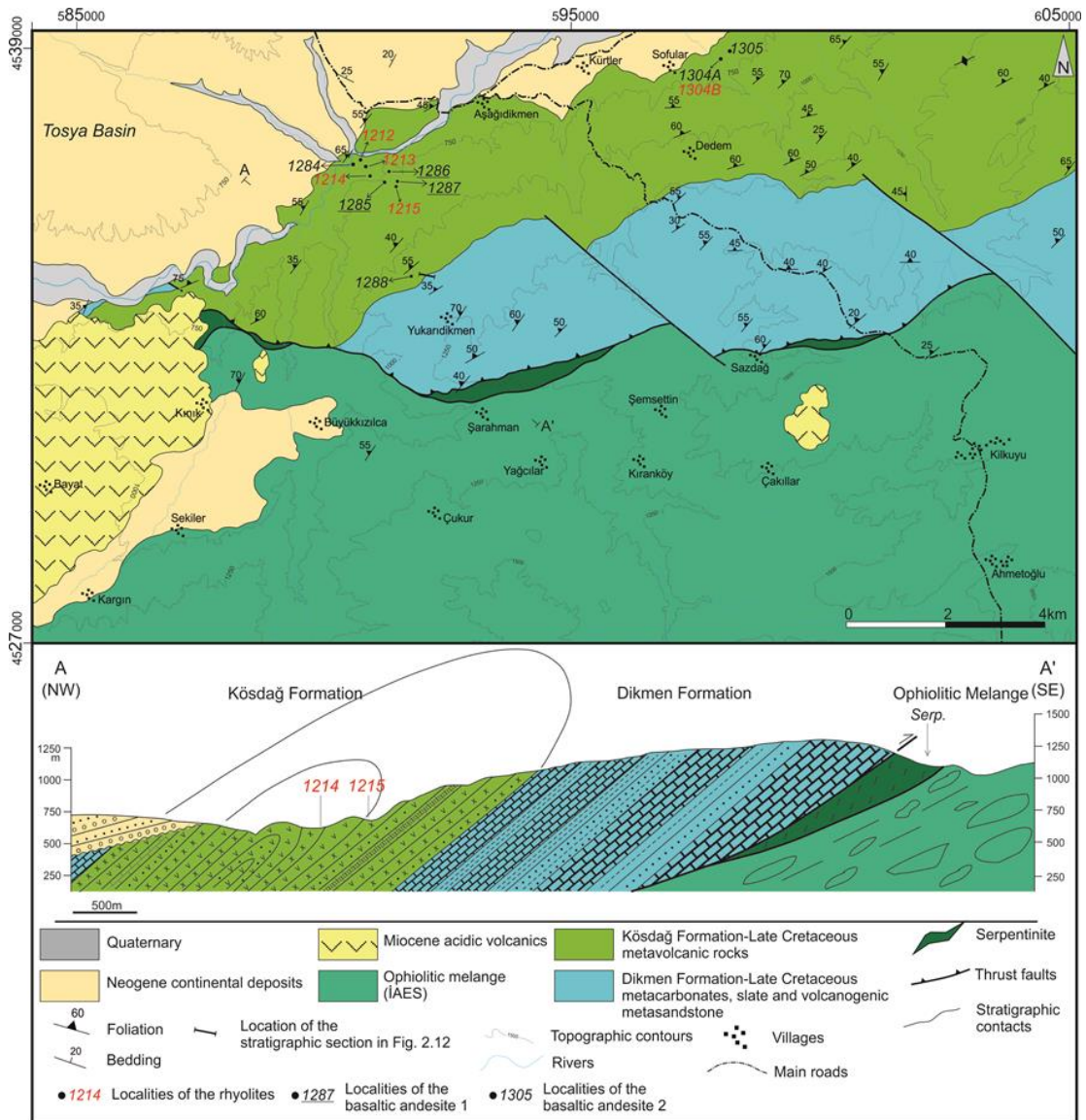


Figure 2.9 : Geological map of the studied section south of Tosya, along the İzmir-Ankara-Erzincan suture with a cross section between A and A'. For location see Fig. 1.3.

2.2.1 Köşdağ Formation

The Köşdağ Formation consists mainly of greenschist facies rhyolitic and basaltic andesitic rocks with their pyroclastic equivalents with a structural thickness of ca. 2 km. Rhyolites and basaltic andesites are intercalated and are easily identified by their

whitish and greenish colors, respectively (Fig. 2.10). Towards the top, the metavolcanic rocks become pyroclastic and finer grained. Recrystallized red pelagic limestone and chert are interbedded with the pyroclastic rocks indicating submarine deposition (Fig. 2.10). The Köşdağ Formation is stratigraphically overlain by recrystallized limestone and slate of the Dikmen Formation (see section 2.2.2 below). The base of the Köşdağ Formation is not exposed in the area studied.

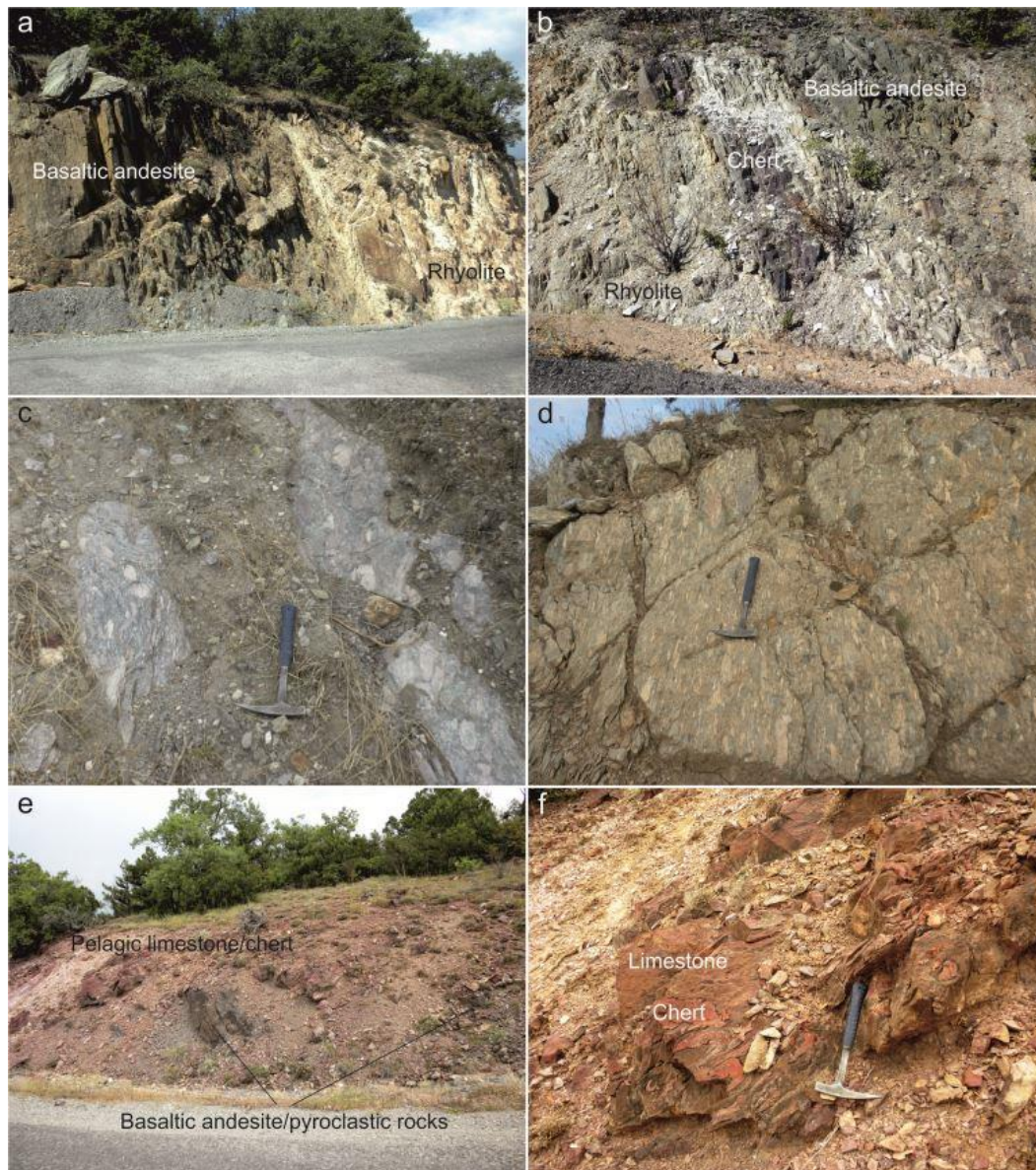


Figure 2.10 : Field photos of the Köşdağ Formation. All rocks have undergone a low-grade metamorphism but are referred here with their protolith names. a) Basaltic andesite and rhyolite. b) Thin chert interbeds within the acidic and basic rocks. Pyroclastic rocks of acidic (c) and andesitic (d) compositions. e) Red pelagic limestone/chert interbeds with basaltic andesitic rocks. f) A close look to the same outcrop in (e). Folded bright cherts occur within the red pelagic limestone.

2.2.2 Dikmen Formation

The Dikmen Formation is a metasedimentary sequence consisting of yellowish and pinkish siliceous slate and recrystallized micritic limestone with light colored volcanogenic metasandstone layers (Fig. 2.11). The recrystallized limestones are thinly bedded, pink and contain deformed radiolaria indicating deposition in a deep marine environment. The majority of the metacarbonates exhibit alternation of dark relatively thickly bedded (up to 50 cm) limestone representing calciturbidites and thin pinkish pelagic limestone (Fig. 2.11c, d). Cenomanian fossils are reported from the recrystallized limestone of the Dikmen Formation (Tüysüz, 1990, 1993), however, our paleontological samples were too recrystallized to yield any fossils.



Figure 2.11 : Field photos of the Dikmen Formation. a) Contact between rhyolite and overlying recrystallized reddish micritic limestone of Dikmen Formation in the upper limb of the overturned anticline. b) Yellowish and reddish slate and recrystallized limestone exposed along the transitional section between Köşdağ and Dikmen formations. c & d) Recrystallized calciturbidite consisting of intercalation of moderately bedded dark levels consisting of transported coarse grains and thinly bedded pinkish pelagic levels.

The Dikmen Formation stratigraphically overlies the volcanic rocks of the Köşdağ Formation. The contact is transitional involving alternation of volcanic and

sedimentary beds although it is overturned. A typical section of the contact is exposed along a ca. 250 m section on the main road to the Yukarıdikmen village. In the section, mostly acidic volcanic rocks with minor pinkish micritic limestone pass into a limestone and shale dominated sedimentary sequence with volcanogenic sandstone (Fig. 2.12).

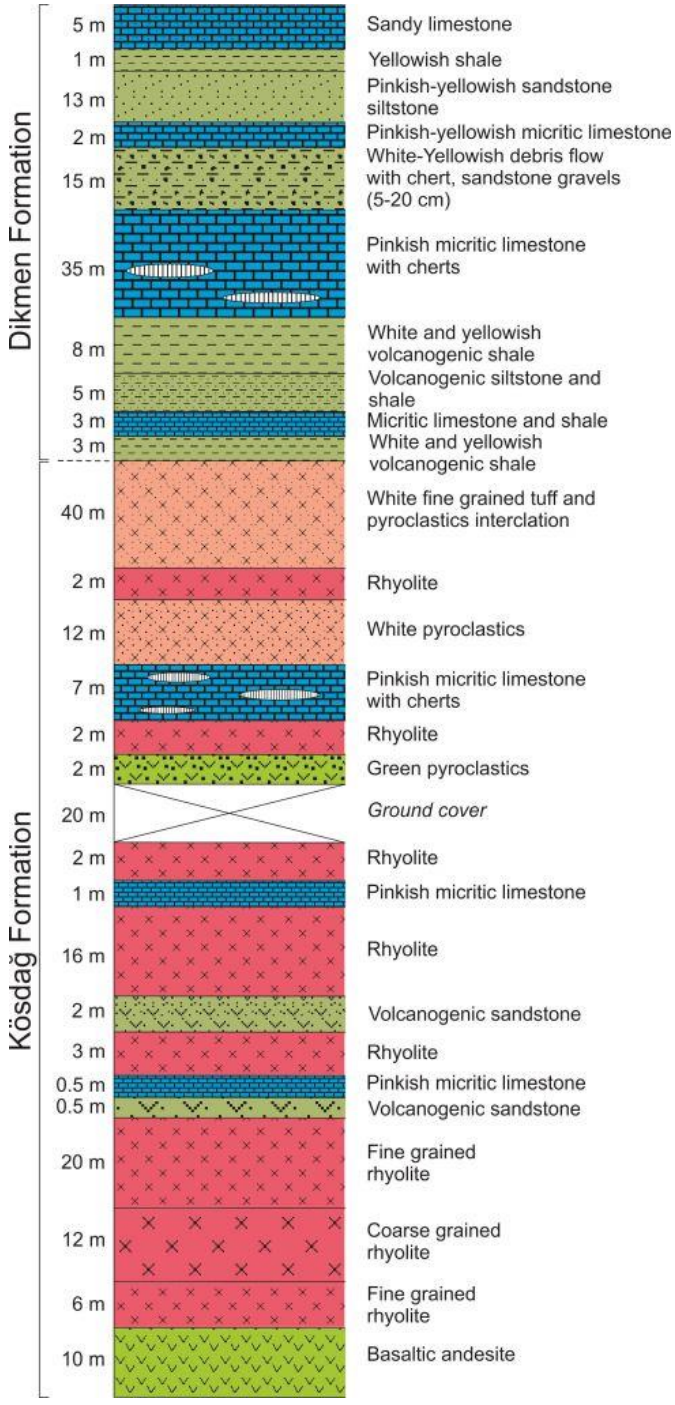


Figure 2.12 : Measured stratigraphic section illustrating the transitional character between the Kösdag Formation and the overlying Dikmen Formation. The section is about 250m and is measured along the main road to Yukarıdikmen village. For location, see Fig. 2.9.

Sedimentary rocks of the Dikmen Formation also overlie the rhyolitic rocks in the northern part of the area studied. This suggests a structure that is characterized by a large southward overturned anticline, whereby the metasedimentary sequence lies both over and under the metavolcanic rocks (Fig. 2.9). The overturned folding probably formed during the southward thrusting of the Köşdağ and Dikmen formations over the ophiolitic mélangé.

2.2.3 Ophiolitic mélangé (İAES)

The southernmost unit of the Kastamonu-Tosya transects is an ophiolitic mélangé overthrust by the accreted arc sequence (Fig. 2.13a). The ophiolitic mélangé forms part of the İzmir-Ankara-Erzincan suture and consists of tectonic slices and blocks of serpentinite, pillow basalts and radiolarian cherts with red pelagic and grey neritic limestones without a clearly defined matrix (Fig. 2.13b). Compared to the Kirazbaşı Complex exposed in the north, the ophiolitic mélangé is characterized by absence of continent derived detritus. The dominant ophiolitic character of the İAES is reported elsewhere in central Turkey (Dilek and Thy, 2006; Çelik et al., 2011; Dangerfield et al., 2011; Rojay, 2013, Sarifakioğlu et al., 2014).



Figure 2.13 : Field photos of the ophiolitic mélangé. a) Serpentinite (green) that is overthrust by recrystallized limestone (pinkish) of Dikmen Formation. b) Pillow basalts.

Along the contact with the overlying arc sequence, NW dipping foliation is observed in the ophiolitic mélangé, which is otherwise generally free of metamorphic minerals. To the south, the ophiolitic mélangé is unconformably overlain by sedimentary rocks of the Çankırı Basin, ca. 4 km thick basin of mainly Tertiary age (Kaymakcı, 2000).

2.3 Cover Units

In the area studied, the oldest cover unit is Maastrichtian limestones exposed as a tectonic sliver along the east-west striking post-Eocene Akçataş fault. It is separated from the Domuzdağ Complex by the Akçataş Fault and is thrust over the Eocene turbidites suggesting a positive flower structure. The limestone is reddish and contains abundant *Helonocyclina* and *Orbitoides* type benthic foraminifera indicating a Maastrichtian deposition age (Fig. 2.14, Ercan Özcan, per. com.). Absence of metamorphism and significant deformation suggest that the Maastrichtian limestone initially unconformably covered the accretionary wedge units.

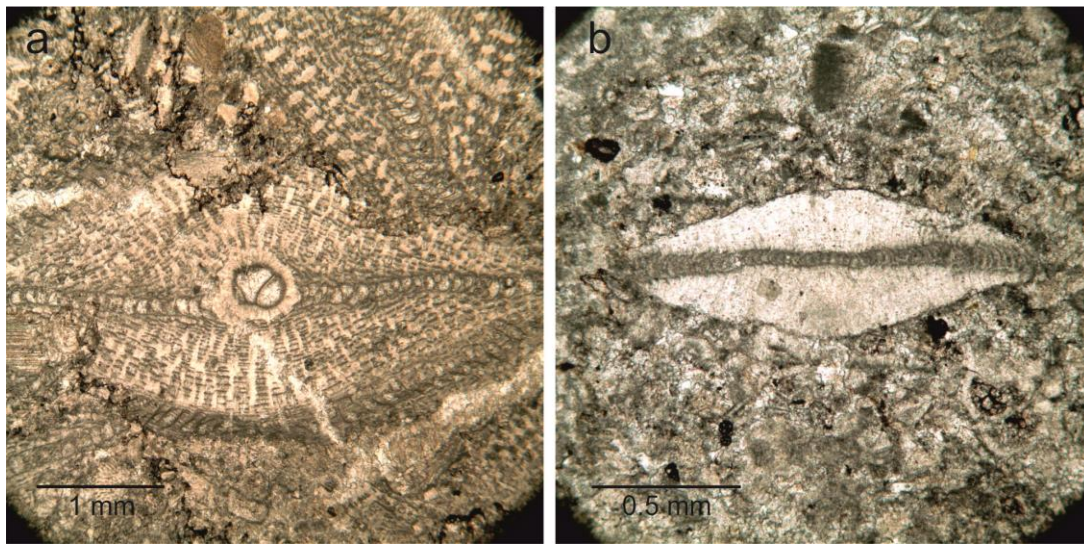


Figure 2.14 : Maastrichtian limestone with *Orbitoides* (a) and *Helonocyclina* (b) type foraminifera.

In the Central Pontides, Eocene limestones crop out widely and unconformably overlie the metamorphic rocks. Benthic foraminifera studies, particularly orthophragminids, on Eocene sedimentary succession reveals an Early-Middle Eocene age (KASB section near Kastamonu and TAŞ section near Taşköprü, Özcan et al., 2007). In the area studied, Eocene sedimentary sequence consists of both limestone and turbidites with abundant benthic Eocene foraminifera including *Nummulites* and *Alveolina*. In the northern part of the area studies, Eocene sequence consists of alternation of white and yellowish sandy limestones (Fig 2.15a). To the south, the sandy limestones pass to a turbidite sequence. The turbidite sequence consists of thin to moderately bedded sand/siltstone and shale/marl alternation (Fig 2.15b). Similar turbidites are also exposed west of the studied area along the Akçataş Fault. To the east, north of the Güney town, the Eocene sequence is represented by

moderate to thickly bedded sparitic limestone (Fig. 2.1). The Eocene sedimentary sequence generally shows subhorizontal bedding.

The Eocene sedimentary succession and the underlying HP/LT metamorphic rocks are covered by Eocene basalts (Fig. 2.15c). Basalt exhibits columnar structures and vesicular textures indicating subaerial cooling (Fig 2.15d). There is no radiometric data on the basalt but it is reported to be Eocene in age (e.g. Uğuz et al., 2002). The fact that the age of the underlying sedimentary sequence is Early to Middle Eocene, a post-Lutetian age can be inferred for the basalt.

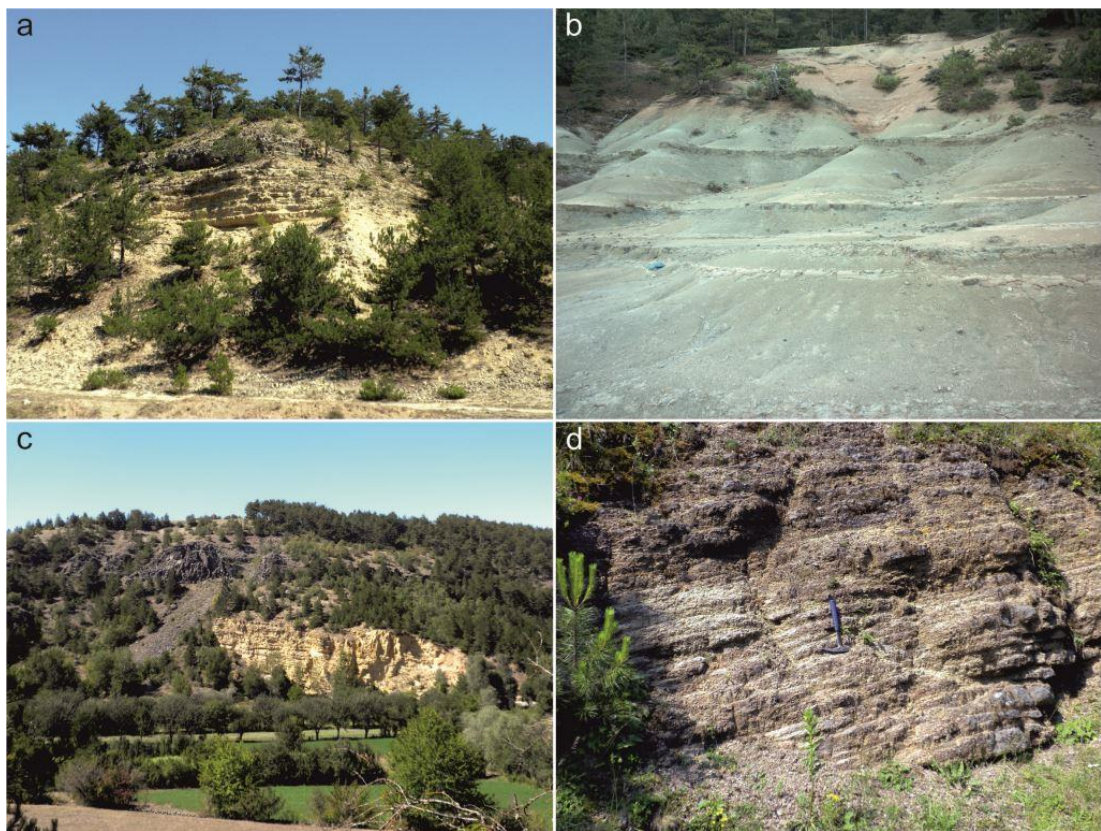


Figure 2.15 : Field photos of the Lower-Middle Eocene limestone (a) and turbidite (b). c) Eocene limestone and overlaying basalt cover. d) Vesicular basalts of probable Eocene age.

In the NW of the studied area, horizontally bedded Neogene clastic rocks crop out on top of hills and unconformably cover the Eocene succession and the post- Lutetian basalts. They consist of weakly bedded and unconsolidated fluvial conglomerate and sandstone. Around Tosya, however, Neogene sedimentary rocks were originated by activity of the North Anatolian Fault (NAF). The rocks comprise unconsolidated thick succession of conglomerates, gravelstone and sandstone that fill the NAF controlled Tosya basin as alluvial fans (Fig. 2.16). In the north, they unconformably

cover the metamorphic rocks of the Kunduz Metamorphics with slightly inclined bedding planes towards to the south. In some localities, unconsolidated Neogene sequence is faulted by the activity of the NAF.



Figure 2.16 : a) A general view of the Tosya Basin between the Kunduz Metamorphics to the north and hills made up from the metavolcanic rocks of the Köşdağ Formation to the south. b & c) Field photos of the NAF-related unconsolidated Neogene gravelstone and sandstone of the Tosya Basin.

2.4 Structural Analysis of the Wedge

In the Central Pontides, general regional structures of the accretionary units trend in SW-NE direction. In the study area, this trend is represented by the extensional shear zone separating the Esenler Unit from the underlying Domuzdağ Complex. Similar contact relations are also observed in the NW of the study area where the Domuzdağ Complex is overlain by the Çangaldağ Complex (Okay et al., 2006a). Orientation of foliation planes of the Esenler Unit varies depending on their proximity to different contacts (Fig. 2.17a). In the north of the study area, Esenler Unit is overthrust by the metavolcanic rocks of the Çangaldağ Complex. Around the thrust, strong stretching lineation developed in the metaflysch and the metavolcanics trending SW-NE and slightly plunging to NE (Fig. 2.17b). Lineations with similar trends are common throughout the metaflysch suggesting a general transport in this direction.

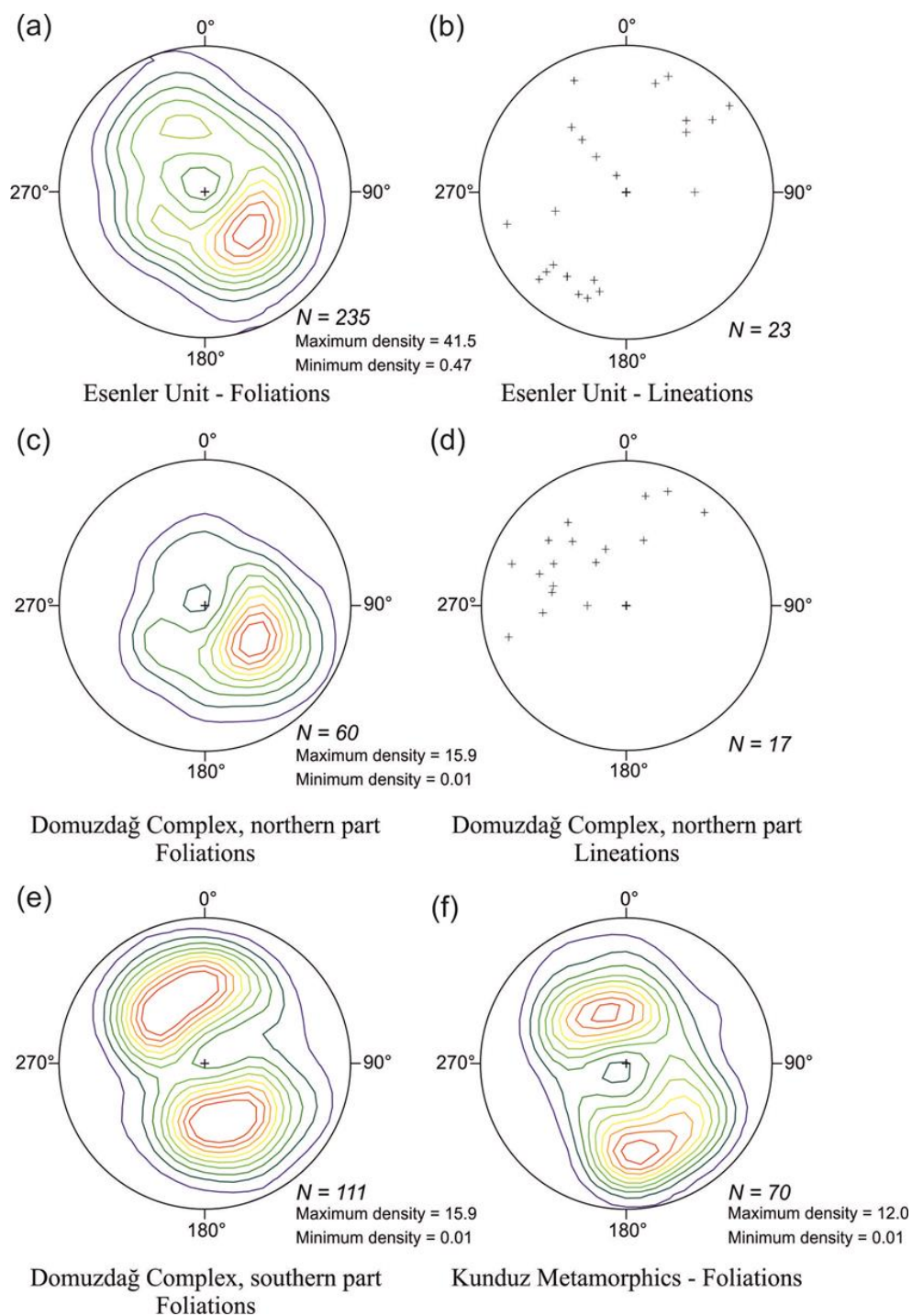


Figure 2.17 : Lower hemisphere, equal area projections of the foliations and the lineations. a) Foliation and b) lineation data from the Eesenler Unit. c) Foliation and d) lineation measurements of the northern part of the Domuzdağ Complex. Lineations are mostly orthogonal to the NW dipping foliation planes and plunge to the NW related exhumation. e) Foliation data from the southern part of the Domuzdağ Complex and f) the Kunduz Metamorphics. Contour interval is 10.

To the south of the extensional shear zone, foliation planes of the Domuzdağ Complex strike SW-NE parallel to the extensional shear zone (Fig. 2.17c). Micaschist exhibit NW plunging stretching lineation orthogonal to the foliation (Fig.

2.17d). Similar lineations are also observed in the blocks and fault gouge of the extensional shear zone. This suggests that they developed by pervasive shearing during exhumation. An east-west striking post-Eocene fault, the Akçataş Fault (Fig. 2.1, 2.2b), overprints the extensional shear zone and separates the Domuzdağ Complex into two sectors. South of the Akçataş fault, foliation planes define large synforms (Fig. 2.17e) bounded possibly by faults parallel to the Akçataş Fault. Such a folding pattern is also observed within the Kunduz Metamorphics (Fig. 2.17f). In the south of the Tosya Basin, the Köşdağ and Dikmen formations show consistent NW dipping foliations and structurally underlie the Central Pontide Supercomplex (Fig. 2.18).

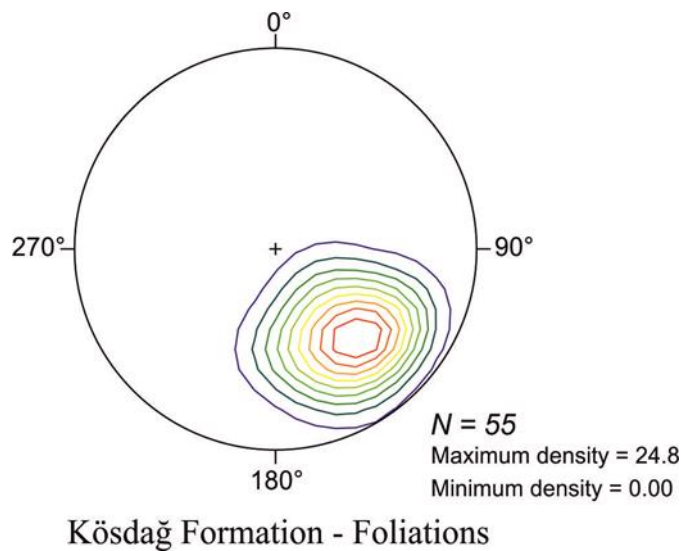


Figure 2.18 : Lower hemisphere, equal area projections of the foliations of the Köşdağ Formation. Contour interval is 10.

3. PETROGRAPHY AND MINERAL CHEMISTRY

This chapter provides detailed petrography and mineral chemistry of the metamorphic and magmatic units in the area studied. The metamorphic units comprise 1) the low-grade metaflysch sequence, the Esenler Unit, 2) underlying HP/LT metabasite dominated the Domuzdağ Complex and the Kunduz Metamorphics. Finally, petrography of the low-grade arc sequence, the Köşdağ Formation is given.

3.1 The Esenler Unit

The Esenler Unit is a metamorphosed flysch sequence composed predominantly of slate/phyllite and metasandstone intercalation with marble olistoliths and tectonic slices of Na-amphibole bearing metabasite and serpentinite. The majority of the metapelitic rocks of the Esenler Unit are weakly recrystallized slates. The slates consist of quartz, phengite, chlorite and albite. They exhibit continuous foliation defined by fine-grained white mica (Fig. 3.1a). Detrital quartz is partly retained in the slate (Fig. 3.1b). Close to the contacts, slate transformed to phyllites that consist of larger grain of quartz, phengite, chlorite and albite. The phyllites show spaced foliation defined by white mica and quartz (Fig. 3.1c, d).

Metasandstones are of greywacke type composed 70-75 % of clasts and 25-30 % of cement. The clasts consist of quartz, plagioclase, and white mica which are embedded by silt to clay sized cement (Fig. 3.2). The cement of the metasandstone is recrystallized and consists mainly of quartz and minor mica. Texturally, the metasandstones are poorly to moderately sorted. The clasts are moderately rounded and generally have irregular outlines.

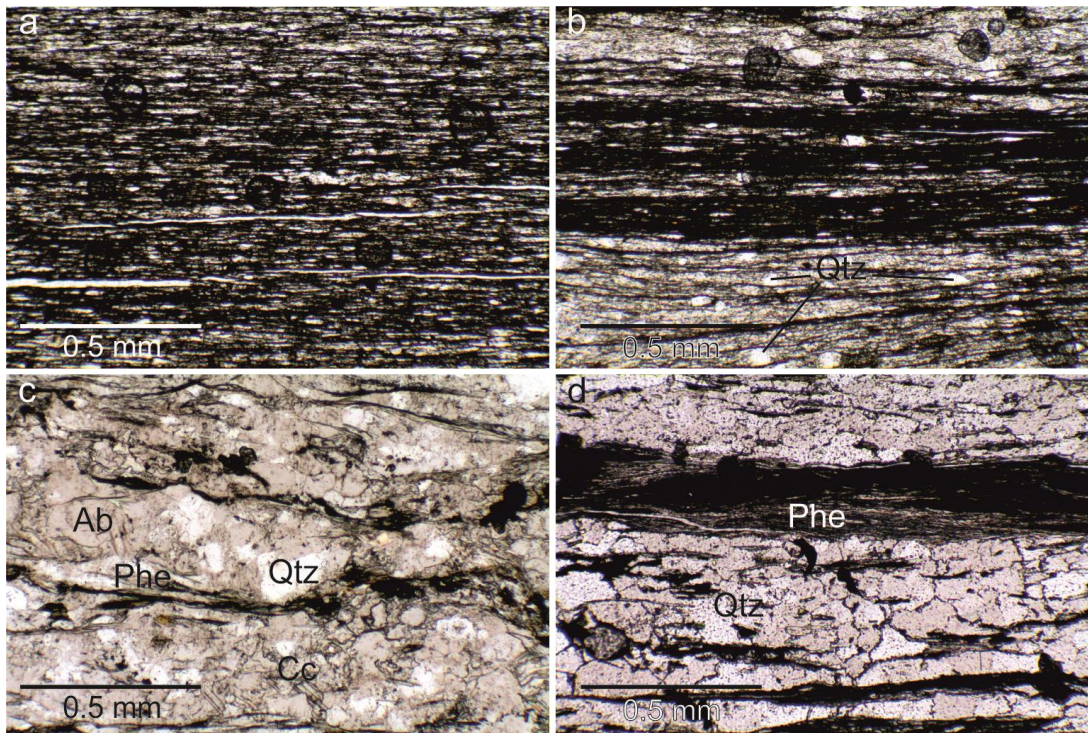


Figure 3.1 : Representative photomicrographs of the metapelitic rocks from the Esenler Unit (plane polarized light). a & b) Fine-grained slates (samples 847 and 853). Foliation is defined by white mica and partly recrystallized detrital quartz. c & d) Coarser grained phyllites with spaced foliation (samples 31 and 879). Ab=albite, Qtz=quartz, Phe=phengite, Cc=calcite.

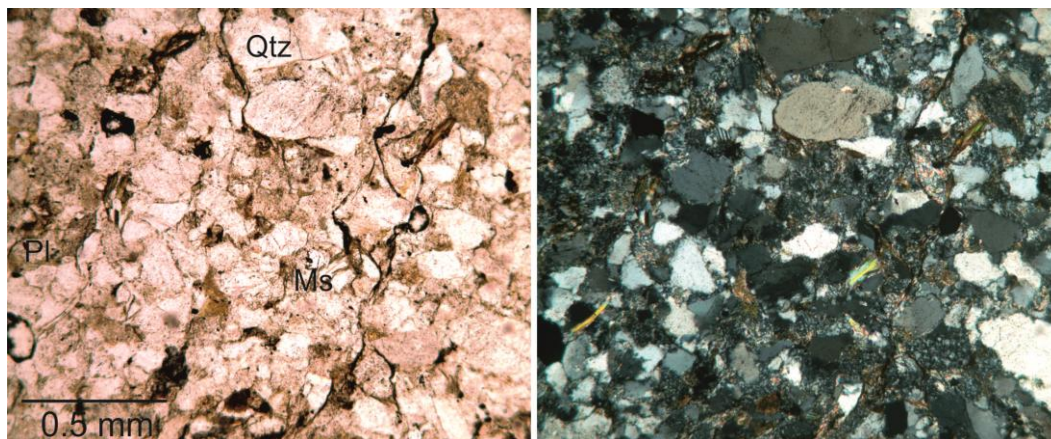


Figure 3.2 : Photomicrographs of a greywacke-type metasandstone from the Esenler Unit under plane (left) and cross (right) polarized light. Majority of the clasts are quartz (Qtz) with minor feldspar (Pl) and white mica (Ms).

Some of the marble blocks within the Esenler Unit show a fibrous fabric possibly representing pseudomorphs after aragonite (Fig. 3.3, Brady et al., 2004; Seaton et al., 2009).

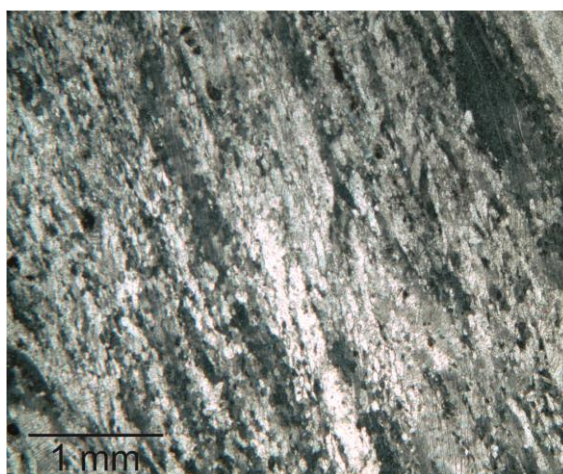


Figure 3.3 : A marble with elongated fibrous calcite.

The majority of the metabasites of the Esenler Unit show incipient blueschist facies metamorphic assemblages (Fig. 3.4). The metabasite consists of sodic- and calcic-amphibole, chlorite, epidote, albite, titanite locally with pumpellyite. The metabasites are usually well foliated defined by oriented sodic-amphibole (Fig. 3.4a).

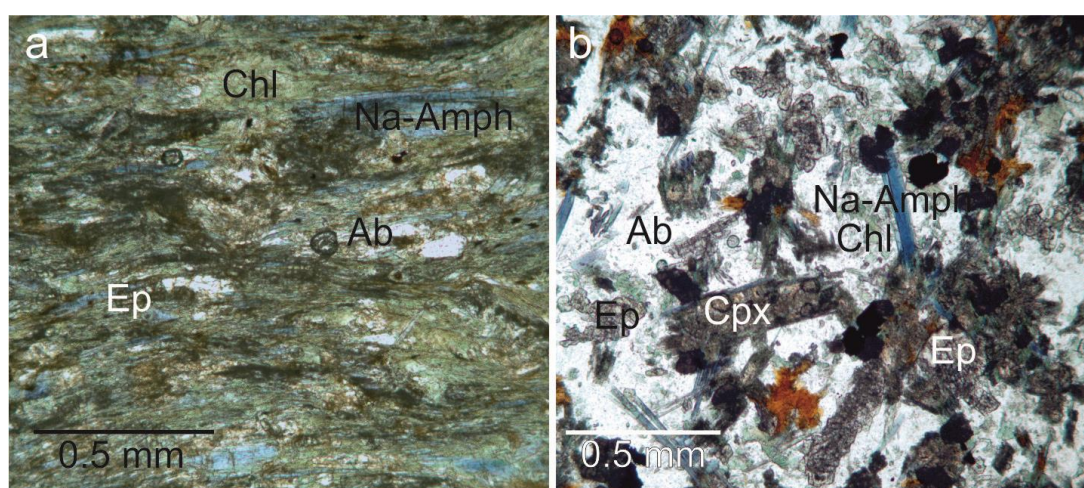


Figure 3.4 : Plane-polarized photomicrographs of incipient blueschist facies metabasites from the Esenler Unit. a) A foliated blueschist. Foliation is defined by sodic-amphibole (Na-amph). b) An unfoliated metabasite with randomly distributed sodic-amphiboles (sample 211B). Cpx= augite relicts; Ep= epidote; Chl= chlorite; Ab= albite.

One of these metabasite samples was analyzed by the electron microprobe. Mineral chemistry data is given in Appx (Tables A.1-A.10). This sample 211B is an unfoliated metabasite with augite relicts (Fig. 3.4b). It is taken from NW of the area studied where plenty of tectonic slices of serpentinites are also found. The metamorphic mineral assemblage of the sample 211B is sodic- and calcic-amphibole, sodic-pyroxene, epidote, chlorite, albite and titanite. Sodic-amphibole forms

randomly distributed prismatic crystals and is of crossite composition (Fig. 3.5). Crossite is rimmed by actinolite. Sodic-pyroxene overgrows and replaces magmatic augite with a compositional range of $\text{Aeg}_{29-40}\text{Jd}_{6-13}\text{Di}_{53-58}$ (Fig. 3.6). Texturally, there are two types of epidote. The first one forms large grains with iron-rich cores ($\text{Fe}^{3+}/(\text{Fe}^{3++\text{Al}}) = 0.36$) (Fig. 3.7). The $\text{Fe}^{3+}/\#$ ratio decreases rimward to 0.23–0.24. The second type forms small grains with pistacite-poor cores ($\text{Fe}^{3+}/(\text{Fe}^{3++\text{Al}}) = 0.14$ –0.17) and Fe-rich rims ($\text{Fe}^{3+}/(\text{Fe}^{3++\text{Al}}) = 0.29$ –0.31). The $\text{Mg}/(\text{Mg}+\text{Fe})$ ratio of chlorites ranges between 0.47–0.57 (Fig. 3.8). Si content of the chlorite increases at the expense of Al while $\text{Mg}\#$ increases. The stable Ti-bearing phase is titanite. Plagioclase is almost pure albite ($\text{An}=0$ –1%).

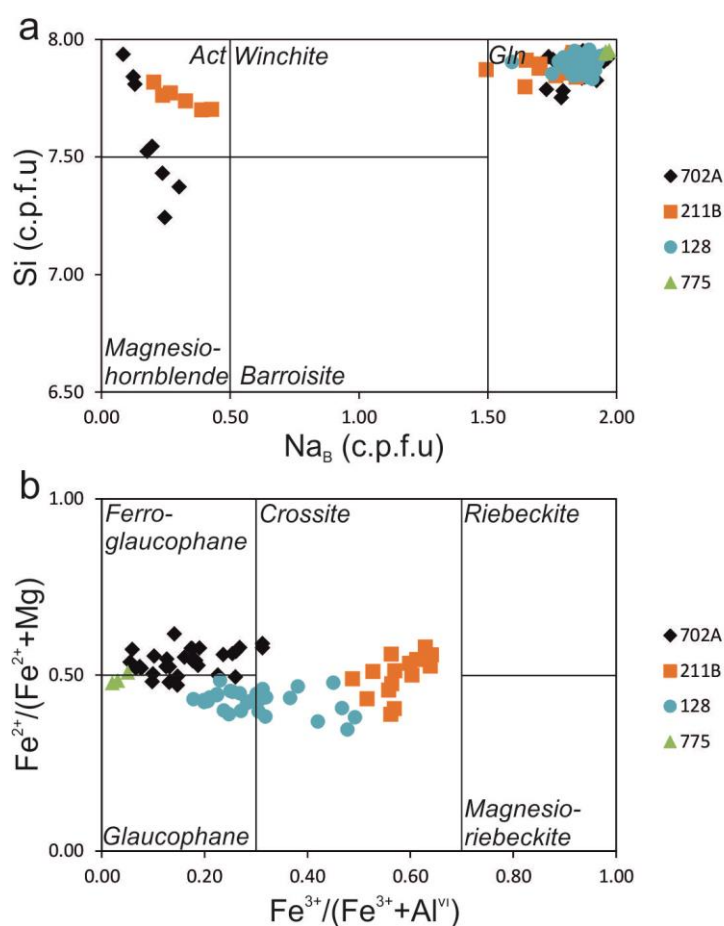


Figure 3.5 : Compositional range of amphibole. Act= actinolite, Gln= glaucophane.

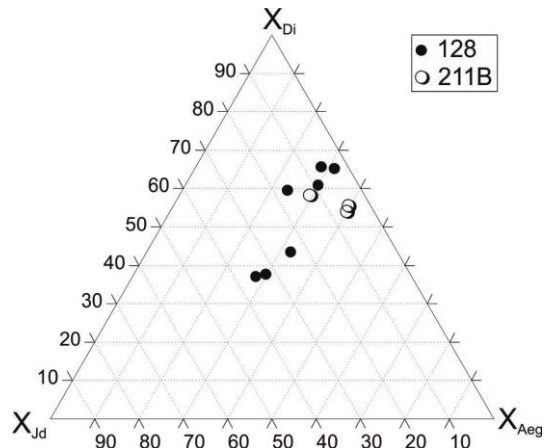


Figure 3.6 : Compositional range of sodic-pyroxene.

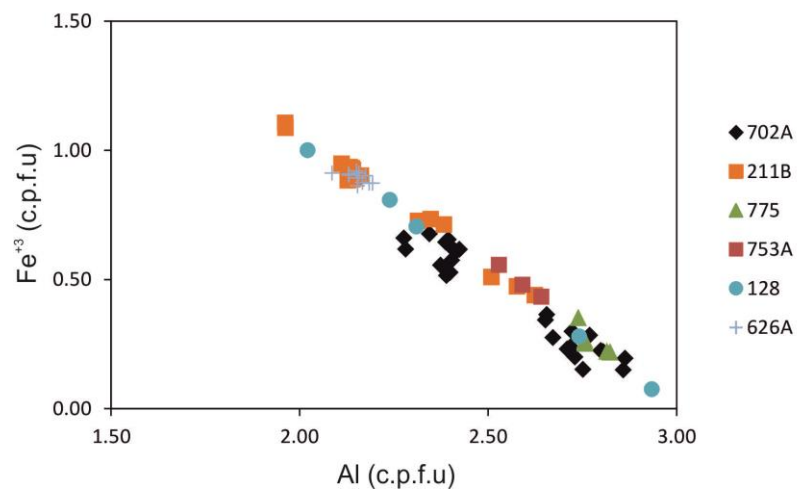


Figure 3.7 : Compositional range of epidotes.

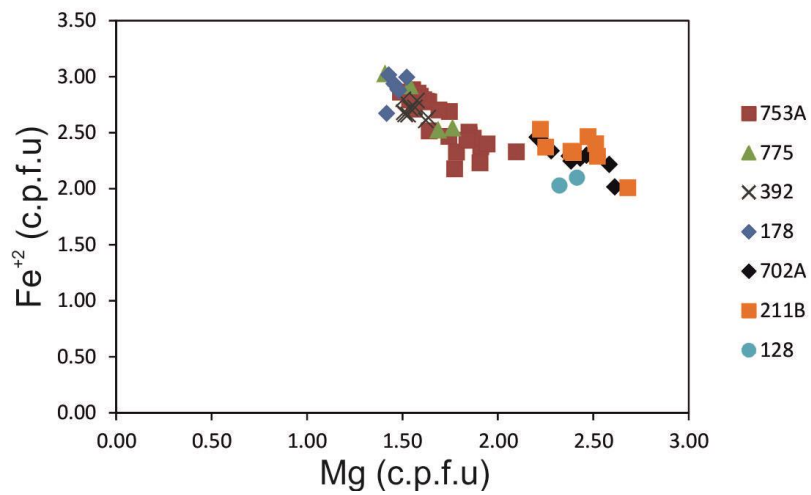


Figure 3.8 : Compositional range of chlorites.

3.2 The Domuzdağ Complex

The Domuzdağ Complex mainly consists of HP/LT metabasites and micaschists with minor serpentinite, metagabbro, metachert, and marble. It represents a subduction-accretionary complex of oceanic origin. Below detailed petrography and mineral chemistry of metabasites and micaschists are given. The analytical data are shown in Appx (Tables A.1-A.10).

3.2.1 Metabasites

The metabasites of the Domuzdağ Complex are mostly well-foliated epidote-blueschist consisting of sodic amphibole + epidote + chlorite + titanite + albite ± garnet (Fig. 3.9a). Augite relicts are retained in some of the epidote-blueschist. The blueschist locally show strong greenschist facies metamorphic overprint and are transformed into albite-chlorite fels (Fig. 3.9b). The HP/LT origin of this albite-chlorite fels is evidenced by relicts of aligned Na-amphibole within the albite domain. Fresh lawsonite-blueschists crop out within the extensional shear zone as blocks. They consist of lawsonite, sodic-amphibole, sodic-pyroxene, chlorite, phengite, epidote, albite and titanite and possibly form part of the Domuzdağ Complex. Detailed petrography and mineral chemistry of a garnet-epidote-blueschist (702A) and a lawsonite-blueschist is provided below.

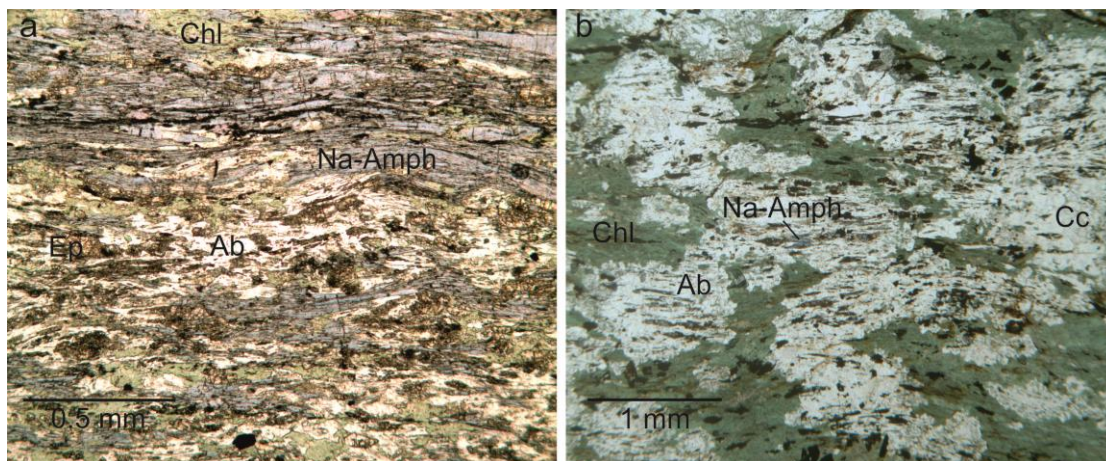


Figure 3.9 : Plane-polarized photomicrographs from the Domuzdağ Complex of a) epidote-blueschist and b) albite-chlorite fels that represents a strongly retrogressed blueschist. Na-amph= sodic-amphibole, Chl= chlorite, Ab= albite, Ep= epidote, Cc= calcite.

3.2.1.1 Lawsonite-blueschist (sample 128)

The sample 128 is an unfoliated metabasite consisting of sodic-amphibole, lawsonite, sodic-pyroxene, chlorite, phengite, epidote, albite and titanite (Fig. 3.10). Sodic-amphibole has crossitic cores rimmed by glaucophane (Fig. 3.5). Glaucophane also forms single grains and is found as inclusion in lawsonite. Sodic-amphibole is partly replaced by albite and chlorite. Lawsonite is partly decomposed to epidote and albite along its rims.

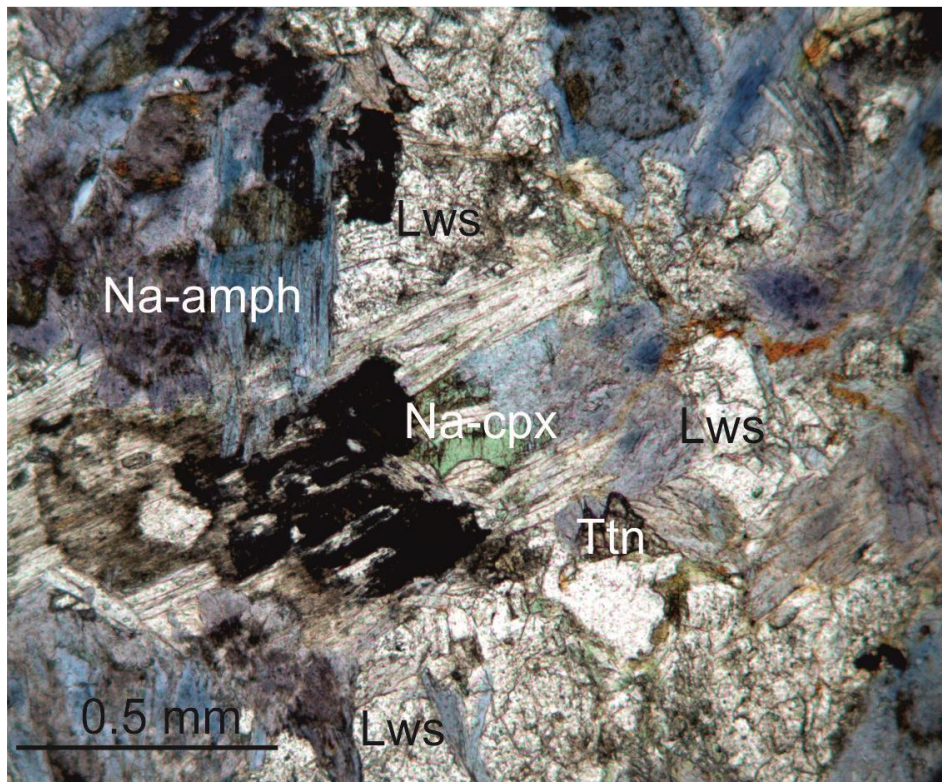


Figure 3.10 : Microphotograph of a lawsonite blueschist (sample 128) from the Domuzdağ Complex. Na-amph= sodic-amphibole, Na-cpx=sodic-pyroxene, Lws= lawsonite, Ttn= titanite.

Sodic-pyroxene shows two compositional ranges: $Jd_{4-18}Aeg_{31-23}Di_{65-59}$ and $Jd_{25-36}Aeg_{32-28}Di_{43-37}$ (Fig. 3.6). Epidote has pistacite-poor cores ($Fe^{3+}\#$: 0.02–0.09) and Fe^{3+} rich rims ($Fe^{3+}\#$: 0.23–0.33)(Fig. 3.7). Chlorite replaces the Na-clinopyroxene and has $Mg/(Mg+Fe)$ ratio ranging between 0.53–0.54 (Fig. 3.8). Plagioclase is albite ($An=0-5\%$) and Ti-bearing phase is titanite. Si content of phengites ranges between 3.41–3.54 cation per formula unit (c. p.f.u.)(Fig. 3.11).

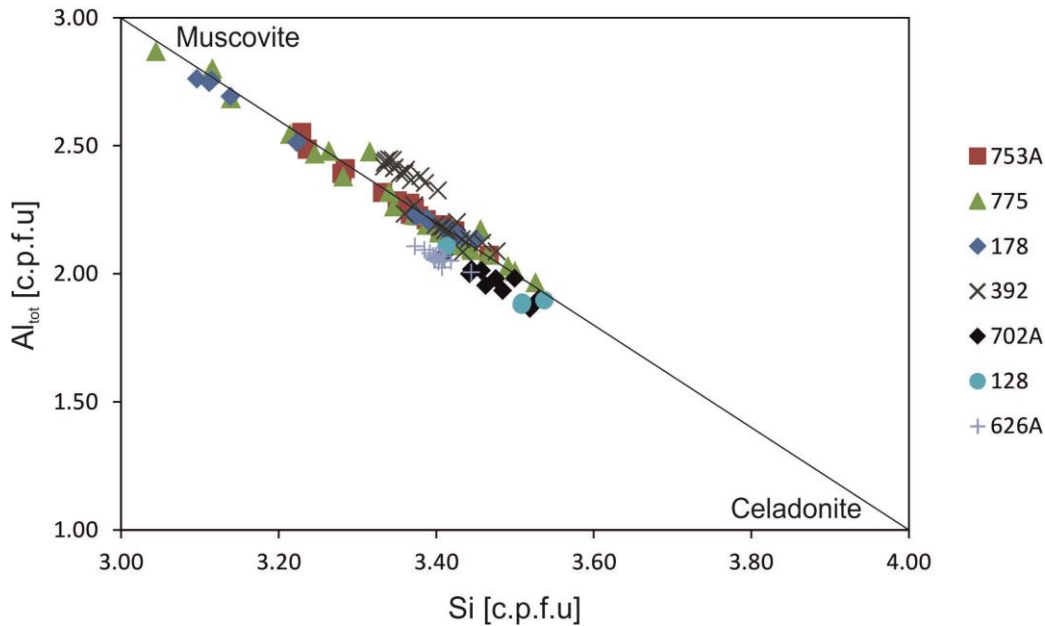


Figure 3.11 : Compositional range of phengites. Al vs Si diagram showing the celadonite exchange. Decreasing Si content mainly depicts the effect of the retrogression.

3.2.1.2 Garnet-epidote-blueschist (sample 702A)

The sample 702A consists of garnet, sodic- and calcic-amphibole, epidote, chlorite, albite, phengite, titanite and magmatic augite relicts (Fig. 3.12a). Garnets grow over the foliation defined by glaucophane and epidote. They are 0.2-0.4 mm across and comprise glaucophane, epidote, and titanite inclusions aligned parallel to the main foliation. Generation of pressure shadows defined by glaucophane, epidote and phengite suggests a syn-kinematic origin (Fig. 3.12a). Compositional range of the garnet is $\text{Alm}_{44-56}\text{Py}_{2-4}\text{Gr}_{39-38}\text{Sp}_{15-2}$ (Fig. 3.13). From core to rim, almandine increases at the expense of spessartine but the sum of these components remains stable with little change in the grossular and pyrope contents. This can also be seen in element maps showing a typical garnet growth zoning evidenced by progressive exchange of Fe and Mn (Fig. 3.12b). The progressive garnet zonation is cut by an augite relict indicating that garnet did not grow in that direction. This suggests that there was no reaction between these two minerals.

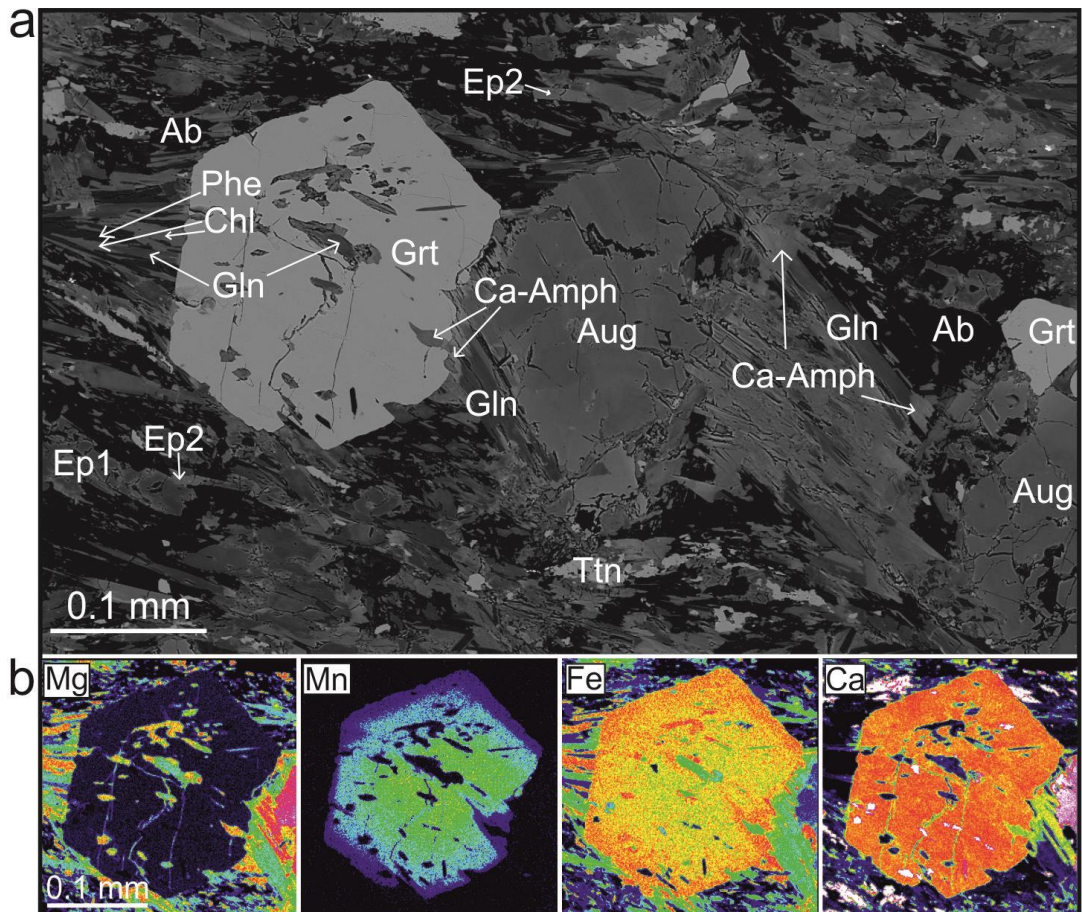


Figure 3.12 : a) BSE image of the garnet-blueschist (702A). Garnet (Grt) exhibits pressure shadow consisting of glaucophane (Gln) + phengite (Phe) + epidote (Ep). Calcic-amphibole (Ca-amph), chlorite (Chl) and albite (Ab) are secondary and replace glaucophane. b) Element mapping of the garnet in Fig. 3.9a with typical growth zoning. Ca and Mg are almost stable. Mn decreases rimward while Fe increases. Ttn=titanite, Aug=augite.

Sodic-amphibole is mostly ferroglaucophane (Fig. 3.5) and replaces augite relicts along their rims or forms aligned prismatic crystals that define the foliation. Sodic-amphibole is partly replaced by calcic-amphibole and secondary chlorite. Epidote has pistacite-poor core ($Fe^{3+\#} = 0.06-0.12$) and pistacite-rich rim ($Fe^{3+\#} = 0.18-0.22$) (Fig. 3.7). Si contents of phengite range between 3.41–3.53 c.p.f.u. (Fig. 3.11). Within the garnet pressure shadows, Si content of phengite decreases rimward (3.50–3.44 c.p.f.u). Mg/ (Mg+Fe) ratio of secondary chlorite ranges between 0.48-0.56 (Fig. 3.8). The stable Ti-bearing phase is titanite. Plagioclase is albite (An=1–6%).

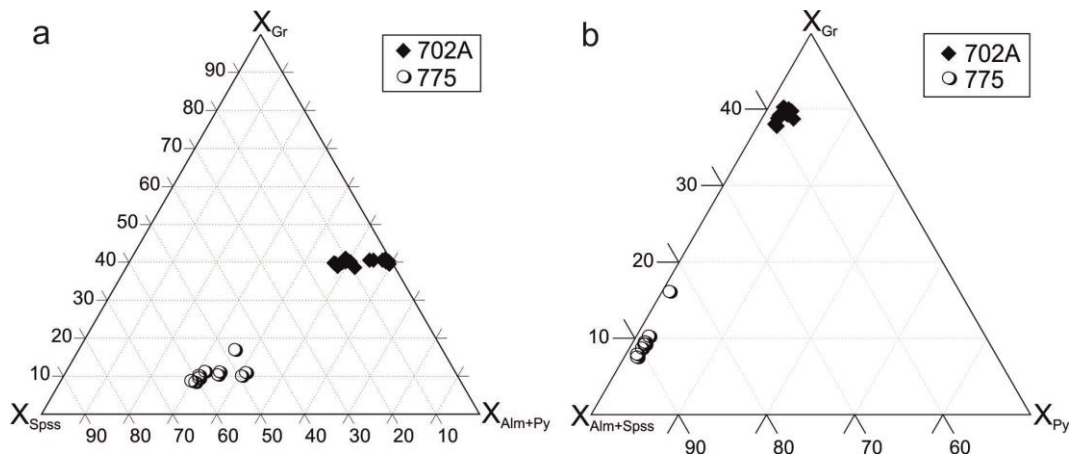


Figure 3.13 : Compositional range of garnets.

3.2.2 Micaschists

Micaschists of the Domuzdağ Complex consists of quartz, phengite, paragonite, albite, chlorite, rutile, apatite ± chloritoid ± garnet ± glaucophane ± tourmaline ± calcite. In the chloritoid-micaschist, there are also abundant pseudomorphs after glaucophane, lawsonite and jadeite. The micaschists exhibit two distinct types of retrogression that was mainly controlled by strain during exhumation. The first types of the micaschists are mainly exposed southeast of the extensional shear zone that separates the Domuzdağ Complex from the overlying Esenler Unit. These micaschists consist of quartz, phengite, paragonite, albite, chlorite, calcite, rutile, apatite and tourmaline (Fig. 3.14). Albite is found as syn-kinematic porphyroblasts with rotated inclusion fabrics. Brown tourmaline is a common accessory phase in this type of micaschists and is found as oriented parallel to foliation or as inclusion in albite porphyroblasts. Calcite is also found as a secondary mineral.

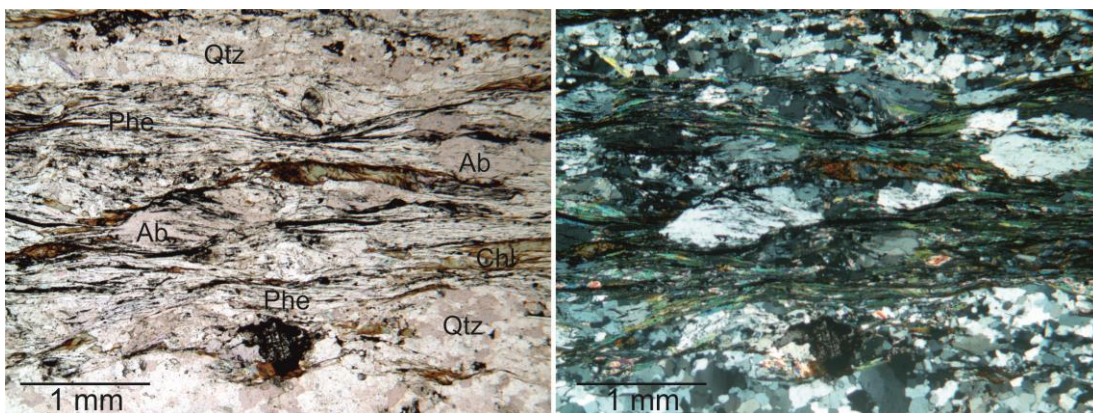


Figure 3.14 : Microphotograph of a retrogressed micaschists from the Domuzdağ Complex with syn-kinematic albite porphyroblasts under plane (left) and cross (right) polarized light. Qtz= quartz, Phe= phengite, Chl= chlorite, Ab= albite.

The second type constitutes chloritoid-micaschists that are exposed farther away from the shear zone (Fig. 3.15a, b). In these chloritoid-micaschists, retrogression is characterized by the pseudomorphing of the peak metamorphic mineral assemblages (Fig. 3.15ac, d). Three peak metamorphic assemblages are identified: 1) garnet-chloritoid-glaucophane with pseudomorphs after lawsonite 2) chloritoid with pseudomorphs after glaucophane and 3) relatively high-Mg chloritoid with pseudomorphs after jadeite in addition to phengite, paragonite, quartz, chlorite, rutile and apatite. Tourmaline or calcite is not found in the chloritoid-micaschists. Albite occurs as secondary tiny aggregates. Below, detailed petrography and mineral chemistry of three chloritoid-micaschists as well as a micaschist with syn-kinematic albite porphyroblasts are described.

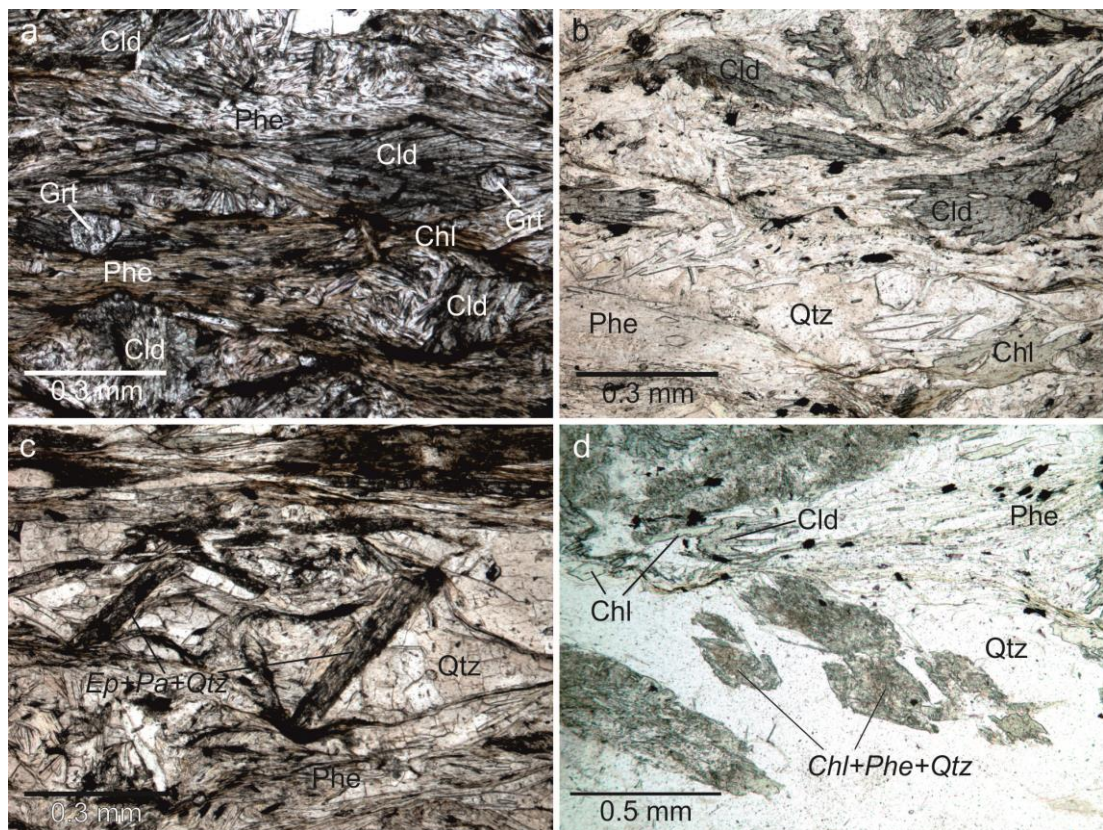


Figure 3.15 : Photomicrographs of the chloritoid-micaschists from the Domuzdağ Complex (plane polarized light). a) Sample 775, a garnet-chloritoid micaschist. b) Sample 753A, a chloritoid-micaschist. c) Syn-kinematic pseudomorphs after lawsonite (sample 775). Former lawsonite was replaced by epidote (Ep), paragonite (Pa) and quartz (Qtz). The syn-kinematic character of the pseudomorphs suggests that they were stable during the peak metamorphic conditions. d) Pseudomorphs after glaucophane (sample 753A). They are replaced by chlorite (Chl), phengite (Phe), and quartz (Qtz). Cld=chloritoid, Grt=garnet.

3.2.2.1 Garnet-chloritoid-micaschist (sample 775)

Sample 775 consists of garnet, chloritoid, glaucophane, phengite, quartz, chlorite, paragonite, albite, rutile and apatite with pseudomorphs after lawsonite (Fig. 3.15a, c). Foliation is determined by phengitic mica and chlorite. Garnet forms tiny euhedral crystals (< 0.3 mm) and contain quartz inclusions (Fig. 3.16). Absence of any pressure shadows and rotational inclusion fabric indicates a post-kinematic origin for the garnets. Chloritoids form large porphyroblasts consisting of radially grown crystals (Fig. 3.16). Foliation bends around them. Most of the glaucophanes are replaced by chlorite + phengite + quartz (Fig. 3.16) but relicts are preserved (Fig. 3.17). Rectangular epidote + paragonite + quartz pseudomorphs are found parallel to the foliation or as rotated crystals suggesting a syn-kinematic growth (Fig. 3.15c). They are interpreted as pseudomorphs after lawsonite. Paragonite is replaced by low-Si phengites. Albite is secondary usually with secondary chlorites. It also replaces glaucophane along the rims.

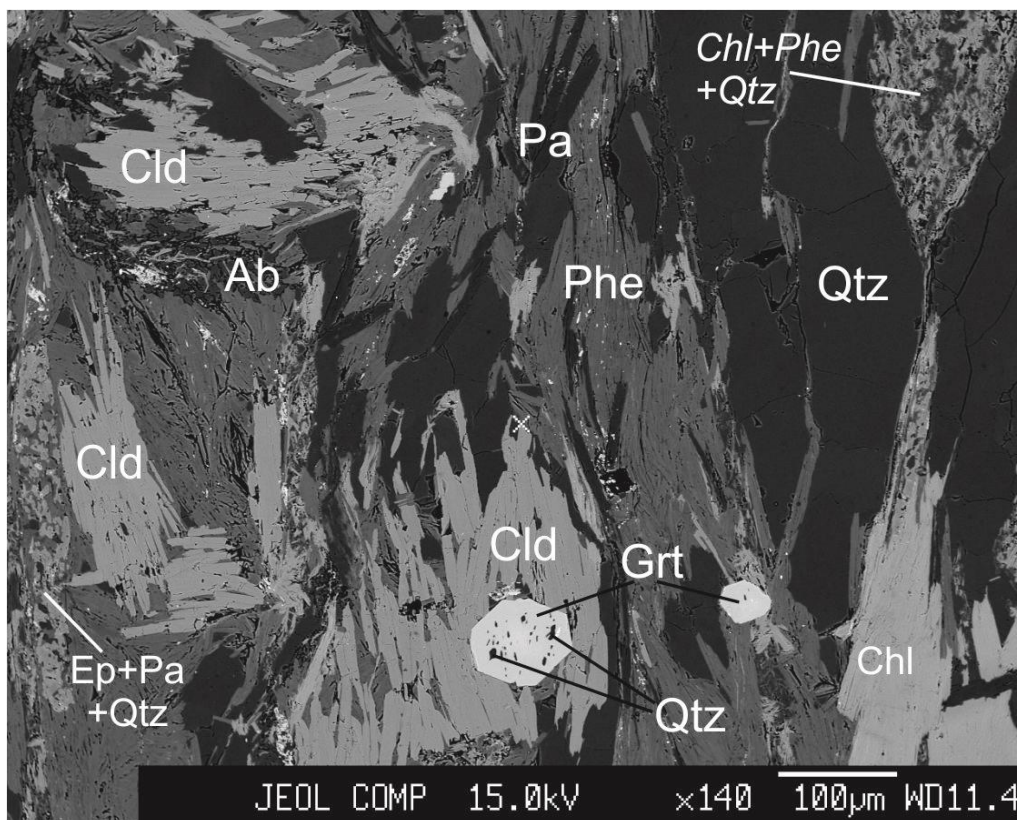


Figure 3.16 : BSE images of the sample 775. Epidote (Ep) + paragonite (Pa) + quartz (Qtz) replaced former lawsonite and chlorite (Chl) + phengite (Phe) + quartz (Qtz) replaced former glaucophane. Albite (Ab) is secondary. Quartz (Qtz) inclusions in garnet (Grt) do not show any rotational fabric. Cld=chloritoid.

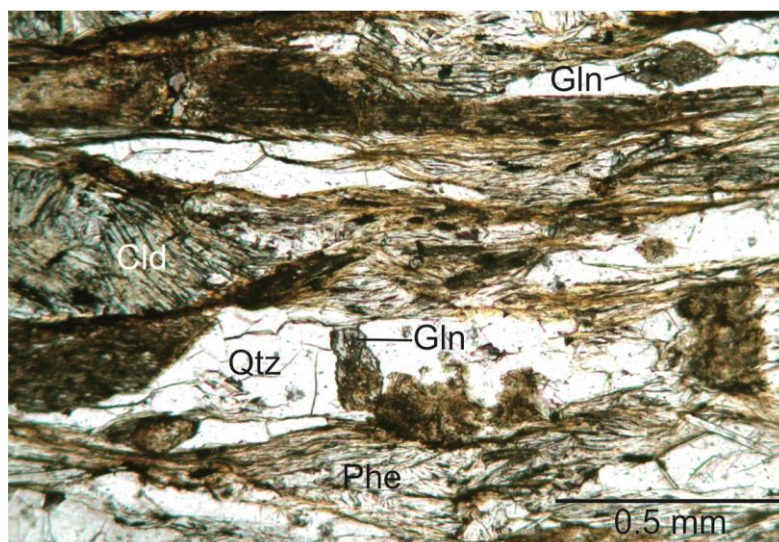


Figure 3.17 : A photomicrograph showing the partly preserved glaucophane (Gln) relicts in the sample 775. The majority of the glaucophanes are replaced by chlorite, phengite and quartz (see Fig 3.16) Qtz= quartz, Phe= phengite.

Garnets of the sample 775 have two distinct compositional ranges with $\text{Alm}_{28-39}\text{Py}_1\text{Grs}_{7-10}\text{Spss}_{63-49}$ in the core and $\text{Alm}_{34}\text{Py}_1\text{Grs}_{16}\text{Spss}_{49}$ in the outermost rim (Fig. 3.13). In the core, X_{Mn} decreases rimward, while X_{Fe} increases proportionally. X_{Ca} slightly increases and is stabilized around 10%. The outermost rim is characterized by a dramatic increase of X_{Ca} to 16% and decrease of X_{Mn} . Element mapping shows that while X_{Ca} continues to increase within the outermost rim, X_{Fe} slightly decreases (Fig. 3.18).

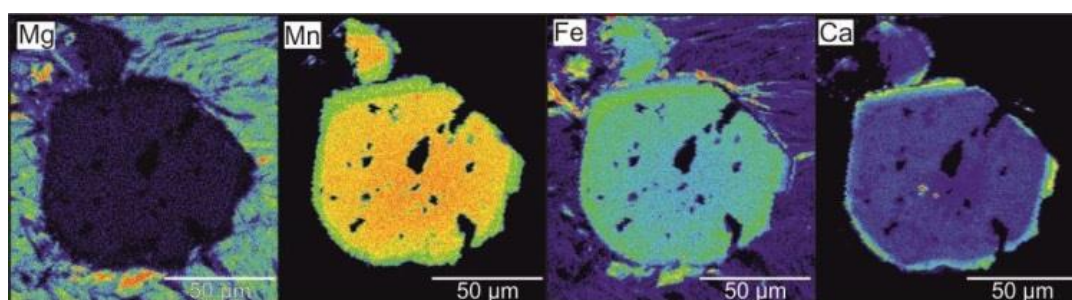


Figure 3.18 : Element mapping of the post-kinematic garnet in sample 775. Dark areas within the garnet are quartz inclusions. Notice the Ca-rich outermost rim possibly depicting increasing rate of lawsonite breakdown.

Compositional range of the chloritoid is $\text{Fe}_{81-83}\text{Mg}_{7-10}\text{Mn}_{11-8}$ (Fig. 3.19). From core to rim, Mn decreases while Fe and Mg increases. Relicts of the glaucophane in sample 775 are almost free of ferric iron component and plot on the glaucophane-ferroglaucophane boundary in a Miyashiro diagram (Fig. 3.5).

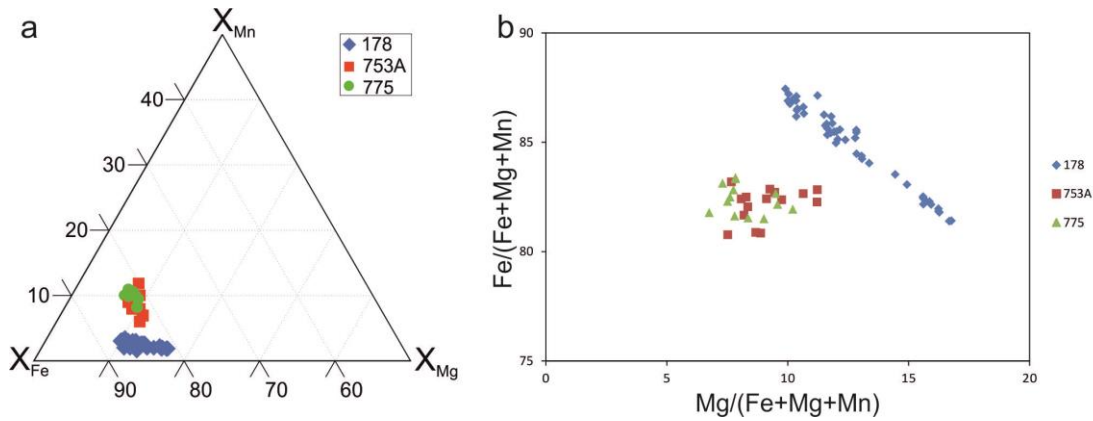


Figure 3.19 : Compositional range of the chloritoids. (a) Ternary compositional diagram. While in sample 178, main exchange occur between Fe and Mg, in the samples 775 and 753A Mg mainly substitute with Mn. (b) X_{Mg} vs X_{Fe} diagram.

Si content of the phengite ranges between 3.50-3.04 (Fig. 3.11). Mg# number of the phengite increases with increasing Si content. Mg/ (Mg+Fe) number of matrix chlorite is 0.32-0.35 (Fig. 3.8). Secondary chlorites have higher Mg# numbers (0.40-0.41) and their Si content increases at the expense of Al. $Fe^{3+}/(Fe^{3+}+Al)$ ratio of the epidotes that replace lawsonite ranges between 7-11% (Fig. 3.7). Plagioclase is almost pure albite.

3.2.2.2 Chloritoid-micaschist (sample 753A)

Sample 753A consists of chloritoid, phengite, quartz, chlorite, paragonite, albite, allanite, rutile, and apatite (Fig. 3.15b). Chloritoid forms large porphyroblasts of radially grown crystals. There are chlorite + phengite + quartz pseudomorphs interpreted as former glaucophane (Fig. 3.15d, 3.20). Chlorite, which was once in equilibrium with glaucophane, penetrates into glaucophane as thin stripes during retrogression (Fig. 3.20). From rim to core, grain size of the pseudomorphing minerals markedly decreases indicative for increasing nucleation rate. Allanite is replaced by epidote at their rim.

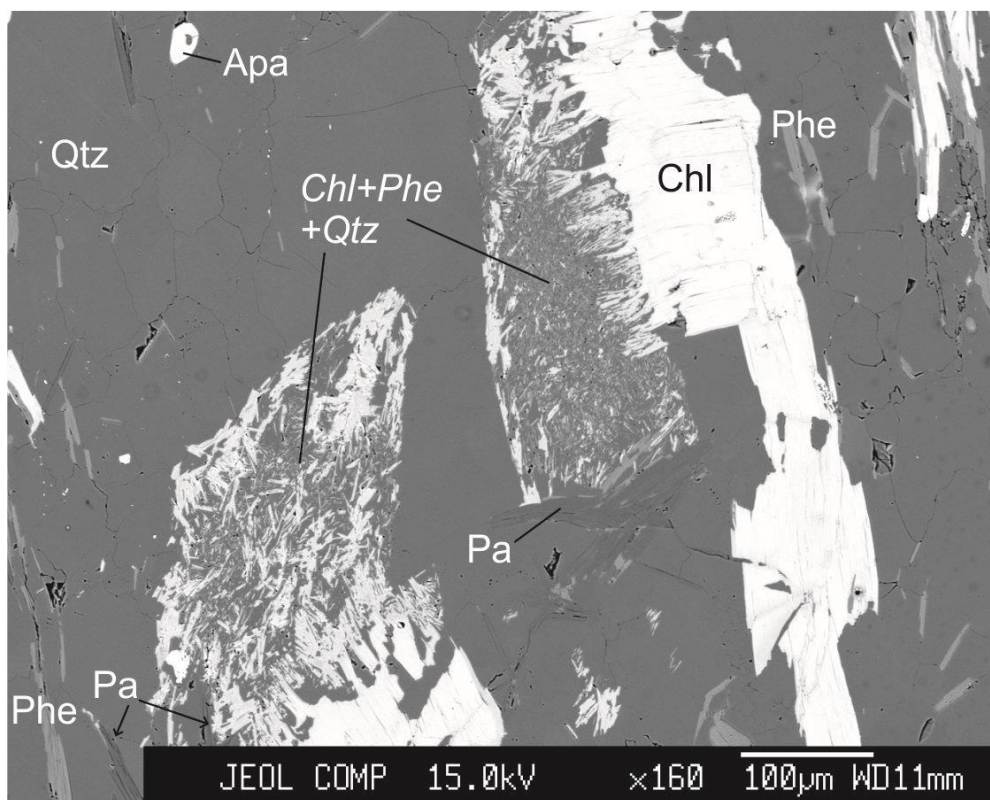


Figure 3.20 : BSE images of the sample 753A. Chlorite (Chl) + phengite (Phe) + quartz (Qtz) replaced former glaucophane. The matrix chlorite penetrates into former glaucophane as secondary thin stripes. Paragonite also possibly replaced former glaucophane along its rims. Apa= apatite.

In the sample 753A, compositional range of the chloritoids is $Fe_{81-83}Mg_{8-11}Mn_{6-12}$ (Fig. 3.19). Fe component slightly increases rimward and then becomes relatively stable. Mg slightly increases and the Mn decreases rimward. Si content of phengite ranges between 3.47-3.23 c.p.f.u (Fig. 3.11). Mg# number increases with increasing Si content. Mg# number of matrix chlorites ranges between 0.34-0.39 and that of secondary chlorites between 0.39-0.47 (Fig. 3.8). The secondary chlorites are also characterized by increasing of Si content at the expense of Al. Fe^{3+} ratio of epidote that replaces allanite ranges between 14-18% (Fig. 3.7). Plagioclase is almost pure albite.

3.2.2.3 Chloritoid-micaschist (sample 178)

Sample 178 consists of chloritoid, phengite, quartz, chlorite, albite, rutile and apatite (Fig. 3.21). Chloritoids are found as aggregates or single crystals parallel to the foliation. They are replaced by both paragonite and chlorite (Fig. 3.21b). There are chlorite + quartz + phengite pseudomorphs within the quartz-rich domains (Fig. 3.21b, c). They have chloritoid-like prismatic outlines and are interpreted as

pseudomorphs after chloritoid. In sample 178, albite is found as tiny grains within rectangular pseudomorphs interpreted as former jadeite (Fig. 3.21a). Around the pseudomorph after jadeite foliation bends and tiny phengite inclusions show rotational fabric indicating a syn-kinematic origin. Paragonite is partly replaced by low-Si phengites.

In sample 178, three generations of chloritoid are identified. Cld1 is relatively rich in Mn and low in Mg with compositional range of $\text{Fe}_{87-84}\text{Mg}_{10-14}\text{Mn}_{3-2}$ (Fig. 3.19). Cld2 is marked by its elevated Mg content with compositional range of $\text{Fe}_{82-81}\text{Mg}_{16-17}\text{Mn}_2$. Finally, the high-Mg Cld2 is replaced by low-Mg and high-Mn chloritoid (Cld3) along the rims. Cld3 are identical in composition with Cld1 ($\text{Fe}_{87}\text{Mg}_{10}\text{Mn}_3$) but show inverse zoning suggesting a retrogressive origin.

Si content of phengite ranges between 3.45-3.10 c.p.f.u (Fig. 3.11). Mg# number increases with increasing Si content. In sample 178, chlorite is a secondary phase replacing the high-Mg chloritoid (Cld2). Mg# number of the chlorite ranges between 0.32-0.35 (Fig. 3.8). Plagioclase is almost pure albite.

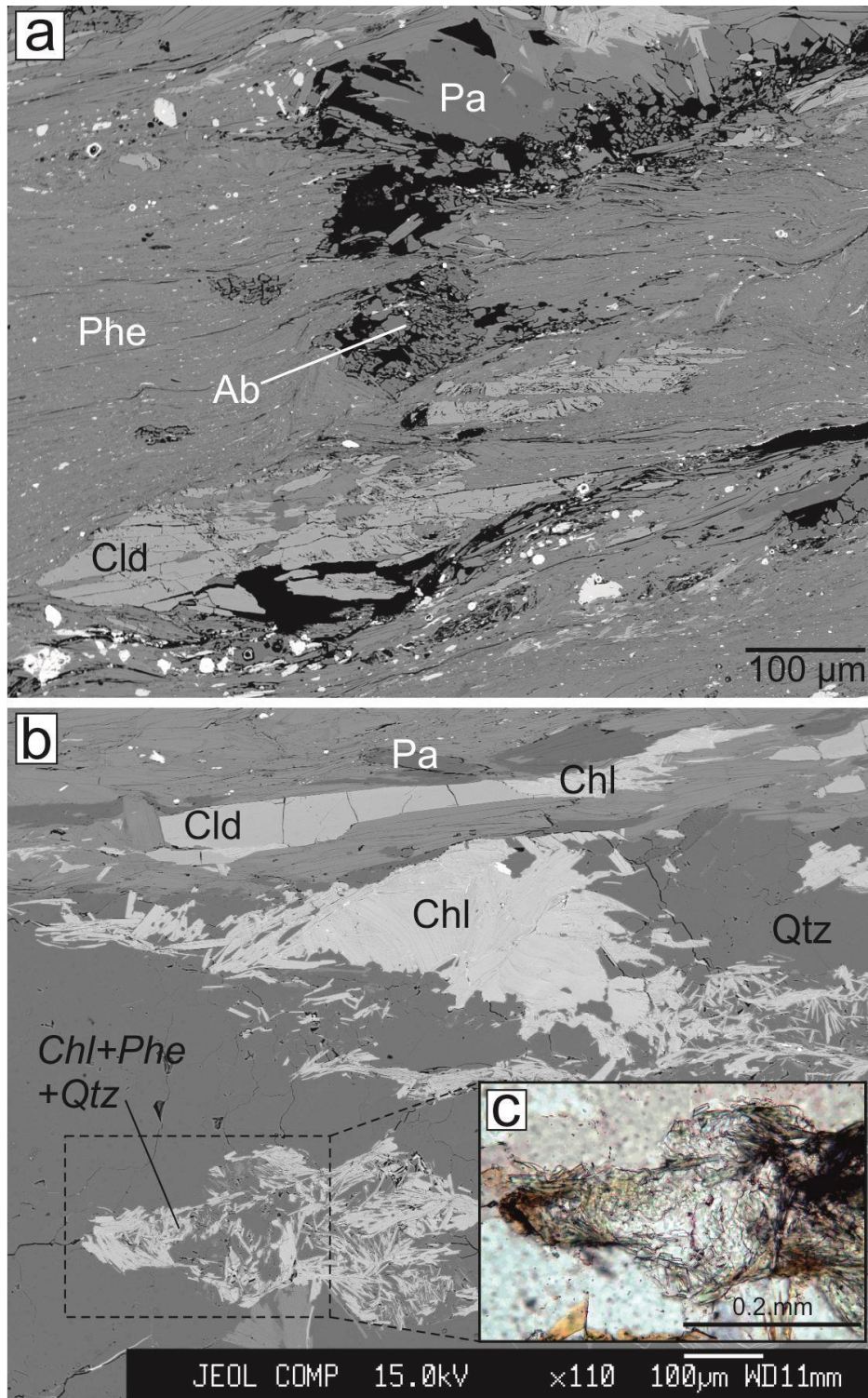


Figure 3.21 : BSE images of the sample 178. a). Chloritoid (Cld) aggregates together with a rectangular pseudomorph at the center of image composed of albite (Ab). Tiny inclusions of phengites within the pseudomorph exhibit rotational fabrics. Foliation also slightly bends around the pseudomorphs indicating its syn-kinematic origin. It is interpreted as former jadeite. b) A pseudomorph after chloritoid (Cld) within the quartz rich domain. It is replaced by chlorite (Chl) + quartz (Qtz) + phengite (Phe). c) The same pseudomorph in “b” under microscope (plane polarized light). Pa= paragonite.

3.2.2.4 Micaschist with albite porphyroblasts (sample 392)

Sample 392 consists of phengite, paragonite, chlorite, quartz, albite, rutile, apatite and tourmaline. Albite forms syn-kinematic porphyroblasts with rotated phengite, paragonite, chlorite and rutile inclusions. Si content of phengites ranges between 3.48-3.33 c.p.f.u (Fig. 3.11). Although they are indistinguishable in terms of texture, in the Si vs Al diagram, phengites with relatively low Si plot above the celadonite exchange trend. A similar separation is visible with the iron contents of the phengites. Fe forms two clusters with similar Mg# ratio around 0.2 and 0.1 c.p.f.u for the high- and low-Si phengites, respectively. While calculating mineral formula, iron is normally treated as ferrous. Recalculation as ferric iron resets the low-Si phengites on the muscovite-celadonite exchange line. Thus, an effect of oxygen fugacity might be inferred. Within the high-Si phengites, Si decreases from core to rim (3.44-3.41 c.p.f.u.) forming rims of low-Si phengite. Albites contain low-Si phengite (3.35-3.39 Si c.p.f.u) inclusions and are mostly surrounded by similar phengites. Paragonite is replaced by low-Si phengites along the rims. Mg/ (Mg+Fe) ratio of chlorite ranges between 0.35-0.38 (Fig. 3.8). There is no significant Al and Si exchange in the chlorite.

3.3 The Kunduz Metamorphics

The Kunduz Metamorphics consist mainly of metabasites and marble with volcanogenic metasandstone, phyllite/metatuff and metachert. Structurally, it is separated into two sectors (Fig. 2.1). In the upper part, the metabasites are mostly greenschists consisting of calcic-amphibole, chlorite, albite, epidote, phengite and titanite sometimes with augite relicts (Fig. 3.22a). There are also sodic-amphibole bearing metabasites preserved locally. These well-foliated blueschists consist of sodic amphibole, albite, epidote, chlorite, phengite, titanite (Fig. 3.22b). Foliation is defined by the sodic-amphibole. Sodic-amphibole also occurs in the metatuff interbedded with the marbles. The metatuff consists of sodic-amphibole, chlorite, epidote, albite, calcite and titanite. Phyllites form interbeds within the metavolcanic rocks and consist of quartz, phengite, albite, bluish-green amphibole, chlorite and stilpnomelane with magmatic augite relicts (Fig. 3.22c). In the lower part of the Kunduz Metamorphics, the magmatic texture and mineralogy of the metabasites are mostly retained. They are weakly metamorphosed basaltic rocks and consist of

pyroxene and altered plagioclase (Fig. 3.22d). Metamorphism is defined by secondary chlorite and albite.

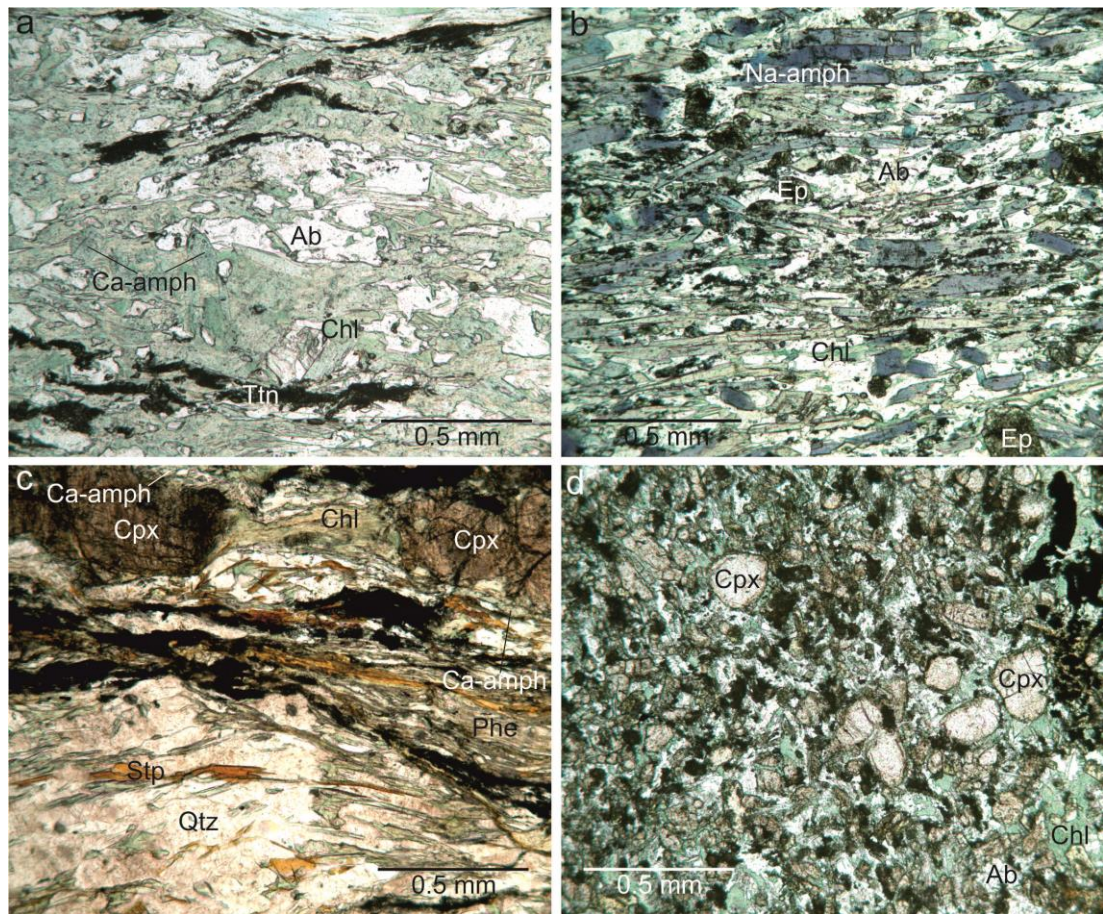


Figure 3.22 : Microphotographs from the Kunduz Metamorphics. a) A greenschist consisting of calcic-amphibole (Ca-amph), chlorite (Chl), albite (Ab) and titanite (Ttn). b) A blueschist consisting of sodic amphibole (Na-amph), epidote (Ep), albite (Ab) and chlorite (Chl). c) a phyllitic metatuff consisting of phengite (Phe), quartz (Qtz), calcic-amphibole (Ca-amph), chlorite (Chl), stilpnomelane (Stp) with relict clinopyroxene (Cpx). d) A weakly metamorphosed metabasite from the lower part of the Kunduz Metamorphics. Cpx= magmatic pyroxene, Chl= chlorite, Ab=albite.

Mineral chemistry of a quartz-micaschist from the Kunduz Metamorphics is investigated (Tables A.1-A.10). The sample is taken from the upper part of the Kunduz Metamorphics and is interlayered with light colored marble and metabasite. This sample 626A consists of quartz, phengitic white mica, epidote, hematite and titanite. Phengites define a weakly developed foliation. Si content of the phengite ranges between 3.37 and 3.44 c.p.f.u (Fig. 3.11). $Fe^{3+}/(Fe^{3+}+Al)$ ratio of the epidote is 0.28-0.30 (Fig. 3.7).

3.4 Köşdağ Formation

The Köşdağ Formation consists mainly of low-grade mafic and felsic volcanic rocks together with pyroclastic rocks. Red recrystallized pelagic limestone and chert are interbedded within the metavolcanic rocks. The mafic rocks are basaltic andesite and andesite consisting mainly of clinopyroxene and plagioclase phenocrysts. Felsic rocks are dacitic to rhyolitic in composition and consist of quartz and feldspar phenocrysts. Below detailed petrography of the rhyolitic and basaltic andesitic/andesitic rocks are given. Their major, trace and rare earth element compositions are provided in the geochemistry chapter (Ch. 7).

3.4.1 Felsic volcanic rocks

Felsic rocks of the Köşdağ Formation mainly consist of plagioclase and locally of quartz and K-feldspar phenocrysts set on a recrystallized and foliated groundmass of feldspar, quartz, chlorite, muscovite and epidote (Fig. 3.23a, b). Besides the single phenocrysts, there are also glomeroporphyritic aggregates consisting of plagioclase, clinopyroxene, opaque (Fe-Ti oxides) and apatite interpreted as cognate mafic xenoliths (Fig. 3.23c, d). They were possibly formed earlier in the magma chamber during differentiation of the parental magma. In more evolved samples with a higher amount of quartz phenocrysts, the xenoliths are absent or consist only of plagioclase clusters sometimes with interstitial clinopyroxene (Fig. 3.23e-h). In the xenoliths, plagioclase and clinopyroxene usually have sharp boundaries with the surrounding groundmass suggesting they are in equilibrium.

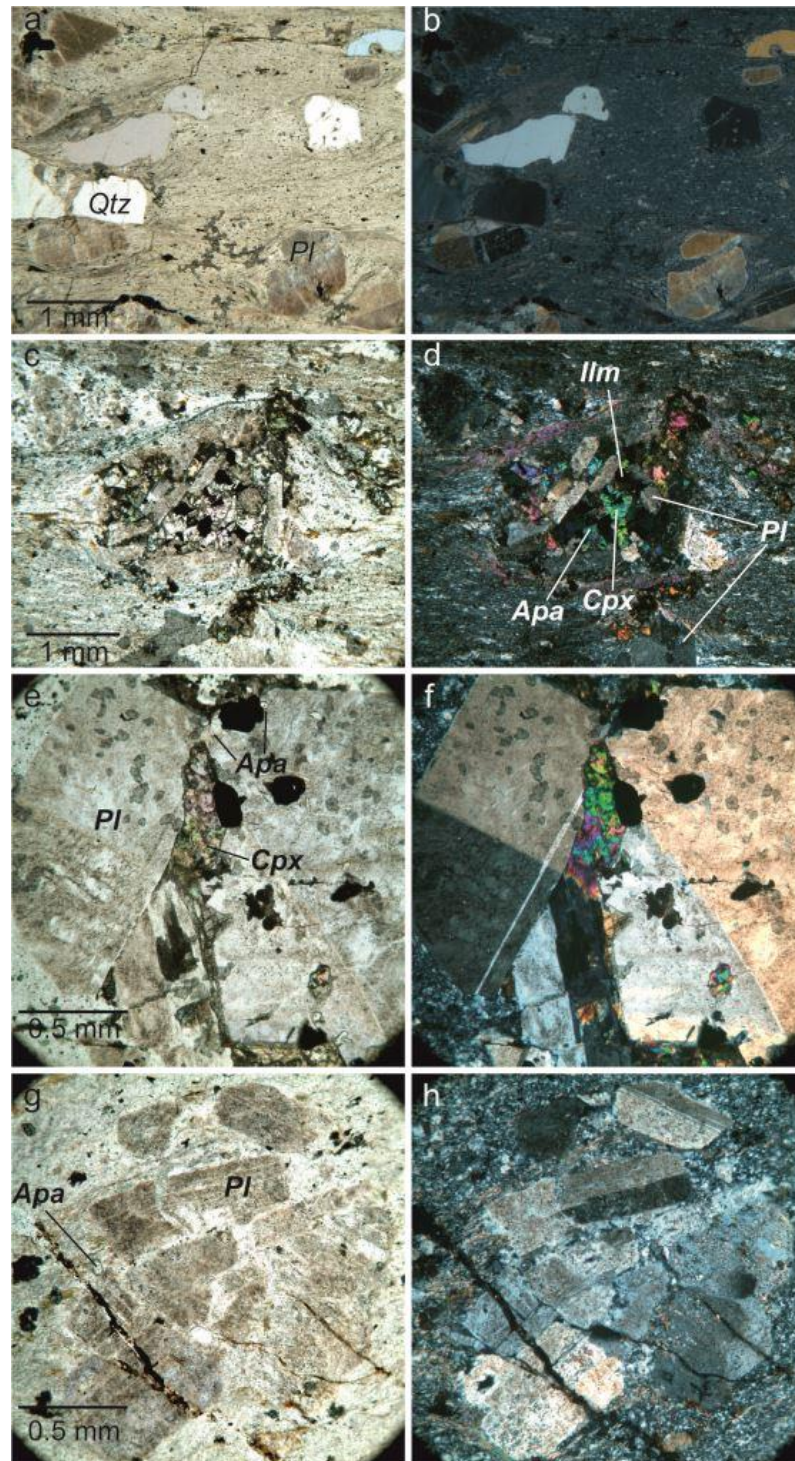


Figure 3.23 : Microphotographs (plane polarized in the left side and cross polarized in the right) of the acidic rocks of the Köşdağ Formation. a & b) SiO_2 saturated metarhyolite with quartz (Qtz) and feldspar (Pl) phenocrysts. c & d) A cognate mafic xenolith within a metarhyolite (1213). It consists of plagioclase (Pl), clinopyroxene, Fe-Ti oxide (Ilm), and apatite. e & f) A cognate xenolith with cumulate-like plagioclases (Pl) with interstitial clinopyroxene (Cpx) in a metarhyolite. Apatite (Apa) and Fe-Ti oxides also occur in the xenolith. g & h) A cumulate-like plagioclase cluster without mafic minerals within a metarhyolite (1304B).

3.4.2 Basaltic andesite/andesite

Basaltic andesite/andesites consist of plagioclase and clinopyroxene. Plagioclase forms large phenocrysts or microliths in the groundmass. Clinopyroxene is free of optical zonation. Mafic cognate xenoliths are not found in basaltic andesite though glomeroporphyritic texture occurs (Fig. 3.24a-d). In an andesite (sample 1286), however, cognate xenoliths consisting of clinopyroxene, plagioclase and apatite are observed (Fig. 3.24e, f). Apatite is also found as monomineralic aggregates in the same sample 1286. In the glomeroporphyritic aggregates, replacement by secondary calcite is common.

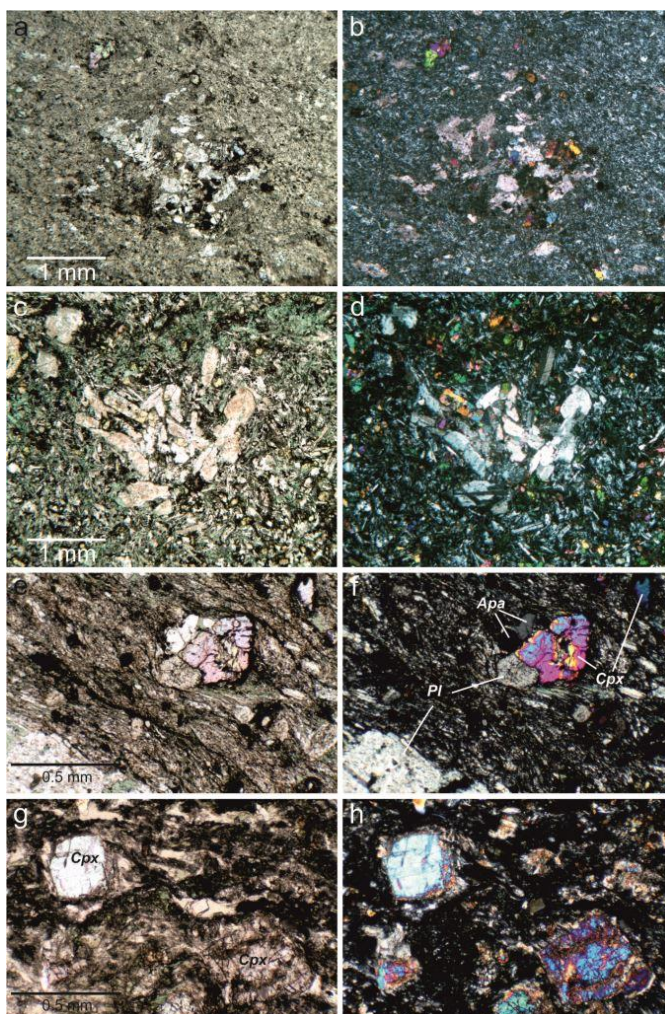


Figure 3.24 : Microphotographs (plane polarized in the left side and cross polarized in the right) of the basaltic andesite/andesite of the Köşdağ Formation. a & b) Glomeroporphyritic cluster within basaltic andesites, sample 1287 (a&b) and sample 1288 (c&d). e & f) A cognate xenolith consisting of clinopyroxene, plagioclase and apatite in an andesite (1286). Apatite is also found as inclusion within the clinopyroxene. g & h) Metabasite with augite relicts. Ca-amphibole replaces the augite along their rims.

Metamorphic mineral assemblages in the metabasaltic-andesites consist of chlorite, epidote, albite and minor actinolite replacing clinopyroxene indicative for greenschist facies metamorphism (3.24g, h). The glassy groundmass of the metarhyolites is completely recrystallized and consists of tiny quartz, albite, white mica, chlorite and epidote grains. The preservation of monomineralic quartz phenocrysts locally with undoluse extinction in the metarhyolites (Fig. 3.23a, b) indicates that the temperatures during the metamorphism were less than 300° C (Stipp et al., 2002).

4. RAMAN MICROSPECTROSCOPY OF CARBONACEOUS MATERIAL

The majority of the pelitic rocks contain primary organic matter consisting of a mixture of C, H, O, N and S known as kerogen (e.g. Tissot and Welte, 1978). With increasing metamorphic temperature, the weakly-ordered atomic structure of the kerogens transform into well-organized graphite called as graphitization (Landis, 1971; Diessel et al., 1978; Itaya, 1981; Beyssac et al., 2002b). Raman microspectrometry is possibly the most efficient method for revealing the degree of graphitization of the carbonaceous material (Pasteris and Wopenka, 1991; Wopenka and Pasteris, 1993; Yui et al., 1996; Beyssac et al., 2002a, 2002b). Recently, calibrations of Raman spectra of carbonaceous material (RSCM) allow deriving precise temperature constraints on metapelitic rocks (Beyssac et al., 2002b; Rahl et al., 2005; Aoya et al., 2010; Lahfid et al., 2010). It is particularly efficient in low-grade metamorphism where index minerals are generally absent for conventional geothermobarometric methods (Beyssac et al., 2004, 2007).

Raman microspectroscopy on carbonaceous material was performed on metapelitic rocks of the Esenler Unit and the Domuzdağ Complex to constrain their peak metamorphic temperatures. The measurements were performed at the Raman Laboratory of the Institute of Earth and Environmental Sciences at Potsdam University. Details of the measurement procedure are given in the methodology part. Below, general parameters of the measured Raman spectra are given. The temperature calculations and the obtained values are discussed in the next chapter under the title of Metamorphic Conditions.

4.1 Esenler Unit

Raman microspectrometry was performed on carbonaceous material of 15 metapelitic rocks including both slates and phyllites. In accordance with the texture, the metapelitic rocks of the Esenler Unit exhibit variable Raman spectra indicating distinct degrees of graphitization and metamorphic temperatures.

The majority of the measured samples are slates which show G (graphite) and D2 defect bands as a single band near 1600 cm⁻¹ (Fig. 4.1). After decomposing, the positions of the bands are 1595 cm⁻¹ (G) and around 1615 cm⁻¹ (D2), respectively (Fig. 4.2a, Table 4.1). The D1 defect band occurs at 1345 cm⁻¹. The slates are also characterized by showing broad D3 and D4 defect bands with high intensities. These bands generally cause upward shift of the spectrum including G, D1 and D2 bands. The D3 band was located mostly between 1520 cm⁻¹ and 1530 cm⁻¹ and the D4 band between 1230 cm⁻¹ and 1245 cm⁻¹ (Fig. 4.2a). One sample (871) differs from the rest by its low intensities of D3 and D4 defect bands (Fig. 4.1).

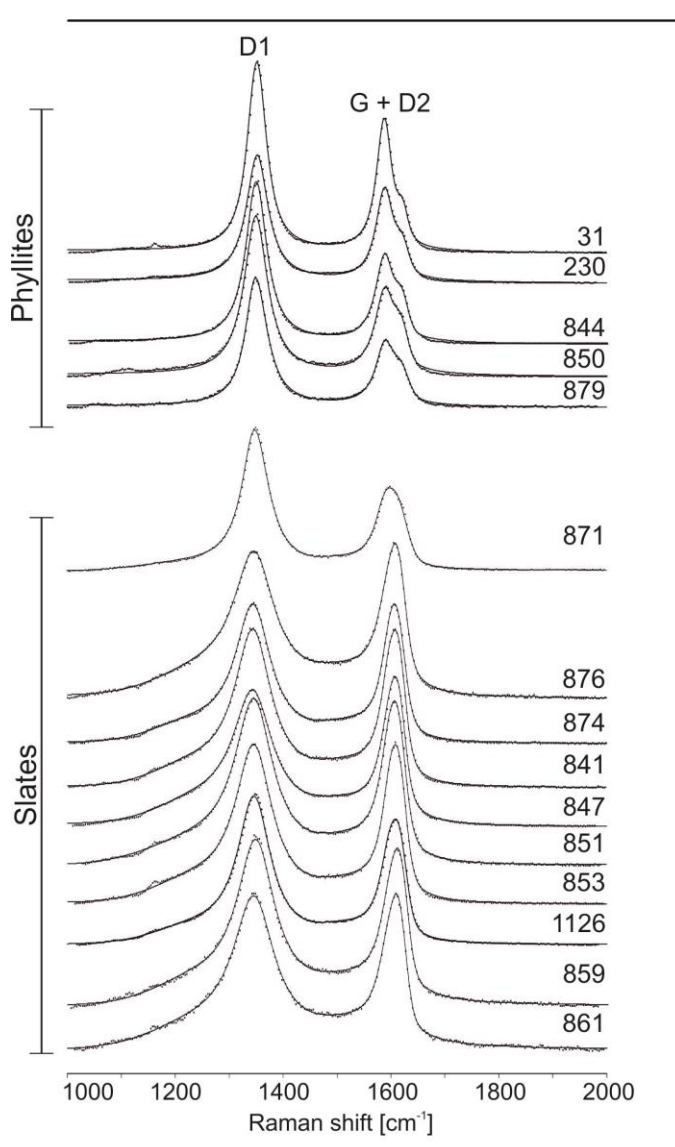


Figure 4.1 : Representative Raman spectra of carbonaceous material of the measured samples from the Esenler Unit. The RSCM forms two clusters corresponding texturally to the slates and phyllites. The sample numbers are given at the right side of the each spectrum.

The phyllite is characterized by the differentiation of the graphite (G) and D2 defect peaks and absence of D3 and D4 defect bands (Fig. 4.1). The G band occurs at 1588-1590 cm⁻¹ and D2 defect band is placed as a shoulder of G band around 1618-1620 cm⁻¹ (Fig. 4.2b). The D1 band of these samples is located at ca. 1352 cm⁻¹.

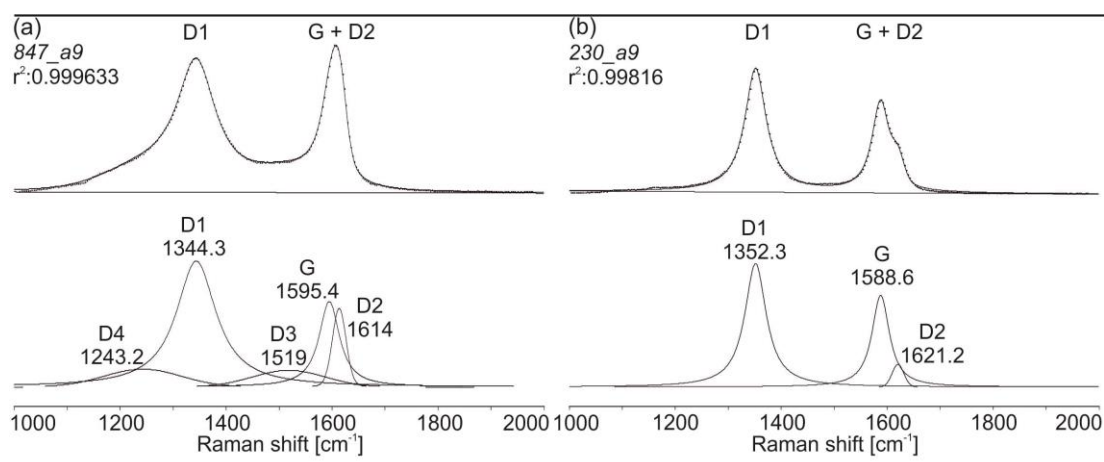


Figure 4.2 : Representative examples of fitting of the measured Raman spectra. a) Low-temperature slates that are characterized by undifferentiating of graphite (G) and D2 defect bands and occurrence of broad D3 and D4 defect bands (sample 847). b) Phyllite showing slightly pronounced G band with D2 occurring on its shoulder (sample 230).

Table 4.1 : Parameters of decomposed Raman spectra of carbonaceous material from the Esenler Unit

Sample	#	G Position	1 σ	G FWHM	1 σ	D1 position	1 σ	D1 FWHM	1 σ
31	24	1587.46	0.63	35.88	1.72	1352.33	0.66	41.90	1.69
230	17	1588.08	1.13	37.57	1.77	1352.00	1.10	45.09	3.25
850	21	1588.82	0.78	44.04	0.99	1350.62	0.70	50.35	2.66
844	25	1587.98	1.00	41.24	1.29	1350.65	1.00	46.95	1.96
879	15	1590.24	0.93	43.30	2.19	1352.16	0.69	46.93	2.43
871	20	1590.15	1.88	47.73	2.38	1350.38	1.30	56.70	4.81
876	23	1594.27	2.35	46.48	5.55	1343.98	2.36	85.92	10.16
874	29	1596.56	0.97	44.73	1.91	1344.10	1.83	81.73	7.74
841	22	1595.57	1.10	42.98	1.91	1343.97	1.43	79.77	5.23
847	30	1595.31	1.11	46.30	3.41	1343.94	1.15	93.20	3.44
851	23	1595.04	1.13	45.84	4.07	1344.89	3.21	84.77	11.70
853	20	1596.01	1.35	45.36	2.64	1346.26	2.83	81.79	11.52
1126	26	1596.08	1.04	44.63	1.74	1346.44	0.80	77.49	3.90
859	19	1595.22	1.82	45.98	1.95	1346.80	1.48	82.82	5.59
861	23	1593.42	1.18	50.71	0.94	1345.82	0.66	94.46	2.30

is the number of the measured spectra used in calculations. 1 σ = standard deviation.

4.2 Domuzdağ Complex

Raman microspectroscopy on carbonaceous material was performed on four micaschists samples from the Domuzdağ Complex. The samples include three chloritoid-micaschists (775, 753A and 178) and a retrogressed micaschist with syn-kinematic albite porphyroblasts (392) exposed southeast of the extensional shear zone.

All of the measured samples show clear G band occurring at ca. 1580 cm⁻¹ in the Raman range (Table 4.2, Figure 4.3). The D1 defect band located at ca. 1552 cm⁻¹ and D2 defect band at ca. 1620 cm⁻¹. In the chloritoid-micaschists, D2 defect band placed on the shoulder of G band whereas in the sample 392, it is slightly differentiated from G band and appear as a separate peak. Intensities of the D1 and D2 bands is variable. Samples 775 and 178 have D1 and D2 band with higher intensities. Sample 753A and 392, however, is characterized by low intensity defect bands.

Table 4.2 : Parameters of decomposed Raman spectra of carbonaceous material from the Domuzdağ Complex.

Sample	#	G Position	1 σ	G FWHM	1 σ	D1 position	1 σ	D1 FWHM	1 σ
775	33	1583.72	0.97	30.99	2.71	1352.62	0.73	43.44	1.26
178	32	1582.16	1.03	28.06	3.71	1351.97	1.08	41.53	2.57
753A	30	1583.38	0.84	25.34	3.51	1354.16	0.84	45.65	3.46
392	25	1581.17	0.64	21.73	1.61	1353.38	1.39	45.26	1.25

is the number of the measured spectra used in calculations. 1 σ = standard deviation.

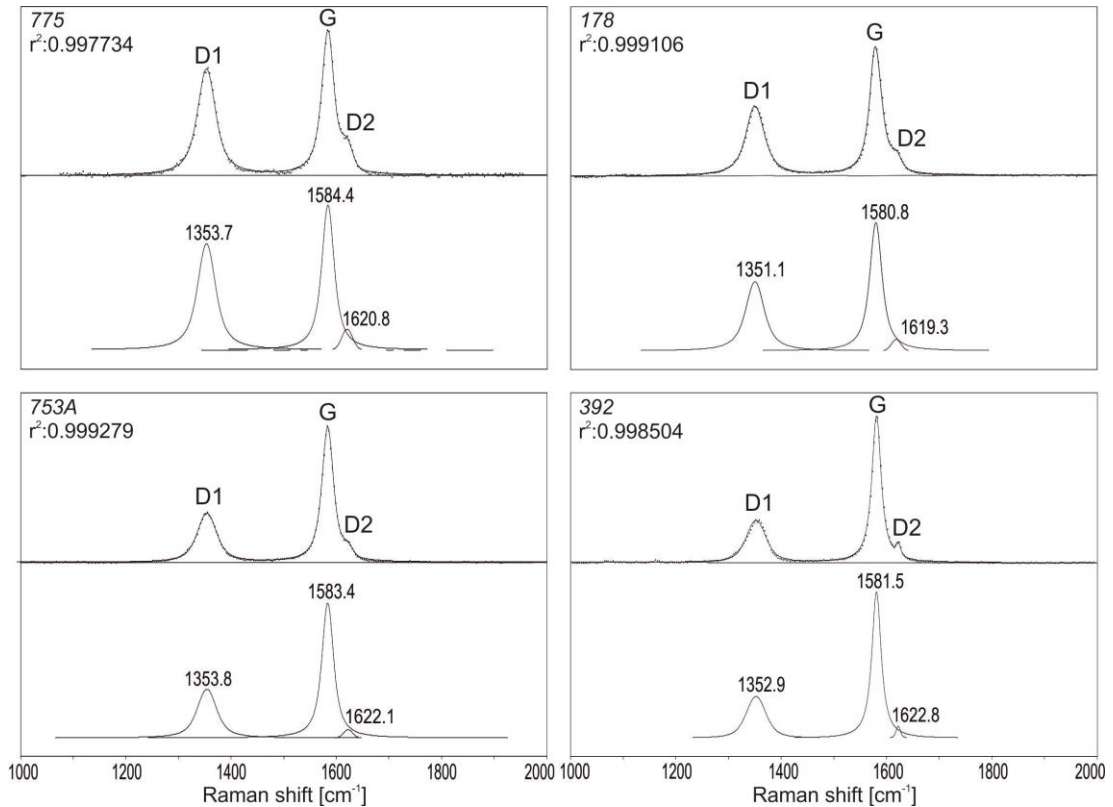


Figure 4.3 : Representative RSCM of the metapelitic rocks of the Domuzdağ Complex.

4.3 Concluding Remarks

Raman microspectroscopy is performed on carbonaceous material of the metapelitic rocks of both the Esenler Unit and tectonically underlying the Domuzdağ Complex. In the low-grade Esenler Unit, Raman spectra of carbonaceous material of the metapelitic rocks show two overlapping groups described as slates and phyllites. The first group (slates) is characterized by 1) occurrences of broad D3 and D4 defect bands 2) appearance of G and D2 defect bands as a single band. The second group (phyllites), however, does not show broad D3 and D4 defect bands. In this group, G and D2 bands are slightly differentiated.

The Domuzdağ Complex is the deep-seated part of the subduction-accretionary wedge and undergone a higher grade blueschist facies metamorphism than the Esenler Unit. This is also confirmed by the RSCM of the micaschist showing a higher degree of graphitization. This is evidenced by the existence of a clear G band and low intensities of the defect bands in the measured Raman spectra.

5. METAMORPHIC CONDITIONS

This chapter presents metamorphic constraints on the HP/LT metamorphism of the subduction-accretionary complexes exposed in the Central Pontides including Esenler Unit and Domuzdağ Complex. The Esenler Unit is a low-grade metaflysch sequence consisting of slate/phyllite and metasandstone intercalation with blocks of marble, sodic-amphibole bearing metabasite and serpentinites. The Domuzdağ Complex consists mainly of deep-seated HP/LT metabasite and micaschists and tectonically underlies the Esenler Unit along an extensional shear zone. Metamorphic conditions of an incipient blueschist facies metabasite lens within the Esenler Unit were constrained by reactions calculated by THERMOCALC (3.33) software (Powell and Holland, 1988). The program uses the thermodynamic data set of Holland and Powell (1998). Activities of the reactions were calculated from the mineral chemistries by the AX program (<https://www.esc.cam.ac.uk/research/research-groups/holland/ax>). Peak metamorphic temperatures of the metapelitic rocks of the Esenler Unit were estimated by their Raman spectra of carbonaceous material.

Peak metamorphic conditions of a lawsonite- and a garnet-blueschist as well as three chloritoid-micaschists from the Domuzdağ Complex were modelled by pseudosections. The pseudosections were produced by Theriak-Domino software. The program calculates equilibrium mineral assemblages of a given bulk rock composition by the Gibbs free energy minimization method (de Capitani & Brown, 1987; de Capitani & Petrakakis, 2010). In addition to the pseudosections, peak metamorphic temperatures of the chloritoid-micaschists were also obtained by their Raman spectra of carbonaceous material.

5.1 Esenler Unit

Below PT constraints of an incipient blueschist facies metabasite lens within the Esenler Unit are given. Peak metamorphic temperatures of the slate and the phyllites of the metaflysch sequence are also constrained using two distinct RSCM

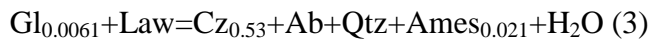
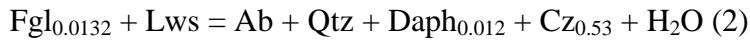
thermometers that were calibrated by Beyssac et al. (2002a) and by Rahl et al. (2005).

5.1.1 Metabasite within the Esenler Unit

The sample 211B consists of sodic- and calcic-amphibole, sodic-pyroxene, epidote, chlorite, albite and titanite with augite relicts. Presences of albite within the sample 211B give an upper limit for the metamorphic pressure. A lower limit of pressure is constrained by the reaction (reaction 1 in Figure 5.1);



A possible lower temperature limit is constrained by absence of lawsonite by the following reactions;



Metamorphic conditions of the sample 211B were constrained as 400 ± 70 °C temperatures and 7–12 kbar pressures (Fig. 5.1).

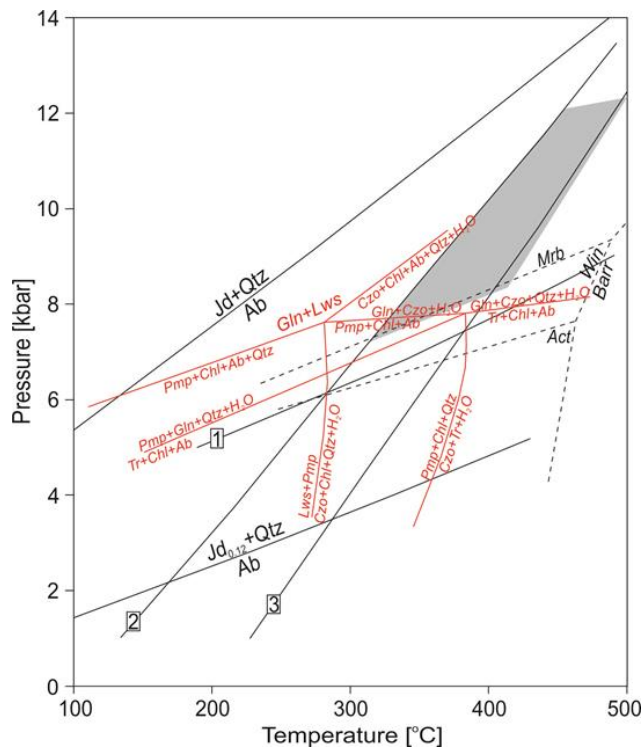


Figure 5.1 : PT conditions of an incipient blueschist facies metabasite within the Esenler Unit. Stabilities of the amphiboles are from Otsuki and Banno (1990) and a petrogenetic grid in NCMASH system for low-grade metabasite is from Schiffman and Day (1999).

5.1.2 Peak metamorphic temperatures of the slate/phyllites

The metapelitic rocks of the Esenler Unit exhibit distinct Raman spectra of carbonaceous material indicating distinct degrees of graphitization and peak metamorphic temperatures. Two groups are identified which texturally correspond to slates and phyllites, respectively. Rahl et al. (2005) calibration constrains peak metamorphic temperatures of slates to ca. 330 °C and of phyllites to 365-380 °C (Table 5.1). Beyssac et al. (2002a)'s calibration estimates ca. 345 °C temperature for the slates and 355-370 °C temperature for the phyllites. A comparison diagram of the temperatures obtained by two calibrations is shown in Figure 5.2.

Table 5.1 : Raman parameters and the calculated peak metamorphic temperatures for the Esenler Unit.

Sample	#	R1	1 σ	R2	1 σ	T ^B (°C)	CI	1 σ	T ^R (°C)	CI	1 σ
31	24	1.48	0.24	0.61	0.03	371	4	11	385	5	12
230	17	1.47	0.16	0.61	0.02	369	3	7	381	4	9
850	21	1.77	0.18	0.64	0.02	357	3	7	370	5	12
844	25	1.80	0.10	0.64	0.01	355	2	4	367	3	8
879	15	1.91	0.10	0.64	0.02	355	4	7	369	8	15
871	20	2.27	0.19	0.67	0.01	344	2	5	334	6	13
876	23	1.66	0.14	0.67	0.01	342	2	4	330	4	9
874	29	1.78	0.19	0.67	0.01	341	1	3	331	3	8
841	22	1.71	0.14	0.67	0.01	342	1	3	332	2	5
847	30	1.53	0.11	0.66	0.01	345	1	4	330	2	6
851	23	1.64	0.22	0.67	0.01	343	2	4	328	4	11
853	20	1.79	0.26	0.67	0.01	341	2	5	328	4	9
1126	26	1.83	0.15	0.68	0.01	340	1	2	331	2	5
859	19	1.55	0.08	0.67	0.01	344	1	3	328	3	6
861	23	1.54	0.07	0.66	0.01	346	1	3	332	2	6

is the amount of spectra that used during temperature calculations. 1 σ = standard deviation; CI= 95% confidence interval. T^B and T^R are the temperature values obtained by calibrations of the Beyssac et al. (2002a) and by the Rahl et al. (2005), respectively.

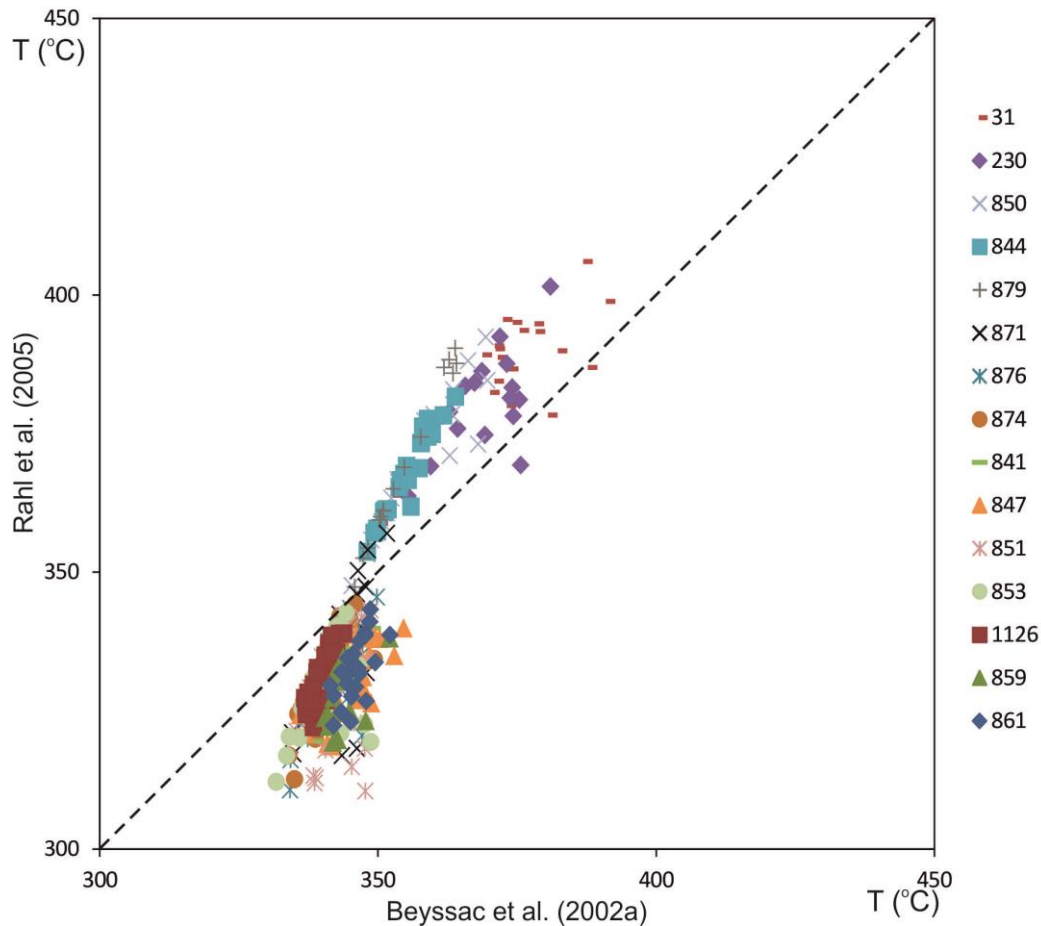


Figure 5.2 : Diagram showing RSCM temperatures of the metapelitic rocks of the Esenler Unit. The temperatures are obtained using calibrations of Beysac et al. (2002a) and Rahl et al. (2005).

5.2 Domuzdağ Complex

The Domuzdağ Complex is a deep-seated oceanic HP/LT subduction-accretionary complex consisting mainly of metabasites and micaschists with minor amount of metachert, marble and serpentinite. Peak metamorphic mineral assemblages of the metabasites are sodic amphibole + epidote + chlorite + titanite ± garnet ± lawsonite. Metamorphic conditions of a lawsonite- and a garnet-blueschist were modelled by pseudosections produced by Theriak-Domino. Micaschists of the Domuzdağ Complex consist of phengite, paragonite, quartz, chlorite, rutile ± chloritoid ± garnet ± glaucophane in addition to pseudomorphs after lawsonite and jadeite. Peak metamorphic conditions of three chloritoid-micaschists were constrained by pseudosections and by Raman spectra of carbonaceous material. The bulk rock chemistry of the samples is shown in Table A.11.

5.2.1 Lawsonite-blueschist

Peak mineral assemblages of the lawsonite-blueschist (sample 128) are sodic-amphibole, lawsonite, sodic-pyroxene, chlorite, phengite and titanite with secondary epidote and albite. The PT conditions of the sample 128 are constrained by a pseudosection (Fig. 5.3). The bulk rock chemistry of the samples is shown in Table A.11. In the modelled PT space, sudden increase of jadeite and decrease of diopside contents of sodic-pyroxene ($Jd_{4-18}Aeg_{31-23}Di_{65-59}$ and $Jd_{25-36}Aeg_{32-28}Di_{43-37}$) overlaps with the first appearance of lawsonite. The peak mineral assemblages of lawsonite + glaucophane + sodic-pyroxene + phengite + chlorite for the sample 128 cover a large P-T area in the modelled PT space. Following the X_{Jd} isopleths of omphacite and Si contents of phengite, metamorphic conditions of the sample 128 are constrained to 12–16 kbar pressure and 370–440 °C temperature (Fig. 5.3).

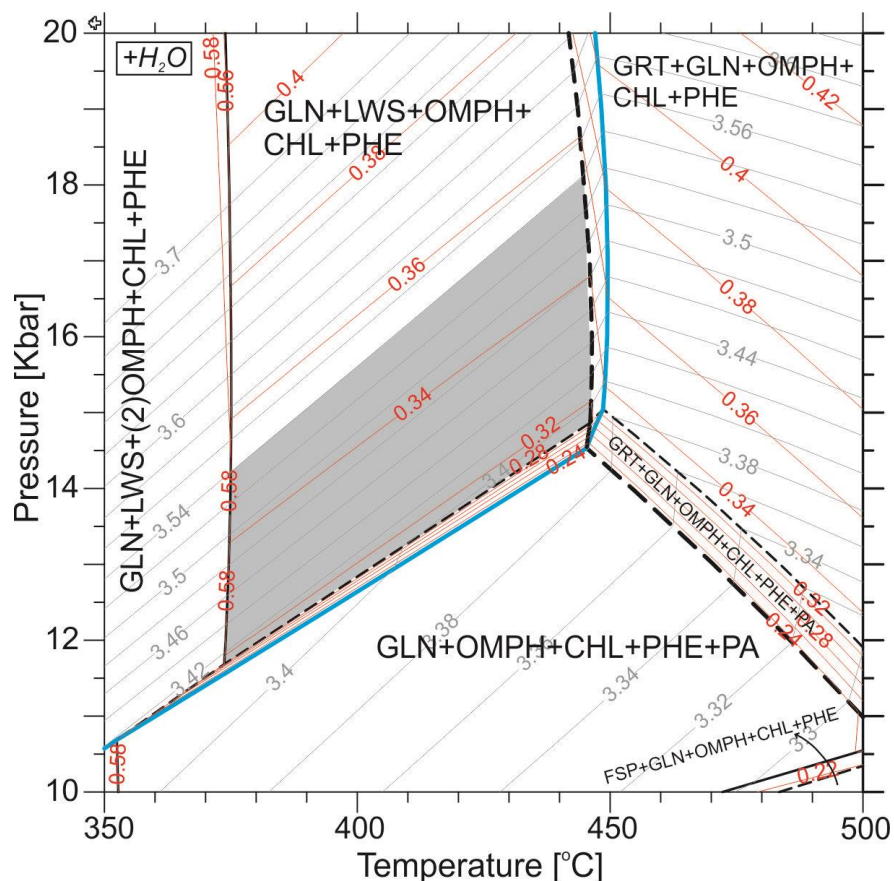


Figure 5.3 : Pseudosection produced by the Theriak-Domino for the sample 128. Thick blue line limits the stability field of lawsonite, thick dashed line garnet and thin dashed line of paragonite in this specific rock composition. According to X_{Jd} (red) of sodic-pyroxene and Si isopleths (grey) of phengite, metamorphic conditions of the sample are constrained to 14 ± 2 kbar and 370–440 °C (the shaded area).

5.2.2 Garnet-blueschist

One garnet-blueschist sample (702A) with an inferred peak metamorphic assemblage of garnet + sodic-amphibole + epidote + phengite is modelled by a pseudosection (Fig. 5.4). The bulk rock chemistry of the sample is given in Table A.11. In the modelled PT space, garnet grows at the expense of epidote. In the shaded area of Figure 5.4, X_{Grs} increases and X_{Alm} decreases with increasing pressure. In sample 702A, grossular component is stable around 40%. This suggests that garnet growth occurred along a path parallel to the X_{Grs} isopleths (Fig. 5.4).

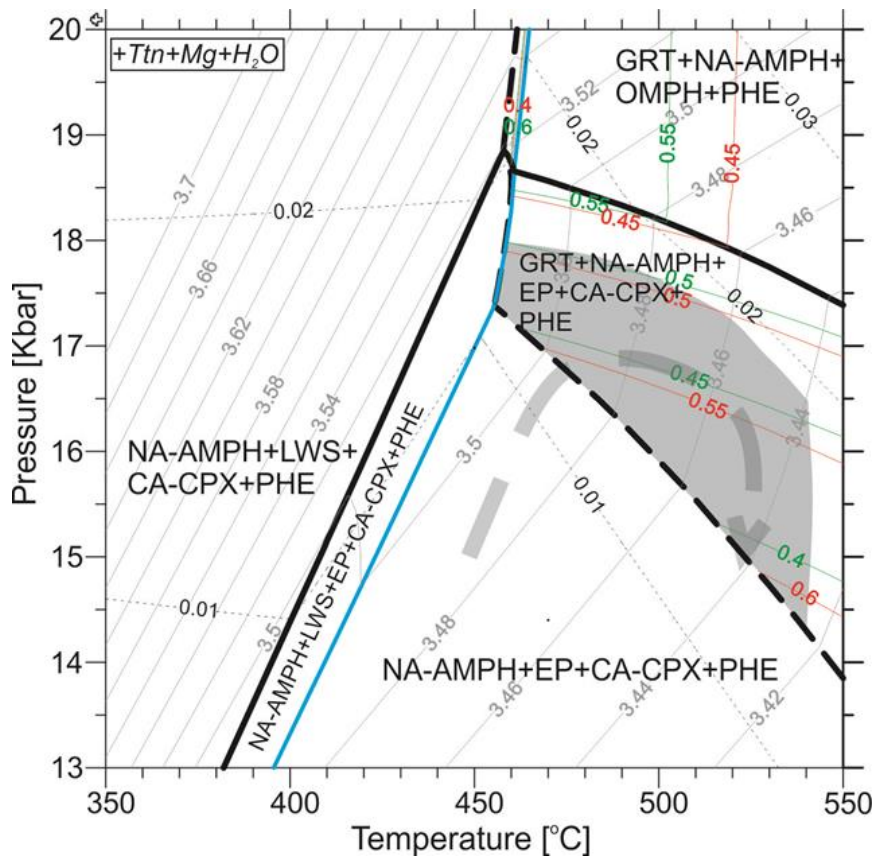


Figure 5.4 : Pseudosection produced by the Theriak-Domino for the sample 702A. For this specific rock composition, thick black line limits stability field of epidote and dashed line of garnet. Stability field of lawsonite is marked by thick blue line. Isopleths; grey, Si content of phengite; green and red, X_{Grs} and X_{Alm} , respectively; dashed isopleth, X_{Jd} . Metamorphic conditions constrained as 17 ± 1 kbar and 500 ± 40 °C (the shaded area).

In the shaded area, Si isopleths of the phengite are orthogonal to the X_{Grs} and X_{Alm} isopleths and decreases along the inferred path. This is in accordance with measured phengite composition in the garnet pressure shadow. Modelled clinopyroxene composition forms hedenbergite and diopside solid solution. Jadeite component appear in the HP part of the PT area after consumption of epidote (X_{Jd} : ~3%).

However, there is no growth of metamorphic clinopyroxene in sample 702A but relicts of augites. Metamorphic conditions are constrained as 17 ± 1 Kbar and 500 ± 40 °C.

5.2.3 Chloritoid-micaschists

Three peak metamorphic assemblages are identified in the chloritoid micaschists: 1) garnet-chloritoid-glaucophane with pseudomorphs after lawsonite 2) chloritoid with pseudomorphs after glaucophane and 3) relatively high-Mg chloritoid (17%) with pseudomorphs after jadeite in addition to phengite, paragonite, quartz, chlorite, rutile and apatite. Peak metamorphic conditions of the chloritoid micaschists were obtained by Raman spectra of carbonaceous material and by pseudosection modelling. The bulk rock chemistry of the samples is shown in Table A.11.

5.2.3.1 Sample 775

An inferred peak metamorphic assemblage of this sample is garnet + chloritoid + glaucophane + lawsonite + phengite + quartz + chlorite + paragonite + rutile + apatite. In the modelled PT space, stability of chloritoid is constrained above ca. 16 kbar (Fig. 5.5). X_{Mg} of the chloritoid is modelled as 8-9% and comparable with the measured values. Garnet growth starts around 445 °C at the expense of lawsonite. Coexistence of lawsonite and garnet is limited in the modelled PT field. Within this area, increase of grossular component is modeled along a path with decreasing pressure without significant change in temperature (Fig. 5.5b). Due to the large and unconstrained effect of Mn in the garnet core, we only account for the grossular content of the outer rim (~16%) indicating pressures of around 18 kbar (Fig. 5.5). Si isopleths of phengite also indicate similar pressures. According to the pseudosections, paragonite is not a stable phase at peak metamorphic conditions and coexistence of paragonite and chloritoid is not expected in the calculated PT space. Thus paragonite was produced by reactions along a retrograde path during exhumation.

Peak metamorphic temperatures are constrained to 415 ± 9 °C and to 407 ± 5 °C by RSCM thermometers using Beyssac et al. (2002a) and Rahl et al. (2005) calibrations, respectively (Table 5.2). These temperatures are slightly lower than the modelled lawsonite + garnet stability field. This possibly related to the effect of Mn

which is excluded from the pseudosection calculations. Metamorphic conditions of the sample 775 are constrained to 17.5 ± 1 kbar and $390-450$ °C.

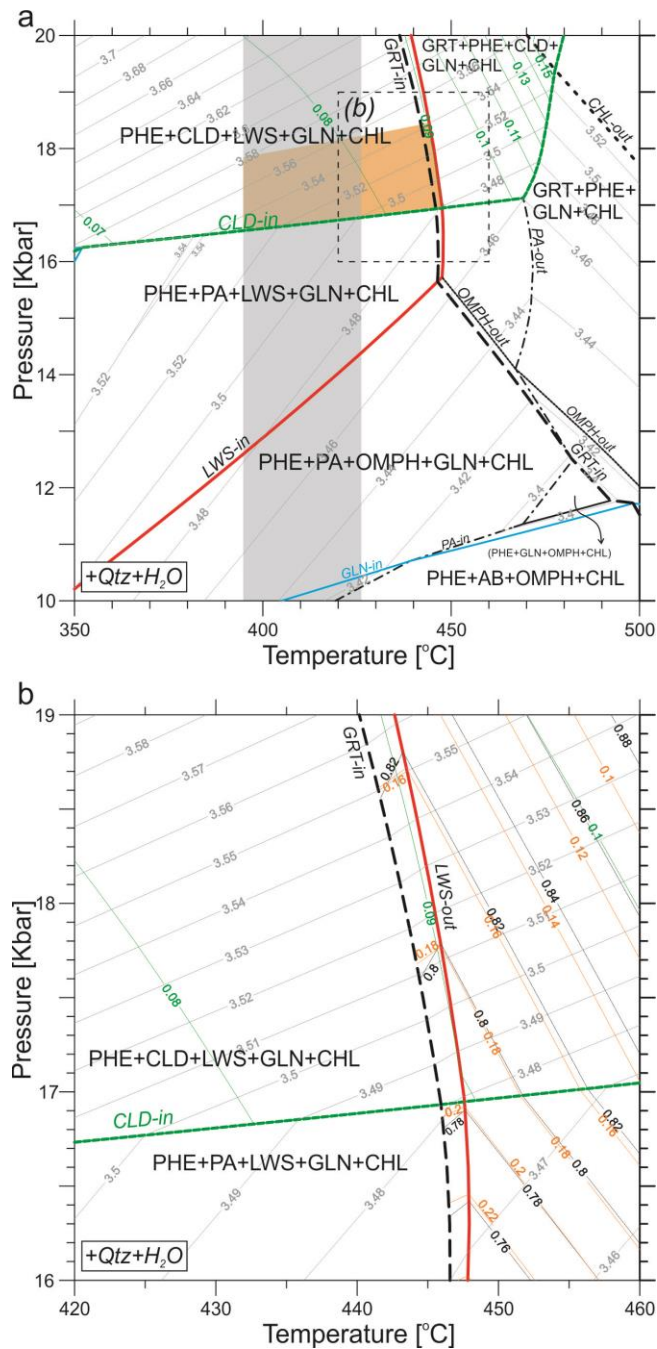


Figure 5.5 : a) Pseudosection modelling for the sample 775. Stability field of garnet is limited by thick black dashed line, of lawsonite by thick red line, of chloritoid by thick green dashed line, of glaucophane by blue line, of paragonite by thin black dashed line for this specific bulk rock composition. b) A detailed part of the pseudosection. Isopleths; grey= Si content of phengite; black and orange are X_{Alm} and X_{Grs} of garnet, respectively, green= X_{Mg} of chloritoid. Vertical grey strip indicates temperature values obtained by the RSCM thermometer based on Rahl et al. (2005) calibration. Metamorphic conditions constrained to 17.5 ± 1 kbar and $390-450$ °C (the shaded area in orange).

Table 5.2 : Raman parameters and the calculated peak metamorphic temperatures for the chloritoid micaschists.

Sample	#	R1	1 σ	R2	1 σ	T ^B (°C)	CI	1 σ	T ^R (°C)	CI	1 σ
775	33	0.86	0.25	0.51	0.06	415	9	25	407	5	15
178	32	0.60	0.23	0.43	0.07	451	11	33	441	11	32
753A	30	0.35	0.17	0.34	0.07	490	12	33	477	14	38

is the amount of spectra that used during temperature calculations. 1 σ = standard deviation; CI= 95% confidence interval. TB and TR are the temperature values obtained by calibrations of the Beyssac et al. (2002a) and by the Rahl et al. (2005), respectively.

5.2.3.2 Sample 753A

Sample 753A has an inferred peak metamorphic assemblage of chloritoid + glaucophane + phengite + quartz + chlorite + paragonite + rutile + apatite + allanite. Peak metamorphic conditions of the sample 753A were modelled by a pseudosection (Fig. 5.6). In sample 753A, Ca is taken up by apatite and allanite. Due to the fact that there is no thermodynamic data available for these minerals, Ca is excluded from the bulk rock composition in the calculation of pseudosection (Table A.11).

For the sample 753A, stability of chloritoid is modelled above ca. 16 kbar similar to the sample 775 (Fig. 5.6). Modelled PT space for the peak metamorphic assemblage of Cld + Phe + Gln + Chl + Qtz resembles sample 775 with larger uncertainties of temperature. In the absence of Ca-Al-silicate minerals, the garnet-in reaction is shifted to higher temperatures. Coexistence of paragonite and chloritoid is not expected in the calculated PT space. It is inferred from the pseudosection that sample 753A experienced similar metamorphic pressure as the sample 775 but higher temperatures (400-475 °C). This is in accordance with the temperature values obtained by RSCM thermometers (Table 5.2). The calibration of Beyssac et al. (2002a) gives 490 ± 12 °C peak metamorphic temperatures and the calibration of Rahl et al. (2005) estimates temperatures of 477 ± 14 °C. Metamorphic conditions of the sample 753A were constrained to 16-18 kbar pressures and 475 ± 40 °C temperatures.

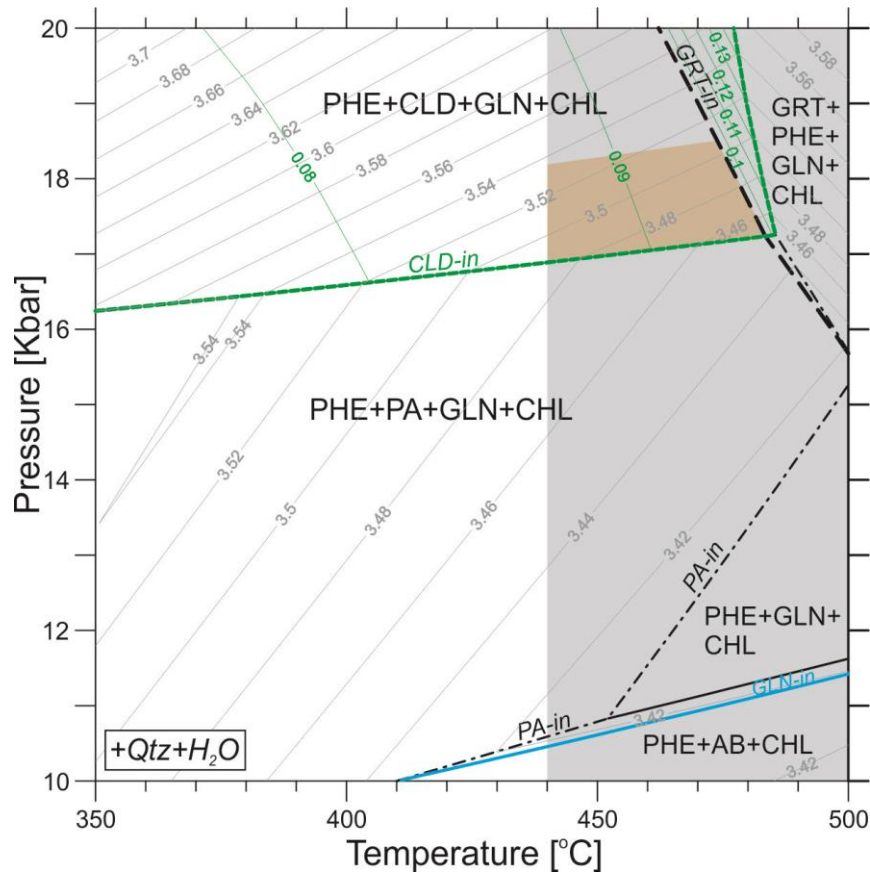


Figure 5.6 : Pseudosection produced by the Theriak-Domino for the sample 753A. Stability field of garnet is limited by thick black dashed line, of chloritoid by thick green dashed line, of glaucophane by blue line, of paragonite by thin black dashed line for this specific bulk rock composition. Isopleths; grey= Si content of phengite, green= X_{Mg} of chloritoid. Vertical grey strip indicates temperature values obtained by the RSCM thermometer based on Rahl et al. (2005) calibration. Metamorphic conditions are constrained to 16-18 kbar and 475 ± 40 °C (the shaded area in orange).

5.2.3.3 Sample 178

The inferred peak metamorphic assemblage of the sample 178 is chloritoid + jadeite + phengite + quartz + rutile + apatite. Metamorphic conditions were constrained by pseudosection modelling (Fig. 5.7). In sample 178, the only Ca-bearing mineral is apatite whereas thermodynamic data is not available for apatite. Hence, Ca is excluded from the pseudosection modelling. In sample 178, there is a considerable amount of iron-sulfide mineral. Hence, iron content was slightly reduced in the bulk rock composition that was used in the calculation.

For the sample 178, coexistence of chloritoid and jadeite is modelled above 20 kbar (Fig. 5.7). Upper and lower limit of the temperature are given by the stabilities of garnet and carpholite, respectively. Absence of glaucophane suggests that it is totally

consumed during growth of chloritoid and jadeite. X_{Mg} of chloritoid coexisting with jadeite increases up to 15% along an increasing pressure path and stays stable after consumption of the glaucophane. Modelled Mg content is identical with the measured composition of Cld2 (0.16-17). The Qtz/Cs transformation forms an upper boundary for metamorphic pressure. Within the modeled peak metamorphic conditions, estimated Si content of phengite is higher than our measurements. This should be related to the retrogression. Peak temperatures from the Raman spectroscopy are 451 ± 11 °C and 441 ± 11 °C by the Beyssac et al. (2002a) and Rahl et al. (2005) calibrations, respectively (Table 5.2). The peak metamorphic conditions of the sample 178 are constrained to 440 ± 30 °C temperatures and 22-25 kbar pressures.

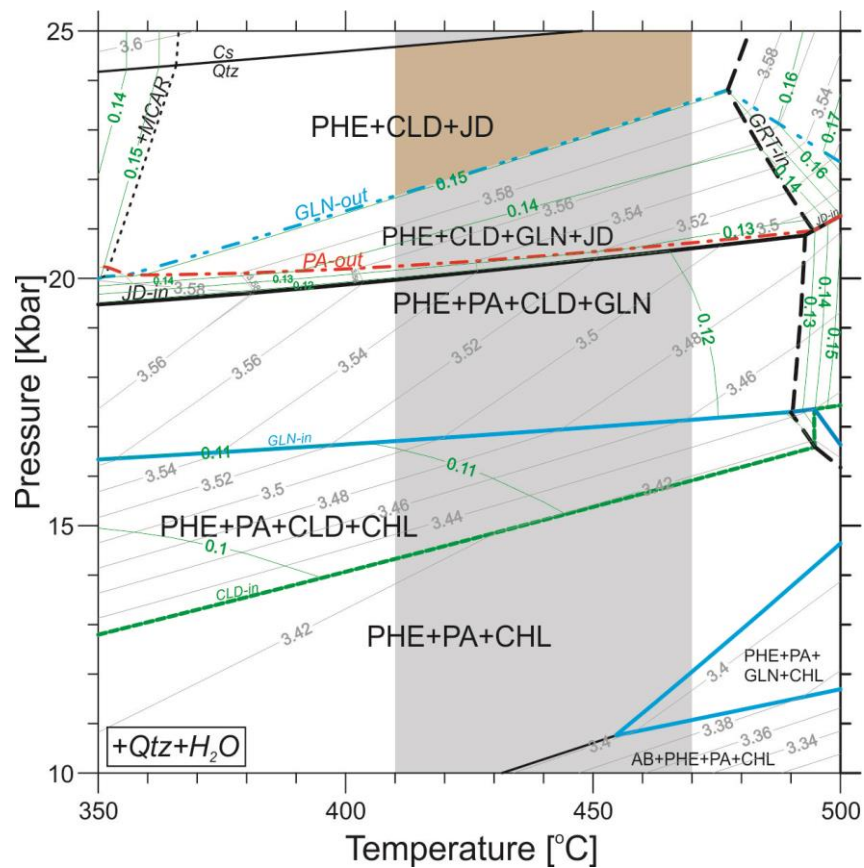


Figure 5.7 : Pseudosection modelling for the sample 178. Stability field of garnet is limited by thick black dashed line, of chloritoid by thick green dashed line, of glaucophane by blue lines, of paragonite by red dashed line for the specific bulk rock composition. Isopleths; grey= Si content of phengite, green= X_{Mg} of chloritoid. Vertical grey strip indicates temperature values obtained by the RSCM thermometer based on Rahl et al. (2005) calibration. Metamorphic conditions constrained to 22-25 kbar and 440 ± 30 °C (the shaded area in orange).

5.3 Concluding Remarks

5.3.1 The Esenler Unit

Raman spectra of carbonaceous material of the metapelitic rocks of the Esenler Unit reveal that their peak metamorphic temperatures range between 330-385 °C. In Figure 5.8, the RSCM temperatures from the Esenler Unit are plotted and contoured on the geological map of the studied area (for sample locations see Table A.12 in the Appx). The map reveals the thermal structure pattern of the accreted Lower Cretaceous distal turbidites.

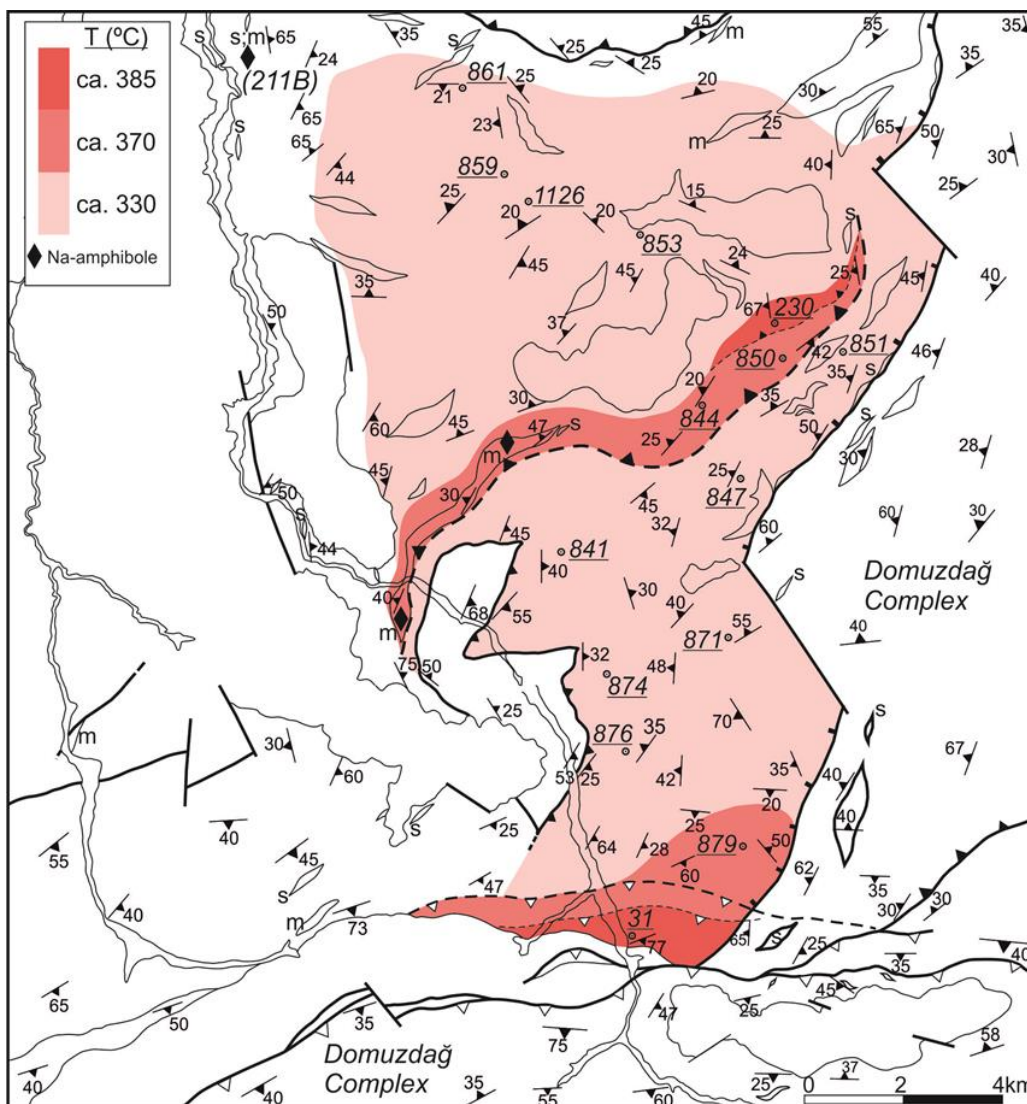


Figure 5.8 : Thermal structure of the accreted distal turbidites. The temperature values are from the calibration of Rahl et al. (2005) due to the fact that it is essentially calibrated for low-grade metamorphic rocks. Relatively high temperature phyllites form a sliver within the low temperature slates. A sliver of Na-amphibole-bearing metabasite is possibly associated with the phyllites.

The most striking aspect of the thermal structure map is that the phyllites (370-385 °C) are exposed as a NE-SW extending slice within the low temperature slates (ca. 330 °C) in the central part of the map (Fig. 5.8). The transition between phyllites and slate is sharp suggesting that they are juxtaposed tectonically. A strip of Na-amphibole bearing metabasites with similar foliation are exposed west of the phyllites suggesting that they are associated with the phyllites. Although obtained temperature values of the sample 871 is similar to the slates, its degree of graphitization is slightly higher than the rest of the slates as revealed by Raman spectra of carbonaceous material (Fig. 4.1 in Ch. 4). This sample is interpreted as showing a gradual increase in metamorphic temperature towards to the contact with the Domuzdağ Complex. To the south of the area studied, however, the metaflysch sequence shows an inverted metamorphic grade, where phyllites structurally overlie the slates. This is related to post-metamorphic deformation along the Akçataş Fault causing underthrusting of the Esenler Unit beneath the Domuzdağ Complex.

PT conditions of a sodic-amphibole bearing metabasite were constrained to 7–12 kbar pressure and 400 ± 70 °C temperatures through THERMOCALC. This metabasite (211B) is exposed as a lens in the northern part of the studied area (Fig. 5.8). Due to its location and the large error range in temperature, it is probably misleading to correlate the obtained PT conditions of the metabasite with RSCM temperatures.

5.3.2 The Domuzdağ Complex

Domuzdağ Complex is a deep-seated subduction-accretionary complex of oceanic origin. Peak mineral assemblages and PT estimates of the metabasite and micaschists of the Domuzdağ Complex reveal that it is composed of metamorphic sequences with distinct PT histories. Metabasites are mostly epidote-blueschist locally with garnet. Metamorphic conditions of a garnet-blueschist (702A) were constrained to 17 ± 1 kbar and 500 ± 40 °C. Lawsonite-blueschists, however, represent a major break in the metamorphic grade. Metamorphic conditions of a lawsonite-blueschist (128) were estimated as 14 ± 2 kbar and 370–440 °C.

The chloritoid-micaschists exhibit generally two peak metamorphic assemblages defined by chloritoid + glaucophane (samples 775 and 753A) and by the inferred chloritoid + jadeite (178) parageneses. The latter is one of the rarely reported HP/LT

mineral assemblages formed at the expense of chloritoid + glaucophane above 20 kbar pressures (Okay, 2002; Proyer, 2003). Metamorphic conditions of the chloritoid-glaucophane-micaschists were constrained to 17.5 ± 1 kbar and 390-450 °C for the sample 775 and 17 ± 1 kbar and 475 ± 40 °C for the 753A, respectively. PT conditions of a chloritoid-jadeite-micaschist is constrained to 22-25 kbar and 440 ± 30 °C. The PT estimates on the chloritoid-micaschists of the Domuzdağ Complex reveal significant depth of burial within the wedge.

Figure 5.9 shows a compilation of the available PT data from the Domuzdağ Complex. The available PT data suggest that the Domuzdağ Complex is composed of metamorphic rocks that were experienced lawsonite-blueschist, epidote±garnet-blueschist and eclogite facies conditions. This suggests that the Domuzdağ Complex is a tectonic stack of distinct metamorphic slices rather than a coherent metamorphic sequence.

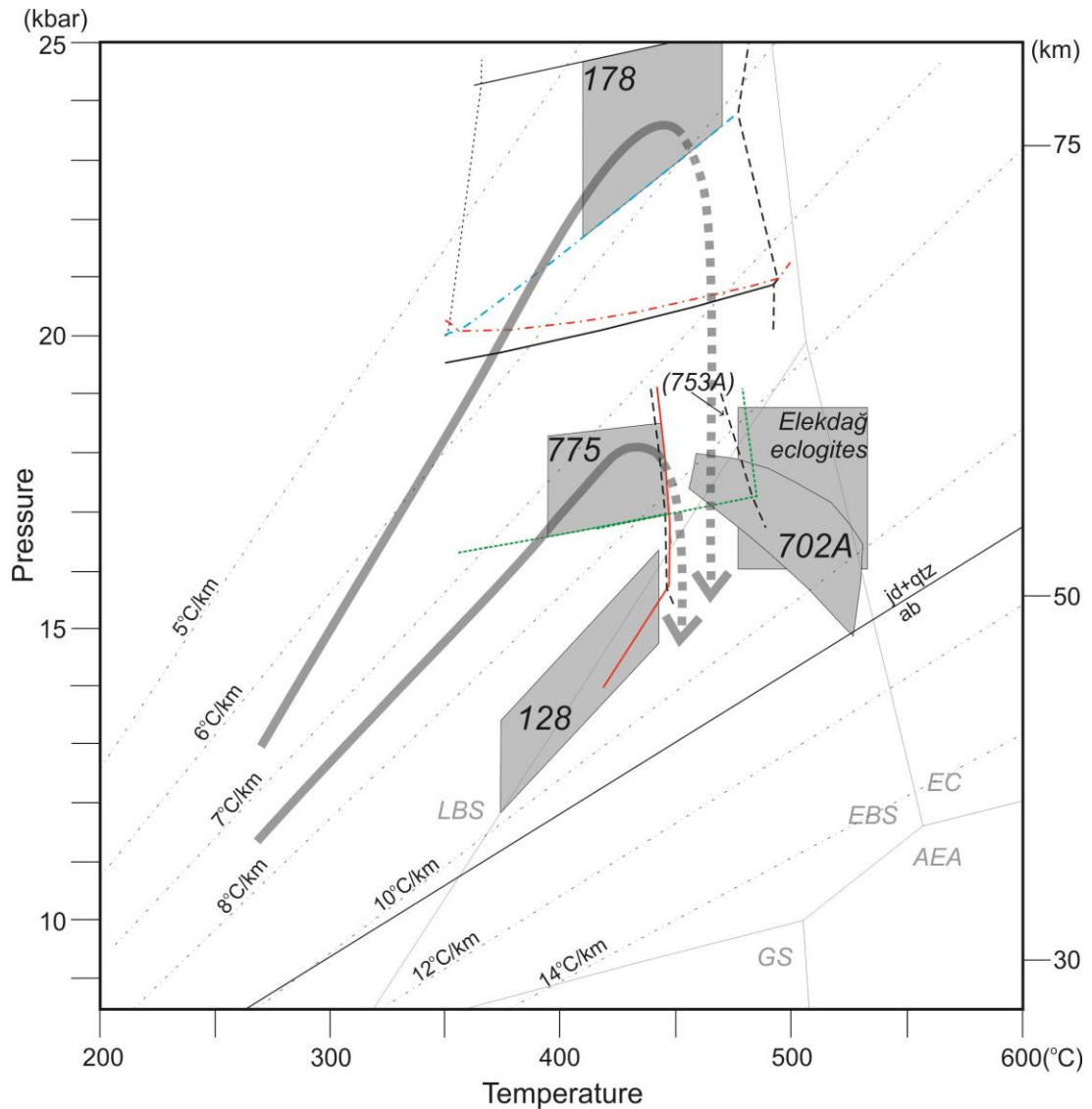


Figure 5.9 : Compilation of the estimated PT data from the Domuzdağ Complex including chloritoid-micaschists, a lawsonite- and a garnet-blueschist. PT conditions of the Elekdağ eclogites are from Okay *et al.* (2006a). Possible PT paths for the sample 178 and 775 are indicated by thick grey lines. The dashed parts are stand for zero strain decompressional exhumation. Metamorphic facies are modified from Evans (1990). Facies: *LBS*: lawsonite-blueschist, *EBS*: epidote-blueschist, *EC*: eclogite, *AEA*: albite-epidote amphibolite, *GS*: greenschist facies. The compilation suggests that Domuzdağ Complex consists of metamorphic rocks that were metamorphosed under distinct PT conditions.

6. GEOCHRONOLOGY

6.1 $^{40}\text{Ar}/^{39}\text{Ar}$ Geochronology

Age of regional HP/LT metamorphism in the area studied is constrained by $^{40}\text{Ar}/^{39}\text{Ar}$ phengite dating method. Phengitic white mica was separated from the accretionary wedge units including the Esenler Unit, the Domuzdağ Complex and the Kunduz Metamorphics. Foliated muscovites from a low-grade metarhyolite of the Köşdağ Formation were also dated to constrain the accretion of the intra-oceanic arc sequence to the overlying accretionary wedge. Sample locations are shown in Figure 2.1 and Figure 2.10. The dating has been conducted at the $^{40}\text{Ar}/^{39}\text{Ar}$ geochronology laboratory of University of Potsdam. The dating system and the procedures are summarized in the methodology part. $^{40}\text{Ar}/^{39}\text{Ar}$ analytical data are given in the Appendix (Table A.13).

6.1.1 Esenler Unit

Two phyllites from the accreted distal turbidites were dated. The samples 31 and 230 both have identical mineralogy and texture. They consist of white mica, quartz, chlorite, albite and calcite (Fig. 6.1). Fine grained phengite and chlorite define the foliation. Both samples show similar Raman spectra of carbonaceous material which constrains their metamorphic temperatures to 370-385 °C (Table 5.1).

The $^{40}\text{Ar}/^{39}\text{Ar}$ phengite ages of the samples 31 and 230 are 101.5 ± 4.8 Ma and 99.9 ± 1.7 Ma, respectively (Fig. 6.2). The ages agree within the 1 sigma error limits and indicate an Albian regional metamorphism and accretion of the distal turbidites.

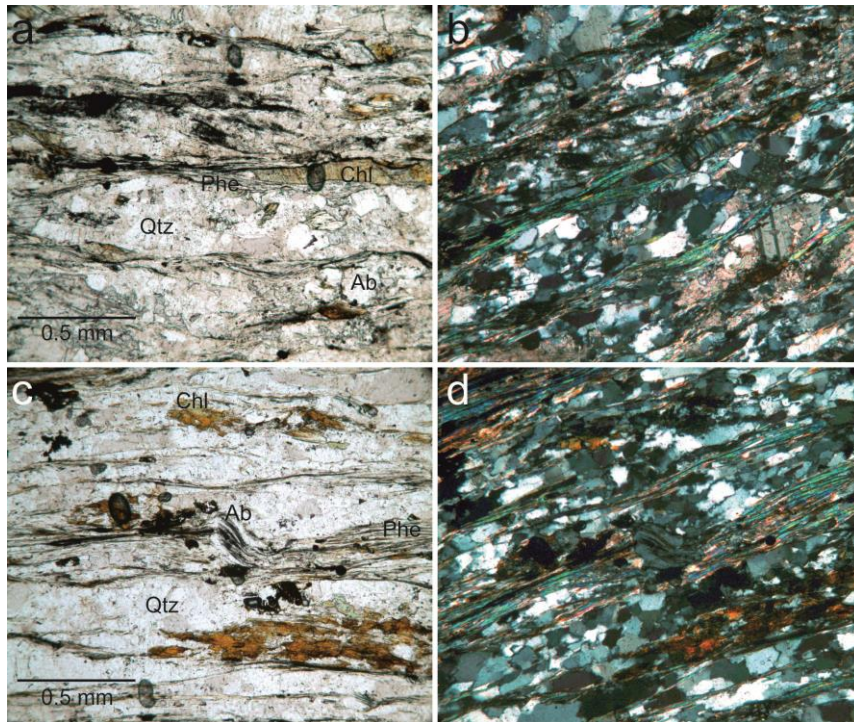


Figure 6.1 : Microphotographs of the samples from the Esenler Unit dated by $^{40}\text{Ar}/^{39}\text{Ar}$ phengite method. a&b) Sample 31 and c&d) sample 230 are phyllites that consist of quartz (Qtz), phengite (Phe), albite (Ab), chlorite (Chl).

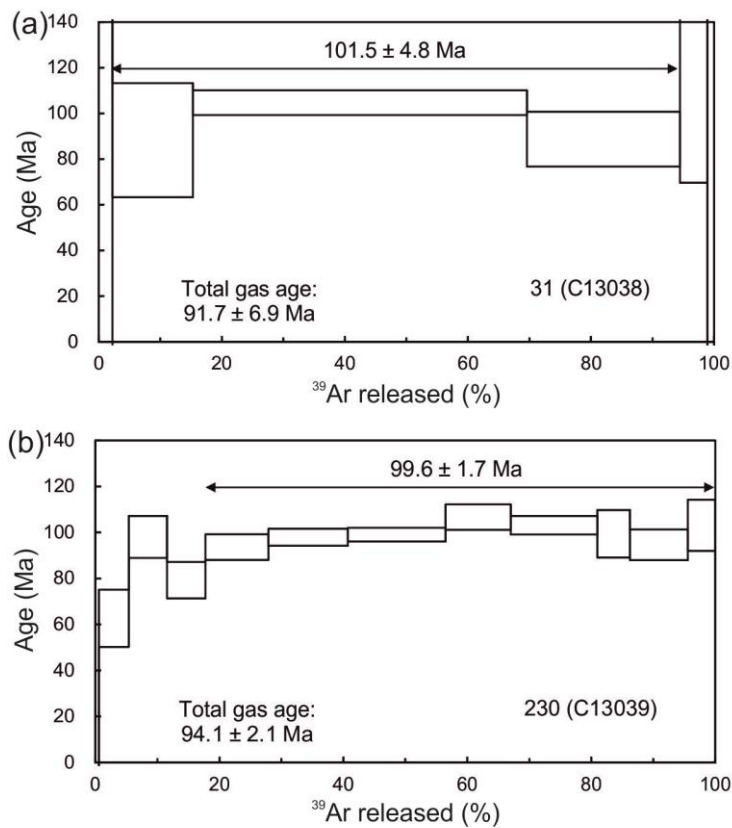


Figure 6.2 : $^{40}\text{Ar}/^{39}\text{Ar}$ age spectra of the analyzed phengites from the (a) sample 31 and (b) sample 230 from the Esenler Unit.

6.1.2 Domuzdağ Complex

$^{40}\text{Ar}/^{39}\text{Ar}$ dating was performed on two micaschists from the Domuzdağ Complex (Fig 6.3). Sample 392 consists of phengite, paragonite, chlorite, quartz, rutile and syn-kinematic albite porphyroblasts with rotational inclusion fabrics. Foliation is defined by phengite (3.33-3.48 Si c.p.f.u) and chlorite. Sample 753A is a chloritoid-micaschist exposed farther away from the extensional shear zone and consists of chloritoid, phengite, chlorite, paragonite, quartz and rutile with pseudomorphs after glaucophane. Chloritoid forms porphyroblasts of radially growing crystals. Foliation, which is defined by phengite and chlorite, bends around the chloritoid porphyroblasts. Si content of phengite ranges between 3.23-3.47 c.p.f.u.

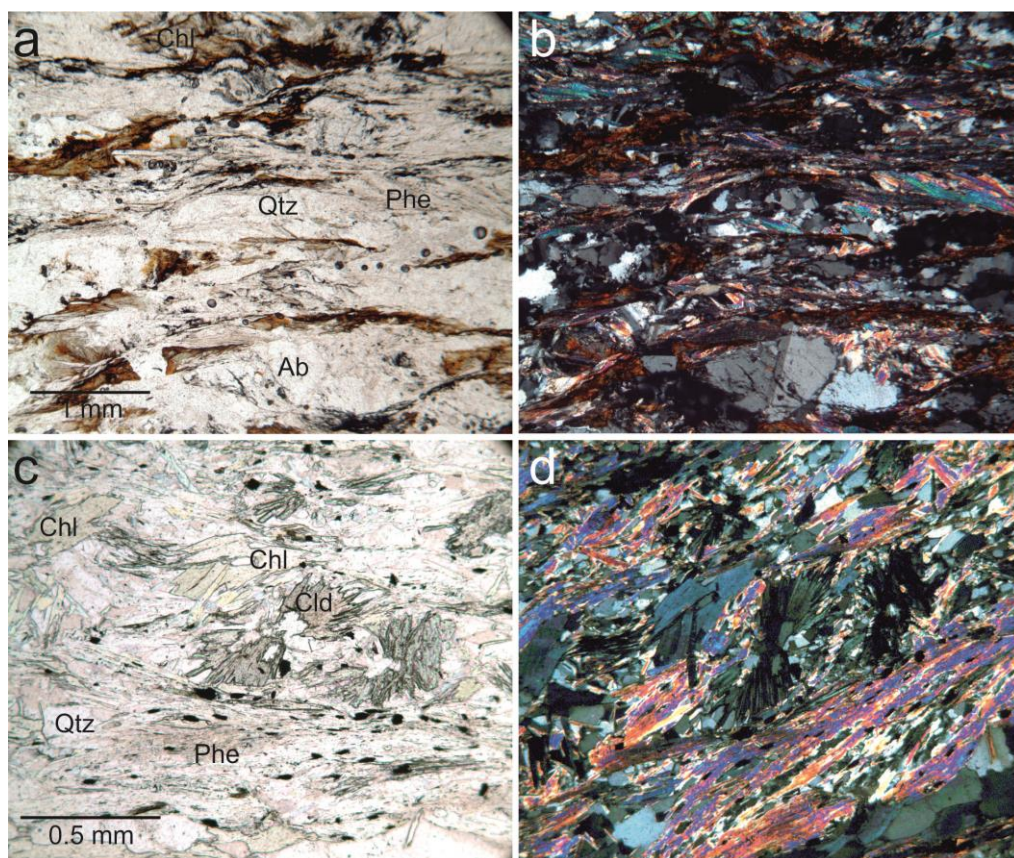


Figure 6.3 : Microphotographs of the samples from the Domuzdağ Complex dated by $^{40}\text{Ar}/^{39}\text{Ar}$ phengite method. a&b) Sample 392 consists of quartz (Qtz), phengite (Phe), albite (Ab), chlorite (Chl). c&d) Sample 753A consists of chloritoid (Cld), quartz (Qtz), phengite (Phe), chlorite (Chl).

Sample 392 exhibits a slightly inclined plateau. A partial plateau age of 100.6 ± 1.3 Ma is obtained (Fig. 6.4a). Sample 753A, however, gives a pronounced plateau age of 91.8 ± 1.8 Ma (Turonian) (Fig. 6.4b). This age is apparently younger than all the other ages.

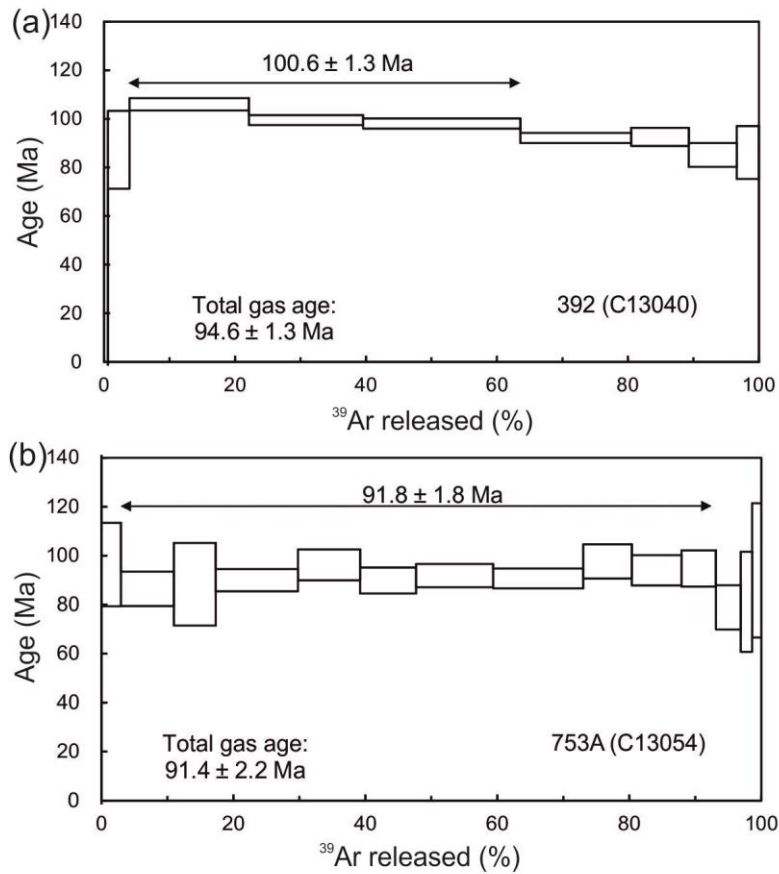


Figure 6.4 : $^{40}\text{Ar}/^{39}\text{Ar}$ age spectra of the analyzed phengites from the Domuzdağ Complex. a) Sample 392, a micaschist. b) Sample 753A, a chloritoid-micaschist.

6.1.3 Kunduz Metamorphics

Two samples from the Kunduz Metamorphics were dated. The first sample (626A) is a quartz-micaschist interlayered with light colored marble and metabasite. It consists of quartz, phengitic white mica, epidote, hematite and titanite. Phengites define a weakly developed foliation (Fig. 6.5a, b). Their Si contents range between 3.37-3.44 c.p.f.u. The second sample (1290) is a well-foliated phyllitic metatuff consisting of quartz, phengite, albite, bluish-green amphibole, chlorite and stilpnomelane with magmatic augite relicts (Fig. 6.5c, d). Amphibole replaces the augite. Phengite defines the foliation. Besides, there is also late tiny white mica of secondary origin.

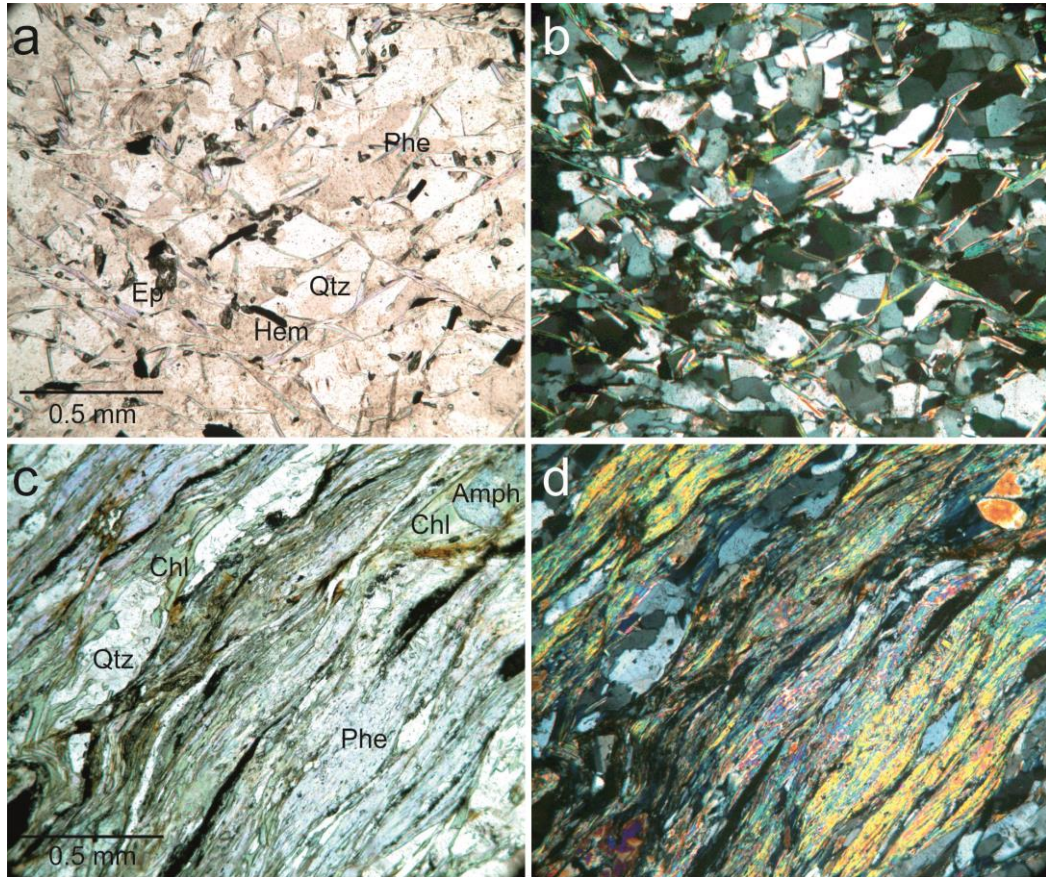


Figure 6.5 : Microphotographs of the samples from the Kunduz Metamorphics dated by $^{40}\text{Ar}/^{39}\text{Ar}$ phengite method. a & b) Sample 626A is a quartz-micaschist consisting of quartz (Qtz), phengite (Phe), hematite (Hem), epidote (Ep). c & d) Sample 1290 is a phyllite consisting of quartz (Qtz), phengite (Phe), chlorite (Chl), calcic-amphibole (Amph).

The $^{40}\text{Ar}/^{39}\text{Ar}$ phengite age of the sample 626A is constrained as 159.3 ± 1 Ma with a pronounced plateau (Fig. 6.6a). Sample 1290 exhibits, however, a disturbed plateau. Released radiogenic Ar is concentrated in 151-161 Ma (Middle Jurassic) in the middle temperature steps and ca. 100 Ma (Albian) with a 101 ± 0.6 Ma in the last 5 steps making an apparent short “plateau” within the steps (Fig. 6.6b). Due to the fact that radiogenic Ar was predominantly released in third and fourth steps (Table A.13), we infer a Middle Jurassic metamorphic age for the sample, which is possibly overprinted during the Albian orogeny.

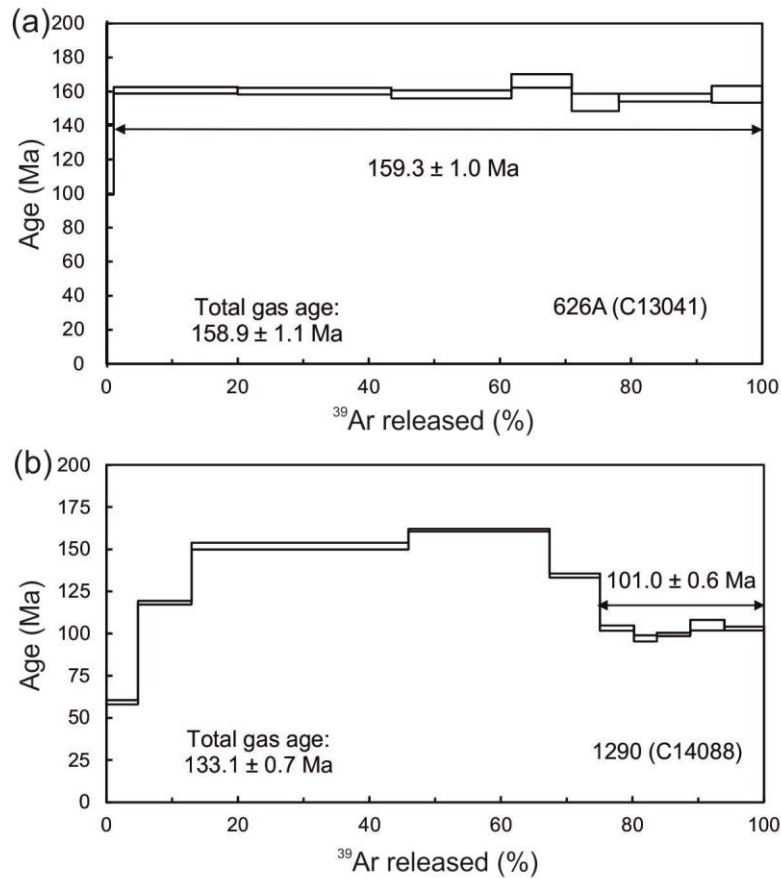


Figure 6.6 : $^{40}\text{Ar}/^{39}\text{Ar}$ age spectra of the analyzed phengites from the Kunduz Metamorphics. a) Sample 626, a quartz-micaschist. b) Sample 1290, a phyllitic metatuff.

6.1.4 Metamorphic age of the Kösdag Formation

The age of the metamorphism in the low-grade metavolcanic rocks of the Kösdag Formation was constrained by $^{40}\text{Ar}/^{39}\text{Ar}$ dating on metamorphic muscovite from a metarhyolite sample. The sample 1214 consists of plagioclase and quartz phenocrysts in a recrystallized and foliated groundmass of quartz, white mica, chlorite and epidote (Fig. 6.7a). Plagioclase is partly replaced by epidote, chlorite and quartz. Quartz phenocrysts exhibit undoluse extinction related to deformation. White mica marks the foliation and bends around the phenocrysts. The $^{40}\text{Ar}/^{39}\text{Ar}$ muscovite age is constrained to 69.86 ± 0.37 Ma with a pronounced plateau in the age spectrum diagram (Fig. 6.7b).

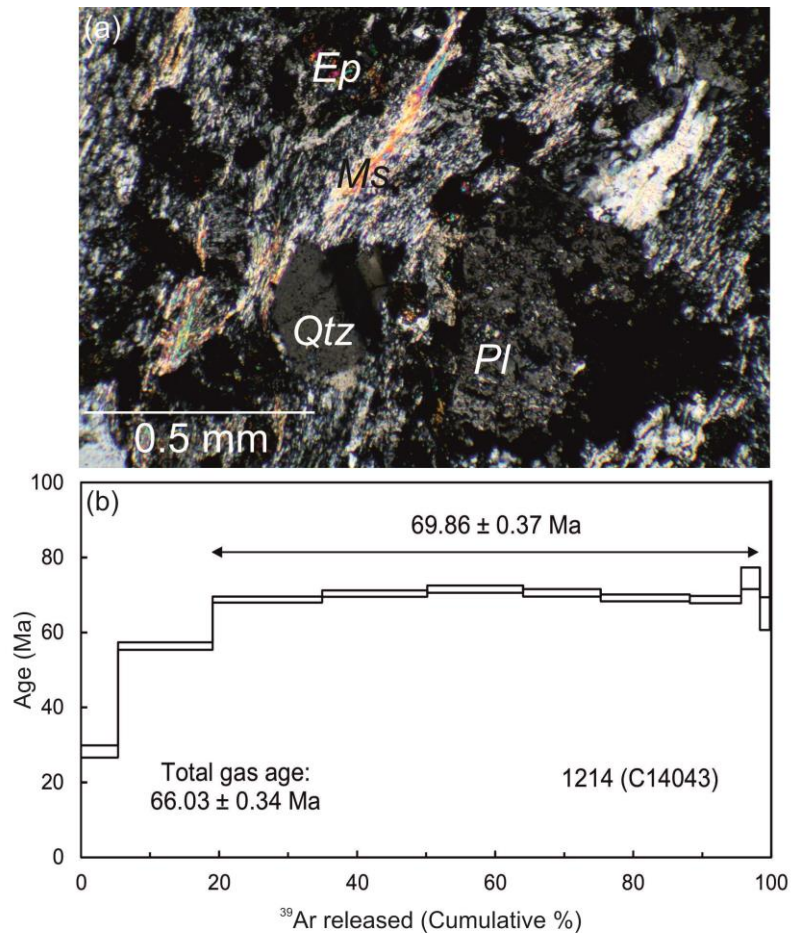


Figure 6.7 : a) Microphotograph of the dated sample 1214 from the Kösdag Formation. The rock consists of quartz (Qtz), plagioclase (Pl), epidote (Ep) and muscovite (Ms). b) $^{40}\text{Ar}/^{39}\text{Ar}$ Ar age spectrum diagram obtained from the muscovites of this sample by stepwise heating method.

6.2 U/Pb Zircon Geochronology

U/Pb zircon dating was performed on the metarhyolites of the Kösdag Formation to unveil the magmatic crystallization age of the accreted intra-oceanic arc-sequence. Zircons were separated from two metarhyolite samples (1214 and 1215) in the Istanbul Technical University. Measurements were performed by LA-ICP-MS at the University of Potsdam. Details of the dating procedure are given in the methodology part. Sample locations are shown in Figure 2.10.

6.2.1 Crystallization age of the Kösdag Formation

Dated zircons from the two metarhyolite samples are mostly euhedral to subhedral (Fig. 6.8). Zircons from the sample 1214 show dark cores with weak or no zoning. They are surrounded by typical oscillatory zoned mantle sometimes with sector

zoning and bright outer rims. In the sample 1215, zircons show cores with weak oscillatory zoning. They are surrounded by bright rims. The core - rim boundary is regular for all zircons magmatic.

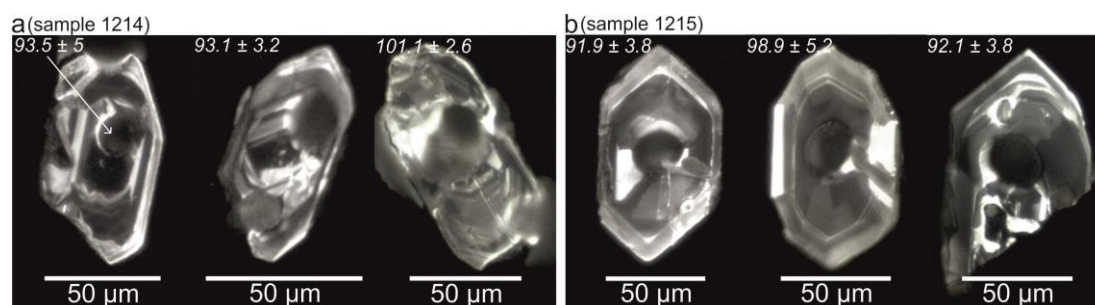


Figure 6.8 : Cathodoluminescence images of the dated zircons from the sample 1214 (a) and 1215 (b).

The dated zircons did not provide concordia ages. Their $^{206}\text{Pb}/^{238}\text{U}$ ages scatter between 90-100 Ma with weighted mean age values of 93.8 ± 1.9 (MSWD= 4.7) and 94.4 ± 1.9 (MSWD= 2.7) for the samples 1214 and 1215, respectively (Fig. 6.9, Table 6.1).

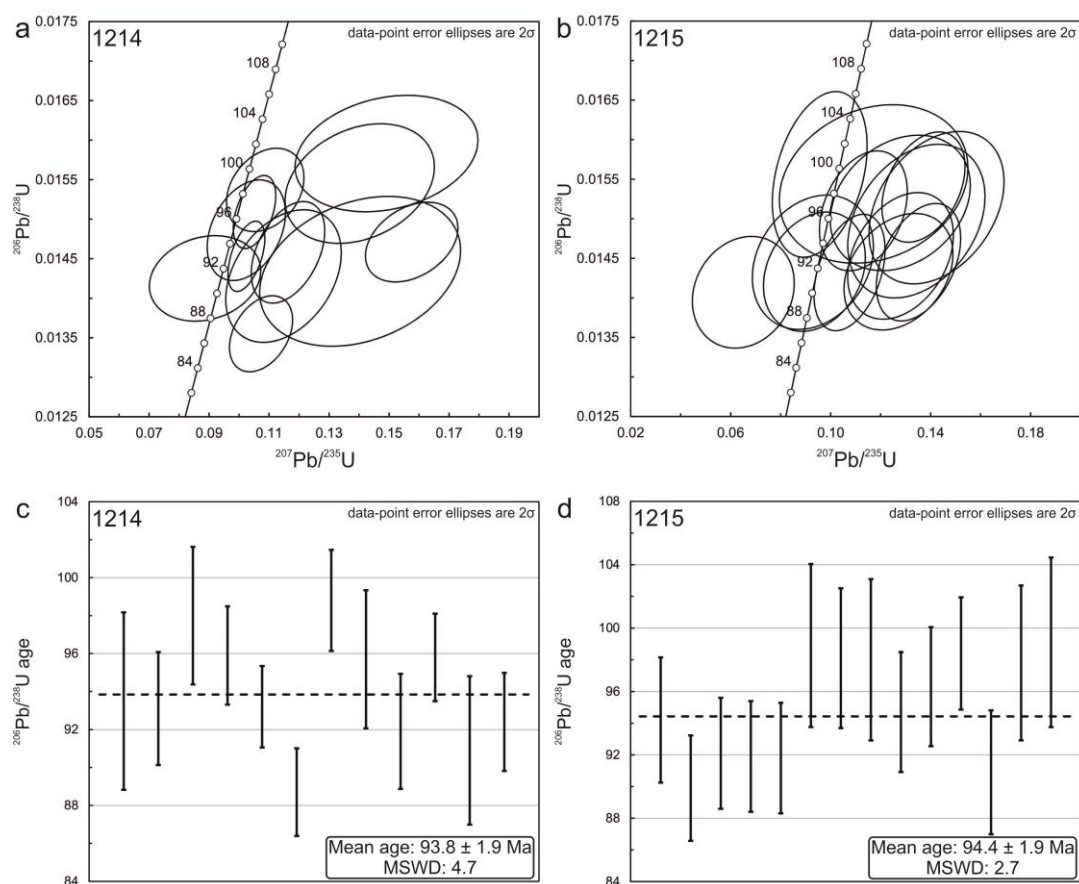


Figure 6.9 : Zircon U/Pb concordia diagram for the sample 1214 (a) and 1215 (b) and their weighted mean age values (c and d).

Table 6.1 : LA-ICP-MS U-Pb data of the measured zircons from the metarhyolites.

No	Isotope ratios						Ages			
	$^{206}\text{Pb}/^{238}\text{U}$	$2\sigma(\%)$	$^{207}\text{Pb}/^{235}\text{U}$	$2\sigma(\%)$	$^{207}\text{Pb}/^{206}\text{Pb}$	$2\sigma(\%)$	$^{206}\text{Pb}/^{238}\text{U}$	$\pm\sigma$	$^{207}\text{Pb}/^{235}\text{U}$	$\pm\sigma$
<i>Sample 1214</i>										
01	0.01434	5.4	0.14037	19.5	0.05315	25	93.5	5	152.5	28
02	0.01486	3.5	0.10243	10.4	0.05054	9.9	93.1	3.2	96.4	9.6
03	0.01583	3.8	0.14917	16.7	0.07511	14.9	98	3.7	127.5	20.2
04	0.01471	2.8	0.15756	8	0.05983	10.1	95.9	2.7	193.4	14.2
05	0.01453	2.5	0.10247	4.9	0.04655	5.3	93.2	2.3	100.5	4.7
06	0.01355	2.9	0.10734	8	0.05125	8	88.7	2.6	102.3	7.8
07	0.01537	2.8	0.10876	9.7	0.04987	9.6	98.8	2.7	108.9	10.1
08	0.01545	4	0.14025	14.5	0.06394	15.7	95.7	3.8	144.8	19.8
09	0.01458	3.6	0.11633	8.6	0.0536	9.2	91.9	3.3	106.5	8.7
10	0.01509	2.5	0.10518	5.5	0.05005	5	95.8	2.4	103.3	5.4
11	0.01428	4.8	0.11484	13.7	0.05142	15.5	90.9	4.3	109.6	14.3
12	0.01425	3.1	0.08868	17.1	0.05556	13	92.4	2.8	97.9	16.1
<i>Sample 1215</i>										
01	0.01453	4.5	0.12798	13.5	0.05887	13.9	94.2	4.2	134.1	17.1
02	0.01407	4.1	0.06508	25.6	0.04529	18.8	89.9	3.7	81.9	20.4
03	0.01432	4.2	0.10757	10.8	0.05428	11.8	92.1	3.8	109.1	11.2
04	0.01445	4.2	0.13518	10.2	0.05372	13.5	91.9	3.8	120.7	11.7
05	0.01433	4.2	0.12716	14	0.05825	14.3	91.8	3.8	125.9	16.7
06	0.01544	5.3	0.11721	26.3	0.0546	28.7	98.9	5.2	115	29
07	0.0152	4.6	0.12789	17.9	0.04998	22.1	98.1	4.5	140.7	23.8
08	0.01497	5.3	0.13432	16.7	0.05782	17.8	98	5.2	139	21.9
09	0.01433	4.3	0.09352	17.8	0.04203	18.8	94.7	4	86.1	14.8
10	0.0151	4.1	0.11311	12.7	0.04938	14.2	96.3	3.9	123.7	14.9
11	0.0154	3.7	0.13715	9.9	0.04944	14	98.4	3.6	131.7	12.3
12	0.01445	4.8	0.09291	21.3	0.05343	18.3	90.9	4.3	86.2	17.8
13	0.01514	5.2	0.14237	15.5	0.05604	20.2	97.8	5	137.2	20.1
14	0.01556	5.5	0.09565	16.2	0.04375	16.9	99.1	5.4	91.2	14.2

6.3 Concluding Remarks

6.3.1 Accretionary wedge

The $^{40}\text{Ar}/^{39}\text{Ar}$ age results are in accordance with previously published data confirming the wide occurrence of Middle Jurassic and Early Cretaceous subduction-accretion complexes in the Central Pontides (Okay et al., 2006a, 2013). The 91.8 ± 1.8 Ma age, the youngest $^{40}\text{Ar}/^{39}\text{Ar}$ age obtained in Central Pontides so far, indicates that subduction-accretion continued until Turonian with a possible southward younging of the deep level accretion and HP/LT regional metamorphism.

Interpretation of the radiogenic ages depends on the isotopic closure concept accepting that the temperature is a fundamental parameter together with grain size

and cooling rate in controlling radiometric ages (Dodson, 1973). Additionally deformation and fluids have significant effect on isotopic diffusion (Villa, 1998). Harrison et al. (2009) report a closure temperature of muscovite grain 100 μm across, cooling at 10 $^{\circ}\text{C}/\text{Ma}$ at 10 kbar as 425 $^{\circ}\text{C}$ for the $^{40}\text{Ar}/^{39}\text{Ar}$ system. The relatively low temperatures of metamorphism (370-385 $^{\circ}\text{C}$ for the Esenler Unit and 400-500 $^{\circ}\text{C}$ for the Domuzdağ Complex) indicate that the obtained ages represent the ages of crystallization. In sample 392, however, the obtained age should be an exhumation age related to recrystallization by pervasive shearing during exhumation. This is evidenced by i) its structural position close to the extensional shear zone with identical lineation development and ii) absence of any peak metamorphic assemblages but syn-kinematic albite porphyroblasts. The 91.8 ± 1.8 Ma age suggests that extensional shearing and exhumation of the Domuzdağ Complex occurred during on-going subduction.

Early-Middle Eocene limestones unconformably overlie the HP/LT metamorphic rocks of the Central Pontide Supercomplex and elsewhere in the Central Pontides (Özcan et al., 2007; Okay et al., 2013). In the area studied, Eocene rocks lie unconformably over the Esenler Unit and Domuzdağ Complex (Fig. 2.1). Furthermore, Helonocyclina and Orbitoides-bearing Maastrichtian limestones are exposed as a tectonic sliver along the post-Eocene Akçataş strike-slip fault. They were most probably deposited on the metamorphic rocks prior to the faulting, which provide an upper age limit for the regional metamorphism and exhumation.

6.3.2 Arc sequence

Zircon U/Pb dating of the metarhyolites reveals that the Köşdağ intra-oceanic paleo-arc formed around 94 ± 2 Ma ago. These ages are slightly younger and partly overlap with the HP/LT metamorphism of the overlying subduction-accretion complexes suggesting a separate subduction for the generation of arc volcanism. Low-grade regional metamorphism of the Köşdağ Formation is constrained to 70 Ma by $^{40}\text{Ar}/^{39}\text{Ar}$ muscovite dating. The fact that the overlying Middle Jurassic and Albian-Turonian HP/LT metamorphic rocks and the Köşdağ Formation share a similar NW dipping foliation suggests that the ca. 70 Ma age represents the final accretion of the intra-oceanic arc sequence to the Laurasian active margin. The youngest $^{40}\text{Ar}/^{39}\text{Ar}$ phengite age from the overlying subduction-accretion complexes is 92 Ma confirming southward younging of an accretionary-type orogen.

7. GEOCHEMISTRY

This chapter deals with petrogenesis and tectonic setting of the accreted arc sequence. Geochemistry of 12 basic and acidic metavolcanic rocks from the Kösdag Formation was investigated in detail including major, trace and rare earth element analysis. The samples were collected along north-south sections within the Kösdag Formation (for location of the samples see Fig. 2.10). The bulk rock compositions were obtained by XRF at the GeoForschungsZentrum-Potsdam (GFZ). Trace and rare earth element (REE) analyses were made by ICP-AES at the University of Potsdam and in ACME Lab, Canada. The analytical data are given in Table 7.1.

7.1 Geochemistry of the Kösdag Formation

7.1.1 Major element compositions

In a total alkalis vs silica diagram, acidic rocks plot in the rhyolite field (Fig. 7.1). Basic compositions are sub-alkaline and mainly plot in the basaltic andesite and andesite fields. One sample plots in the basaltic trachy-andesite field (sample 1305). Basaltic andesites are tholeiitic and calc-alkaline (Fig. 7.2). Occurrence of abundant xenoliths and low-grade metamorphism, however, affect the bulk rock chemistry of the volcanic rocks, making further discussion redundant. Trace elements are generally regarded as being immobile during metamorphism.

Table 7.1 : Major, trace and rare earth element analysis of the metavolcanic rocks.

Sample	Rhyolite					BA1			BA2			
	1212	1213	1214	1215	1304B	1285	1286	1287	1284	1288	1304A	1305
<i>Major oxides (wt%)</i>												
SiO ₂	74.20	75.61	73.51	78.50	75.88	55.36	61.04	54.10	51.21	53.51	50.55	53.51
TiO ₂	0.48	0.53	0.43	0.30	0.31	0.91	0.80	0.85	0.91	0.83	1.07	1.27
Al ₂ O ₃	12.00	11.49	12.12	11.22	12.55	16.03	15.80	13.78	17.44	13.61	14.68	17.24
Fe ₂ O ₃	3.61	3.34	3.56	1.73	1.93	9.86	7.31	12.39	10.81	12.15	12.68	9.86
MnO	0.08	0.05	0.10	0.02	0.04	0.09	0.07	0.19	0.11	0.18	0.20	0.29
MgO	0.59	0.27	2.14	0.41	1.01	5.03	2.76	3.53	5.43	3.48	5.95	5.39
CaO	2.88	2.64	3.14	1.88	0.58	5.73	4.04	6.75	6.10	6.65	5.00	1.51
Na ₂ O	1.82	3.99	0.98	4.89	4.32	0.73	3.82	4.11	0.91	4.06	2.60	5.78
K ₂ O	2.56	0.80	1.14	0.15	1.57	1.00	0.70	0.03	1.50	0.03	0.01	0.21
P ₂ O ₅	0.11	0.14	0.07	0.06	0.05	0.14	0.20	0.08	0.13	0.08	0.13	0.29
LOI	1.54	1.04	2.76	0.78	1.67	4.93	3.34	4.00	5.22	5.32	6.93	4.51
Total	99.86	99.90	99.94	99.94	99.90	99.81	99.88	99.81	99.77	99.91	99.80	99.87
<i>Trace and rare earth elements (ppm)</i>												
Sc	13.1	17.6	15.3	10.7	6.2	31.9	27.4	25.8	39.0	47.9	42.3	32.6
Cr	<10	10	<10	<10	10	15	12	34	41	30	34	14
V	45	22	34	26	16	199	93	343	567	354	453	100
Ni	<10	<10	<10	<10	<10	<10	<10	14	7.8	13.4	9.1	<10
Co									26.4	32.8	32.8	
Cu									61.8	59.9	77.1	
Zn	45	43	49	29	39	96	108	96	92	87	91	128
Ga	12	13	16	10	<10	19	18	15	21.7	14.5	15.6	16
Rb	63	31	31	15	43	31	34	15	45	16	16	17
Sr	162	247	226	126	150	349	150	72	227	73	145	93
Y	27.2	28.7	33.3	29.3	18.3	27.1	31.7	34.9	24.9	21.1	22.3	33.1
Zr	130	91	159	166	137	99	128	58	58	54	65	128
Nb									1.0	1.1	1.2	
Th									0.6	0.4	0.2	
Cs									0.3	0.4	<0.1	
Ba	426	139	256	70	424	304	285	69	316	81	74	134
Pb									0.2	0.5	1.4	
Ta									<0.1	<0.1	<0.1	
Hf									1.2	1.4	1.4	
U									0.2	0.1	0.2	
La	10.02	9.54	10.85	11.39	10.91	11.03	12.32	13.97	4.90	2.90	3.90	9.22
Ce	22.33	19.56	24.94	21.99	24.24	24.58	28.63	31.58	10.30	7.00	9.50	23.72
Pr	2.21	2.13	2.67	2.73	2.50	2.75	3.34	3.80	1.48	1.00	1.43	3.16
Nd	12.97	11.91	14.23	13.02	12.64	14.23	17.03	17.97	7.90	5.20	7.10	15.75
Sm	3.68	3.55	4.16	3.60	3.06	4.05	4.86	5.01	2.25	1.79	2.37	4.92
Eu	1.32	1.51	1.35	1.00	0.98	1.52	1.88	1.83	0.96	0.72	0.85	1.76
Gd	4.43	4.62	5.36	4.14	3.31	4.73	5.85	6.00	3.65	2.73	3.16	6.00
Tb	0.78	0.87	0.96	0.74	0.57	0.82	1.05	1.09	0.66	0.55	0.59	1.10
Dy	5.03	5.29	6.15	4.89	3.47	5.11	6.43	6.61	4.22	3.48	3.65	6.73
Ho	0.91	1.00	1.23	1.01	0.63	0.99	1.26	1.27	0.90	0.76	0.83	1.35
Er	3.22	3.38	3.86	3.41	2.23	3.23	4.02	4.25	2.75	2.55	2.54	4.30
Tm	0.53	0.56	0.59	0.58	0.42	0.54	0.65	0.69	0.39	0.36	0.34	0.67
Yb	3.31	3.26	3.92	3.88	2.71	3.42	4.04	4.14	2.51	2.38	2.38	4.28
Lu	0.51	0.50	0.59	0.61	0.45	0.53	0.62	0.63	0.40	0.41	0.36	0.64
Eu/Eu*	1	1.14	0.87	0.79	0.94	1.06	1.08	1.02	1.02	1	0.95	0.99
La _N /Yb _N	2.04	1.97	1.87	1.98	2.71	2.17	2.06	2.27	1.32	0.82	1.1	1.45
La _N /Sm _N	1.71	1.69	1.64	1.99	2.24	1.71	1.59	1.75	1.37	1.02	1.04	1.18

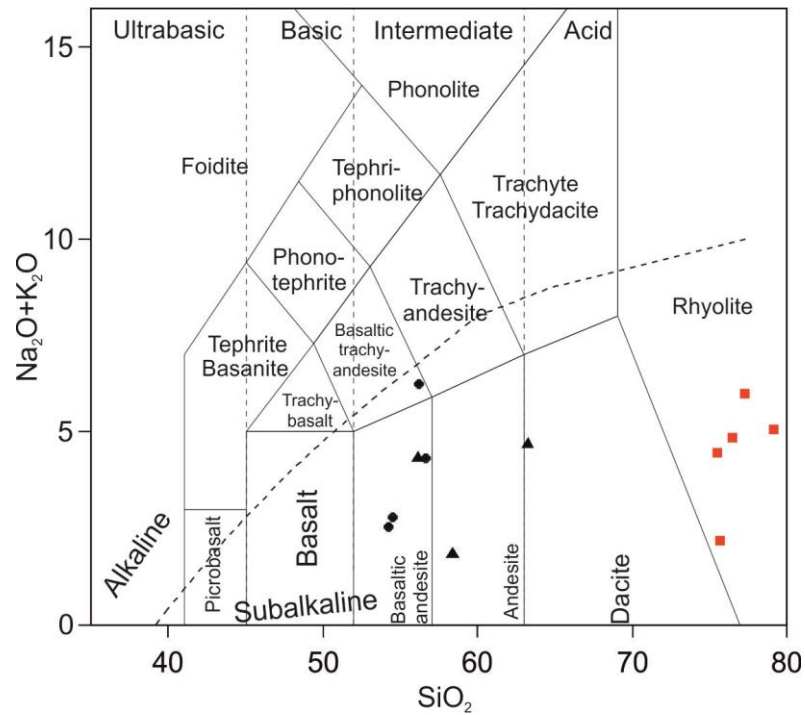


Figure 7.1 : Total alkali vs silica classification diagram (Le Bas et al., 1986) of the metavolcanic rocks of the Kösdag Formation. Symbols are in accordance with REE diagram in Fig. 7.3a.

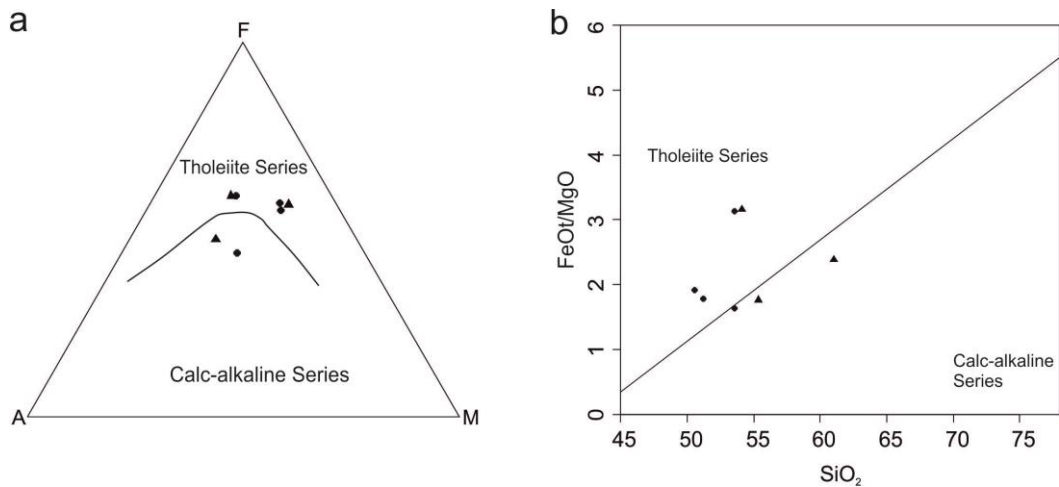


Figure 7.2 : a) AFM (Irvine and Barager, 1971) and b) SiO₂ vs FeO/MgO (Miyashiro, 1974) diagrams for the basaltic andesite/andesite of the Kösdag Formation.

7.1.2 Trace and rare earth element compositions

Metavolcanic rocks exhibit two distinct REE patterns when normalized to chondrite (Fig. 7.3a). Both the rhyolites and some of the basaltic andesite/andesite, denoted as BA1, show relative enrichment of the LREE with respect to HREE ($La_N/Yb_N = 1.87\text{--}2.71$ and $2.06\text{--}2.27$, respectively). While the rhyolites show both positive and

negative Eu anomalies ($Eu/Eu^*=0.79-1.14$), BA1 do not have any significant Eu anomaly ($Eu/Eu^*=1.02-1.08$).

The second group of basaltic andesites (BA2) are characterized by relatively flat REE pattern ($La_N/Yb_N= 0.82-1.45$). In this group, one sample differs with its higher amounts of REE (sample 1305, dashed line in Fig. 7.3a). Eu/Eu^* ratio of BA2 ranges between 0.95-1.02.

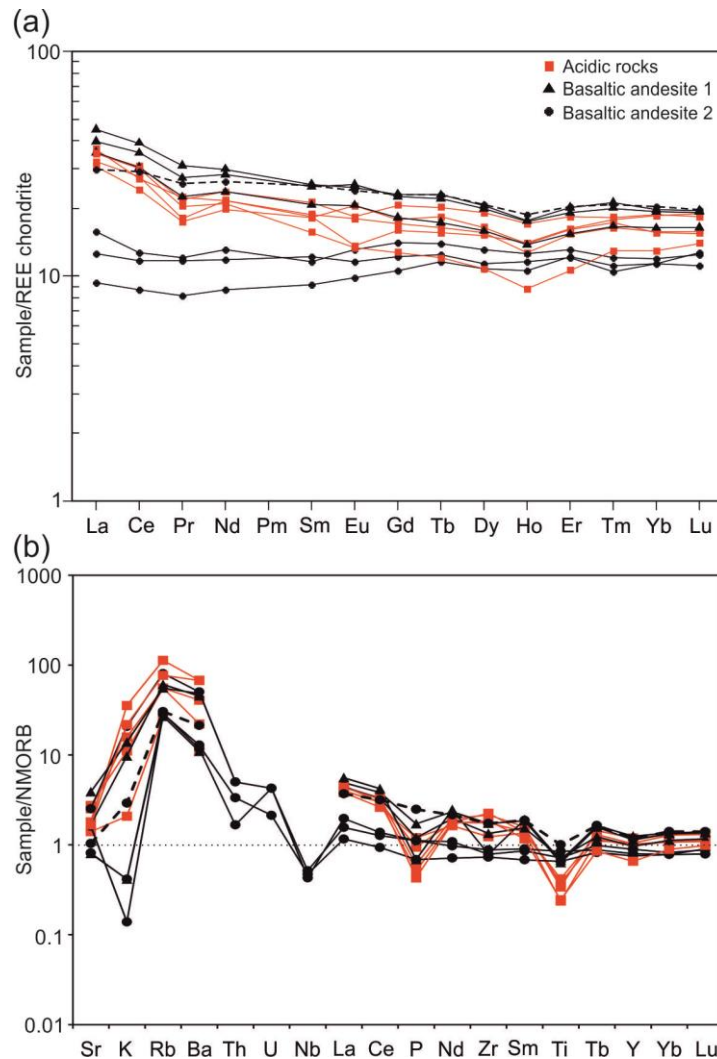


Figure 7.3 : a) Chondrite normalized REE diagram for the metavolcanic rocks according to normalization values of Boynton (1984). b) NMORB normalized multi-element spider diagram of the metavolcanic rock normalized to Sun and McDonough (1989) values.

In an N-MORB normalized spider diagram, rhyolites and the first group of basaltic andesites (BA1) are characterized by i) enrichment of fluid-mobile LIL elements and ii) depletion of Ti and P with clear negative anomalies (Fig. 7.3b). BA2, although

enriched in LIL elements does not show Ti or P depletion except the one with elevated amounts of REE (sample 1305), which shows a weak Ti negative anomaly.

7.2 Interpretation of the Analytical Data

Enrichment of fluid-mobile LILE and depletion of HFSE (Ti, P and Nb) of the metavolcanic rocks indicate supra-subduction magmatism (Tatsumi et al., 1986; Pearce and Peate, 1995; You et al., 1996; Münker et al., 2004). The similarity between the REE patterns of the rhyolites and the first group of basaltic andesites (BA1) suggest that they are genetically related. Their REE pattern is identical with calc-alkaline series in island arc volcanism (Gill, 1981; Fujinawa, 1992). Rhyolites with abundant gabbroic xenoliths show positive Eu anomalies. However, in the rhyolites without gabbroic xenoliths, there is a pronounced negative Eu anomaly. The absence of any Eu anomaly in the genetically related first group of basaltic andesites (BA1) indicates that plagioclase was not an important phase in the differentiation of BA1. This fits-well with the experimental data of Müntener et al. (2001) showing that increasing water content in the primitive arc magma suppresses plagioclase crystallization to later stages in favor of crystallization of pyroxene. In the cognate xenoliths, apatite and Fe-Ti oxides are common accessory phases. Hence, fractionation of apatite and ilmenite might be inferred for the P and Ti depletion. There is again a positive correlation between the degree of depletion of Ti and P with the absence of cognate xenoliths and SiO₂ saturation of the rhyolites. We infer that BA1 and rhyolites are cogenetic and have a common parental magma.

The flat REE pattern of the BA2 is identical with an island arc low-K tholeiite series (Jakeš and Gill, 1970; Fujinawa, 1992). Absence of any Eu anomaly suggests plagioclase was not an accumulated phase. In BA2, there is no Ti and P depletion suggesting there was no fractionation of ilmenite or apatite. Absence of HFSE depletion and LILE enrichment is concordant with its island arc tholeiitic character (Winter, 2001). Weak negative Ti anomaly and elevated amounts of REE of the sample 1305 suggest that this sample is more evolved than the rest of BA2.

7.3 Concluding Remarks

Petrography, mineralogy and geochemistry of the metavolcanic rocks indicate that they are mainly composed of basaltic andesite and rhyolite with abundant cognate

gabbroic/mafic xenoliths. Trace and rare earth element compositions of the metavolcanic rocks, depletion of HFSE and enrichment of LILE, indicate supra-subduction volcanism. Recently, Berber et al. (2014) also reported geochemical data from the Köşdağ metavolcanic rocks, which fall in the andesite/basalt, andesite and dacite fields in a Nb/Y versus Zr/TiO₂ diagram. Trace and rare earth element compositions of the samples also indicate a supra-subduction origin, which resemble our BA1 and rhyolites. The lithological association and the geochemistry of the metavolcanic rocks indicate that the Köşdağ Formation formed in a submarine arc setting.

The low-grade arc-sequence is sandwiched between the Laurasian active margin represented by a Cretaceous accretionary wedge and the Gondwana-derived Kırşehir Massif along the İAES. Absence of continent derived detritus within the arc sequence suggests that the Köşdağ Arc was isolated from any continental domain during its formation (Rice et al., 2006). A possible tectonic scenario is that the Köşdağ Arc represents an island arc separated from the Laurasian margin from a marginal sea forming a natural barrier for continental detritus supply (Rice et al., 2006). This scenario mainly based on the assumption that the overlying Middle Jurassic and Cretaceous subduction-accretionary complexes in the north were part of the Triassic basement of the Sakarya Zone. However, the ages of the overlying HP/LT metamorphic rocks (114-92 Ma, Okay et al., 2006, 2013 and this study) suggest that subduction was still going on in the north when the Köşdağ Arc was formed (ca. 94 ± 2 Ma, see Ch. 6). This suggests a dual subduction along the Laurasian margin rather than a slab-roll related opening of a marginal basin (Fig. 7.4a). It is also noteworthy that the overlying HP/LT metamorphic rocks lack of any intrusive or volcanic rocks coeval to the Köşdağ Arc volcanism. Hence, we propose that the Köşdağ Arc formed initially in an intra-oceanic setting located south of the Laurasian active margin.

Late Cretaceous intra-oceanic arc volcanism of the Köşdağ Arc was relatively short-lived suggesting that the arc was an infant stage (Stern, 2010). This is based on the short time span of volcanism constrained by zircon age data, and the possible Cenomanian age of the overlying pelagic limestones of the Dikmen Formation (Tüysüz 1990, 1993). Termination of volcanism is indicated by absence of any volcanic layers in the sediments of the overlying Dikmen Formation. Extinction of

the Köşdağ Arc should have occurred before the collision of the Kırşehir Massif as indicated by the pelagic character of the overlying Dikmen Formation. This is probably related to the southward migration of the arc volcanism leaving the Köşdağ as a remnant arc (Fig. 7.4b). South of the Köşdağ Formation, unmetamorphosed Upper Cretaceous arc-related calc-alkaline to tholeiitic basalts and basaltic andesites with pyroclastic rocks interbedded with pelagic limestone crop out along the İAES (Yaylaçayı Formation in Fig. 1.3, Rice et al., 2006; Tüysüz et al., 1995). The Yaylaçayı Formation is interpreted as an intra-oceanic arc sequence (Tüysüz et al., 1995) and might represent products of the inferred southward migration of the Köşdağ arc volcanism. Such slab rollback controlled migration of the arc volcanism is also proposed for the Upper Cretaceous (ca. 68-76 Ma, $^{40}\text{Ar}/^{39}\text{Ar}$ whole rock and biotite ages) alkaline magmatic rocks within the İAES; possibly with respect to the Yaylaçayı Formation (Sarifakioğlu et al., 2014). Arc migration is best seen at present in the Izu-Bonin-Mariana arc system. This arc system was rifted episodically from the Palau Kyushu and West Mariana ridges located to the west which represent the remnant arcs (Stern et al., 2003; Takahashi et al., 2007; Stern, 2010).

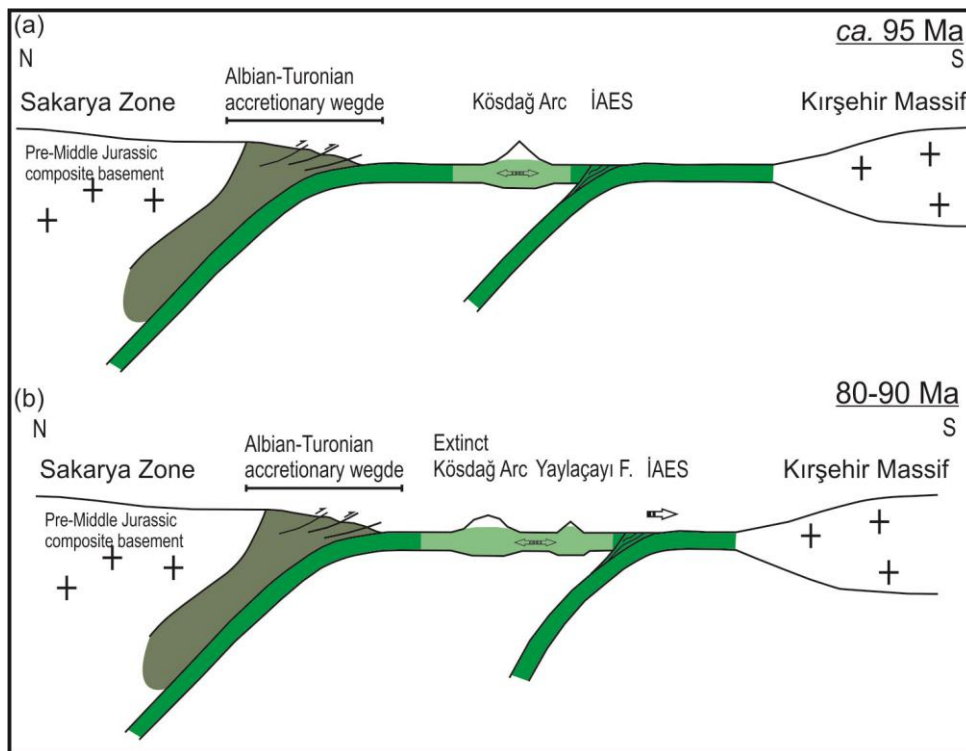


Figure 7.4 : a) Cartoon model showing the Late Cretaceous tectonic configuration of the Central Pontides. a) The Köşdağ Arc formed at ca. 95 Ma in an intra-oceanic setting located south of the Laurasian active margin. b) Slab rollback controlled arc migration leading to the termination of volcanism in the Köşdağ Arc.

An intriguing aspect of the intra-oceanic arc sequence is the occurrence of voluminous felsic volcanic rocks. Arc-related meter-sized blocks of rhyolites associated with larger basaltic rocks were also reported within the ophiolitic mélange farther southwest near Eldivan (Dangerfield et al., 2011). Previously, it was generally accepted that intra-oceanic volcanic arcs are dominated by basalts and basaltic andesites (e.g. Ewart et al., 1977; Gill, 1981; Hawkins et al., 1984; Gamble et al., 1997). However, acidic volcanic rocks have also been reported in the last decades from the modern intra-oceanic volcanic arcs (e.g. Robin et al., 1993; Monzier et al., 1994; Worthington et al., 1999). There are two models for their genesis a) differentiation of the parental magma generated in the mantle wedge through fractional crystallization and crystal accumulation (Pearce et al., 1995; Straub, 1995), b) re-melting of the andesitic (Tamura and Tatsumi, 2002) or basaltic (Leat et al., 2003; Smith et al., 2003) sub-arc crust. Our petrographic and geochemical data support the fractional crystallization and accumulation model for the formation of the rhyolites. This is evidenced by 1) identical trace and rare earth elements of both the BA1 and the rhyolites characterized by LREE enrichment and depletion of Ti and P 2) occurrences of abundant Fe-Ti oxide and apatite-bearing mafic cognate xenoliths within the rhyolites and an andesite. Cumulate-like clusters of plagioclase with interstitial clinopyroxene and monomineralic cluster of apatite further support accumulation as a main agent in differentiation of the parental magma.

Occurrence of cognate mafic xenoliths is compatible with the exposed intra-oceanic sub-arc crustal rocks consisting mainly of gabbro (DeBari and Coleman, 1989; DeBari and Sleep, 1991; Miller and Christensen, 1994; Greene et al., 2006; Hacker et al., 2008; Jagoutz et al., 2010; Petterson, 2010). Distinct Eu/Eu* ratios of the BA1 (1.02-1.08) and the rhyolites (0.79-1.14) suggest that plagioclase accumulation played a major role during differentiation of the felsic rocks from a common mafic parental melt. A recent experimental work showed that at the late stage of the differentiation of the primitive arc magmas, fractionation of amphibole, plagioclase and Fe-Ti oxide (extraction of amphibole-bearing gabbroic rocks) can increase the SiO₂ content of the remaining melt from 53% up to 78% (Nandedkar et al., 2014). This is in accordance with the trace and rare earth element signature of the rhyolite and with the cognate mafic xenoliths found within the rhyolites.

8. GEODYNAMICS

The Central Pontides is an interesting and newly recognized accretionary-type orogenic area formed along the southern Laurasian active continental margin. The region is characterized by Mesozoic subduction-accretionary complexes called as Central Pontide Supercomplex exposed over a large area. The majority of subduction-accretionary complexes form an Albian-Turonian accretionary wedge consisting of both continental and oceanic crust derived HP/LT metamorphic rocks, mélanges and forearc deposits. The continental accretionary rocks are a low-grade HP metaflysch sequence consisting of phyllite/metasandstone intercalation with recrystallized limestone, Na-amphibole-bearing metabasite and serpentinite (the Esenler and Martin formations). It represents distal parts of a large Lower Cretaceous submarine turbidite fan deposited on the Laurasian active continental margin that was subsequently accreted and metamorphosed during Albian. The accreted continental metaclastic rocks are tectonically underlain by a metabasite dominated oceanic deep-seated HP/LT metamorphic sequence (the Domuzdağ Complex) along an extensional shear zone. Middle Jurassic subduction-accretion complexes are found within the Albian-Turonian wedge as tectonically emplaced slices. At the latest Cretaceous, a nascent Late Cretaceous (94 ± 2 Ma) intra-oceanic arc was accreted to the Albian-Turonian wedge along İAES, the main tectonic division throughout Turkey separating Laurasia from Gondwana-derived continental blocks. In this tectonic framework, the Central Pontides consists of subduction and accretion related units which are sandwiched between the southern Laurasian active margin and the Gondwana-derived Kırşehir Block without involvement of any continental fragments. This indicates a major contribution of pre-collisional accretionary continental growth of the Laurasian active continental margin during Tethyan subduction.

Below, geodynamic implication of this new accretionary-type orogenic area is discussed in terms of tectonic thickening of the wedge and exhumation of the deep

seated HP/LT metamorphic rocks. Finally, the accretionary units are correlated with surrounding region to understand their role in regional geological studies.

8.1 Tectonic Thickening of the Albian-Turonian Accretionary Wedge

In the Central Pontides, the Albian-Turonian accretionary wedge is characterized by the presence of voluminous accreted terrigenous metaclastic rocks. They represent accreted distal parts of a large Lower Cretaceous submarine turbidite fan. The proximal parts of the turbidite fan is exposed farther north (Okay et al., 2013). This makes the Central Pontides one of the key areas for understanding the tectonic thickening of an accretionary wedge under high amount of sediment flux into the trench, which has a primary effect on frontal enlarging of the wedge by offscraping and shallow level underplating of the continental detritus (e.g. Platt et al., 1985; McCall, 2002).

The uniform lithology of the accreted turbidite sequence makes recognition of structural elements such as major faults difficult. Besides, due to the rheological weakness of the slate and phyllites, the primary structural framework can be easily overprinted by subsequent, younger deformation events. RSCM of the metapelitic rocks of the Esenler Unit, however, revealed that the accreted distal turbidites consist of metamorphic packets with distinct peak metamorphic temperatures. A major portion of the wedge is formed by low-temperature slates that possibly represent scraped off turbidites coming to the trench. The phyllites most likely formed during shallow level underplating of continental detritus beneath the offscraped distal turbidites. The associated incipient blueschist facies metabasite sliver was peeled off from the sinking oceanic crust and mixed tectonically with the phyllites during underplating along the basal décollement (Kimura and Ludden, 1995).

Recognition of the relatively high-temperature phyllites as a sliver within the low-temperature slates is significant and provides new insights on the structure of the Albian-Turonian accretionary wedge. There are no kinematic data for the tectonic emplacement of the underplated phyllites into the offscraped turbidites. The youngest deformation in the studied area is represented by post-Eocene east-west striking oblique strike-slip faulting which strongly modified the southern part of the area studied. The post-Eocene deformation is characterized by northward tilting and emplacement of the higher-grade Domuzdağ Complex over the Esenler Unit.

However, this northward tilting is absent in the phyllites that are exposed as a slice within the slates in central part of studied area. These phyllites and the associated metabasite sliver show gently NW dipping foliation planes similar to the general structural trend of the Albian-Turonian wedge. This suggests that their tectonic emplacement occurred during syn-subduction stacking.

In accretionary wedges, out-of-sequence thrusting is a common phenomenon in order to maintain the critical wedge taper during tectonic thickening of the wedge (Platt, 1986; Morley, 1988). It can juxtapose distinct metamorphic sequences during accretion within the wedge. Vitrinite reflectance studies revealed a sharp thermal discontinuity in the Cretaceous Shimanto accretionary complex, Japan, which is interpreted as an out-of-sequence thrust (Ohmori et al., 1997). Tectonic emplacement of the underplated phyllites and incipient blueschist facies metabasites within the lower-temperature offscraped slates is thus regarded as controlled by out-of-sequence thrusting causing tectonic thickening and uplift of the wedge (Fig. 8.1).

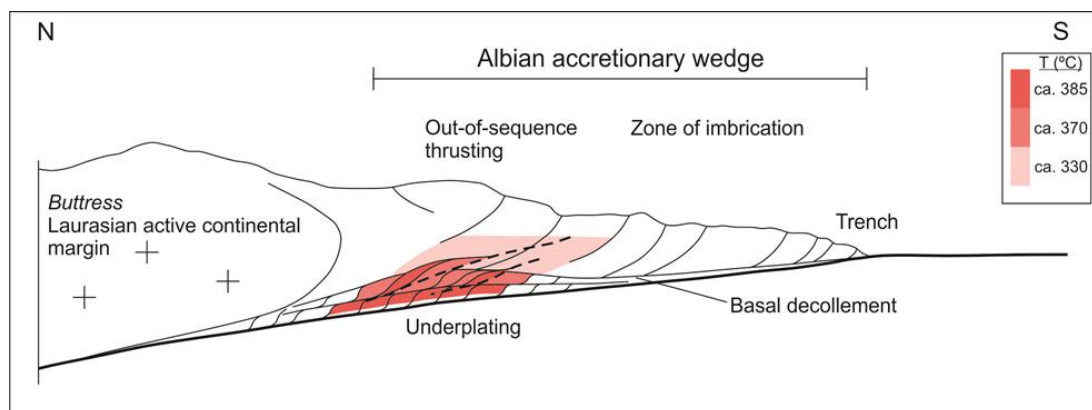


Figure 8.1 : A model showing a possible initial situation of the phyllites and the slates within the Albian accretionary wedge. While the slates represent the offscraped distal turbidites, the phyllite possibly represent underplated metasediments of the turbidite fan. Out-of-sequence thrusting (dashed thick lines) is proposed for uplift and tectonic emplacement of the phyllites. The model is modified after Moore et al. (2001).

The accreted distal turbidites are tectonically underlain by oceanic crust-derived HP/LT metabasite and micaschist along an extensional shear zone. The underlying oceanic unit comprises the major proportion of the wedge and consists of a tectonically thickened eclogite to blueschist facies metamorphic sequence (Okay et al., 2006a, 2013). In the area studied, deep-seated metabasites are epidote-blueschist locally with garnet. Lawsonite-blueschist blocks within the extensional shear zone indicate a major break in the metamorphic grade. The tectonic position of the

lawsonite-blueschists suggests that they formed at the earlier stages of the accretion along the overriding plate boundary. Lawsonite stability is generally regarded as indicative for relatively cold thermal setting and fast exhumation (Zack et al., 2004; Whitney and Davis, 2006; Tsujimori et al., 2006b). There are many parameters that can affect the thermal structure of a subduction zone including age of the slab, convergence rate, geometry of subduction, shear related heating etc. (Peacock, 1996). Numerical modelling indicates that temperatures at the upper part of a subduction zone along the plate contact are primarily determined by frictional heating (van den Beukel and Wortel, 1987). Accordingly, Peacock (1992) showed that occurrence of blueschist facies low temperatures rocks are associated with low shear stress and low shear heating along the subduction zone. We infer that during the initial stage of the Albian convergence, accretion was characterized by low shear stress generating a relatively cold thermal structure where the lawsonite-blueschists formed. With southward growth of the wedge, the thermal setting is modified in favor of epidote-blueschist facies metamorphism related to increase of shear stress within the prism. Although the chloritoid-micaschist samples 775 and 753A have identical depth of burial, the latter experienced considerably higher temperatures revealed by the different degrees of graphitization. It is noteworthy that these two samples of chloritoid-micaschists are exposed close to each other without a clear tectonic boundary in between. Source of the extra heat of the sample 753A might also be originated by relatively high shear stress within the wedge. This may point significance of shear stress deviation across a developing accretionary prism and dispute a steady-state thermal setting even in a limited area.

So far, majority of the studies on deep-seated HP/LT metamorphic rocks are focused on their exhumation (e.g. Platt, 1993; Sedlock, 1999; Jolivet et al., 2003; Ganne et al., 2006; Brun and Faccenna, 2008; Agard et al., 2009). However, tectonic thickening of these metamorphic sequences requires considerable amount of space along the plate interface, which is generally disregarded. Platt (1986) proposed a general thickening mechanism of the wedge by sediment underplating in a stable subduction zone configuration. Steady state thickening of the wedge is compensated by extension of the wedge (gravity-driven collapse) which also exhumes the HP/LT metamorphic rocks. Such steady state wedge configuration is also set up for analog sandbox experiments where thickening simply compensated by uplift of the

overburden (e.g. Malavieille, 2010). Although this mechanism may cause thickening and uplift of shallow level underplated rocks (e.g. accreted distal turbidites of the Esenler Unit, see above), it is unlikely to solve the space problem along the plate interface for the tectonic thickening of deep-seated eclogite to blueschist facies metamorphic sequences (e.g. Domuzdağ Complex). Most of the subduction zones, however, are far from being in a stable configuration, and are characterized by advancing or retreating trench migration (Uyeda and Kanamori, 1979; Carlson and Melia, 1984; Lallemand et al., 2008). The latter is attributed to the slab rollback, which causes extension of the overriding plate (Garfunkel et al. 1986; Schellart, 2008). By interpreting seismic reflection data, Minelli and Faccenna (2010) reported a post-Messinian basal décollement ramp related to slab rollback in the Calabrian wedge, Italy, which caused frontal thrust propagation and underplating. It is discussed by the same authors that forward propagation of décollement associated with slab rollback can cause crustal thickening (Minelli and Faccenna, 2010). By analogy with the Calabrian wedge, slab rollback also seems the most plausible process that can create a necessary space along plate interface for progressive deep level basal accretion. Thickening of the HP/LT metamorphic sequences by continuous underplating of oceanic basalts and sediments is possibly achieved by décollement propagation along the retreating subduction interface. By extending the overriding plate, slab rollback also plays a major role in subsequent exhumation of the deep-seated metamorphic sequence suggesting that tectonic thickening and exhumation of deeply underplated rocks are connected (Figure 8.2).

Estimated arc-parallel strain rates in modern fore-arc regions suggest that extensional strain is more common than compression (McCaffrey, 1996). The extension of the Albian-Turonian accretionary wedge is structurally evidenced by the extensional shear zone and footwall micaschists with syn-kinematic albite porphyroblasts. $^{40}\text{Ar}/^{39}\text{Ar}$ dating on phengites reveals that the extensional pervasive shearing occurred in a syn-subduction setting during the Late Cretaceous. Upper Cretaceous leucite-bearing alkaline volcanic rocks and related turbidites possibly were extruded and deposited above the thinning accretionary wedge. All these data suggest a pre-collisional diffusive and broad extension of the overriding plate from back arc (opening of the Black Sea) to fore-arc region. To the south, accretion of the Köşdağ

paleo-arc to the Albian-Turonian wedge is constrained to ca. 70 Ma providing an upper age limit for pre-collisional extension of the wedge.

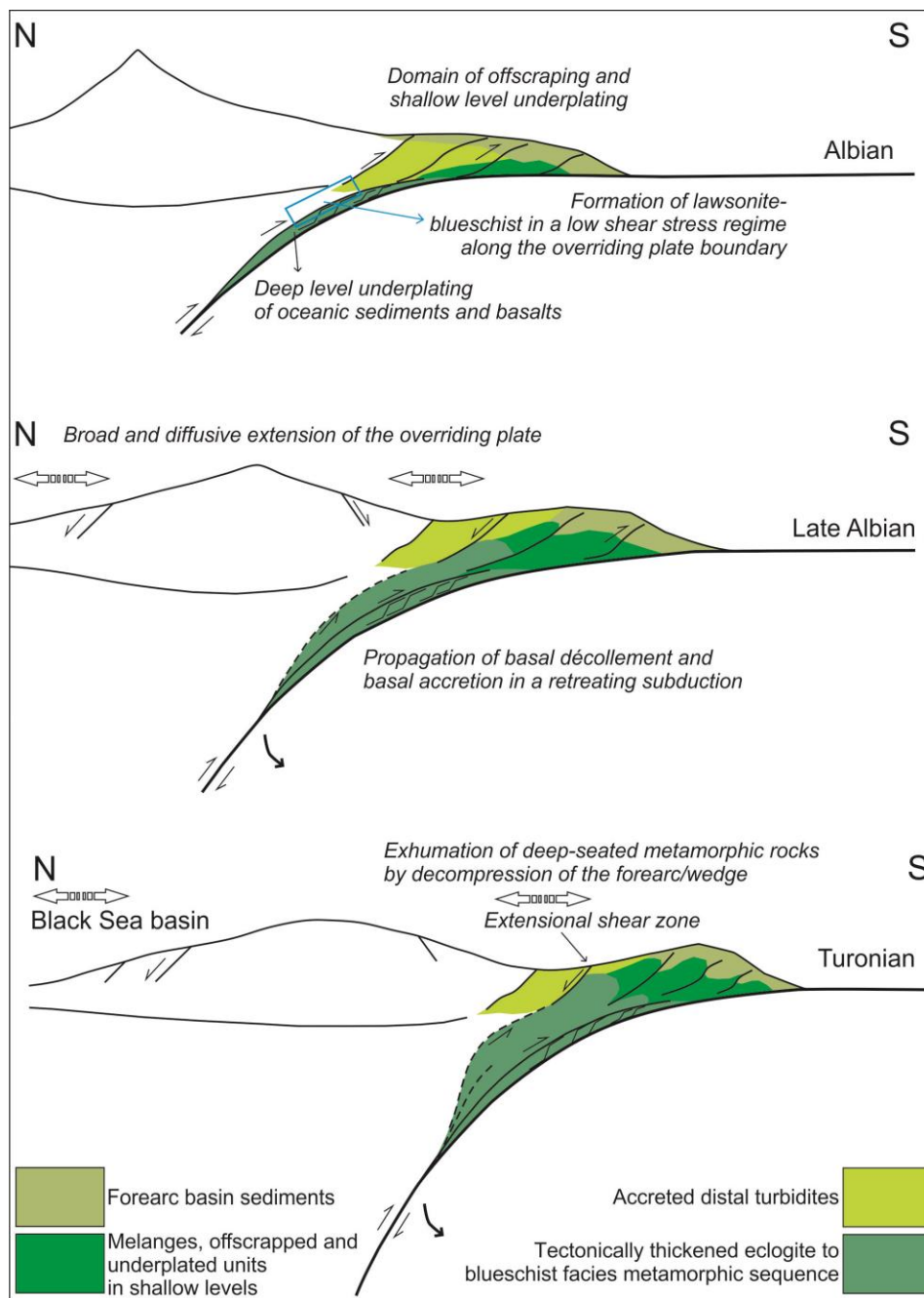


Figure 8.2 : Model for the tectonic evolution of the Albian-Turonian wedge with a possible tectonic thickening and subsequent exhumation mechanism of the deep seated subduction-accretion complexes. During Albian, the wedge was dominated by accretion of clastic detritus. Lawsonite blueschists possibly formed during initial low shear stress Albian subduction. Late Albian to Turonian evolution of the wedge was mainly controlled by slab rollback, which creates the necessary space for deep level underplating by décollement propagation. Synchronous extension of the wedge by slab rollback, subsequently exhumes the deep-seated metamorphic sequence.

It is noteworthy that progressive material accretion and subsequent exhumation should appear with a younging pattern towards the trench. This fits with the 91.8 ± 1.8 Ma age obtained from a chloritoid-micaschist exposed relatively south compared to 100.6 ± 1.3 Ma age in the north.

8.2 Exhumation of the Deep-Seated Domuzdağ Complex

Unlike the HP/LT coherent metamorphic sequences formed by continental subduction as in western Alps, NW Turkey and Oman (e.g. Chopin, 1981, 1984; El-Shazly and Liou, 1991; Okay, 2002), the subduction-accretionary HP/LT metamorphic rocks are formed by tectonic accumulation of down going material by underplating mainly of oceanic crustal lithologies. These two distinct types of metamorphic sequences do not only differ in their way of formations but also in their mode and rate of exhumation (e.g. Agard et al., 2009). Buoyancy-driven exhumation plays a key role in subducted continental margins or continental blocks in a rate close to the plate velocities (Chemenda et al., 1996). Exhumation of the deeply underplated oceanic accretionary rocks, however, is rather complicated and different mechanisms may operate. One of the earliest models is the flow concept based on the upward motion of the blocks within the subduction channel or wedge (Cloos, 1982; Cloos and Shreve, 1988). Later, removal of the overburden achieved largely by extension was the main focus. Different tectonic scenarios were proposed for the generation of extension including gravitational collapse due to tectonic thickening (Platt, 1986, 1993), slab rollback triggered by subduction of small continental blocks (Brun & Faccenna, 2008) or slab rollback itself (Jolivet et al. 2003). The number of geological, petrologic, and structural data to test the models, however, is limited. One important constraint comes from the available PT data suggesting that unlike the subducted continental margins that can experienced UHP conditions, exhumation of oceanic subduction-accretionary complexes is limited to rocks buried to ca. 80 km (Agard et al. 2009; Whitney et al. 2014). As already pointed by Whitney et al. (2014), this depth intriguingly overlaps with the inferred maximum decoupling depth (MDD) below which the sinking slab is coupled with viscously flowing mantle wedge (Wada and Wang, 2009; Wada et al., 2008). The MDD or “point of no return” most probably forms also a natural limit for tectonic accumulation along the sinking

slab or ultimate tip of the subduction-accretionary wedges controlled by forearc lithospheric thickness.

In many HP/LT metamorphic areas, extension-related structures have been reported suggesting extension plays a key role in their exhumation (for example Avigad & Garfunkel 1991; Wallis et al. 1993; Sedlock 1999, Agard et al. 2001; Jolivet et al. 2003). Similarly, in the Central Pontides, the most pronounced structural feature of the Albian-Turonian accretionary wedge is the extensional shear zone, which separates the deep-seated oceanic Domuzdağ Complex from overlying low-grade accreted distal turbidites. It forms the main boundary between the accreted continental and oceanic rocks and was probably worked as the basal decollement during initial stages of Albian convergence. Southeast of the extensional shear zone, the footwall micaschists were formed by pervasive ductile shearing during extension-induced exhumation. In these micaschists, calcite and tourmaline are common suggesting high fluid flux during ductile pervasive shearing accompanying the exhumation. Increasing ferric iron content of the low-Si phengites is also consistent with the increasing fluid activity. Similar retrogressive textures are also observed in the eclogites of the Domuzdağ Complex. Large tourmaline crystals together with secondary chlorites are interpreted as retrogression associated with infiltration of oceanic crust derived B- and Na-rich fluids during exhumation (Altherr et al., 2004).

Farther away from the shear zone, the chloritoid-micaschists represent zero strain domains bounded possibly by localized shear zones (Fig. 8.3). Although the chloritoid micaschist were formed under varying metamorphic conditions, their retrograde nature are identical characterized by static replacement of the peak metamorphic assemblages, which now occur as pseudomorphs. Absence of tourmaline suggests that the chloritoid-micaschists did not interact with B-rich fluids during zero strain exhumation. Decomposition of hydrous minerals by decompression can release significant amount of fluid which could be source of fluids during exhumation of deep-seated rock (Zheng et al., 2007). Breakdown of lawsonite to garnet and finally to epidote by decompression is most likely fluid source for the sample 775. In the other two samples, however, product minerals like chlorite have more H₂O than the reactant minerals chloritoid or glaucophane. The source of the required fluid is ambiguous. An explanation could be that the chloritoid micaschists were never completely dry. These fluids within the rocks may form the

source of water needed during zero strain exhumation and static retrogression. This may suggest that the chloritoid-micaschists possibly represent closed-systems in terms of fluid flux/infiltration during their exhumation and were retrograded by contained fluids. Grossular-rich outer rim of the post kinematic garnets and the nature of the pseudomorphs support decompression without additional heat.

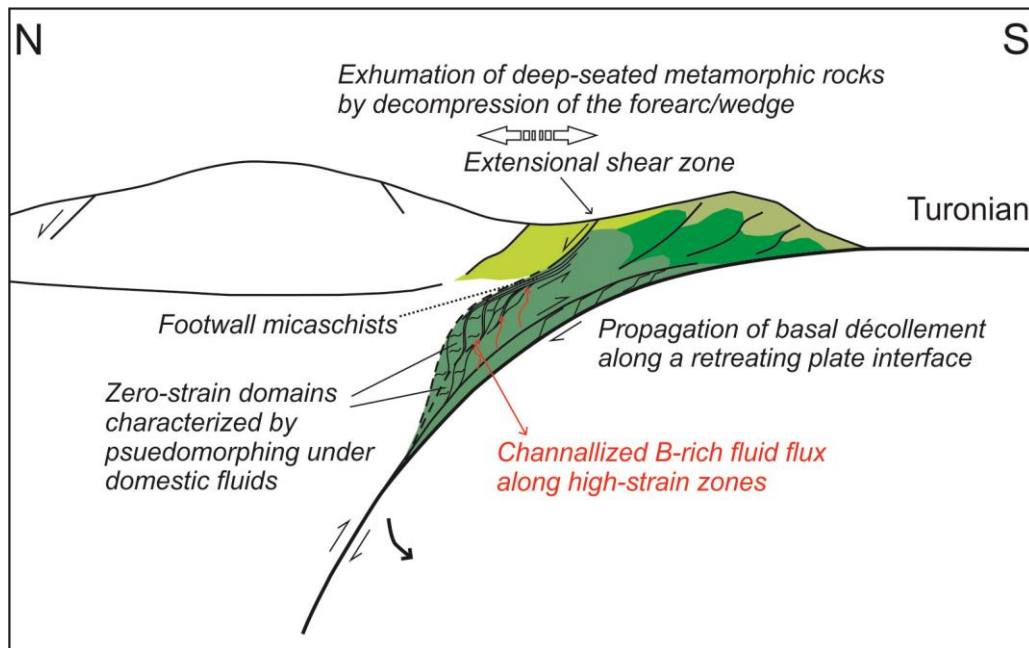


Figure 8.3 : An exhumation model for the deeply underplated oceanic HP/LT metamorphic sequence by decompression of the wedge along a retreating slab. Zero strain domains are characterized by partly preservation of the peak metamorphic assemblages. Retrogression is manifested by pseudomorphs formed through trapped fluids. B-rich fluids are generated from the newly underplating oceanic metabasalts and metasediments through dehydration reactions. The fluids then were channelized and migrated upward along the high-strain shear zones.

The Domuzdağ Complex was exhumed as a whole to shallow levels along the brittle extensional shear zone. Coupling of the chloritoid-micaschists with different depth of burial (sample 178 with samples 775 and 753A) within the wedge, however, is ambiguous. An upper limit of the exhumation of the Domuzdağ Complex is provided by the Maastrichtian limestone exposed as a tectonic sliver along the Akçataş Fault. The limestone probably unconformably covered the Domuzdağ Complex. This enables calculation of an average exhumation rate for the Domuzdağ Complex, particularly for the chloritoid-micashist sample 753A. The $^{40}\text{Ar}/^{39}\text{Ar}$ phengite dating on the sample 753A constrained the HP/LT metamorphism to ca. 92 Ma. This suggests ca. 50 km uplift (slightly less than 17 kbar) in 22 Ma (92-70 Ma). These parameters give a 2.3 mm/y average exhumation rate for the sample 753A.

As already discussed in section 8.1, syn-subduction decompression of the Albian-Turonian wedge is most likely triggered by the slab retreat caused tectonic thickening and subsequent exhumation of the deep seated metamorphic sequence. Brun & Faccenna (2008) pointed out that exhumation of HP metamorphic rocks is associated with subduction of continental blocks triggering slab rollback. In the case of the Central Pontides where orogeny was of accretionary-type, however, there is no evidence of a subduction of a crustal fragment that may trigger the slab retreat.

8.3 Comparative Regional Geology

The Cretaceous accretionary complexes in western Turkey are poor in trench-fill turbidites, unlike those in the Central Pontides. The absence of trench-fill turbidites suggests insufficient sediment supply which has a major effect on frontal enlargement of an accretionary wedge. Another difference is that in NW Turkey the accretionary complexes are shallow level and therefore constitute slightly metamorphosed tectonic mélanges of Late Cretaceous age (Okay, 2002; Topuz et al., 2008; Göncüoğlu et al., 2008, 2014; Aygül et al., 2012; Akbayram et al., 2013, Plunder et al., 2013). Related deep-seated HP/LT metamorphic rocks are generally of continental origin representing subducted passive continental margins. These include Çamlıca-Kemer metamorphic complexes (Okay and Satır, 2000; Aygül et al., 2012; Şengün et al., 2012) and Tavşanlı-Afyon zones (Sherlock et al., 1999; Okay, 2002; Okay and Whitney, 2010; Plunder et al., 2013; Pourteau et al., 2010, 2013). Absence of tectonically thickened deep-seated subduction-accretionary complexes may be related to the along strike variation of the slab-rollback. It is noteworthy that Upper Cretaceous alkaline volcanic sequence, which lies unconformably over the accretionary complexes in the Central Pontides, is also not reported in NW Turkey.

To the east, the Tokat Massif, consists of metamorphic rocks similar to those from the Central Pontides. Bozkurt et al. (1997) reported a low grade metaclastic unit with abundant recrystallized limestone, serpentinite and radiolarian chert blocks which is comparable with Esenler Unit. Radiolaria contents give a Late Jurassic age for the cherts (Bozkurt et al., 1997). There are also Na-amphibole-bearing metabasite, metapelites with ophiolitic rocks representing an oceanic accretionary unit (Kuytul Formation, Yılmaz et al., 1997b). Age of the regional metamorphism in the Tokat Massif, however, is accepted as Triassic though there is no absolute age data.

Along strike variations of the subduction-accretion complexes within the Anatolian scale depict the diversity of tectonic settings. In western Turkey, convergence was Alpine-type dominated by continental subduction and collisions. To the east, however, it was of accretionary type causing tectonic continental growth. The distinct tectonic settings are most likely controlled by physical behavior of the sinking slab.

In the Pontides, Middle Jurassic subduction-accretion complexes (Çelik et al., 2011; Topuz et al., 2012; Okay et al., 2013; Marroni et al., 2014) or arc sequences consisting of intrusive and volcanic rocks with associated LP/HT metamorphic rocks (Genç and Tüysüz, 2010; Göçmengil et al., 2013; Okay et al., 2014) are increasingly reported in the last several years. This suggests that Middle Jurassic represents a period of convergence in Tethyan realm. In the CPS, the Middle Jurassic accretionary complexes lie south of the Albian-Turonian ones, contrary to what is expected in an evolving subduction-accretion system. The possible Albian metamorphic overprint in the Middle Jurassic metamorphic rocks suggests that tectonic emplacement occurred during Albian orogeny. Subduction obliquity can cause significant along strike tectonic transport by using zones of weakness (e.g., Fitch 1972; Beck, 1983; Jarrard, 1986; McCaffrey, 1992). Emplacement of the Middle Jurassic metamorphic rocks is most probably related to oblique convergence during the Albian subduction. E-W trending post-Eocene strike slip faults (e.g. Akçataş fault; Figure 1.2, 2.1) are widespread in the Central Pontides and might have also caused further eastward tectonic transport.

8.3.1 Late Cretaceous intra-oceanic Köşdağ arc and supra-subduction ophiolites

Although intra-oceanic arcs comprise about 40% of the present volcanic arcs by length (Leat and Larter, 2003), they are rarely reported in geological record. Recognition of former intra-oceanic arcs exposed within older orogenic belts is important. They can play a key role in regional tectonic studies due to i) their ultimate collision/accretion along convergent margins causing tectonic growth of the continental crust (Taylor, 1967; Şengör et al., 1993; Rudnick, 1995; Clift and Vannucchi, 2004) and ii) possible linkage with supra-subduction ophiolite obduction (Dilek, 2003; Pearce, 2003). Most of the obducted ophiolitic bodies are underlain by thin metamorphic soles consisting of strongly sheared high-grade metabasic rocks (Williams and Smyth, 1973; Malpas et al., 1973; Spray, 1984; Jamieson, 1986;

Hacker, 1990; Wakabayashi and Dilek, 2000). These metamorphic soles are generally interpreted as marking the initiation of intra-oceanic subduction, although associated intra-oceanic arcs are generally not recognized. Despite the well-described exposures of Tethyan supra-subduction ophiolites found as obducted on Gondwana-derived continental fragments (Thuizat et al., 1981; Dilek et al., 1999; Searle and Cox, 1999; Robertson, 2002; Malpas et al., 2003; Önen, 2003; Çakır, 2009; Hébert et al., 2012; Hässig et al., 2013a, 2013b; Yalınız et al., 1996, 2000a, 2000b), presumed arcs are generally not well defined within the Alpine-Himalayan range.

The intra-oceanic Köşdağ paleo-arc is exposed along the İAES, which is the main division between the former Laurasia and Gondwana. In the northeastern part of the İAES, greenschist facies basaltic andesites, andesite and associated pyroclastic rocks are exposed, which are known as Karadağ Formation (Rice et al., 2006, 2009). The rocks show supra-subduction geochemical signature and interpreted as products of an Upper Cretaceous oceanic arc. It is proposed that Karadağ Formation forms the lateral continuation of the Köşdağ Formation. In western and central Anatolia, the age of the supra-subduction ophiolite obduction on Gondwana-derived terranes, as revealed by the dating of the metamorphic soles, is similar to that of the Köşdağ Arc. The $^{40}\text{Ar}/^{39}\text{Ar}$ ages from the amphibolites of the metamorphic sole range generally between 90-94 Ma (Dilek et al., 1999; Parlak and Delaloye, 1999; Önen and Hall, 2000; Önen, 2003; Çelik et al., 2006) and predate the HP/LT metamorphism of the subducted Anatolide-Tauride continental margin (ca. 80 Ma; Sherlock et al., 1999). Hence, we infer that the Köşdağ Arc forms part of the presumed intra-oceanic arc associated with the supra-subduction ophiolite generation that is obducted on the Gondwana-derived the Anatolide-Taurides.

The linkage of Tethyan closure from Turkey to Iran is evidenced by Late Cretaceous blueschists exposed within the Tethyan subduction-accretionary complexes in Armenia (90-95 Ma, Rolland et al., 2009) and in Iran (e.g. 85-95 Ma, Agard et al., 2006). Furthermore, Rolland et al. (2009) also reported a metamorphic event at ca. 71-73 Ma. It is interpreted as accretion of South Armenian Block and southward subduction jump (Rolland et al., 2012). These ages are similar to the accretion of the Köşdağ Arc at ca. 70 Ma suggesting that the final amalgamation of the Gondwana-derived continental blocks, Laurasian active margin and the intra-oceanic arc occurred at the latest Cretaceous along the İAES. Initiation of a Late Cretaceous

intra-oceanic subduction in the Tethyan realm is mainly evidenced by formation and obduction of the supra-subduction ophiolites. Along the Sevan-Akera suture, Amasia ophiolite was obducted over the South Armenian continental block, eastward extension of the Anatolide-Tauride Block (Galoyan et al., 2009; Rolland et al., 2010; Sosson et al., 2010). Garnet amphibolites with ca. 90 Ma isotopic age are interpreted as the metamorphic sole rocks (Hässig et al., 2011). It is proposed that NE Anatolian and Armenian ophiolite obduction occurred as a single event (Hässig et al., 2013a, 2013b). Ophiolitic fragments within the Zagros orogeny widely show supra-subduction affinity (Babaie et al., 2006; Desmons and Beccaluva, 1983; Moghadam et al., 2010). $^{40}\text{Ar}/^{39}\text{Ar}$ dating on hornblende and U/Pb dating on zircons from the plagiogranites give ca. 92-93 Ma (Babaie et al., 2006) and ca. 101-103 Ma (Moghadam et al., 2013) ages, respectively. An associated Cretaceous arc sequence consisting of island arc volcanic and volcanoclastic rocks with pelagic sediments structurally overlie the ophiolitic rocks (Babaie et al., 2001). The geology of Oman is strikingly similar to the geology of NW Turkey characterized by ophiolite obduction and continental subduction. U/Pb zircon geochronology of the plagiogranites/trondhjemites revealed that the Semail ophiolite formed ca. 95 Ma ago (Tilton et al., 1981; Warren et al., 2005). $^{40}\text{Ar}/^{39}\text{Ar}$ ages from the metamorphic soles are identical with ophiolite formation (Hacker et al., 1996; Searle and Cox, 1999; Warren et al., 2005). U/Pb zircon ages of the eclogite underlying the ophiolite constrain the continental subduction in Oman as ca. 80 Ma (Warren et al., 2003).

Remnants of Late Cretaceous intra-oceanic paleo-arcs are also reported farther east along the Indus suture of Himalayas. In north Pakistan, sub-arc crustal rocks and metamorphosed basic to intermediate volcanic rocks known as Kohistan intra-oceanic paleo-arc crop out over large areas (Coward et al., 1987; Petterson, 2010). Ages of the zircons and garnets from the lower parts of the arc ranges between 90-100 Ma (Yamamoto & Nakamura, 1996; Anczkiewicz & Vance, 2000; Schaltegger et al., 2002). There are also gabbroic rocks with ca. 85 Ma U/Pb zircon age (Schaltegger et al., 2002) which were associated with intra-arc extension-related mantle diapirs (Burg et al., 1998). Further east along the Indus suture, Dras Volcanics are accepted as continuation of the Kohistan paleo-arc (Honegger et al., 1982; Radhakrishna et al., 1984; Clift et al., 2002; Robertson & Collins, 2002). Associated possible metamorphic soles are exposed at the base of the ophiolite

fragments within the Indus Suture and were dated as 80-90 Ma (Malpas et al., 2003). It is proposed that ophiolite obduction occurred as a single event from Oman to eastern Himalaya along the northern margin of India during Late Cretaceous-Paleocene before the ca. 55 Ma India-Asia collision (Searle et al., 1997).

All these data reveal existence of connected Late Cretaceous intra-oceanic subduction along the sinking Tethyan slab (e.g. Aitchison et al., 2000) which is also supported by mantle tomographic imaging (Fig. 8.4; Van der Voo et al., 1999). It generated ensimatic arcs ultimately accreted to Laurasian active margin (such as in the Central Pontides and in the Himalayas) and associated supra-subduction ophiolite obduction on Gondwana-derived terranes (e.g. in NW Turkey and Oman).

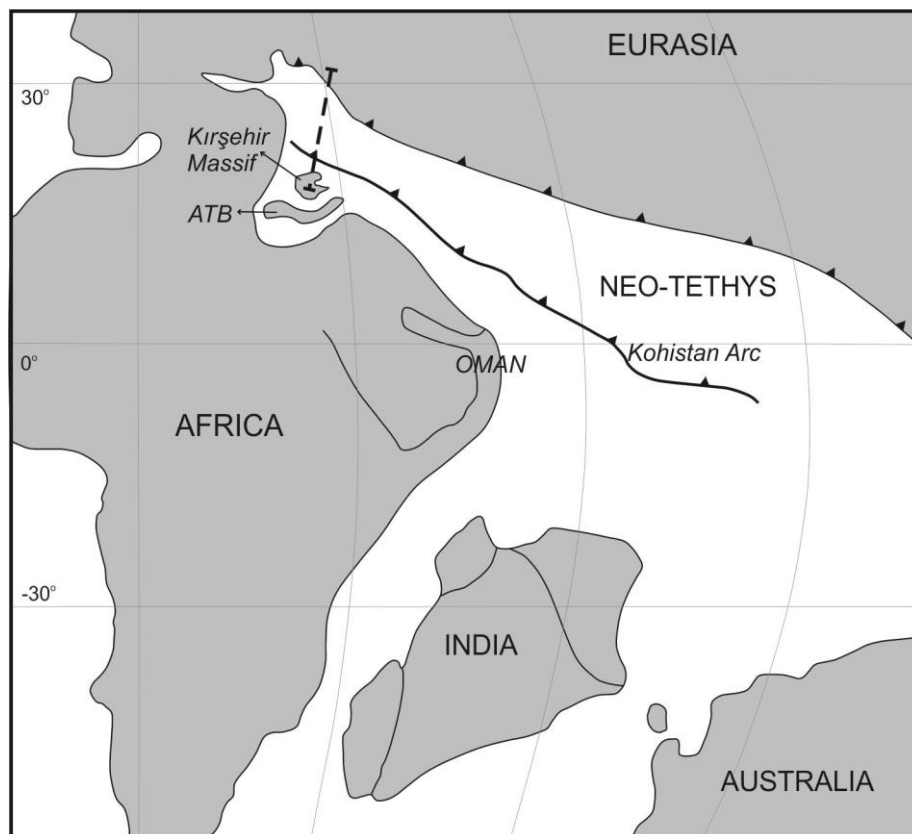


Figure 8.4 : Paleogeographic sketch map at ca. 95 Ma showing the dual subduction during Tethyan consumption (modified from Van der Voo et al. (1999)). Dashed line indicates location of the N-S section along the Central Pontides in Figure 7.4. ATB: Anatolide-Tauride Block.

9. CONCLUSIONS

The Central Pontides is a new accretionary-type orogenic area within the Alpine-Himalayan orogenic belt characterized by pre-collisional tectonic continental growth of Laurasian margin. The region comprises Mesozoic subduction-accretion complexes and an accreted intra-oceanic arc that are sandwiched between Laurasian active continental margin and Gondwana-derived the Kırşehir Block. The subduction-accretion complexes mainly consist of an Albian-Turonian accretionary wedge consisting of HP/LT metamorphic rocks of continental and oceanic origin, forearc deposits as well as mélangé and cover an area of 50 km by 100 km in the Central Pontides. In the north, the wedge is characterized by voluminous accreted metaclastic rocks consisting of slate/phyllite and metasandstone intercalation with recrystallized limestone, Na-amphibole-bearing metabasite (PT= 7–12 kbar and 400 ± 70 °C) and serpentinite blocks. This metaflysch sequence represents distal parts of a large Lower Cretaceous submarine turbidite fan deposited on active Laurasian continental margin and subsequently accreted. RSCM of the metapelitic rocks of the metaflysch sequence reveals that the accreted distal turbidites have undergone low temperature (ca. 330 °C) metamorphism. Phyllites with higher metamorphic temperatures (ca. 380 °C) occur as a slice within the low-temperature slates. The phyllites are associated with a strip of Na-amphibole bearing metabasites and possibly represent shallow level underplated terrigenous metaclastic rocks along the basal decollement. The metabasites were possibly peeled off from the sinking oceanic crust and underplated. The phyllites and the Na- amphibole bearing metabasites were tectonically emplaced within the offscraped part of the wedge by possibly out-of-sequence thrusting causing tectonic thickening and uplift of the wedge. $^{40}\text{Ar}/^{39}\text{Ar}$ phengite ages from the phyllites are ca. 100 Ma, indicating Early Cretaceous subduction.

The accreted continental metaclastic rocks are underlain by HP/LT metamorphic rocks of oceanic origin along an extensional shear zone. The oceanic metamorphic sequence mainly comprises tectonically thickened deep-seated eclogite to blueschist

facies metabasites and micaschists with minor serpentinite, metagabbro, metachert and marble. In the studied area, metabasites are epidote-blueschists locally with garnet (PT= 17 ± 1 kbar and 500 ± 40 °C). Lawsonite-blueschists are exposed along the extensional shear zone (PT= 14 ± 2 kbar and 370–440 °C). They are possibly associated with low shear stress regime of the initial stage of convergence. South of the extensional shear zone, the footwall micaschists consist of quartz, phengite, paragonite, chlorite, rutile with syn-kinematic albite porphyroblast formed by pervasive shearing during exhumation. These type of micaschists are tourmaline-bearing and their retrograde nature suggests high-fluid flux along shear zones. Peak metamorphic assemblages are partly preserved in the chloritoid-micaschist farther away from the shear zone representing the zero strain domains during exhumation. Three peak metamorphic assemblages are identified and their PT conditions were constrained by pseudosections produced by Theriak-Domino and by Raman spectra of carbonaceous material: 1) garnet-chloritoid-glaucophane with pseudomorphs after lawsonite (P: 17.5 ± 1 Kbar, T: 390-450 °C) 2) chloritoid with pseudomorphs after glaucophane (P: 16-18 Kbar, T: 475 ± 40 °C) and 3) relatively high-Mg chloritoid (17%) with pseudomorphs after jadeite (P:22-25 Kbar; T: 440 ± 30 °C) in addition to phengite, paragonite, quartz, chlorite, rutile and apatite. The last mineral assemblage is interpreted as the transformation of the chloritoid + glaucophane assemblage to chloritoid + jadeite paragenesis with increasing pressure. Absence of tourmaline suggests that the chloritoid-micaschist did not interact with B-rich fluids during zero strain exhumation. $^{40}\text{Ar}/^{39}\text{Ar}$ phengite age of a pervasively sheared footwall micaschist is constrained to 100.6 ± 1.3 Ma and that of a chloritoid-micaschist is constrained to 91.8 ± 1.8 Ma suggesting exhumation during on-going subduction with a southward younging of the basal accretion and regional metamorphism. To the south, the subduction-accretionary complexes consist of blueschist and greenschist facies metabasite, marble and volcanogenic metasediment intercalation. $^{40}\text{Ar}/^{39}\text{Ar}$ phengite dating reveals that this part of the wedge is of Middle Jurassic age which is partly overprinted during Albian. Emplacement of the Middle Jurassic subduction-accretion complexes is possibly associated with obliquity of the Albian convergence.

Peak metamorphic assemblages and PT estimates suggest that the Domuzdağ Complex is a metamorphic stack of tectonic slices rather than a coherent

metamorphic sequence. Coupling and exhumation of the distinct metamorphic slices are controlled by decompression of the wedge possibly along a retreating subduction. Structurally, decompression of the wedge is evident by the extensional shear zone and the footwall micaschists with syn-kinematic albite porphyroblasts. Mineral chemistry and textures of the chloritoid-micaschists (post-kinematic garnets with increasing grossular content and pseudomorphing minerals) also support decompression model without an extra heating.

Thickening of subduction-accretion complexes is attributed to i) significant amount of clastic sediment supply from the overriding continental domain and ii) deep level basal underplating by propagation of the décollement along a retreating subduction. Underplating by basal décollement propagation and subsequent exhumation of the deep-seated subduction-accretion complexes are connected and controlled by slab rollback creating a necessary space for progressive basal accretion along the plate interface and extension of the wedge above for exhumation of the tectonically thickened metamorphic sequences. This might be the most common mechanism of the tectonic thickening and subsequent exhumation of deep-seated HP/LT subduction-accretion complexes.

To the south, the Albian-Turonian accretionary wedge structurally overlies a low-grade arc-sequence which is thrust over the ophiolitic rocks of the İzmir-Ankara-Erzincan suture (İAES), separating the Laurasian active margin from Gondwana-derived terranes. The arc sequence consists of low-grade metavolcanic rocks and stratigraphically overlying recrystallized micritic limestone with rare volcanogenic metasediments. The metavolcanic rocks mainly consist of rhyolite and basaltic andesite with pyroclastic equivalents that are interbedded with pelagic limestone and chert. Geochemistry of the metavolcanic rocks indicates supra-subduction volcanism evidenced by depletion of HFSE and enrichment of LILE. The tectonic setting and absence of continent derived detritus within the arc sequence indicate an intra-oceanic setting. Abundant cognate gabbroic xenoliths and identical trace and rare earth elements compositions show that rhyolites and some of the basaltic andesites/andesites (BA1) are cogenetic and felsic rocks of the Köşdağ Formation were derived from a common mafic parental magma by fractional crystallization and accumulation processes.

Zircons from two metarhyolite samples give 93.8 ± 1.9 Ma and 94.4 ± 1.9 Ma U/Pb ages indicating Cenomanian-Turonian arc magmatism. These ages are slightly younger and partly overlap with the age of the HP/LT metamorphism of the overlying subduction-accretionary complexes (114-92 Ma). The tectonic setting and age data favor a separate subduction for the arc sequence that is formed in an intra-oceanic setting at the southern offshore of the Laurasian active continental margin. This is supported by the absence of terrigenous detritus within arc sequence and by basaltic andesites with island arc tholeiite REE pattern (BA2). The low-grade regional metamorphism of the arc sequence is constrained to 69.9 ± 0.4 Ma by $^{40}\text{Ar}/^{39}\text{Ar}$ muscovite dating indicating that the arc sequence was part of a wide Cretaceous subduction-accretionary complex by the latest Cretaceous; confirming southward younging of an accretionary-type orogenic area. Abrupt non-collisional termination of arc volcanism is best explained by southward migration of the arc volcanism similar to the Izu-Bonin-Mariana arc system.

Age of the intra-oceanic arc volcanism is coeval with the metamorphic sole ages of the obducted supra-subduction ophiolites in NW Turkey. This suggests that the Köşdağ paleo-arc forms part of the presumed but missing intra-oceanic arc associated with the initial subduction stage leading regional ophiolite obduction. Remnants of a Late Cretaceous intra-oceanic paleo-arc and supra-subduction ophiolites can be traced eastward within the Alp-Himalayan orogenic belt. This reveals that Late Cretaceous intra-oceanic subduction was a widespread event. It resulted in arc accretion to Laurasian active margin and supra-subduction ophiolite obduction on Gondwana-derived terranes.

REFERENCES

- Agard, P., Jolivet, L., Goffé, B.** (2001). Tectonometamorphic evolution of the Schistes Lustrés complex: implications for the exhumation of HP and UHP rocks in the Western Alps. *Bulletin de la Société Géologique de France*, 172, 617–636.
- Agard, P., Monié, P., Gerber, W., Omrani, J., Molinaro, M., Meyer, B., Labrousse, L., Vrielynck, B., Jolivet, L., Yamato, P.** (2006). Transient, synobduction exhumation of Zagros blueschists inferred from P–T, deformation, time and kinematic constraints: implications for Neotethyan wedge dynamics. *Journal of Geophysical Research*, 111, B11401, doi:10.1029/2005JB004103.
- Agard, P., Yamato, P., Jolivet, L., Burov, E.** (2009). Exhumation of oceanic blueschists and eclogites in subduction zones: Timing and mechanisms. *Earth Science Reviews*, 92, 53–79.
- Aitchison, J.C., Badengzhu, Davis, A. M., Liu, J., Luo, H., Malpas, J. G., McDermid, I. R. C., Wu, H., Ziabrev, S., Zhou, M. F.** (2000). Remnants of a Cretaceous intra-oceanic subduction system within the Yarlung-Zangbo suture zone, southern Tibet. *Earth and Planetary Science Letters*, 183, 231–244.
- Akbayram, K., Okay, A. I., and Satir, M.** (2013). Early Cretaceous closure of the Intra-Pontide Ocean in western Pontides (northwestern Turkey). *Journal of Geodynamics*, 65, 38–55.
- Altherr, R., Topuz, G., Marschall, H., Zack, T., Ludwig, T.** (2004). Evolution of a tourmaline-bearing lawsonite eclogite from the Elekdag area (Central Pontides, N Turkey): Evidence for infiltration of slab-derived B-rich fluids during exhumation. *Contributions to Mineralogy and Petrology*, 148, 409–425.
- Anczkiewicz, R. and Vance, D.** (2000). Isotopic constraints on the evolution of metamorphic conditions in the Jijal–Patan Complex and Kamila Belt of the Kohistan Arc, Pakistan Himalaya. In: Khan, M. A., Treloar, P. J., Searle, M. P. & Jan, M. Q. (eds) *Tectonics of the Nanga Parbat Syntaxis and the Western Himalaya*. Geological Society, London, Special Publications, 170, 321–331.
- Aoya, M., Kouketsu, Y., Endo, S., Shimizu, H., Mizukami, T., Nakamura, D., Wallis, S.** (2010). Extending the applicability of the Raman carbonaceous-material geothermometer using data from contact metamorphic rocks. *Journal of Metamorphic Geology*, 28, 895–914.
- Avigad, D. and Garfunkel, Z.** (1991). Uplift and exhumation of high-pressure metamorphic terrains: the example of the Cycladic blueschist belt (Aegean Sea). *Tectonophysics*, 188, 357–372.

- Aysal, N., Ustaömer, T., Öngen, S., Keskin, M., Köksal, S., Peytcheva, I., Fanning, M.** (2012). Origin of the Early-Middle Devonian magmatism in the Sakarya Zone, NW Turkey: Geochronology, geochemistry and isotope systematics. *Journal of Asian Earth Sciences*, *45*, 201–222.
- Aygül, M., Topuz, G., Okay, A. I., Satır, M., Meyer, H-P.** (2012). The Kemer Metamorphic Complex (NW Turkey): A subducted continental margin of the Sakarya Zone. *Turkish Journal of Earth Sciences*, *21*, 19–35.
- Babaie, H. A., Ghazi, A. M., Babaei, A., La Tour, T. E., Hassanipak, A. A.** (2001). Geochemistry of arc volcanic rocks of the Zagros Crush Zone, Neyriz, Iran. *Journal of Asian Earth Sciences*, *19*, 61–76.
- Babaie, H. A., Babaei, A., Ghazi, A. M., Arvin, M.** (2006). Geochemical, $^{40}\text{Ar}/^{39}\text{Ar}$ age, and isotopic data for crustal rocks of the Neyriz ophiolite, Iran. *Canadian Journal of Earth Sciences*, *43*, 57–70.
- Barkurt, M. Y., Bilginer, E., Pehlivan, Ş., Örcen, S.** (1990). Geology of the Kastamonu-Ovacık region. MTA Report No: 9079 (in Turkish).
- Barr, S. R., Temperley, S., Tarney, J.** (1999). Lateral growth of the continental crust through deep level subduction–accretion: a re-evaluation of central Greek Rhodope. *Lithos*, *46*, 69–94.
- Beck, M. E.** (1983). On the mechanism of tectonic transport in zones of oblique subduction. *Tectonophysics*, *93*, 1–11.
- Berber, F., Göncüoğlu, M. C., Sayit, K.** (2014). Geochemistry and tectonic significance of the Köseadağ metavolcanic rocks from the Sakarya Zone, northern Turkey. Proceedings of 20th CBGA Congress, Tirana, Albania. Abstract Book, v.1, pp. 161–163.
- Beyssac, O., Goffé, B., Chopin, C., Rouzaud, J. N.** (2002a). Raman spectra of carbonaceous material in metasediments: a new geothermometer. *Journal of Metamorphic Geology*, *20*, 859–871.
- Beyssac, O., Rouzaud, J. N., Goffé, B., Brunet, F., Chopin, C.** (2002b). Characterization of high-pressure, low-temperature graphitization: a Raman microspectroscopy and HRTEM study. *Contributions to Mineralogy and Petrology*, *143*, 19–31.
- Beyssac, O., Bollinger, L., Avouac, J. P., Goffe, B.** (2004). Thermal metamorphism in the Lesser Himalaya of Nepal determined from Raman spectroscopy of carbonaceous material. *Earth and Planetary Science Letters*, *225*, 233–241.
- Beyssac, O., Simoes, M., Avouac, J. P., Farley, K. A., Chen, Y.-G., Chan, Y.-C., Goffe, B.** (2007). Late Cenozoic metamorphic evolution and exhumation of Taiwan. *Tectonics*, *26*, TC6001, doi:10.1029/2006TC002064.
- Boynton, W. V.** (1984). Geochemistry of the rare earth elements: meteorite studies. In: Henderson, P. (Ed), *Rare Earth Element Geochemistry*, Elsevier, Amsterdam, pp. 63–114.

- Bozkurt, E., Holdsworth, B. K., Koçyiğit, A.** (1997). Implications of Jurassic chert identified in the Tokat Complex, northern Turkey. *Geological Magazine*, 134, 91–97.
- Boztuğ, D.** (1992). Daday-Devrekani Masifi güney kesiminin litostratigrafi birimleri ve tektoniği. *Maden Tetkik ve Arama Dergisi*, 114, 1–20.
- Boztuğ, D., Jonckheere, R. C., Heizler, M., Ratschbacher, L., Harlavan, Y., Tichomirova, M.** (2009). Timing of post-obduction granitoids from intrusion through cooling to exhumation in central Anatolia, Turkey. *Tectonophysics*, 473, 223–233.
- Brady, J. B., Markley, M. J., Schumacher, J. C., Cheney, J. T., Bianciardi, G. A.** (2004). Aragonite pseudomorphs in high-pressure marbles of Syros, Greece. *Journal of Structural Geology*, 26, 3–9.
- Brun, J. P and Faccenna, C.** (2008). Exhumation of high-pressure rocks driven by slab rollback. *Earth and Planetary Science Letters*, 272, 1–7.
- Burg, J.-P., Bodinier, J.-L., Chaudhry, S., Hussain, S., Dawood, H.** (1998). Infra-arc mantle-crust transition and intra-arc mantle diapirs in the Kohistan Complex (Pakistani Himalaya): petro-structural evidence. *Terra Nova*, 10, 74–80.
- Calvert, A. J.** (2004). Seismic reflection imaging of two megathrust shear zones in the northern Cascadia subduction zone. *Nature*, 428, 163–167.
- Carlson, R. L., Melia, P. J.** (1984). Subduction hinge migration. *Tectonophysics*, 102, 399–411.
- Cawood, P. A, Kröner, A., Collins, W. J., Kusky, T. M., Mooney, W. D., Windley, B. F.** (2009). Accretionary orogens through Earth history. In Cawood, P. A., Kröner, A. (Eds), *Earth Accretionary Systems in Space and Time*. Geological Society, London, Special Publications, 318, 1–36.
- Chemenda, A. I., Mattauer, M., Bokun, A. N.** (1996). Continental subduction and a mechanism for exhumation of high-pressure metamorphic rocks: new modelling and field data from Oman. *Earth and Planetary Science Letters*, 143, 173–182.
- Chen, F., Siebel, W., Satır, M., Terzioğlu, N., Saka, K.** (2002). Geochronology of the Karadere basement (NW Turkey) and implications for the geological evolution of the İstanbul Zone. *International Journal of Earth Sciences*, 91, 469–481.
- Chopin, C.** (1981). Talc–phengite: a widespread assemblage in high-grade pelitic blueschists of the western Alps. *Journal of Petrology*, 22, 628–650.
- Chopin, C.** (1984). Coesite and pure pyrope in high-grade blueschists of the Western Alps: a first record and some consequences. *Contribution to Mineralogy and Petrology*, 86, 107–118.
- Clift, P., and Vannucchi, P.** (2004). Controls on tectonic accretion versus erosion in subduction zones: implications for the origin and recycling of the continental crust. *Review of Geophysics*, 42, RG2001, 1–31.

- Clift, P. D., Hannigan, R., Blusztajn, J., Draut, A. E.** (2002). Geochemical evolution of the Dras–Kohistan Arc during collision with Eurasia: Evidence from the Ladakh Himalaya, India. *The Island Arc*, *11*, 255–273.
- Cloos, M.** (1982). Flow mélanges: numerical modeling and geologic constraints on their origin in the Franciscan Subduction Complex. *Geological Society of America Bulletin*, *93*, 330–345.
- Cloos, M.** (1993). Lithospheric buoyancy and collisional orogenesis: Subduction of oceanic plateaus, continental margins, island arcs, spreading ridges, and seamounts. *Geological Society of America Bulletin*, *105*, 715–737.
- Cloos, M., and Shreve, R. L.** (1988). Subduction-channel model of prism accretion, mélange formation, sediment subduction, and subduction erosion at convergent plate margins. 2: Implications and discussion. *Pure Appl. Geophys.*, *128*, 501–545.
- Coward, M. P., Butler, R. W. H., Khan, M. A., Knipe, R. J.** (1987). The tectonic history of Kohistan and its implications for Himalayan structure. *Journal of the Geological Society London*, *144*, 377–391.
- Çakır, Ü.** (2009). Structural and geochronological relationships of metamorphic soles of eastern Mediterranean ophiolites to surrounding units: indicators of intra-oceanic subduction and emplacement. *International Geology Review*, *51*, 189–215.
- Çelik, Ö. F., Delaloye, M., Feraud, G.** (2006). Precise ^{40}Ar – ^{39}Ar ages from the metamorphic sole rocks of the Tauride Belt ophiolites, southern Turkey: implications for the rapid cooling history. *Geological Magazine*, *143*, 213–227.
- Çelik, Ö. F., Marzoli, A., Marschik, R., Chiaradia, M., Neubauer, F., Öz, İ.** (2011). Early-Middle Jurassic intra-oceanic subduction in the İzmir-Ankara-Erzincan Ocean, Northern Turkey. *Tectonophysics*, *509*, 120–134.
- Dangerfield, A., Harris, R., Sarıfakıoğlu, E., Dilek, Y.** (2011). Tectonic evolution of the Ankara Mélange and associated Eldivan ophiolite near Hançili, central Turkey. In Wakabayashi, J., and Dilek, Y., (eds.), *Mélanges: Processes of Formation and Societal Significance*, Geological Society of America Special Paper, *480*, p.143–169.
- Dean, W. T., Monod, O., Rickards, R. B., Demir, O., Bultynck, P.** (2000). Lower Palaeozoic stratigraphy and palaeontology, Karadere-Zirze area, Pontus Mountains, northern Turkey. *Geological Magazine*, *137*, 555–582.
- DeBari, S. M., and Coleman, R. G.** (1989). Examination of the deep levels of an island arc: evidence from the Tonsina ultramafic-mafic assemblage, Tonsina, Alaska. *Journal of Geophysical Research*, *94*, 4373–4391.
- DeBari, S. M., and Sleep, N. H.** (1991). High-Mg, low-Al bulk composition of the Talkeetna island arc, Alaska: implications for primary magmas and the nature of arc crust. *Geological Society of America Bulletin*, *103*, 37–47.

- de Capitani, C., and Brown, T. H.** (1987). The computation of chemical equilibrium in complex systems containing non-ideal solutions. *Geochimica et Cosmochimica Acta*, *51*, 2639–2652.
- de Capitani, C., and Petrakakis, K.** (2010). The computation of equilibrium assemblage diagrams with Theriak/Domino software. *American Mineralogist*, *95*, 1006–1016.
- Desmons, J., and Beccaluva, L.** (1983). Mid-ocean ridge and island-arc affinities in ophiolites from Iran: paleogeographic implications. *Chemical Geology*, *39*, 39–63.
- Dickinson, W. R.** (2008). Accretionary Mesozoic–Cenozoic expansion of the Cordilleran continental margin in California and adjacent Oregon. *Geosphere*, *4*, 329–353.
- Diessel, C. F. K., Brothers, N. R., Black, P. M.** (1978). Coalification and graphitization in high-pressure schists in New Caledonia. *Contribution to Mineralogy and Petrology*, *68*, 63–78.
- Dilek, Y.** (2003). Ophiolite concept and its evolution, In Dilek, Y. and Newcomb, S. (Eds), *Ophiolite Concept and the Evolution of Geological Thought*. Geological Society of America Special Papers, *373*, pp. 1–16.
- Dilek, Y. and Thy, P.** (2006). Age and petrogenesis of plagiogranite intrusions in the Ankara, mélange, central Turkey. *The Island Arc*, *15*, 44–57.
- Dilek, Y., Thy, P., Hacker, B., Grundving, S.** (1999). Structure and petrology of Tauride ophiolites and mafic dike intrusions (Turkey): implications for the Neotethyan ocean. *Geological Society of America Bulletin*, *111*, 1192–1216.
- Dodson, M. H.** (1973). Closure temperature in cooling geochronological and petrological systems. *Contribution to Mineralogy and Petrology*, *40*, 259–274.
- Dunkl, I., Mikes, T., Frei, D., Gerdes, A., Eynatten, H.** (2009). PepiAGE: Data Reduction Program for Time-Resolved U/Pb Analyses. I. Dunkl, Göttingen. <http://www.sediment.unigoettingen.de/staff/dunkl/>.
- El-Shazly, A. K., and Liou, J.G.** (1991). Glaucofanite chloritoid-bearing assemblages from NE Oman: petrologic significance and a petrogenetic grid for high P metapelites. *Contribution to Mineralogy and Petrology*, *107*, 180–201.
- Ewart, A., Brothers, R. N., Mateen, A.** (1977). An outline of the geology and geochemistry, and the possible petrogenetic evolution of the volcanic rocks of the Tonga-Kermadec-New Zealand island arc. *Journal of Volcanology and Geothermal Research*, *2*, 205–250.
- Fitch, T. J.** (1972). Plate convergence, transcurrent faults, and internal deformation adjacent to Southeast Asia and the western Pacific. *Journal of Geophysical Research*, *77*, 4432–4460.
- Foster, D. A., and Gray, D. R.** (2000). Evolution and structure of the Lachlan Fold Belt (Orogen) of Eastern Australia. *Annual Reviews of Earth and Planetary Science*, *28*, 47–80.

- Fujinawa, A.** (1992). Distinctive REE patterns for tholeiitic and calc-alkaline magma series co-occurring at Adatara volcano, Northeast Japan. *Geochemical Journal*, 26, 395–409.
- Fuis, G. S., et al.** (2008). Trans-Alaska Crustal Transect and continental evolution involving subduction underplating and synchronous foreland thrusting. *Geology*, 36, 267–270.
- Galoyan, G., Rolland, Y., Sosson, M., Corsini, M., Billo, S., Verati, C., Melkonyan, R.** (2009). Geology, geochemistry and $^{40}\text{Ar}/^{39}\text{Ar}$ dating of Sevan ophiolites (Lesser Caucasus, Armenia): evidence for Jurassic back-arc opening and hot spot event between the South Armenian Block and Eurasia. *Journal of Asian Earth Sciences*, 34, 135–153.
- Gamble, J. A., Christie, R. H. K., Wright, I. C., Wysoczanski, R. J.** (1997). Primitive K-rich magmas from Clark Volcano, southern Kermadec arc: a paradox in the K- depth relationship. *The Canadian Mineralogist*, 35, 275–290.
- Ganne, J., Marquer, D., Rosenbaum, G., Bertrand, J-M., Fudral, S.** (2006). Partitioning of deformation within a subduction channel during exhumation of high-pressure rocks: a case study from the Western Alps. *Journal of Structural Geology*, 28, 1193–1207.
- Garfunkel, Z., Anderson, C. A., Schubert, G.** (1986). Mantle circulation and the lateral migration of subducted slabs. *Journal of Geophysical Research*, 91, 7205–7223.
- Genç, Ş. C., Tüysüz, O.** (2010). Tectonic setting of the Jurassic bimodal magmatism in the Sakarya Zone (Central and Western Pontides), Northern Turkey: A geochemical and isotopic approach. *Lithos*, 118, 95–111.
- Genç, Ş. C., Gülmez, F., Tüysüz, O., Karacık, Z., Roden, M. F., Billor, M. Z., Hames, W. E.** (2013). High to ultrahigh potassic alkaline volcanic belt along the Ankara-Erzincan suture (northern Turkey): new geochemical and Ar-Ar data constraining petrogenesis with implications for the late Cretaceous subduction of the Neotethys Ocean. *Geophysical Research Abstracts*, Vol. 15, EGU2013-4607.
- Genç, Ş. C., Gülmez, F., Karacık, Z., Tüysüz, O., Prelevic, D., Roden, M. F., Hames, W. E., Billor, M. Z.** (2014). Subduction-related High- to Ultrahigh-Potassic Rocks of the Ankara-Erzincan Suture Belt of Turkey: a geochemical and isotopic approach to source and petrogenesis. *Geophysical Research Abstracts*, Vol. 16, EGU2014-14565-1.
- Gill, J. B.** (1981). *Orogenic Andesites and Plate Tectonics*. Springer Verlag, Berlin.
- Göçmengil, G., Altıntaş, İ. E., Topuz, G., Çelik, Ö. F., Özkan, M.** (2013). Diverse tectonic settings of formation of the metaigneous rocks in the Jurassic metamorphic accretionary complexes (Refahiye, NE Turkey) and their geodynamic implications. *Geodinamica Acta*, DOI: 10.1080/09853111.2013.858946.
- Göncüoğlu, M. C., Gürsu, S., Tekin, U. K., Köksal, S.** (2008). New data on the evolution of the Neotethyan oceanic branches in Turkey: Late Jurassic ridge spreading in the Intra-Pontide Branch. *Ophioliti*, 33, 153–164.

- Göncüoğlu, M. C., Marroni, M., Pandolfi, L., Ellero, A., Ottria, G., Catanzariti, R., Tekin, U. K., Sayit, K.** (2014). The Arkot Dağ Mélange in Araç area, central Turkey: Evidence of its origin within the geodynamic evolution of the Intra-Pontide suture zone. *Journal of Asian Earth Sciences*, 85, 117–139.
- Görür, N.** (1988). Timing of opening of the Black Sea basin. *Tectonophysics*, 147, 247–262.
- Greene, A. R., DeBari, S. M., Kelemen, P. B., Blusztajn, J., Clift, P. D.** (2006). A Detailed Geochemical Study of Island Arc Crust: the Talkeetna Arc Section, South–Central Alaska. *Journal of Petrology*, 47, 1051–1093.
- Gülmez, F., Genç, Ş. C., Prelevic, D.** (2014). Petrology and geochemistry of late Cretaceous lamprophyric rocks from North Anatolian Ophiolitic Mélange-Turkey. *Geophysical Research Abstracts*, 16, EGU2014-14914.
- Gutscher, M.-A., Kukowski, N., Malavieille, J., Lallemand, S.** (1998). Episodic imbricate thrusting and underthrusting: analog experiments and mechanical analysis applied to the Alaskan accretionary wedge. *Journal of Geophysical Research*, 103, 10161–10176.
- Hacker, B. R.** (1990). Simulation of the metamorphic and deformational history of the metamorphic sole of the Oman ophiolite. *Journal of Geophysical Research*, 95, 4895–4907.
- Hacker, B. R., Mosenfelder, J. L., Gnos, E.** (1996). Rapid emplacement of the Oman ophiolite: thermal and geochronologic constraints. *Tectonics*, 15, 1230–1247.
- Hacker, B. R., Mehl, L., Kelemen, P. B., Rioux, M., Behn, M. D., Luffi, P.** (2008). Reconstruction of the Talkeetna intraoceanic arc of Alaska through thermobarometry. *Journal of Geophysical Research*, 113, B03204, doi:10.1029/2007JB005208.
- Harrison, T. M., Célérier, J., Aikman, A. B., Hermann, J., Heizler, M. T.** (2009). Diffusion of ⁴⁰Ar in muscovite. *Geochimica et Cosmochimica Acta*, 73, 1039–1051.
- Hässig, M., Rolland, Y., Sosson, M., Galoyan, G.** (2011). New P-T-t data on the metamorphic sole of the Amasia ophiolites and implications for the geodynamical process, NW of the Sevan-Akera suture zone, Lesser Caucasus (Armenia). *Geophysical Research Abstracts*, Vol. 13, EGU2011-7462-1.
- Hässig, M., Rolland, Y., Sosson, M., Galoyan, G., Müller, C., Avagyan, A., Sahakyan, L.** (2013a). New structural and petrological data on the Amasia ophiolites (NW Sevan–Akera suture zone, Lesser Caucasus): Insights for a large scale obduction in Armenia and NE Turkey. *Tectonophysics*, 588, 135–153.
- Hässig, M., Rolland, Y., Sosson, M., Galoyan, G., Sahakyan, L., Topuz, G., Çelik, Ö. F., Avagyan, A., Müller, C.** (2013b). Linking the NE Anatolian and Lesser Caucasus ophiolites: evidence for large-scale obduction of oceanic crust and implications for the formation of the Lesser Caucasus-Pontides Arc. *Geodinamica Acta*, 26, 311–330.

- Hawkins, J. W., Bloomer, S. H., Evans, C. A., Melchior, J. T.** (1984). Evolution of intra-oceanic arc–trench systems. *Tectonophysics*, *102*, 175–205.
- Hébert, R., Bezard, R., Guilmette, C., Dostal, J., Wang, C. S., Liu, Z. F.** (2012). The Indus–Yarlung Zangbo ophiolites from Nanga Parbat to Namche Barwa syntaxes, southern Tibet: first synthesis of petrology, geochemistry, and geochronology with incidences on geodynamic reconstructions of Neo-Tethys. *Gondwana Research*, *22*, 377–397.
- Hippolyte, J.-C., Müller, C., Kaymakçı, N., Sangu, E.** (2010). Dating of the Black Sea Basin: new nannoplankton ages from its inverted margin in the Central Pontides (Turkey). In: Sosson, M, Kaymakci, N, Stephenson, RA, Bergerat, F, Starostenko, V, (Eds). *Sedimentary Basin Tectonics from the Black Sea and Caucasus to the Arabian Platform*, Geological Society, London, Special Publications, *340*, 113–136.
- Holland, T., and Powell, R.** (1998). An internally consistent thermodynamic data set for phases of petrological interest. *Journal of Metamorphic Geology*, *16*, 309–343.
- Honegger, K., Dietrich, V., Frank, W., Gansser, A., Thöni, M., Trommsdorff, K.** (1982). Magmatism and metamorphism in the Ladakh Himalayas. *Earth and Planetary Science Letters*, *60*, 253–292.
- İlbeyli, N., Pearce, J. A., Thirlwall, M. F., Mitchell, J. G.** (2004). Petrogenesis of collision related plutonics in Central Anatolia, Turkey. *Lithos*, *72*, 163–182.
- Isozaki, Y.** (1996). Anatomy and genesis of a subduction-related orogen: A new view of geotectonic subdivision and evolution of the Japanese Islands. *The Island Arc*, *5*, 289–320.
- Itaya, T.** (1981). Carbonaceous material in pelitic schists of the Sanbagawa metamorphic belt in central Shikoku, Japan. *Lithos*, *14*, 215–224.
- Jackson, S. E., Pearson, N. J., Griffin, W. L., Belousova, E. A.** (2004). The application of laser ablation-inductively coupled plasma-mass spectrometry to in situ U–Pb zircon geochronology. *Chemical Geology*, *211*, 47–69.
- Jagoutz, O., Müntener, O., Ulmer, P., Pettke, T., Burg, J.-P., Dawood, H., Hussain, S.** (2010). Petrology and Mineral Chemistry of Lower Crustal Intrusions: the Chilas Complex, Kohistan (NW Pakistan). *Journal of Petrology*, *48*, 1895–1953.
- Jakeš, P., and Gill, J.** (1970). Rare earth elements and the island arc tholeiitic series. *Earth and Planetary Science Letters*, *9*, 17–28.
- Jamieson, R. A.** (1986). P-T paths from high temperature shear zones beneath ophiolites. *Journal of Metamorphic Geology*, *4*, 3–22.
- Jarrard, R. D.** (1986). Terrane motion by strike-slip faulting of forearc slivers. *Geology*, *14*, 780–783.
- Jolivet, L., Faccenna, C., Goffé, B., Burov, E., Agard, P.** (2003). Subduction tectonics and exhumation of high-pressure metamorphic rocks in the Mediterranean orogens. *American Journal of Science*, *303*, 353–409.

- Karig, D. E., Sharman, G. F.** (1975). Subduction and accretion in trenches. *Geological Society of America Bulletin*, 86, 377–389.
- Kaymakçı, N.** (2000). *Tectono-stratigraphical evolution of the Çankırı Basin (Central Anatolia, Turkey)*. Ph.D. Thesis, Utrecht University, The Netherlands. *Geologica Ultraiectina*, no. 190, 248 pp.
- Kimura, G., Ludden, J.** (1995). Peeling oceanic crust in subduction zones. *Geology*, 23, 217–220.
- Kimura, G., Maruyama, S., Isozaki, Y., Terabayashi, M.** (1996). Well-preserved underplating structure of the jadeitized Franciscan complex, Pacheco Pass, California. *Geology*, 24, 75–78.
- Kimura, H., Takeda, T., Obara, K., Kasahara, K.** (2010). Seismic evidence for active underplating below the megathrust earthquake zone in Japan. *Science*, 329, 210–212.
- Köksal, S., Romer, R. L., Göncüoğlu, M., Toksoy-Köksal, F.** (2004). Timing of post-collisional H-type to A-type granitic magmatism: U-Pb titanite ages from the Alpine central Anatolian granitoids (Turkey). *International Journal of Earth Sciences*, 93, 974–989.
- La Bas, M. J., Le Maitre, R. W., Streckeisen, A., Zanettin, B.** (1986). A chemical classification of volcanic rocks based on the total alkali-silica diagram. *Journal of Petrology*, 27, 745–750.
- Lallemand, S., Heuret, A., Faccenna, C., Funiciello, F.** (2008). Subduction dynamics as revealed by trench migration. *Tectonics*, 27, TC3014, doi:10.1029/2007TC002212.
- Landis, C. A.** (1971). Graphitization of dispersed carbonaceous materials in metamorphic rocks. *Contribution to Mineralogy and Petrology*, 30, 34–45.
- Leat, P. T., Larter, R. D.** (2003). Intra-oceanic subduction systems: introduction. In: Larter, R.D., Leat, P.T. (Eds), *Intra-Oceanic Subduction Systems: Tectonic and Magmatic Processes*, Geological Society London, Special Publications , 219, pp. 1–17.
- Leat, R. T., Smellie, J. L., Millar, I. L., Larter, R. D.** (2003). Magmatism in the South Sandwich arc. In: Larter, R.D., Leat, R.T. (Eds), *Intra-Oceanic Subduction Systems: Tectonic and Magmatic Processes*, Geological Society London, Special Publications, 219, pp. 285–313.
- Lefebvre, C., Meijers, M. J. M., Kaymakçı, N., Peynircioğlu, A., Langereis, C. G., van Hinsbergen, D. J. J.** (2013). Reconstructing the geometry of central Anatolia during the late Cretaceous: Large-scale Cenozoic rotations and deformation between the Pontides and Taurides. *Earth and Planetary Science Letters*, 366, 83–98.
- Malavieille, J.** (2010). Impact of erosion, sedimentation, and structural heritage on the structure and kinematics of orogenic wedges: Analog models and case studies. *GSA Today*, 20, no. 1, doi: 10.1130/GSATG48A.1.
- Malpas, J., Stevens, R. K., Strong, D. F.** (1973). Amphibolite associated with the Newfoundland ophiolite: its classification and tectonic significance. *Geology*, 1, 45–47.

- Malpas, J., Zhou, M. F., Robinson, P. T., Reynolds, P. H.** (2003). Geochemical and geochronological constraints on the origin and emplacement of the Yarlung Zangbo ophiolites, Southern Tibet. In: Dilek, Y., Robinson, P.T. (Eds.), *Ophiolites in Earth History*, Geological Society of London Special Publication, 218, pp. 191–206.
- Marroni, M., Frassi, C., Göncüoğlu, M. C., Di Vincenzo, G., Pandolfi, L., Rebay, G., Ellero, A., Ottria, G.** (2014). Late Jurassic amphibolite-facies metamorphism in the Intra-Pontide Suture Zone (Turkey): an eastward extension of the Vardar Ocean from the Balkans into Anatolia? *Journal of the Geological Society*, doi: 10.1144/jgs2013-104.
- Maruyama, S.** (1997). Pacific-type orogeny revisited: Miyashiro-type orogeny proposed. *The Island Arc*, 6, 91–120.
- McCaffrey, R.** (1992). Oblique plate convergence, slip vectors, and forearc deformation. *Journal of Geophysical Research*, 97, 8905–8915.
- McCaffrey, R.** (1996). Estimates of modern arc-parallel strain rates in fore arcs. *Geology*, 24, 27–30.
- McCall, G. J. H.** (2002). A summary of the geology of the Iranian Makran. In: Clift, P. D., Kroon, D., Gaedicke, C., Craig, J. (Eds), *The Tectonic and Climatic Evolution of the Arabian Sea Region*. Geological Society, London, Special Publications, 195, 147–204.
- Meijers, M. J. M., Vrouwe, B., van Hinsbergen, D. J. J., Kuiper, K. F., Wijbrans, J., Davies, G. R., Stephenson, R. A., Kaymakci, N., Matenco, L., Saintot, A.** (2010a). Jurassic arc volcanism on Crimea (Ukraine): Implications for the paleo-subduction zone configuration of the Black Sea region. *Lithos*, 119, 412–426.
- Meijers, M. J. M., Nuretdin, K., van Hinsbergen, D. J. J., Langereis, C. G., Stephenson, R. A., Hippolyte, J.-C.** (2010b). Late Cretaceous to Paleocene oroclinal bending in the central Pontides (Turkey). *Tectonics*, 29, TC4016, doi: 10.1029/2009TC002620.
- Miller, D. J., and Christensen, N. I.** (1994). Seismic signature and geochemistry of an island arc: A multidisciplinary study of the Kohistan accreted terrane, northern Pakistan. *Journal of Geophysical Research*, 99, 11623–11642.
- Minelli, L., and Faccenna, C.** (2010). Evolution of the Calabrian accretionary wedge (central Mediterranean), *Tectonics*, 29, TC4004, doi:10.1029/2009TC002562.
- Moghadam, H. S., Stern, R. J., Rahgoshay, M.** (2010). The Dehshir ophiolite (central Iran): geochemical constraints on the origin and evolution of the Inner Zagros ophiolite belt. *GSA Bulletin*, 122, 1516–1547.
- Moghadam, H. S., Corfu, F., Stern, R. J.** (2013). U-Pb zircon ages of Late Cretaceous Nain-Dehshir ophiolites, central Iran. *Journal of the Geological Society*, 170, 175–184.
- Monzier, M., Robin, C., Eissen, J.-P.** (1994). Kuwae (~1425 A. D.): the forgotten caldera. *Journal of Volcanology and Geothermal Research*, 59, 207–218.

- Moore, J. C., Biju-Duval, B., Bergen, J. A., Blackington, G., Claypool, G. E., Dowan, D. S., Duennebie, F., Guerra, R. T., Hemleben, C. H. J. et al.** (1982). Offscraping and underthrusting of sediment at the deformation front of the Barbados Ridge: Deep Sea Drilling Project Leg 78A. *Geological Society of America Bulletin*, 93, 1065–1077.
- Moore, J. C., Diebold, J., Fisher, M. A., Sample, J., Brocher, T., Talwani, M., Ewing, J., von Huene, R., Rowe, C., Stone, D., Stevens, C., Sawyer, D.** (1991). EDGE deep seismic reflection transect of the eastern Aleutian arc-trench layered lower crust reveals underplating and continental growth. *Geology*, 19, 420–424.
- Moore, G. F., Taira, A., Klaus, A., Becker, L., Boeckel, B., Cragg, B. A., Dean, A., Fergusson, C. L., Henry, P., Hirano, S., et al.** (2001). New insights into deformation and fluid flow processes in the Nankai Trough accretionary prism: results of Ocean Drilling Program Leg 190. *Geochem Geophys Geosy*, 2, 1058, doi:10.1029/2001GC000166.
- Morley, C. K.** (1988). Out-of-sequence thrusts. *Tectonics*, 7, 539–561.
- Münker, C., Wörner, G., Yogodzinski, G., Churikova, T.** (2004). Behaviour of high field strength elements in subduction zones: constraints from Kamchatka–Aleutian arc lavas. *Earth and Planetary Science Letters*, 224, 275–293.
- Müntener, O., Kelemen, P. B., Grove, T. L.** (2001). The role of H₂O during crystallization of primitive arc magmas under uppermost mantle conditions and genesis of igneous pyroxenites: an experimental study. *Contribution to Mineralogy and Petrology*, 141, 643–658.
- Nandedkar, R. H., Ulmer, P., Müntener, O.** (2014). Fractional crystallization of primitive, hydrous arc magmas: an experimental study at 0.7 GPa. *Contribution to Mineralogy and Petrology*, 167, DOI 10.1007/s00410-014-1015-5.
- Nemanich, R. J., and Solin, S. A.** (1979). First- and second-order Raman scattering from finite-size crystals of graphite. *Physical Review B*, 20, 392–401.
- Nikishin, A. M., Okay, A. I., Tüysüz, O., Demirer, A., Wannier, M., Amelin, N., Petrov, E.** (2015). The Black Sea basins structure and history: New model based on new deep penetration regional seismic data. Part 2: Tectonic history and paleogeography. *Marine and Petroleum Geology*, 59, 656–670.
- Nzegge, O. M., Satır, M., Siebel, W., Taubald, H.** (2006). Geochemical and isotopic constraints on the genesis of the Late Palaeozoic Deliktas, and Sivrikaya granites from the Kastamonu granitoid belt (Central Pontides, Turkey). *Neues Jahrbuch für Mineralogie*, 183, 27–40.
- Ohmori, K., Taira, A., Tokuyama, H., Sakaguchi, A., Okamura, M., Aihara, A.** (1997). Paleothermal structure of the Shimanto accretionary prism, Shikoku, Japan: role of an out-of-sequence thrust. *Geology*, 25, 327–330.
- Okay, A. I.** (1989). Tectonic units and sutures in the Pontides, Northern Turkey. In: Şengör A.M.C. (Ed.), *Tectonic evolution of the Tethyan region*. Kluwer academic publishers, pp 109–116.

- Okay, A. I.** (2000). Was the Late Triassic orogeny in Turkey caused by the collision of an oceanic plateau? In: Bozkurt, E., Winchester, J.A., Piper, J.D.A. (Eds.), *Tectonics and Magmatism in Turkey and Surrounding Area*. Geological Society of London, Special Publication, 173, 25–41.
- Okay, A. I.** (2002). Jadeite-chloritoid-glaucophane-lawsonite blueschists in northwest Turkey: unusually high P/T ratios in continental crust. *Journal of Metamorphic Geology*, 20, 757–768.
- Okay, A. I., and Monié, P.** (1997). Early Mesozoic subduction in the Eastern Mediterranean: evidence from Triassic eclogite in northwest Turkey. *Geology*, 25, 595–598.
- Okay, A. I., and Tüysüz, O.** (1999). Tethyan sutures of northern Turkey. In: Durand, B., Jolivet, L., Horvath, F., Seranne, M. (Eds), *The Mediterranean Basins: Tertiary Extension Within the Alpine Orogen*. Geological Society, London, Special Publication, 156, 475–515.
- Okay, A. I., and Satır, M.** (2000). Upper Cretaceous Eclogite-Facies Metamorphic Rocks from the Biga Peninsula, Northwest Turkey. *Turkish Journal of Earth Sciences*, 9, 47–56.
- Okay, A. I., and Göncüoğlu, M. C.** (2004). Karakaya Complex: A review of data and concepts. *Turkish Journal of Earth Sciences*, 13, 77–95.
- Okay, A. I., and Whitney, D. L.** (2010). Blueschists, eclogites, ophiolites and suture zones in northwest Turkey: a review and a field excursion guide. *Ophioliti*, 35, 131–172.
- Okay, A.I., and Nikishin, A.M.** (2015). Tectonic evolution of the southern margin of Laurasia in the Black Sea region. *Int Geol Rev*, doi: <http://dx.doi.org/10.1080/00206814.2015.1010609>.
- Okay, A. I., Şengör, A. M. C., Görür, N.** (1994). Kinematic history of the opening of the Black Sea and its effect on the surrounding regions. *Geology*, 22, 267–270.
- Okay, A. I., Monod, O., Monie, P.** (2002). Triassic blueschists and eclogites from northwest Turkey: vestiges of the Paleo-Tethyan Subduction. *Lithos*, 64, 155–178.
- Okay, A. I., Satır, M., Maluski, H., Siyako, M., Monie, P., Metzger, R., Akyüz, S.** (1996). Palaeo- and Neo-Tethyan events in northwest Turkey. In: Yin, E., Harrison, M. (Eds.) *Tectonics of Asia*. Cambridge University Press, pp. 420–441.
- Okay, A. I., Tüysüz, O., Satır, M., Özkan-Altner, S., Altner, D., Sherlock, S., Eren, R. H.** (2006a). Cretaceous and Triassic subduction-accretion, HP/LT metamorphism and continental growth in the Central Pontides, Turkey. *Geological Society of America Bulletin*, 118, 1247–1269.
- Okay, A. I., Satır, M., Siebel, W.** (2006b). Pre-Alpide Palaeozoic and Mesozoic orogenic events in the Eastern Mediterranean region. In: Gee, D.G., Stephenson, R.A. (Eds), *European Lithosphere Dynamics*. Geological Society, London, Memoirs, 32, 389–405.
- Okay, A. I., Sunal, G., Sherlock, S., Altner, D., Tüysüz, O., Kylander-Clark, A. R. C., Aygül, M.** (2013). Early Cretaceous sedimentation and orogeny

on the active margin of Eurasia: Southern Central Pontides, Turkey. *Tectonics*, 32, 1247–1271.

- Okay, A. I., Sunal, G., Tüysüz, O., Sherlock, S., Keskin, M., Kylander-Clark, A. R. C.** (2014). Low-pressure–high-temperature metamorphism during extension in a Jurassic magmatic arc, Central Pontides, Turkey. *Journal of Metamorphic Geology*, 32, 49–69.
- Okay, A. I., Altıner, D., Kılıç, A. M.** (2015). Triassic limestone, turbidites and serpentinite—the Cimmeride orogeny in the Central Pontides. *Geological Magazine*, doi:10.1017/S0016756814000429.
- Otsuki, M., and Banno, S.** (1990). Prograde and retrograde metamorphism of hematite-bearing basic schists in the Sanbagawa belt in central Shikoku. *Journal of Metamorphic Geology*, 8, 425–439.
- Önen, A. P.** (2003). Neotethyan ophiolitic rocks of the Anatolides of NW Turkey and comparison with Tauride ophiolites. *Journal of the Geological Society*, 160, 947–962.
- Önen, A. P., and Hall, R.** (2000). Sub-ophiolite metamorphic rocks from NW Anatolia, Turkey. *Journal of Metamorphic Geology*, 18, 483–495.
- Özcan, E., Less, G., Kertesz, B.** (2007). Late Ypresian to middle Lutetian Orthophragminid record from central and northern Turkey: Taxonomy and remarks on zonal scheme. *Turkish Journal of Earth Sciences*, 16, 281–318.
- Özgül, N.** (2012). Stratigraphy and some structural features of the İstanbul Palaeozoic. *Turkish Journal of Earth Sciences*, 21, 817–866.
- Parlak, O., and Delaloye, M.** (1999). Precise $^{40}\text{Ar}/^{39}\text{Ar}$ ages from the metamorphic sole of the Mersin ophiolite (Southern Turkey). *Tectonophysics*, 301, 145–58.
- Pasteris, J. D.** (1989). In situ analysis in geological thin-sections by Laser Raman microprobe microspectroscopy: a cautionary note. *Applied Spectroscopy*, 43, 567–570.
- Peacock, S. M.** (1992). Blueschist-facies metamorphism, shear heating, and P-T-t paths in subduction shear zones. *Journal of Geophysical Research*, 97, 17693–17707.
- Peacock, S. M.** (1996). Thermal and petrologic structure of subduction zones. In: Bebout, G.E., Scholl, D.W., Kirby, S.H., Platt, J. P. (Eds), *Subduction Top to Bottom*. American Geophysical Union, Washington, D. C.. doi: 10.1029/GM096p0119.
- Pearce, J. A.** (2003). Subduction zone ophiolites: the search for modern analogues, In Dilek, Y. and Newcomb, S. (Eds), *Ophiolite Concept and the Evolution of Geological Thought*. Geological Society of America, Special Papers, 373, pp. 269–293.
- Pearce, J. A., and Peate, D. W.** (1995). Tectonic implications of the composition of volcanic arc magmas. *Annual Review of Earth and Planetary Sciences*, 23, 251–285.

- Pearce, J. A., Baker, P. E., Harvey, P. K., Luff, I. W.** (1995). Geochemical evidence for subduction fluxes, mantle melting and fractional crystallization beneath the South Sandwich island arc. *Journal of Petrology*, *36*, 1073-1109.
- Petterson, M. G.** (2010). A Review of the geology and tectonics of the Kohistan island arc, north Pakistan. In: Kusky, T. M., Zhai, M.-G., Xiao, W. (Eds), *The Evolving Continents: Understanding Processes of Continental Growth*. Geological Society London, Special Publications, *338*, pp. 287–327.
- Pickett, E. A., and Robertson, A. H. F.** (2004). Significance of the volcanogenic Nilüfer Unit and related components of the Triassic Karakaya Complex for Tethyan subduction/accretion processes in NW Turkey. *Turkish Journal of Earth Sciences*, *13*, 97–144.
- Platt, J. P.** (1986). Dynamics of orogenic wedges and the uplift of high-pressure metamorphic rocks. *Geological Society of America Bulletin*, *97*, 1037–1053.
- Platt, J. P.** (1993). Exhumation of high-pressure rocks: a review of concepts and processes. *Terra Nova*, *5*, 119–133.
- Platt, J. P., Leggett, J. K., Young, J., Raza, H., Alam, S.** (1985). Large scale sediment underplating in the Makran accretionary prism, southwest Pakistan. *Geology*, *13*, 507–511.
- Plunder, A., Agard, P., Chopin, C., Okay, A. I.** (2013). Geodynamics of the Tavşanlı zone, western Turkey: Insights into subduction/obduction processes. *Tectonophysics*, *608*, 884–903.
- Pourteau, A., Candan, O., Oberhänsli, R.** (2010). High-Pressure metasediments in central Turkey: constraints on the Neotethyan closure history. *Tectonics*, *29*, TC5004.
- Pourteau, A., Sudo, M., Candan, O., Lanari, P., Vidal, O., Oberhänsli, R.** (2013). Neotethys closure history of Anatolia: insights from ^{40}Ar – ^{39}Ar geochronology and P–T estimation in high-pressure metasedimentary rocks. *Journal of Metamorphic Geology*, *31*, 585–606.
- Powell, R., and Holland, T.** (1988). An internally consistent thermodynamic dataset with uncertainties and correlations : 3. Application methods, worked examples and a computer program. *Journal of Metamorphic Geology*, *6*, 173–204.
- Proyer, A.** (2003). Metamorphism of pelites in NKFMAASH - a new petrogenetic grid with implications for the preservation of high-pressure mineral assemblages during exhumation. *Journal of Metamorphic Geology*, *21*, 493–509.
- Radhakrishna, T., Divakara Rao, V., Murali, A. V.** (1984). Geochemistry of Dras volcanics and the evolution of the Indus suture ophiolites. *Tectonophysics*, *108*, 135-153.
- Rahl, J. M., Anderson, K. M., Brandon, M. T., Fassoulas, C.** (2005). Raman spectroscopic carbonaceous material thermometry of low-grade

metamorphic rocks: calibration and application to tectonic exhumation in Crete, Greece. *Earth and Planetary Science Letters*, 240, 339–354.

- Rice, S. P., Robertson, A. H. F., Ustaömer, T.** (2006). Late Cretaceous–early Ceneozoic tectonic evolution of the Eurasian active margin in the Central and Eastern Pontides, northern Turkey. In: Robertson, A. H. F., Mountrakis, D. (Eds.), *Tectonic development of the Eastern Mediterranean region*. Geological Society, London, Special Publications, 260, 413–445.
- Rice, S. P., Robertson, A. H. F., Ustaömer, T., İnan, N., Tash, K.** (2009). Late Cretaceous–Early Eocene tectonic development of the Tethyan suture zone in the Erzincan area, Eastern Pontides, Turkey. *Geological Magazine*, 146, 567–590.
- Robertson, A. H. F.** (2002). Overview of the genesis and emplacement of Mesozoic ophiolites in the Eastern Mediterranean Tethyan region. *Lithos*, 65, 1–67.
- Robertson, A. H. F., and Ustaömer, T.** (2004). Tectonic evolution of the Intra-Pontide suture zone in the Armutlu Peninsula NW Turkey. *Tectonophysics*, 381, 175–209.
- Robertson, A. H. F., Parlak, O., Ustaömer, T., Tash, K., İnan, N., Dumitrica, P., Karaođlan, F.** (2013). Subduction, ophiolite genesis and collision history of Tethys adjacent to the Eurasian continental margin: new evidence from the Eastern Pontides, Turkey. *Geodinamica Acta*, 26, 230–293, DOI: 10.1080/09853111.2013.877240.
- Robin, C., Eissen, J.-R., Monzler, M.** (1993). Giant tuff cone and 12-km-wide associated caldera at Ambrym Volcano (Vanuatu, New Hebrides Arc). *Journal of Volcanology and Geothermal Research*, 55, 225–238.
- Rojay, B.** (2013). Tectonic evolution of the Cretaceous Ankara Ophiolitic Mélange during the Late Cretaceous to pre-Miocene interval in Central Anatolia, Turkey. *Journal of Geodynamics*, 65, 66–81.
- Rolland, Y., Billo, S., Corsini, M., Sosson, M., Galoyan, G.** (2009). Blueschists of the Amassia–Stepanavan Suture Zone (Armenia): linking Tethys subduction history from E-Turkey to W-Iran. *International Journal of Earth Science*, 98, 533–550.
- Rolland, Y., Galoyan, G., Sosson, M., Melkonyan, R., Avagyan, A.** (2010). The Armenian ophiolites: insights for Jurassic Back-arc formation, lower Cretaceous hot-spot magmatism and upper Cretaceous obduction over the South Armenian Block. In: Sosson, M., Kaymakci, N., Stephanson, R.A., Bergarat, F., Starostenko, V. (Eds.), *Sedimentary Basin Tectonics from the Black Sea and Caucasus to the Arabian Platform*, Geological Society of London Special Publication, 340, 353–382.
- Rolland, Y., Perinçek, D., Kaymakci, N., Sosson, M., Barrier, E., Avagyan, A.** (2012). Evidence for ~80–75 Ma subduction jump during Anatolide–Tauride–Armenian block accretion and ~48 Ma Arabia–Eurasia collision in Lesser Caucasus–East Anatolia. *Journal of Geodynamics*, 56, 76–85.

- Rudnick, R. L.** (1995). Making continental crust. *Nature*, 378, 571–578.
- Sadezky, A., Muckenhuber, H., Grothe, H., Niessner, R., Pöschl, U.** (2005). Raman microspectroscopy of soot and related carbonaceous materials: spectral analysis and structural information. *Carbon*, 43, 1731–1742.
- Sample, J. C., and Fisher, D. M.** (1986). Duplex accretion and underplating in an ancient accretionary complex, Kodiak Islands, Alaska. *Geology*, 14, 160–163.
- Sarifakioglu, E., Dilek, Y., Sevin, M.** (2014). Jurassic–Paleogene intraoceanic magmatic evolution of the Ankara Mélange, north-central Anatolia, Turkey. *Solid Earth*, 5, 77–108.
- Schaltegger, U., Zeilinger, G., Frank, M., Burg, J. P.** (2002). Multiple mantle sources during island arc magmatism: U–Pb and Hf isotopic evidence from the Kohistan arc complex, Pakistan. *Terra Nova*, 14, 461–468.
- Scharf, A., Handy, M. R., Ziemann, M. A., Schmid, S. M.** (2013). Peak-temperature patterns of polyphase metamorphism resulting from accretion, subduction and collision (eastern Tauern Window, European Alps) – a study with Raman microspectroscopy on carbonaceous material (RSCM). *Journal of Metamorphic Geology*, 31, 863–880.
- Schellart, W. P.** (2008). Subduction zone trench migration: Slab driven or overriding-plate-driven? *Physics of the Earth and Planetary Interiors*, 170, 73–88.
- Schumacher, J. C.** (1997). The estimation of the proportion of ferric iron in the electron-microprobe analysis of amphiboles. *The Canadian Mineralogist*, 35, 238–246.
- Searle, M., and Cox, J.** (1999). Tectonic setting, origin and obduction of the Oman ophiolite. *Geological Society of America Bulletin*, 111, 104–122.
- Searle, M., Corfield, R. I., Stephenson, B., McCarron, J.** (1997). Structure of the North Indian continental margin in the Ladakh–Zaskar Himalayas: implications for the timing of obduction of the Spontang ophiolite, India–Asia collision and deformation events in the Himalaya. *Geological Magazine*, 134, 297–316.
- Seaton, N. C. A., Whitney, D. L., Teyssier, C., Toraman, E., Heizler, M. T.** (2009). Recrystallization of high-pressure marble (Sivrihisar, Turkey). *Tectonophysics*, 479, 241–253.
- Sedlock, R. L.** (1999). Evaluation of exhumation mechanisms for coherent blueschists in western Baja California, Mexico. In: Ring, U., Brandon, M. T., Lister, G. S., Willett, S. D. (Eds) *Exhumation Processes: Normal Faulting, Ductile Flow and Erosion*. Geological Society, London, Special Publications, 154, 29–54.
- Seely, D. R., Vail, P. R., Walton, G. G.** (1974). Trench slope model. In: Burk, C.A., Drake, C.L. (Eds.), *The Geology of the Continental Margins*. Springer, New York, pp. 249–260.
- Sherlock, S., Kelley, S. P., Inger, S., Harris, N., Okay, A. I.** (1999). ^{40}Ar – ^{39}Ar and Rb–Sr geochronology of high-pressure metamorphism and exhumation

history of the Tavsanli Zone, NW Turkey. *Contributions to Mineralogy and Petrology*, 137, 46–58.

- Smith, I. E. M., Worthington, T. J., Stewart, R. B., Price, R. C., Gamble, J. A.** (2003). Felsic volcanism in the Kermadec arc, SW Pacific: crustal recycling in an oceanic setting. In: Larter, R.D., Leat, P.T. (Eds), *Intra-Oceanic Subduction Systems: Tectonic and Magmatic Processes*, Geological Society London, Special Publications, 219, pp. 99–118.
- Sosson, M., Rolland, Y., Müller, C., Danelian, T., Melkonyan, R., Kekelia, S., Adamia, S., Babazadeh, V., Kangarli, T., Avagyan, A., Galoyan, G., Mosar, J.** (2010). Subductions, obduction and collision in the Lesser Caucasus (Armenia Azerbaijan, Georgia), new insights. In: Sosson, M., Kaymakci, N., Stephanson, R., Bergarat, F., Starostenko, V. (Eds.), *Sedimentary Basin Tectonics from the Black Sea and Caucasus to the Arabian Platform*, Geological Society of London Special Publication, 340, 329–352.
- Spaggiari, C. V., Gray, D. R., Foster, D. A.** (2002). Blueschist metamorphism during accretion in the Lachlan Orogen, south-eastern Australia. *Journal of Metamorphic Geology*, 20, 711–726.
- Spray, J. G.** (1984). Possible causes and consequences of upper mantle decoupling and ophiolite displacement. In: Gass, I.G., Lippard, S.J., Shelton, A.W. (Eds.), *Ophiolites and oceanic lithosphere*, Geological Society London, Special Publication, 13, pp. 255–268.
- Stern, R. J.** (2010). The anatomy and ontogeny of modern intra-oceanic arc systems. In: Kusky, T.M., Zhai, M.-G., Xiao, W. (Eds), *The Evolving Continents: Understanding Processes of Continental Growth*, Geological Society, London, Special Publications, 338, pp. 7–34.
- Stern, R. J., Fouch, M. J., Klemperer, S. L.** (2003). An overview of the Izu-Bonin-Mariana subduction factory. In: Eiler, J. (Ed.), *Inside the Subduction Factory*, American Geophysical Union, Geophysical Monograph, 138, pp. 175–222.
- Stipp, M., Stünitz, H., Heilbronner, R., Schmid, S. M.** (2002). The eastern Tonale fault zone: a ‘natural laboratory’ for crystal plastic deformation of quartz over a temperature range from 250 to 700 °C. *Journal of Structural Geology*, 24, 1861–1884.
- Straub, S. M.** (1995). Contrasting compositions of Mariana Trough fallout tephra and Mariana Island arc volcanics: a fractional crystallization link. *Bulletin of Volcanology*, 57, 403–421.
- Sun, S. S., and McDonough, W. F.** (1989). Chemical and isotopic systematics of oceanic basalts: Implications for mantle composition and processes. In: Saunders, A.D., Norry, M.J. (Eds), *Magmatism in Ocean Basins*, Geological Society, London, Special Publication, 42, pp. 313–345.
- Sunal, G.** (2012). Devonian magmatism in the western Sakarya Zone, Karacabey region, NW Turkey. *Geodinamica Acta*, 25, 183–201.

- Şengün, F., Davis, P. B., Tunç, İ. O., Yiğitbaş, E.** (2012). Petrology and geochemistry of eclogites from the Biga Peninsula, Northwest Turkey, *Geodinamica Acta*, 25, 248–266.
- Şengör, A. M. C., Natal'in, B. A., Burtman, V. S.** (1993). Evolution of the Altaid tectonic collage and Palaeozoic crustal growth in Eurasia. *Nature*, 364, 299–307.
- Şengör, A. M. C., and Natal'in, B. A.** (1996). Turkic-Type Orogeny and its role in the making of the continental crust. *Annual Review of Earth and Planetary Sciences*, 24, 263–337.
- Takahashi, N., Kodaira, S., Klemperer, S. L., Tatsumi, Y., Kaneda, Y., Suyehiro, K.** (2007). Crustal structure and evolution of the Mariana intra-oceanic island arc. *Geology*, 35, 203–206.
- Takasu, A., Wallis, S. R., Banno, S., Dallmeyer, R. D.** (1994). Evolution of the Sambagawa metamorphic belt, Japan. *Lithos*, 33, 119–133.
- Tamura, Y., and Tatsumi, Y.** (2002). Remelting of an Andesitic Crust as a Possible Origin for Rhyolitic Magma in Oceanic Arcs: an Example from the Izu–Bonin Arc. *Journal of Petrology*, 43, 1029–1047.
- Tatsumi, Y., Hamilton, D., Nesbitt, R. W.** (1986). Chemical characteristics of fluid phase released from a subducted lithosphere and origin of arc magmas: Evidence from high-pressure experiments and natural rocks. *Journal of Volcanology and Geothermal Research*, 29, 293–309.
- Taylor, S. R.** (1967). The origin and growth of continents. *Tectonophysics*, 4, 17–34.
- Thuizat, R., Whitechurch, H., Montigny, R., Juteau, T.** (1981). K–Ar dating of some intra-ophiolitic metamorphic soles from the East Mediterranean: new evidence for oceanic thrusting before obduction. *Earth and Planetary Science Letters*, 52, 302–310.
- Tilton, G. R., Hopson, C. A., Wright, J. E.** (1981). Uranium-lead isotopic ages of the Samail ophiolite, Oman, with applications to Tethyan Ocean ridge tectonics. *Journal of Geophysical Research*, 86, 2763–2775.
- Tissot, B. P., and Welte, D. H.** (1978). Petroleum Formation and Occurrence. A New Approach to Oil and Gas Exploration. Springer-Verlag, Berlin.
- Topuz, G., Altherr, R., Kalt, A., Satır, M., Werner, O., Schwartz, W. H.** (2004). Aluminous granulites from the Pular Complex, NE Turkey: a case of partial melting, efficient melt extraction and crystallisation. *Lithos*, 72, 183–207.
- Topuz, G., Altherr, R., Schwartz, W. H., Dokuz, A., Meyer, H-P.** (2007). Variscan amphibolites-facies rocks from the Kurtoğlu metamorphic complex (Gümüşhane area, Eastern Pontides, Turkey). *International Journal of Earth Sciences*, 96, 861–873.
- Topuz, G., Okay, A. I., Altherr, R., Satır, M., Schwarz, W. H.** (2008). Late Cretaceous blueschist facies metamorphism in southern Thrace (Turkey) and its geodynamic implications. *Journal of Metamorphic Geology*, 26, 895–913.

- Topuz, G., Göçmengil, G., Rolland, Y., Çelik, Ö. F., Zack, T., Schmitt, A. K.** (2013a). Jurassic accretionary complex and ophiolite from northeast Turkey: No evidence for the Cimmerian continental ribbon. *Geology*, *41*, 255–258.
- Topuz G., Çelik Ö. F., Şengör A. M. C., Altıntaş İ. E., Zack T., Rolland Y., Barth M.** (2013b). Jurassic ophiolite formation and emplacement as backstop to a subduction-accretion complex in northeast Turkey, the Refahiye ophiolite, and relation to the Balkan ophiolites. *American Journal of Science*, *313*, 1054–1087.
- Topuz, G., Okay, A. I., Altherr, R., Schwarz, W. H., Sunal, G., Altinkaynak, L.** (2014). Triassic warm subduction in northeast Turkey: Evidence from the Ağvanis metamorphic rocks. *The Island Arc*, DOI: 10.1111/iar.12068.
- Tsujimori, T., Matsumoto, K., Wakabayashi, J., Liou, J. G.** (2006a). Franciscan eclogite revisited: Reevaluation of the P–T evolution of tectonic blocks from Tiburon Peninsula, California, U.S.A. *Mineralogy and Petrology*, *88*, 243–267.
- Tsujimori, T., Sisson, V. B., Liou, J. G., Harlow, G. E., Sorensen, S. S.** (2006b). Very-low temperature record of the subduction process: a review of worldwide lawsonite eclogites. *Lithos*, *92*, 609–624.
- Tuinstra, F., and Koenig, J. L.** (1970). Raman spectrum of graphite. *Journal of Chemical Physics*, *53*, 1126–1130.
- Tüysüz, O.** (1990). Tectonic evolution of a part of the Tethyside orogenic collage: The Kargı Massif, northern Turkey. *Tectonics*, *9*, 141–160.
- Tüysüz, O.** (1993). A geotraverse from the Black Sea to the Central Anatolia: Tectonic evolution of the northern Neo-Tethys. *Türkiye Petrol Jeologları Derneği Bülteni*, *5*, 1–33.
- Tüysüz, O.** (1999). Geology of the Cretaceous sedimentary basins of the Western Pontides. *Geological Journal*, *34*, 75–93.
- Tüysüz, O., and Tekin, U. K.** (2007). Timing of imbrication of an active continental margin facing the northern branch of Neotethys, Kargı Massif, northern Turkey. *Cretaceous Research*, *28*, 754–764.
- Tüysüz, O., Dellaloğlu, A. A., Terzioğlu, N.** (1995). A magmatic belt within the Neo-Tethyan suture zone and its role in the tectonic evolution of northern Turkey. *Tectonophysics*, *243*, 173–191.
- Uğuz, M. F., Sevin, M., Duru, M.** (2002). *Geological Map of Turkey. 1: 500.000 scaled Sinop sheet*. Maden Tetkik ve Arama Genel Müdürlüğü, Ankara.
- Ujje, K.** (1997). Off-scraping accretionary process under the subduction of young oceanic crust: The Shimanto Belt of Okinawa Island, Ryukyu Arc. *Tectonics*, *16*, 305–322.
- Ustaömer, P. A., and Rogers, G.** (1999). The Bolu Massif: remnant of a pre-Early Ordovician active margin in the west Pontides, northern Turkey. *Geological Magazine*, *136*, 579–592.

- Ustaömer, P. A., Mundil, R., Renne, P. R.** (2005). U/Pb and Pb/Pb zircon ages for arc-related intrusions of the Bolu Massif (W Pontides, NW Turkey): evidence for Late Precambrian (Cadomian) age. *Terra Nova*, *17*, 215–223.
- Ustaömer, T., and Robertson A. H. F.** (1993). A Late Paleozoic-Early Mesozoic marginal basin along the active southern continental margin of Eurasia: Evidence from the Central Pontides (Turkey) and adjacent regions. *Geological Journal*, *28*, 219–238.
- Ustaömer, T., and Robertson A. H. F.** (1994). Late Paleozoic marginal basin and subduction-accretion: the Paleotethyan Küre Complex, Central Pontides, northern Turkey. *Journal of the Geological Society*, *151*, 291–305.
- Ustaömer, T., and Robertson, A. H. F.** (1997). Tectonic-sedimentary evolution of the North-Tethyan margin in the Central Pontides of northern Turkey, In: Robinson, A.G., (Ed.), *Regional and Petroleum Geology of the Black Sea and Surrounding Region*. American Association of Petroleum Geologists, Memoir 68, pp. 255–290.
- Ustaömer, T., and Robertson, A. H. F.** (1999). Geochemical evidence used to test alternative plate tectonic models for pre-Upper Jurassic (Palaeotethyan) units in the Central Pontides, N Turkey. *Geological Journal*, *34*, 25–53.
- Uyeda, S., and Kanamori, H.** (1979). Back-arc opening and the mode of subduction. *Journal of Geophysical Research*, *84*, 1049–1061.
- van den Beukel, J., and Wortel, R.** (1987). Temperatures and shear stresses in the upper part of a subduction zone. *Geophysical Research Letters*, *14*, 1057–1060.
- van der Voo, R., Spakman, W., Bijwaard, H.** (1999). Tethyan subducted slabs under India. *Earth and Planetary Science Letters*, *171*, 7–20.
- Villa, I. M.** (1998). Isotopic closure. *Terra Nova*, *10*, 42–47.
- Wada, I., and Wang, K.** (2009). Common depth of slab-mantle decoupling: Reconciling diversity and uniformity of subduction zones. *Geochem., Geophys., Geosyst.*, *10*, Q10009, doi:10.1029/2009GC002570.
- Wada, I., Wang, K., He, J., Hyndman, R. D.** (2008). Weakening of the subduction interface and its effects on surface heat flow, slab dehydration, and mantle wedge serpentinization. *Journal of Geophysical Research*, *113*, B04402, doi:10.1029/2007JB005190.
- Wakabayashi, J., and Dilek, Y.** (2000). Spatial and temporal relationships between ophiolites and their metamorphic soles: A test of models of forearc ophiolite genesis. In: Dilek, Y., Moores, E.M., Elthon, D., Nicolas, A. (Eds.), *Ophiolites and Oceanic Crust: New Insights from Field Studies and Ocean Drilling Program*, Geological Society of America, Special Paper, *349*, pp. 53–64.
- Wallis, S., Platt, J., Knott, S.** (1993). Recognition of syn-convergence extension in accretionary wedges with examples from the Calabrian Arc and the Eastern Alps. *American Journal of Science*, *293*, 463–494.

- Warren, C. J., Parrish, R. R., Searle, M. P., Waters, D. J.** (2003). Dating the subduction of the Arabian continental margin beneath the Semail ophiolite, Oman. *Geology*, *31*, 889-892.
- Warren, C. J., Parrish, R. R., Waters, D. J., Searle, M. P.** (2005). Dating the geologic history of Oman's Semail ophiolite: insights from U-Pb geochronology. *Contribution to Mineralogy and Petrology*, *150*, 403–422.
- Whitney, D. L., and Hamilton, M. A.** (2004). Timing of high-grade metamorphism in central Turkey and the assembly of Anatolia. *Journal of the Geological Society London*, *161*, 823–828.
- Whitney, D. L., and Davis, P. B.** (2006). Why is lawsonite eclogite so rare? Metamorphism and preservation of lawsonite eclogite, Sivrihisar, Turkey. *Geology*, *34*, 473–476.
- Whitney, D. L., Teyssier, C., Fayon, A. K., Hamilton, M. A., Heizler, M. J.** (2003). Tectonic controls on metamorphism, partial melting, and intrusion: Timing of regional metamorphism and magmatism of the Niğde Massif, Turkey. *Tectonophysics*, *376*, 37-60.
- Whitney, D. L., Teyssier, C., Seaton, N. C. A., Fornash, K. F.** (2014). Petrofabrics of high-pressure rocks exhumed at the slab-mantle interface from the “point of no return” in a subduction zone (Sivrihisar, Turkey). *Tectonics*, *33*, 2315–2341, doi:10.1002/2014TC003677.
- Williams, H., and Smyth, W. R.** (1973). Metamorphic aureoles beneath ophiolite suites and Alpine periodotites: tectonic implications with west Newfoundland example. *American Journal of Science*, *273*, 594–621.
- Winter, J. D.** (2001). *An Introduction to Igneous and Metamorphic Petrology*. Prentice-Hall Inc., New Jersey.
- Wopenka, B., Pasteris, J. D.** (1993). Structural characterization of kerogens to granulite-facies graphite: applicability of Raman microprobe spectroscopy. *American Mineralogist*, *78*, 533–557.
- Worthington, T. J., Gregory, M. R., Bondarenko, V.** (1999). The Denham Caldera on Raoul Volcano: dacitic volcanism in the Tonga–Kermadec arc. *Journal of Volcanology and Geothermal Research*, *90*, 29–48.
- Yalınz, M. K., Floyd, P. A., Göncüoğlu, M. C.** (1996). Supra-subduction zone ophiolites of Central Anatolia: geochemical evidence from the Sarıkaraman Ophiolite, Aksaray, Turkey. *Mineralogical Magazine*, *60*, 697–710.
- Yalınz, M. K., Göncüoğlu, M. C., Özkan-Altın, S.** (2000a). Formation and emplacement ages of the SSZ-type Neotethyan ophiolites in Central Anatolia, Turkey: palaeotectonic implications. *Geological Journal*, *35*, 53–68.
- Yalınz, M. K., Floyd, P. A., Göncüoğlu, M. C.** (2000b). Geochemistry of volcanic rocks from the Çiçekdağ Ophiolite, Central Anatolia, Turkey, and their inferred tectonic setting within the northern branch of the Neotethyan Ocean. In: Bozkurt, E., Winchester, J.A., and Piper, J.D.A. (Eds), *Tectonics and Magmatism in Turkey and the*

Surrounding Area, Geological Society Special Publication, 173, 203–218.

- Yamamoto, H., and Nakamura, E.** (1996). Sm–Nd dating of garnet granulites from the Kohistan Complex, northern Pakistan. *Journal of the Geological Society*, 153, 965–969.
- Ye, S., Flueh, E. R., Klaeschen, D., von Huene, R.** (1997). Crustal structure along the EDGE transect beneath the Kodiak shelf off Alaska derived from OBH seismic refraction data. *Geophysical Journal International*, 130, 283–302.
- Yılmaz, O., and Boztuğ, D.** (1986). Kastamonu granitoid belt of northern Turkey: First arc plutonism product related to the subduction of the Paleo-Tethys. *Geology*, 14, 179–183.
- Yılmaz, Y., and Şengör, A. M. C.** (1985). Paleo-Tethyan ophiolites in northern Turkey; petrology and tectonic setting. In: Desmons, J. (Ed.), *Ophiolites Through Times*, Conf. Proceed, 10, (2-3), pp. 485–504.
- Yılmaz, Y., Tüysüz, O., Yiğitbaş, E., Genç, Ş. C., Şengör, A. M. C.** (1997a). Geology and tectonic evolution of the Pontides. In: Robinson, A.G. (Ed), *Regional and Petroleum Geology of the Black Sea and Surrounding Region*, American Association of Petroleum Geologists, Memoir, 68, 183–226.
- Yılmaz, Y., Serdar, H. S., Genç, C., Yigitbaş, E., Gürer, Ö. F., Elmas, A., Yıldırım, M., Bozcu, M., Gürpınar, O.** (1997b). The Geology and Evolution of the Tokat Massif, South-Central Pontides, Turkey. *International Geology Review*, 39, 365–382.
- Yiğitbaş, E., Tüysüz, O., Serdar, H. S.** (1990). The geological characteristics of the Late Cretaceous active margin in the Central Pontides. Proceedings of 8th Petroleum Congress of Turkey, p. 141–151.
- Yiğitbaş, E., Kerrich, R., Yılmaz, Y., Elmas, A., Xie, Q.** (2004). Characteristics and geochemistry of Precambrian ophiolites and related volcanics from the İstanbul–Zonguldak Unit, Northwestern Anatolia, Turkey: following the missing chain of the Precambrian South European suture zone to the east. *Precambrian Research*, 132, 179–206.
- You, C.-F., Castillo, P. R., Gieskes, J. M., Chan, L. H., Spivack, A. J.** (1996). Trace element behavior in hydrothermal experiments: Implications for fluid processes at shallow depths in subduction zones. *Earth and Planetary Science Letters*, 140, 41–52.
- Yui, T.-F., Huang, E., Xu, J.** (1996). Raman spectrum of carbonaceous material: a possible metamorphic grade indicator for low-grade metamorphic rocks. *Journal of Metamorphic Geology*, 14, 115–124.
- Zack, T., Rivers, T., Brumm, R., Kronz, A.** (2004). Cold subduction of oceanic crust: implications from a lawsonite eclogite from the Dominican Republic. *European Journal of Mineralogy*, 16, 909–916.
- Zheng, Y.-F., Gao, T.-S., Wu, Y.-B., Gong, B., Liu, X. M.** (2007). Fluid flow during exhumation of deeply subducted continental crust: zircon U-Pb

age and O-isotope studies of a quartz vein within ultrahigh-pressure eclogite. *Journal of Metamorphic Geology*, 25, 267–283.

APPENDICES

APPENDIX A: Geological maps and cross sections.

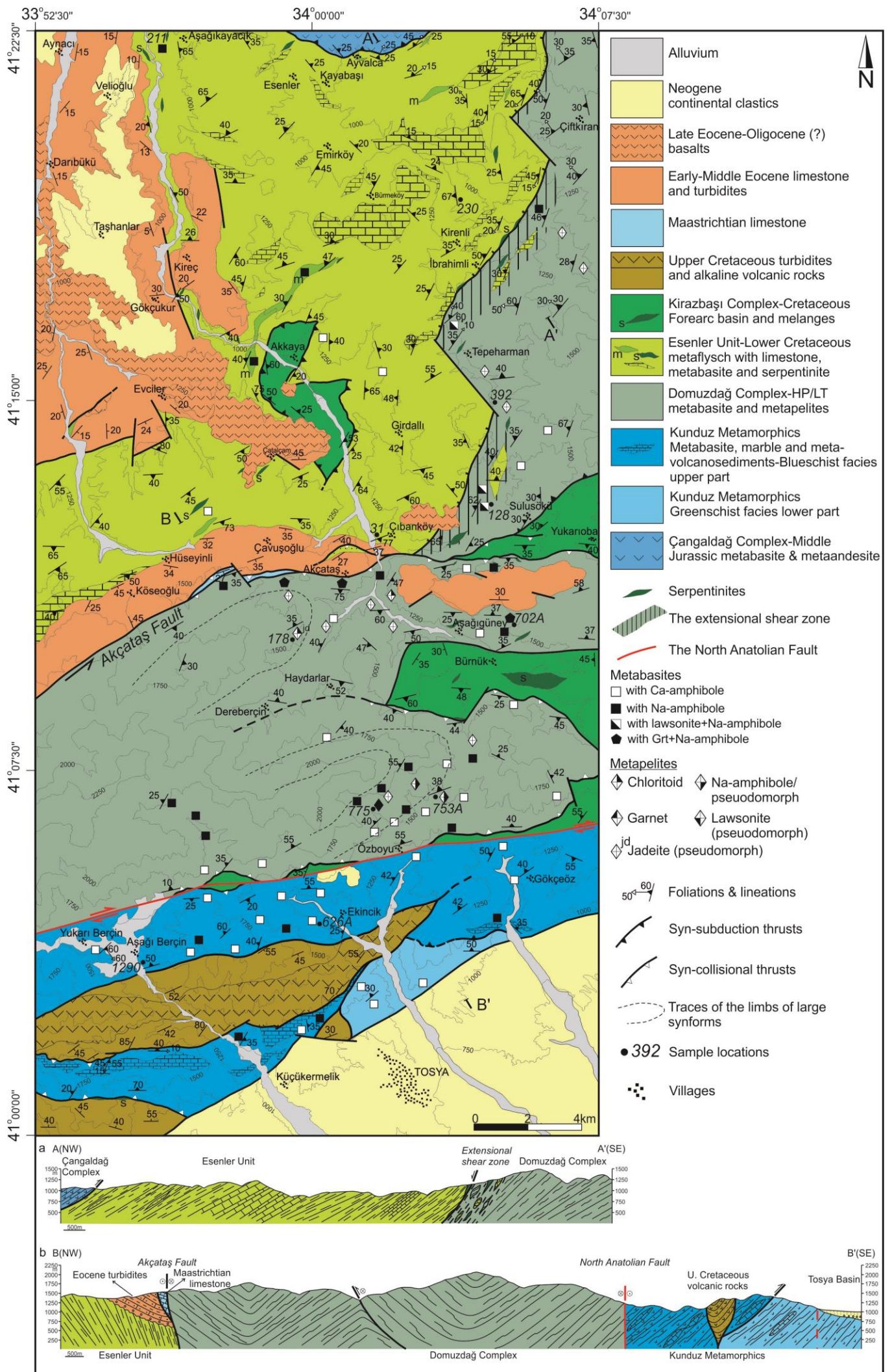


Figure A.1 : Geological map of the area studied across the Central Pontide Supercomplex between Kastamonu-Tosya with cross sections.

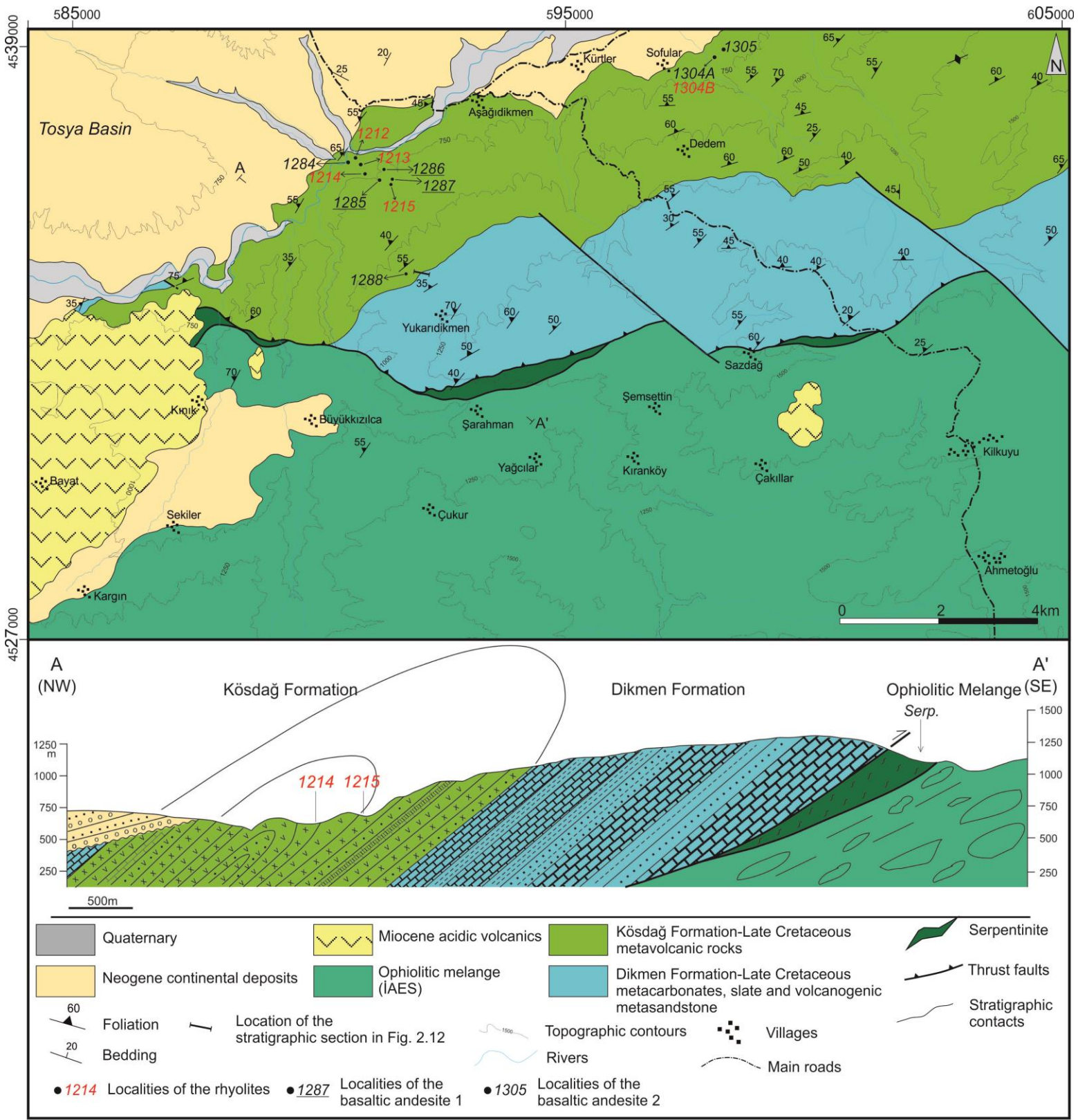


Figure A.2 : Geological map of the studied section south of Tosya, along the İzmir-Ankara-Erzincan suture with a cross section between A and A'.

Table A.1 : Mineral chemistry of the measured amphiboles. Mineral formula calculations are based on 23 oxygens.

Na-Amph	211B ^a	211B	211B	211B	211B	211B	211B	211B	211B	211B	211B	211B	211B	211B	211B
	252	258	259	260	262	269	270	271	299	300	313	316	317	319	323
SiO ₂	53.93	54.83	55.16	54.56	53.66	54.03	54.43	54.78	53.41	53.90	53.43	53.32	53.78	53.10	54.14
TiO ₂	0.05	0.26	0.02	0.05	0.05	0.02	0.06	0.02	0.02	0.05	0.02	0.09	0.08	0.04	0.04
Al ₂ O ₃	4.98	5.38	5.19	4.98	4.46	5.11	5.90	5.83	4.65	5.07	5.63	4.85	5.98	5.30	5.89
Cr ₂ O ₃	0.01	0.00	0.02	0.00	0.01	0.00	0.00	0.00	0.00	0.00	0.00	0.00	0.00	0.00	0.00
FeO	23.43	18.69	19.63	20.55	24.14	21.97	20.33	19.42	24.36	22.17	22.76	23.06	20.94	22.60	21.33
MnO	0.17	0.15	0.13	0.16	0.15	0.19	0.14	0.11	0.11	0.17	0.14	0.15	0.15	0.16	0.15
MgO	6.52	8.73	8.84	8.41	6.56	7.27	7.53	8.35	5.96	7.18	6.14	6.71	7.29	6.49	7.08
CaO	0.75	0.82	0.53	1.63	1.45	1.46	0.42	0.53	0.74	0.89	0.91	1.36	0.81	1.00	1.00
Na ₂ O	6.45	6.66	6.56	5.87	5.97	6.01	6.47	6.53	6.37	6.35	6.41	6.19	6.52	6.31	6.34
K ₂ O	0.09	0.01	0.01	0.03	0.02	0.01	0.01	0.01	0.01	0.01	0.02	0.02	0.01	0.02	0.02
Total	96.37	95.52	96.08	96.23	96.47	96.06	95.31	95.57	95.63	95.78	95.45	95.73	95.57	95.02	95.98
Si	7.884	7.914	7.933	7.911	7.877	7.895	7.944	7.926	7.901	7.883	7.874	7.844	7.839	7.856	7.885
Ti	0.006	0.028	0.002	0.005	0.005	0.002	0.006	0.003	0.003	0.005	0.002	0.010	0.009	0.005	0.004
Al	0.858	0.914	0.880	0.851	0.771	0.881	1.015	0.994	0.811	0.873	0.978	0.840	1.027	0.924	1.011
Cr	0.001	0.000	0.002	0.000	0.001	0.000	0.000	0.000	0.000	0.000	0.000	0.000	0.000	0.000	0.000
Fe ³⁺	1.172	1.063	1.074	0.962	1.158	1.027	0.913	0.980	1.208	1.150	1.098	1.212	1.120	1.161	0.999
Fe ²⁺	1.692	1.194	1.288	1.530	1.806	1.658	1.568	1.370	1.805	1.562	1.707	1.625	1.433	1.635	1.598
Mn	0.021	0.018	0.016	0.020	0.019	0.023	0.018	0.013	0.014	0.021	0.018	0.019	0.019	0.020	0.018
Mg	1.421	1.879	1.896	1.818	1.436	1.584	1.638	1.801	1.314	1.566	1.348	1.471	1.584	1.431	1.537
Ca	0.117	0.127	0.082	0.253	0.227	0.228	0.066	0.081	0.117	0.139	0.143	0.214	0.127	0.159	0.156
Na	1.828	1.864	1.828	1.650	1.699	1.703	1.832	1.832	1.827	1.801	1.832	1.765	1.844	1.809	1.791
K	0.016	0.002	0.001	0.005	0.004	0.002	0.003	0.002	0.002	0.001	0.004	0.004	0.002	0.004	0.003
Total	15.016	15.002	15.001	15.005	15.004	15.002	15.003	15.002	15.002	15.001	15.004	15.004	15.002	15.004	15.003

^a Ferric iron content is according to the maximum ferric iron correction of Schumacher (1997). 15eK for the sample 211B.

Table A.1 (continued) : Mineral chemistry of the measured amphiboles. Mineral formula calculations are based on 23 oxygens.

Na-Amph	128 ^a	128	128	128	128	128	128	128	128	128	128	128	128	128	128
	<i>145</i>	<i>146</i>	<i>148</i>	<i>151</i>	<i>152</i>	<i>159</i>	<i>165</i>	<i>167</i>	<i>168</i>	<i>169</i>	<i>171</i>	<i>176</i>	<i>178</i>	<i>181</i>	<i>188</i>
SiO ₂	57.08	56.84	56.60	56.25	56.21	56.49	56.91	56.80	56.13	57.04	56.97	57.90	56.57	56.49	56.31
TiO ₂	0.09	0.21	0.02	0.00	0.11	0.08	0.07	0.31	0.09	0.08	0.08	0.03	0.15	0.38	0.05
Al ₂ O ₃	10.52	9.57	8.64	5.79	9.04	8.37	10.16	9.81	6.39	8.84	9.65	10.22	5.96	9.82	7.80
Cr ₂ O ₃	0.00	0.04	0.00	0.02	0.00	0.00	0.00	0.00	0.01	0.05	0.02	0.00	0.00	0.03	0.00
FeO	14.45	14.32	15.45	16.39	15.82	15.13	14.45	14.86	18.09	16.42	15.46	15.00	17.77	15.19	17.33
MnO	0.34	0.36	0.47	0.46	0.42	0.53	0.35	0.32	0.14	0.20	0.12	0.25	0.29	0.28	0.13
MgO	8.31	8.81	9.11	10.30	8.43	9.20	8.30	8.70	8.94	8.22	8.23	8.24	9.39	8.15	8.38
CaO	0.56	1.00	1.67	2.70	0.99	1.31	0.58	0.68	1.49	0.60	0.50	0.37	1.36	0.80	1.15
Na ₂ O	7.40	6.93	6.76	5.96	7.19	6.91	7.26	7.12	6.62	7.12	7.49	7.31	6.81	7.15	6.82
K ₂ O	0.03	0.03	0.03	0.06	0.03	0.05	0.01	0.02	0.01	0.02	0.02	0.01	0.01	0.02	0.04
Total	98.78	98.10	98.75	97.92	98.23	98.07	98.09	98.62	97.91	98.58	98.54	99.33	98.32	98.31	98.01
Si	7.868	7.885	7.853	7.903	7.849	7.877	7.896	7.832	7.905	7.913	7.904	7.923	7.923	7.857	7.901
Ti	0.009	0.022	0.002	0.000	0.011	0.008	0.008	0.032	0.010	0.008	0.008	0.003	0.016	0.039	0.005
Al	1.710	1.564	1.413	0.959	1.487	1.376	1.661	1.595	1.061	1.446	1.577	1.648	0.984	1.610	1.290
Cr	0.000	0.004	0.000	0.002	0.000	0.000	0.000	0.000	0.001	0.005	0.002	0.000	0.000	0.003	0.000
Fe ³⁺	0.389	0.452	0.556	0.789	0.545	0.585	0.406	0.570	0.849	0.611	0.428	0.450	0.880	0.425	0.690
Fe ²⁺	1.276	1.210	1.236	1.137	1.302	1.180	1.271	1.144	1.281	1.295	1.365	1.267	1.201	1.342	1.344
Mn	0.040	0.042	0.056	0.054	0.050	0.063	0.041	0.038	0.016	0.023	0.014	0.029	0.035	0.033	0.016
Mg	1.708	1.821	1.884	2.157	1.756	1.912	1.717	1.789	1.877	1.700	1.701	1.680	1.961	1.691	1.753
Ca	0.083	0.148	0.249	0.406	0.148	0.196	0.086	0.100	0.224	0.089	0.075	0.055	0.204	0.119	0.172
Na	1.978	1.864	1.819	1.624	1.946	1.869	1.953	1.903	1.809	1.916	2.015	1.939	1.849	1.927	1.856
K	0.005	0.005	0.005	0.011	0.006	0.008	0.001	0.003	0.002	0.003	0.004	0.002	0.002	0.004	0.006
Total	15.065	15.018	15.073	15.040	15.100	15.073	15.041	15.019	15.035	15.007	15.094	15.006	15.055	15.050	15.035

^a 13eCNK for the sample 128.

Table A.1 (continued) : Mineral chemistry of the measured amphiboles. Mineral formula calculations are based on 23 oxygens.

Na-Amph	128 ^a	128	128	128	128	128	128	128	128	128	128	128	128	128
	189	191	192	193	194	195	196	198	199	200	201	202	204	205
SiO ₂	56.21	56.41	56.50	56.82	56.01	56.97	55.94	56.36	55.91	56.57	57.47	56.82	57.41	56.90
TiO ₂	0.20	0.03	0.00	0.09	0.08	0.09	0.10	0.11	0.09	0.12	0.01	0.04	0.00	0.19
Al ₂ O ₃	8.93	8.53	9.97	8.80	8.95	8.41	7.03	9.22	6.54	9.90	10.08	6.89	10.57	9.77
Cr ₂ O ₃	0.01	0.00	0.00	0.00	0.01	0.03	0.00	0.00	0.00	0.00	0.01	0.01	0.00	0.03
FeO	15.58	16.64	16.55	16.30	16.98	16.67	18.22	16.04	19.82	16.07	14.38	16.44	14.34	14.19
MnO	0.29	0.13	0.22	0.24	0.31	0.21	0.17	0.23	0.11	0.24	0.26	0.34	0.28	0.26
MgO	8.57	8.23	7.62	8.16	7.77	8.21	7.91	8.03	7.57	8.02	8.41	9.46	8.30	8.83
CaO	1.07	0.89	1.12	0.63	1.15	0.79	1.07	0.89	0.43	0.63	0.29	0.97	0.23	0.65
Na ₂ O	7.05	6.83	7.06	6.83	6.72	7.12	6.81	6.97	6.87	7.56	7.49	7.10	7.22	7.13
K ₂ O	0.02	0.02	0.03	0.01	0.02	0.01	0.03	0.02	0.01	0.02	0.01	0.03	0.01	0.02
Total	97.93	97.73	99.06	97.88	98.01	98.51	97.27	97.87	97.33	99.11	98.41	98.09	98.35	97.96
Si	7.861	7.903	7.844	7.920	7.857	7.935	7.950	7.888	7.932	7.831	7.935	7.933	7.900	7.883
Ti	0.021	0.003	0.000	0.010	0.009	0.009	0.011	0.012	0.009	0.012	0.001	0.005	0.000	0.020
Al	1.473	1.409	1.631	1.445	1.480	1.381	1.178	1.520	1.094	1.615	1.641	1.134	1.714	1.595
Cr	0.001	0.000	0.000	0.000	0.001	0.003	0.000	0.000		0.000	0.001	0.001	0.000	0.004
Fe ³⁺	0.526	0.652	0.442	0.661	0.609	0.569	0.696	0.518	1.000	0.483	0.392	0.774	0.490	0.486
Fe ²⁺	1.296	1.297	1.480	1.240	1.383	1.374	1.469	1.359	1.351	1.377	1.268	1.144	1.160	1.158
Mn	0.034	0.016	0.026	0.028	0.037	0.025	0.020	0.027	0.013	0.028	0.030	0.040	0.033	0.030
Mg	1.787	1.719	1.577	1.697	1.625	1.705	1.676	1.676	1.601	1.655	1.732	1.969	1.702	1.825
Ca	0.160	0.133	0.167	0.094	0.173	0.117	0.162	0.134	0.066	0.093	0.043	0.145	0.034	0.096
Na	1.912	1.856	1.900	1.845	1.829	1.922	1.876	1.891	1.889	2.028	2.005	1.922	1.926	1.914
K	0.004	0.004	0.005	0.002	0.004	0.002	0.005	0.004	0.002	0.003	0.002	0.004	0.002	0.003
Total	15.076	15.004	15.072	15.002	15.006	15.042	15.043	15.029	15.002	15.124	15.050	15.071	15.005	15.014

^a 13eCNK for the sample 128.

Table A.1 (continued) : Mineral chemistry of the measured amphiboles. Mineral formula calculations are based on 23 oxygens.

Na-Amph	702A ^a	702A	702A	702A	702A	702A	702A	702A	702A	702A	702A	702A	702A	702A	702A
	<i>1</i>	<i>20</i>	<i>22</i>	<i>25</i>	<i>26</i>	<i>30</i>	<i>36</i>	<i>38</i>	<i>41</i>	<i>43</i>	<i>54</i>	<i>55</i>	<i>60</i>	<i>63</i>	<i>64</i>
SiO ₂	55.96	56.34	54.97	55.64	56.14	55.80	55.65	56.12	55.72	56.48	55.71	56.84	55.79	56.28	56.32
TiO ₂	0.03	0.07	0.02	0.05	0.09	0.05	0.07	0.16	0.11	0.01	0.10	0.25	0.10	0.05	0.12
Al ₂ O ₃	12.05	10.29	10.26	7.96	9.12	9.27	9.77	10.07	9.95	11.01	9.48	11.37	10.52	10.29	9.63
Cr ₂ O ₃	0.01	0.02	0.00	0.02	0.00	0.00	0.00	0.00	0.00	0.03	0.01	0.01	0.00	0.00	0.03
FeO	15.92	15.58	18.10	20.18	18.88	18.44	17.05	17.92	18.53	14.56	19.26	15.09	16.66	17.05	16.74
MnO	0.12	0.11	0.26	0.09	0.08	0.09	0.13	0.12	0.15	0.03	0.08	0.08	0.04	0.11	0.07
MgO	6.28	7.55	6.26	6.00	6.29	6.55	6.84	6.29	6.28	8.50	6.09	7.12	6.84	6.70	7.36
CaO	0.52	1.40	1.79	0.85	0.62	1.14	1.21	0.81	0.84	1.41	0.66	0.65	1.02	0.76	0.90
Na ₂ O	7.66	6.72	6.58	6.83	7.09	6.90	6.90	7.18	6.90	6.88	7.20	7.39	6.84	7.10	6.99
K ₂ O	0.06	0.02	0.03	0.02	0.01	0.03	0.02	0.03	0.04	0.05	0.03	0.01	0.01	0.03	0.02
Total	98.60	98.10	98.27	97.65	98.32	98.26	97.63	98.68	98.50	98.95	98.59	98.80	97.81	98.37	98.16
Si	7.825	7.883	7.787	7.951	7.916	7.883	7.882	7.882	7.830	7.781	7.854	7.884	7.848	7.885	7.889
Ti	0.003	0.007	0.002	0.005	0.010	0.005	0.007	0.017	0.011	0.001	0.010	0.026	0.010	0.006	0.012
Al	1.986	1.697	1.712	1.341	1.516	1.543	1.631	1.666	1.648	1.788	1.575	1.858	1.744	1.699	1.590
Cr	0.001	0.002	0.000	0.003	0.000	0.000	0.000	0.000	0.000	0.003	0.001	0.001	0.000	0.000	0.004
Fe ³⁺	0.115	0.274	0.352	0.588	0.505	0.441	0.325	0.332	0.533	0.386	0.525	0.139	0.367	0.355	0.431
Fe ²⁺	1.747	1.549	1.792	1.824	1.721	1.738	1.694	1.773	1.645	1.292	1.746	1.612	1.593	1.643	1.530
Mn	0.014	0.013	0.031	0.011	0.010	0.011	0.015	0.014	0.017	0.004	0.009	0.009	0.004	0.013	0.008
Mg	1.309	1.575	1.323	1.278	1.322	1.380	1.445	1.316	1.316	1.745	1.280	1.471	1.434	1.399	1.536
Ca	0.078	0.210	0.272	0.130	0.093	0.173	0.183	0.122	0.126	0.207	0.099	0.096	0.154	0.114	0.135
Na	2.077	1.824	1.806	1.893	1.938	1.890	1.895	1.955	1.879	1.837	1.967	1.988	1.864	1.929	1.899
K	0.010	0.004	0.006	0.003	0.002	0.005	0.004	0.005	0.007	0.008	0.005	0.002	0.002	0.005	0.003
Total	15.165	15.038	15.084	15.027	15.033	15.068	15.082	15.082	15.011	15.052	15.071	15.086	15.020	15.049	15.037

^a 13eCNK for the sample 702A.

Table A.1 (continued) : Mineral chemistry of the measured amphiboles. Mineral formula calculations are based on 23 oxygens.

Na-Amph	702A ^a	702A	702A	702A	702A	702A	702A	702A	702A	702A	702A	702A	702A	702A	702A
	65	72	74	77	79	83	95	101	105	106	109	110	116	122	123
SiO ₂	56.95	56.89	55.91	56.87	56.82	55.76	56.23	56.72	57.14	56.71	55.67	57.37	55.14	55.93	56.49
TiO ₂	0.00	0.08	0.06	0.02	0.01	0.42	0.07	0.05	0.01	0.06	0.15	0.03	0.09	0.04	0.00
Al ₂ O ₃	11.07	11.98	10.16	11.13	11.41	7.97	11.08	11.23	11.15	10.74	8.10	11.72	11.59	11.31	11.06
Cr ₂ O ₃	0.03	0.00	0.02	0.03	0.01	0.12	0.00	0.00	0.00	0.00	0.00	0.03	0.01	0.00	0.02
FeO	14.83	14.61	17.72	14.83	14.84	17.28	15.85	16.09	14.45	15.81	19.97	14.82	16.19	18.07	16.86
MnO	0.01	0.10	0.07	0.04	0.02	0.03	0.06	0.11	0.02	0.10	0.13	0.10	0.20	0.18	0.21
MgO	7.73	7.01	6.16	7.81	7.59	7.84	7.01	6.53	7.77	7.28	6.21	7.04	6.63	5.49	6.48
CaO	0.87	0.39	0.87	0.84	0.64	1.55	0.97	0.33	0.98	1.24	0.96	0.24	1.43	0.82	0.71
Na ₂ O	7.13	7.17	6.90	7.17	7.33	6.75	7.05	7.53	7.05	6.41	6.88	7.57	6.89	7.02	7.04
K ₂ O	0.02	0.02	0.03	0.05	0.03	0.02	0.03	0.02	0.01	0.03	0.02	0.02	0.03	0.03	0.03
Total	98.63	98.22	97.90	98.77	98.71	97.74	98.34	98.59	98.58	98.37	98.11	98.92	98.20	98.90	98.86
Si	7.881	7.883	7.900	7.857	7.856	7.902	7.852	7.906	7.904	7.879	7.917	7.918	7.752	7.840	7.858
Ti	0.000	0.008	0.007	0.002	0.001	0.045	0.008	0.005	0.001	0.006	0.016	0.003	0.009	0.005	0.000
Al	1.806	1.956	1.691	1.812	1.859	1.331	1.824	1.844	1.818	1.759	1.358	1.907	1.920	1.869	1.813
Cr	0.003	0.000	0.003	0.003	0.001	0.013	0.000	0.000	0.000	0.000	0.000	0.003	0.002	0.000	0.000
Fe ³⁺	0.254	0.218	0.336	0.288	0.264	0.434	0.254	0.199	0.188	0.370	0.581	0.152	0.243	0.281	0.356
Fe ²⁺	1.461	1.475	1.757	1.426	1.452	1.615	1.597	1.676	1.483	1.467	1.794	1.559	1.661	1.837	1.605
Mn	0.001	0.011	0.009	0.004	0.003	0.003	0.007	0.012	0.002	0.012	0.016	0.012	0.024	0.021	0.025
Mg	1.594	1.449	1.298	1.608	1.564	1.657	1.459	1.357	1.603	1.507	1.317	1.448	1.390	1.148	1.343
Ca	0.129	0.057	0.132	0.125	0.095	0.235	0.144	0.049	0.145	0.185	0.146	0.035	0.215	0.123	0.106
Na	1.914	1.925	1.889	1.920	1.965	1.854	1.910	2.034	1.891	1.726	1.898	2.025	1.879	1.909	1.898
K	0.004	0.004	0.005	0.008	0.005	0.004	0.005	0.003	0.002	0.005	0.004	0.004	0.005	0.005	0.005
Total	15.047	14.986	15.026	15.053	15.066	15.093	15.059	15.086	15.039	14.916	15.048	15.064	15.099	15.037	15.009

^a 13eCNK for the sample 702A.

Table A.1 (continued) : Mineral chemistry of the measured amphiboles. Mineral formula calculations are based on 23 oxygens.

Na-Amph	775 ^a	775	775
	6	7	17
SiO ₂	57.69	57.46	57.12
TiO ₂	0.03	0.05	0.13
Al ₂ O ₃	12.43	12.18	11.79
Cr ₂ O ₃	0.00	0.00	0.00
FeO	12.88	13.14	13.92
MnO	0.12	0.15	0.13
MgO	7.71	7.56	7.15
CaO	0.04	0.06	0.07
Na ₂ O	7.39	7.32	7.33
K ₂ O	0.01	0.01	0.01
Total	98.29	97.91	97.64
Si	7.933	7.945	7.947
Ti	0.003	0.005	0.014
Al	2.015	1.985	1.934
Cr	0.000	0.000	0.000
Fe ³⁺	0.083	0.075	0.120
Fe ²⁺	1.398	1.444	1.499
Mn	0.013	0.017	0.015
Mg	1.581	1.558	1.482
Ca	0.005	0.009	0.011
Na	1.970	1.962	1.977
K	0.002	0.001	0.001
Total	15.002	15.001	15.001

^a 15eK for the sample 775.

Table A.1 (continued) : Mineral chemistry of the measured amphiboles. Mineral formula calculations are based on 23 oxygens.

Ca-Amph	211B ^a	211B	211B	211B	211B	211B	702A	702A	702A	702A	702A	702A
	244	249	261	285	291	324	126	133	21	39	44	56
SiO ₂	52.13	52.63	52.26	52.27	52.67	52.29	51.71	54.84	50.38	49.30	51.63	53.64
TiO ₂	0.02	0.04	0.03	0.01	0.03	0.48	0.06	0.02	0.04	0.01	0.02	0.03
Al ₂ O ₃	1.80	1.37	1.79	1.30	1.04	1.51	4.47	1.19	5.50	6.71	4.20	1.52
Cr ₂ O ₃	0.00	0.00	0.00	0.00	0.00	0.02	0.01	0.00	0.03	0.00	0.00	0.01
FeO	19.42	17.87	19.07	17.28	17.25	17.11	16.63	13.44	19.85	19.11	16.26	16.38
MnO	0.28	0.26	0.30	0.28	0.25	0.27	0.08	0.17	0.15	0.09	0.06	0.09
MgO	11.57	12.82	12.15	12.84	12.91	12.78	12.14	15.75	10.19	10.22	14.58	13.47
CaO	9.93	10.77	9.76	10.65	11.08	10.40	11.54	11.84	10.83	11.15	9.89	11.97
Na ₂ O	1.59	1.00	1.36	0.97	0.86	1.24	1.08	0.45	1.56	1.41	0.85	0.46
K ₂ O	0.13	0.10	0.09	0.10	0.06	0.11	0.19	0.04	0.24	0.32	0.07	0.05
Total	96.87	96.86	96.81	95.72	96.15	96.18	97.90	97.72	98.78	98.31	97.55	97.61
Si	7.702	7.726	7.658	7.753	7.797	7.723	7.545	7.824	7.373	7.242	7.297	7.808
Ti	0.002	0.004	0.003	0.001	0.004	0.054	0.006	0.002	0.004	0.001	0.002	0.004
Al	0.313	0.237	0.309	0.228	0.182	0.262	0.768	0.200	0.949	1.161	0.699	0.260
Cr	0.000	0.000	0.000	0.000	0.000	0.000	0.001	0.000	0.003	0.000	0.000	0.000
Fe ³⁺	0.654	0.609	0.900	0.580	0.443	0.518	0.182	0.398	0.410	0.383	1.462	0.240
Fe ²⁺	1.745	1.585	1.438	1.563	1.693	1.596	1.848	1.205	2.019	1.965	0.461	1.754
Mn	0.035	0.033	0.037	0.035	0.032	0.033	0.010	0.020	0.019	0.011	0.008	0.011
Mg	2.548	2.806	2.655	2.840	2.850	2.814	2.641	3.350	2.223	2.238	3.072	2.922
Ca	1.572	1.695	1.532	1.693	1.757	1.645	1.803	1.809	1.698	1.754	1.498	1.868
Na	0.455	0.285	0.387	0.280	0.247	0.354	0.305	0.124	0.444	0.402	0.233	0.130
K	0.024	0.019	0.018	0.018	0.012	0.021	0.035	0.006	0.045	0.059	0.012	0.010
Total	15.052	14.999	14.937	14.991	15.016	15.021	15.144	14.940	15.187	15.216	14.743	15.008

^a 15eCNK for the samples 211B and 702A.

Table A.2 : Mineral chemistry of the measured phengitic white micas. Mineral formula calculations are based on 11 oxygens.

Phengite	775	775	775	775	775	775	775	775	775	775	775	775	775	775	775
	10	11	23	213	216	218	222	225	228	233	239	240	248	252	255
SiO ₂	52.53	53.71	47.68	51.18	50.43	49.91	51.14	49.02	51.67	50.47	52.09	50.75	51.41	47.12	47.08
TiO ₂	0.08	0.05	0.10	0.07	0.18	0.15	0.27	0.63	0.08	0.20	0.15	0.10	0.24	0.10	0.03
Al ₂ O ₃	25.90	25.39	34.58	26.73	27.64	28.61	30.10	30.13	26.22	32.51	27.77	27.43	32.57	35.91	35.65
Cr ₂ O ₃	0.02	0.00	0.01	0.04	0.02	0.01	0.02	0.03	0.02	0.06	0.03	0.02	0.00	0.03	0.00
FeO	2.44	2.33	1.93	2.75	3.91	3.83	2.93	2.25	2.58	3.12	3.17	3.12	1.85	0.82	1.32
MnO	0.04	0.06	0.03	0.10	0.08	0.04	0.10	0.04	0.05	0.14	0.07	0.04	0.06	0.02	0.06
MgO	3.85	4.17	1.17	3.45	2.33	2.27	2.45	2.08	3.44	1.32	2.67	2.77	1.46	0.50	0.59
CaO	0.01	0.00	0.07	0.02	0.00	0.01	0.02	0.01	0.01	0.07	0.03	0.00	0.09	0.00	0.09
Na ₂ O	0.11	0.10	0.53	0.22	0.25	0.29	0.34	0.41	0.12	0.45	0.23	0.29	0.32	0.73	1.75
K ₂ O	10.35	10.75	10.09	10.60	10.47	10.23	9.32	10.34	10.54	9.58	8.29	10.63	8.83	9.81	8.41
Total	95.33	96.57	96.18	95.16	95.30	95.34	96.68	94.93	94.73	97.91	94.50	95.14	96.81	95.05	94.99
Si	3.491	3.526	3.139	3.427	3.388	3.346	3.340	3.282	3.466	3.264	3.456	3.404	3.316	3.116	3.112
Ti	0.004	0.003	0.005	0.004	0.009	0.007	0.013	0.032	0.004	0.010	0.007	0.005	0.011	0.005	0.002
Al	2.028	1.964	2.683	2.109	2.188	2.261	2.317	2.377	2.072	2.478	2.172	2.168	2.476	2.799	2.777
Cr	0.001	0.000	0.001	0.002	0.001	0.000	0.001	0.002	0.001	0.003	0.002	0.001	0.000	0.002	0.000
Fe ³⁺	0.000	0.000	0.000	0.000	0.000	0.000	0.000	0.000	0.000	0.000	0.000	0.000	0.000	0.000	0.000
Fe ²⁺	0.136	0.128	0.106	0.154	0.220	0.214	0.160	0.126	0.145	0.169	0.176	0.175	0.100	0.046	0.073
Mn	0.002	0.003	0.002	0.006	0.005	0.002	0.006	0.002	0.003	0.008	0.004	0.002	0.003	0.001	0.003
Mg	0.381	0.408	0.115	0.345	0.233	0.227	0.238	0.208	0.344	0.127	0.265	0.277	0.140	0.049	0.058
Ca	0.001	0.000	0.005	0.001	0.000	0.001	0.001	0.001	0.001	0.005	0.002	0.000	0.006	0.000	0.007
Na	0.015	0.012	0.067	0.028	0.032	0.037	0.044	0.053	0.016	0.056	0.029	0.037	0.040	0.094	0.224
K	0.877	0.900	0.848	0.905	0.897	0.875	0.776	0.883	0.901	0.790	0.701	0.910	0.726	0.827	0.709
Total	6.936	6.945	6.971	6.981	6.973	6.972	6.897	6.965	6.953	6.909	6.815	6.980	6.818	6.939	6.964

Table A.2 (continued) : Mineral chemistry of the measured phengitic white micas. Mineral formula calculations are based on 11 oxygens.

Phengite	775	775	775	775	775	775	775	775	775	753A	753A	753A	753A	753A
	257	260	264	267	270	273	278	281	282	75	76	78	79	81
SiO ₂	48.10	48.20	50.29	46.48	50.82	51.79	51.46	51.60	52.31	51.04	51.30	50.60	50.01	48.55
TiO ₂	0.26	0.23	0.16	0.12	0.09	0.07	0.09	0.05	0.07	0.13	0.09	0.10	0.17	0.16
Al ₂ O ₃	31.02	32.37	28.19	37.15	27.34	26.66	26.59	27.07	25.46	27.72	27.58	27.34	28.13	30.04
Cr ₂ O ₃	0.00	0.01	0.04	0.02	0.04	0.03	0.00	0.00	0.00	0.00	0.03	0.04	0.00	0.04
FeO	2.59	2.29	2.77	1.04	2.92	3.02	2.91	2.51	2.26	2.90	2.44	2.64	3.33	3.20
MnO	0.06	0.12	0.10	0.02	0.03	0.08	0.08	0.04	0.04	0.07	0.03	0.03	0.06	0.09
MgO	1.48	1.23	2.73	0.49	3.14	3.46	3.41	3.39	3.89	2.82	3.10	2.97	2.50	1.83
CaO	0.05	0.05	0.05	0.16	0.01	0.02	0.01	0.02	0.00	0.00	0.00	0.02	0.00	0.00
Na ₂ O	0.58	0.59	0.26	3.16	0.20	0.19	0.13	0.18	0.10	0.20	0.13	0.19	0.24	0.34
K ₂ O	10.24	10.15	10.34	6.67	10.55	10.29	10.29	10.48	10.76	10.31	10.41	10.29	10.34	10.18
Total	94.37	95.23	94.92	95.31	95.14	95.60	94.97	95.33	94.88	95.19	95.09	94.21	94.76	94.42
Si	3.246	3.215	3.372	3.044	3.404	3.445	3.444	3.436	3.500	3.408	3.421	3.411	3.367	3.281
Ti	0.013	0.012	0.008	0.006	0.004	0.003	0.005	0.002	0.003	0.006	0.005	0.005	0.009	0.008
Al	2.467	2.544	2.228	2.867	2.158	2.090	2.097	2.124	2.008	2.182	2.167	2.172	2.232	2.392
Cr	0.000	0.001	0.002	0.001	0.002	0.001	0.000	0.000	0.000	0.000	0.001	0.002	0.000	0.002
Fe ³⁺	0.000	0.000	0.000	0.000	0.000	0.000	0.000	0.000	0.000	0.000	0.000	0.000	0.000	0.000
Fe ²⁺	0.146	0.128	0.156	0.057	0.163	0.168	0.163	0.140	0.126	0.162	0.136	0.149	0.187	0.181
Mn	0.003	0.007	0.005	0.001	0.002	0.005	0.005	0.002	0.002	0.004	0.002	0.002	0.003	0.005
Mg	0.149	0.122	0.273	0.048	0.313	0.343	0.340	0.336	0.388	0.281	0.308	0.298	0.251	0.185
Ca	0.004	0.004	0.003	0.011	0.001	0.002	0.001	0.001	0.000	0.000	0.000	0.002	0.000	0.000
Na	0.076	0.076	0.034	0.401	0.026	0.024	0.017	0.023	0.012	0.026	0.016	0.025	0.031	0.045
K	0.881	0.863	0.885	0.557	0.902	0.873	0.879	0.890	0.918	0.878	0.886	0.885	0.888	0.877
Total	6.986	6.971	6.965	6.995	6.975	6.954	6.950	6.956	6.958	6.947	6.941	6.951	6.968	6.975

Table A.2 (continued) : Mineral chemistry of the measured phengitic white micas. Mineral formula calculations are based on 11 oxygens.

Phengite	753A	753A	753A	753A	753A	753A	753A	753A	753A	753A	753A	753A	753A	753A
	83	92	93	108	112	123	127	130	131	139	143	146	148	150
SiO ₂	50.66	50.93	50.53	50.41	48.96	51.15	48.18	50.28	50.85	49.46	48.69	50.11	49.62	50.12
TiO ₂	0.08	0.06	0.17	0.14	0.07	0.06	0.14	0.15	0.07	0.10	0.05	0.13	0.18	0.13
Al ₂ O ₃	27.21	27.34	27.98	27.51	30.49	25.94	31.40	28.12	26.92	29.19	32.64	28.73	28.71	28.45
Cr ₂ O ₃	0.01	0.05	0.01	0.04	0.04	0.01	0.07	0.00	0.01	0.04	0.01	0.00	0.01	0.02
FeO	2.43	2.46	3.70	2.90	2.62	2.99	3.12	3.26	2.72	3.15	1.96	3.01	2.75	2.59
MnO	0.06	0.05	0.10	0.06	0.08	0.06	0.15	0.07	0.05	0.07	0.06	0.05	0.03	0.07
MgO	3.05	2.94	2.25	2.59	1.98	3.25	1.49	2.41	3.33	2.07	1.48	2.15	2.43	2.56
CaO	0.00	0.02	0.00	0.01	0.00	0.00	0.01	0.00	0.00	0.00	0.00	0.01	0.00	0.00
Na ₂ O	0.12	0.18	0.16	0.16	0.34	0.10	0.33	0.24	0.16	0.23	0.42	0.33	0.22	0.22
K ₂ O	10.48	10.37	10.36	10.26	10.14	10.24	9.90	10.41	10.33	10.30	10.02	10.07	10.14	10.16
Total	94.10	94.40	95.25	94.06	94.71	93.79	94.77	94.93	94.44	94.61	95.33	94.59	94.09	94.32
Si	3.419	3.424	3.388	3.407	3.285	3.467	3.236	3.378	3.423	3.332	3.229	3.367	3.351	3.372
Ti	0.004	0.003	0.009	0.007	0.003	0.003	0.007	0.007	0.003	0.005	0.003	0.007	0.009	0.007
Al	2.164	2.166	2.211	2.191	2.411	2.072	2.486	2.226	2.136	2.317	2.551	2.275	2.285	2.256
Cr	0.000	0.003	0.000	0.002	0.002	0.001	0.004	0.000	0.001	0.002	0.000	0.000	0.001	0.001
Fe ³⁺	0.000	0.000	0.000	0.000	0.000	0.000	0.000	0.000	0.000	0.000	0.000	0.000	0.000	0.000
Fe ²⁺	0.137	0.138	0.207	0.164	0.147	0.170	0.175	0.183	0.153	0.177	0.109	0.169	0.155	0.146
Mn	0.003	0.003	0.005	0.003	0.004	0.003	0.008	0.004	0.003	0.004	0.003	0.003	0.002	0.004
Mg	0.307	0.294	0.224	0.261	0.198	0.328	0.149	0.241	0.334	0.208	0.146	0.215	0.245	0.256
Ca	0.000	0.001	0.000	0.000	0.000	0.000	0.000	0.000	0.000	0.000	0.000	0.001	0.000	0.000
Na	0.016	0.024	0.021	0.021	0.045	0.013	0.043	0.031	0.021	0.030	0.054	0.043	0.029	0.029
K	0.902	0.889	0.886	0.885	0.868	0.886	0.849	0.892	0.887	0.885	0.848	0.863	0.874	0.872
Total	6.954	6.946	6.952	6.942	6.962	6.943	6.957	6.963	6.960	6.961	6.943	6.942	6.949	6.943

Table A.2 (continued) : Mineral chemistry of the measured phengitic white micas. Mineral formula calculations are based on 11 oxygens.

Phengite	178	178	178	178	178	178	178	178	178	178	178	178	178	178	178
	22	23	24	29	30	33	37	42	45	46	47	52	56	57	58
SiO ₂	46.70	50.75	50.58	48.06	51.07	51.64	50.79	51.05	46.06	50.58	46.98	50.10	50.22	46.70	49.80
TiO ₂	0.16	0.11	0.17	0.20	0.15	0.10	0.12	0.22	0.13	0.16	0.18	0.14	0.16	0.09	0.08
Al ₂ O ₃	35.05	27.40	27.23	31.78	27.51	27.10	27.50	27.10	34.85	27.91	34.19	27.78	28.08	34.99	27.89
Cr ₂ O ₃	0.00	0.03	0.05	0.02	0.00	0.02	0.00	0.02	0.03	0.04	0.02	0.05	0.02	0.09	0.02
FeO	1.81	2.58	3.26	3.14	2.50	1.96	2.35	3.05	2.32	3.10	2.06	2.56	3.36	1.77	3.02
MnO	0.03	0.02	0.03	0.02	0.03	0.01	0.00	0.03	0.03	0.01	0.01	0.03	0.01	0.01	0.01
MgO	0.72	2.97	2.59	1.36	2.99	3.24	3.11	3.01	0.73	2.57	0.89	2.79	2.53	0.84	2.69
CaO	0.00	0.00	0.00	0.01	0.00	0.00	0.00	0.00	0.00	0.00	0.00	0.00	0.00	0.00	0.01
Na ₂ O	0.70	0.22	0.27	0.39	0.24	0.13	0.32	0.22	0.56	0.27	0.68	0.29	0.21	0.63	0.24
K ₂ O	9.44	10.18	10.22	9.91	10.19	10.49	10.22	10.11	9.52	10.40	9.75	10.08	10.17	9.79	10.04
Total	94.61	94.26	94.39	94.89	94.67	94.68	94.41	94.81	94.23	95.03	94.75	93.82	94.77	94.90	93.78
Si	3.115	3.415	3.413	3.223	3.420	3.450	3.411	3.423	3.096	3.390	3.139	3.389	3.376	3.112	3.377
Ti	0.008	0.006	0.009	0.010	0.007	0.005	0.006	0.011	0.006	0.008	0.009	0.007	0.008	0.005	0.004
Al	2.756	2.173	2.166	2.512	2.171	2.134	2.177	2.141	2.761	2.205	2.692	2.215	2.225	2.748	2.229
Cr	0.000	0.002	0.002	0.001	0.000	0.001	0.000	0.001	0.002	0.002	0.001	0.003	0.001	0.004	0.001
Fe ³⁺	0.000	0.000	0.000	0.000	0.000	0.000	0.000	0.000	0.000	0.000	0.000	0.000	0.000	0.000	0.000
Fe ²⁺	0.101	0.145	0.184	0.176	0.140	0.110	0.132	0.171	0.131	0.174	0.115	0.145	0.189	0.098	0.171
Mn	0.002	0.001	0.002	0.001	0.001	0.001	0.000	0.001	0.002	0.001	0.001	0.002	0.001	0.000	0.001
Mg	0.072	0.298	0.260	0.136	0.298	0.322	0.311	0.301	0.073	0.257	0.089	0.281	0.253	0.083	0.272
Ca	0.000	0.000	0.000	0.001	0.000	0.000	0.000	0.000	0.000	0.000	0.000	0.000	0.000	0.000	0.000
Na	0.091	0.028	0.036	0.051	0.031	0.017	0.041	0.029	0.073	0.035	0.088	0.038	0.028	0.082	0.031
K	0.803	0.874	0.880	0.848	0.871	0.894	0.876	0.865	0.817	0.889	0.831	0.869	0.872	0.832	0.868
Total	6.947	6.943	6.952	6.960	6.939	6.933	6.953	6.943	6.961	6.961	6.965	6.949	6.953	6.964	6.954

Table A.2 (continued) : Mineral chemistry of the measured phengitic white micas. Mineral formula calculations are based on 11 oxygens.

Phengite	178	178	178	392	392	392	392	392	392	392	392	392	392	392	392
	<i>64</i>	<i>95</i>	<i>102</i>	<i>1</i>	<i>3</i>	<i>5</i>	<i>6</i>	<i>9</i>	<i>11</i>	<i>14</i>	<i>15</i>	<i>18</i>	<i>20</i>	<i>21</i>	<i>23</i>
SiO ₂	49.77	51.02	50.77	51.84	51.76	51.51	52.25	51.09	51.76	51.92	51.28	51.56	51.35	51.82	50.86
TiO ₂	0.16	0.07	0.16	0.18	0.15	0.09	0.19	0.19	0.25	0.18	0.15	0.07	0.16	0.19	0.15
Al ₂ O ₃	27.91	27.11	26.92	30.59	30.94	31.94	28.48	28.83	31.67	27.90	31.75	31.30	28.08	30.87	31.31
Cr ₂ O ₃	0.00	0.00	0.01												
FeO	3.45	2.27	2.95	1.88	1.62	1.40	4.03	3.81	1.84	3.52	1.76	1.60	3.48	2.28	2.11
MnO	0.01	0.00	0.00	0.01	0.01	0.00	0.03	0.01	0.02	0.02	0.00	0.00	0.01	0.00	0.00
MgO	2.55	3.26	2.79	1.41	1.27	1.28	2.45	2.72	1.35	2.68	1.47	1.40	2.69	1.42	1.46
CaO	0.00	0.01	0.00	0.03	0.02	0.02	0.09	0.02	0.02	0.02	0.04	0.02	0.00	0.00	0.01
Na ₂ O	0.24	0.17	0.20	0.49	0.45	0.54	0.25	0.29	0.45	0.38	0.46	0.51	0.29	0.50	0.41
K ₂ O	9.87	10.31	10.21	9.72	9.85	9.64	8.18	9.82	9.68	10.06	9.53	9.76	9.96	9.76	9.68
Total	93.97	94.22	94.01	96.15	96.10	96.43	96.01	96.79	97.04	96.68	96.44	96.22	96.03	96.85	95.99
Si	3.372	3.431	3.432	3.386	3.380	3.345	3.426	3.360	3.347	3.416	3.335	3.362	3.400	3.368	3.334
Ti	0.008	0.004	0.008	0.009	0.007	0.004	0.009	0.009	0.012	0.009	0.007	0.003	0.008	0.009	0.007
Al	2.229	2.149	2.145	2.355	2.381	2.444	2.201	2.235	2.414	2.163	2.434	2.405	2.191	2.365	2.419
Cr	0.000	0.000	0.001	0.000	0.000	0.000	0.000	0.000	0.000	0.000	0.000	0.000	0.000	0.000	0.000
Fe ³⁺	0.000	0.000	0.000	0.000	0.000	0.000	0.000	0.000	0.000	0.000	0.000	0.000	0.000	0.000	0.000
Fe ²⁺	0.196	0.128	0.167	0.103	0.088	0.076	0.221	0.210	0.100	0.194	0.096	0.087	0.193	0.124	0.116
Mn	0.000	0.000	0.000	0.000	0.000	0.000	0.002	0.000	0.001	0.001	0.000	0.000	0.000	0.000	0.000
Mg	0.258	0.327	0.281	0.137	0.123	0.124	0.240	0.267	0.130	0.263	0.142	0.136	0.266	0.138	0.142
Ca	0.000	0.001	0.000	0.002	0.002	0.001	0.007	0.002	0.002	0.002	0.002	0.001	0.000	0.000	0.000
Na	0.031	0.022	0.026	0.062	0.057	0.068	0.032	0.036	0.056	0.049	0.058	0.064	0.037	0.063	0.052
K	0.853	0.884	0.880	0.810	0.821	0.799	0.684	0.824	0.799	0.844	0.791	0.812	0.841	0.809	0.809
Total	6.947	6.945	6.940	6.864	6.860	6.862	6.822	6.943	6.861	6.940	6.865	6.870	6.936	6.877	6.880

Table A.2 (continued) : Mineral chemistry of the measured phengitic white micas. Mineral formula calculations are based on 11 oxygens.

Phengite	392	392	392	392	392	392	392	392	392	392	392	392	392	392	392
	24	26	27	29	33	34	35	36	37	40	41	43	44	46	50
SiO ₂	51.38	51.34	51.20	51.22	53.10	52.47	51.45	52.54	52.24	51.20	51.49	51.07	51.90	51.51	51.55
TiO ₂	0.31	0.24	0.19	0.13	0.17	0.17	0.16	0.18	0.23	0.20	0.14	0.20	0.15	0.15	0.19
Al ₂ O ₃	29.31	31.87	31.31	31.83	27.05	27.30	27.76	27.65	30.29	30.96	31.11	27.77	27.37	26.54	28.01
Cr ₂ O ₃															
FeO	3.95	1.73	1.91	1.57	3.27	3.33	3.38	3.20	1.92	2.23	1.89	3.64	3.19	3.42	3.80
MnO	0.02	0.01	0.01	0.02	0.00	0.00	0.00	0.01	0.00	0.00	0.00	0.01	0.00	0.02	0.04
MgO	1.98	1.19	1.39	1.13	2.88	2.63	2.81	2.93	1.60	1.39	1.52	2.39	2.94	3.00	2.42
CaO	0.03	0.02	0.03	0.01	0.06	0.02	0.00	0.01	0.00	0.01	0.03	0.00	0.01	0.15	0.06
Na ₂ O	0.29	0.46	0.44	0.57	0.30	0.39	0.28	0.34	0.35	0.52	0.35	0.32	0.37	0.23	0.26
K ₂ O	9.35	9.68	9.59	9.68	9.93	9.91	10.03	9.86	9.71	9.43	9.69	9.95	10.17	11.18	10.21
Total	96.63	96.54	96.08	96.17	96.85	96.22	95.88	96.72	96.35	95.96	96.23	95.36	96.11	96.23	96.55
Si	3.372	3.337	3.347	3.340	3.477	3.459	3.411	3.442	3.402	3.354	3.360	3.409	3.433	3.433	3.405
Ti	0.015	0.012	0.010	0.006	0.008	0.008	0.008	0.009	0.011	0.010	0.007	0.010	0.007	0.007	0.009
Al	2.267	2.441	2.412	2.447	2.087	2.121	2.169	2.135	2.325	2.390	2.392	2.184	2.133	2.085	2.180
Cr	0.000	0.000	0.000	0.000	0.000	0.000	0.000	0.000	0.000	0.000	0.000	0.000	0.000	0.000	0.000
Fe ³⁺	0.000	0.000	0.000	0.000	0.000	0.000	0.000	0.000	0.000	0.000	0.000	0.000	0.000	0.000	0.000
Fe ²⁺	0.217	0.094	0.104	0.086	0.179	0.184	0.187	0.175	0.105	0.122	0.103	0.203	0.176	0.191	0.210
Mn	0.001	0.001	0.001	0.001	0.000	0.000	0.000	0.000	0.000	0.000	0.000	0.000	0.000	0.001	0.002
Mg	0.194	0.115	0.136	0.110	0.281	0.258	0.278	0.286	0.156	0.136	0.148	0.238	0.290	0.298	0.238
Ca	0.002	0.001	0.002	0.001	0.004	0.001	0.000	0.001	0.000	0.001	0.002	0.000	0.001	0.011	0.004
Na	0.037	0.058	0.055	0.072	0.038	0.049	0.036	0.043	0.044	0.066	0.045	0.041	0.048	0.030	0.033
K	0.783	0.803	0.800	0.805	0.829	0.833	0.848	0.824	0.807	0.788	0.807	0.847	0.858	0.951	0.860
Total	6.889	6.861	6.865	6.869	6.905	6.914	6.938	6.915	6.849	6.868	6.863	6.933	6.946	7.007	6.942

Table A.2 (continued) : Mineral chemistry of the measured phengitic white micas. Mineral formula calculations are based on 11 oxygens.

Phengite	626A	626A	626A	626A	626A	626A	626A	626A	626A	626A	626A	626A	626A	626A	626A
	47	48	51	52	53	58	60	61	64	65	67	75	77	79	83
SiO ₂	49.78	50.36	49.98	50.30	50.34	49.91	50.43	50.15	50.57	51.01	50.62	50.97	50.35	50.96	51.40
TiO ₂	0.11	0.10	0.11	0.12	0.08	0.12	0.16	0.10	0.12	0.07	0.16	0.13	0.14	0.10	0.09
Al ₂ O ₃	26.39	25.85	26.22	25.68	25.73	25.69	25.96	25.71	26.14	26.37	26.35	25.94	25.92	25.68	25.39
Cr ₂ O ₃	0.00	0.00	0.02	0.03	0.02	0.00	0.00	0.02	0.03	0.00	0.01	0.01	0.01	0.04	0.01
FeO	4.03	4.39	4.13	4.26	4.17	4.23	4.39	4.25	4.31	4.13	4.40	4.03	4.30	4.78	4.18
MnO	0.05	0.05	0.03	0.04	0.01	0.05	0.06	0.08	0.06	0.04	0.04	0.04	0.08	0.06	0.07
MgO	3.61	3.73	3.55	3.54	3.61	3.46	3.59	3.72	3.61	3.69	3.45	3.70	3.37	3.87	3.73
CaO	0.01	0.02	0.00	0.00	0.01	0.00	0.00	0.00	0.01	0.01	0.00	0.00	0.02	0.01	0.00
Na ₂ O	0.39	0.28	0.41	0.26	0.23	0.34	0.31	0.22	0.23	0.18	0.32	0.33	0.36	0.25	0.18
K ₂ O	10.62	10.83	10.57	10.76	10.91	10.64	10.79	10.98	10.86	11.12	10.86	10.59	10.62	10.84	11.00
Total	94.99	95.61	95.00	95.00	95.12	94.42	95.69	95.23	95.94	96.63	96.20	95.74	95.16	96.59	96.04
Si	3.373	3.398	3.385	3.411	3.410	3.405	3.398	3.398	3.397	3.400	3.392	3.419	3.407	3.407	3.445
Ti	0.006	0.005	0.005	0.006	0.004	0.006	0.008	0.005	0.006	0.004	0.008	0.006	0.007	0.005	0.005
Al	2.108	2.056	2.094	2.052	2.054	2.065	2.062	2.054	2.070	2.072	2.081	2.050	2.067	2.024	2.005
Cr	0.000	0.000	0.001	0.002	0.001	0.000	0.000	0.001	0.002	0.000	0.001	0.000	0.000	0.002	0.001
Fe ³⁺	0.000	0.000	0.000	0.000	0.000	0.000	0.000	0.000	0.000	0.000	0.000	0.000	0.000	0.000	0.000
Fe ²⁺	0.229	0.248	0.234	0.242	0.236	0.241	0.247	0.241	0.242	0.230	0.246	0.226	0.243	0.267	0.234
Mn	0.003	0.003	0.001	0.002	0.001	0.003	0.003	0.005	0.003	0.002	0.002	0.002	0.004	0.004	0.004
Mg	0.364	0.375	0.358	0.358	0.365	0.352	0.361	0.376	0.362	0.367	0.345	0.370	0.340	0.386	0.372
Ca	0.001	0.001	0.000	0.000	0.001	0.000	0.000	0.000	0.001	0.001	0.000	0.000	0.002	0.000	0.000
Na	0.051	0.036	0.054	0.035	0.030	0.044	0.041	0.029	0.030	0.023	0.042	0.043	0.047	0.032	0.023
K	0.918	0.932	0.913	0.931	0.943	0.926	0.928	0.950	0.931	0.946	0.928	0.906	0.916	0.924	0.940
Total	7.052	7.054	7.046	7.038	7.045	7.042	7.047	7.058	7.042	7.045	7.045	7.024	7.034	7.053	7.030

Table A.2 (continued) : Mineral chemistry of the measured phengitic white micas. Mineral formula calculations are based on 11 oxygens.

Phengite	626A	626A	702A	702A	702A	702A	702A	702A	702A	702A	702A	702A
	84	86	18	27	28	45	46	61	92	96	128	131
SiO ₂	50.49	50.94	52.31	53.47	50.94	51.13	50.27	51.96	52.47	51.68	51.25	51.97
TiO ₂	0.14	0.15	0.12	0.11	0.12	0.05	0.08	0.09	0.04	0.08	0.12	0.07
Al ₂ O ₃	25.90	25.99	25.83	25.70	25.11	24.48	25.96	23.36	23.96	24.34	25.47	25.13
Cr ₂ O ₃	0.03	0.03	0.00	0.00	0.00	0.03	0.00	0.07	0.01	0.02	0.03	0.01
FeO	4.43	4.70	3.58	4.05	4.22	3.98	3.76	4.00	3.33	3.77	3.57	3.71
MnO	0.02	0.04	0.03	0.04	0.04	0.02	0.05	0.02	0.00	0.00	0.00	0.04
MgO	3.67	3.64	3.81	3.85	3.62	4.04	3.50	4.27	4.03	4.09	3.69	3.62
CaO	0.00	0.00	0.10	0.04	0.01	0.38	0.02	0.19	0.05	0.04	0.03	0.05
Na ₂ O	0.35	0.30	0.10	0.11	0.14	0.13	0.10	0.13	0.07	0.11	0.23	0.10
K ₂ O	10.77	10.82	11.05	9.73	11.30	10.77	11.14	10.88	11.33	11.31	11.23	11.46
Total	95.79	96.60	96.93	97.11	95.51	95.01	94.87	94.96	95.29	95.44	95.61	96.16
Si	3.399	3.403	3.458	3.500	3.442	3.463	3.410	3.519	3.530	3.484	3.445	3.476
Ti	0.007	0.008	0.006	0.005	0.006	0.003	0.004	0.004	0.002	0.004	0.006	0.004
Al	2.055	2.046	2.012	1.983	2.000	1.954	2.075	1.865	1.900	1.934	2.018	1.981
Cr	0.002	0.002	0.000	0.000	0.000	0.002	0.000	0.004	0.001	0.001	0.002	0.000
Fe ³⁺	0.000	0.000	0.000	0.000	0.000	0.000	0.000	0.000	0.000	0.000	0.000	0.000
Fe ²⁺	0.249	0.263	0.198	0.222	0.239	0.226	0.213	0.227	0.187	0.212	0.201	0.207
Mn	0.001	0.002	0.002	0.002	0.002	0.001	0.003	0.001	0.000	0.000	0.000	0.002
Mg	0.368	0.362	0.375	0.376	0.365	0.408	0.354	0.431	0.404	0.411	0.370	0.361
Ca	0.000	0.000	0.007	0.003	0.001	0.027	0.001	0.014	0.004	0.003	0.002	0.004
Na	0.046	0.039	0.012	0.013	0.018	0.017	0.013	0.018	0.009	0.014	0.030	0.013
K	0.925	0.922	0.932	0.813	0.974	0.930	0.964	0.940	0.973	0.973	0.963	0.978
Total	7.051	7.046	7.002	6.917	7.048	7.030	7.037	7.022	7.009	7.037	7.036	7.026

Table A.2 (continued) : Mineral chemistry of the measured phengitic white micas. Mineral formula calculations are based on 11 oxygens.

Phengite	128	128	128	128
	<i>143</i>	<i>144</i>	<i>160</i>	<i>173</i>
SiO ₂	53.93	51.74	51.82	50.59
TiO ₂	0.07	0.04	0.07	0.05
Al ₂ O ₃	24.52	23.60	23.54	26.50
Cr ₂ O ₃	0.01	0.00	0.04	0.00
FeO	4.61	4.03	4.11	5.30
MnO	0.09	0.05	0.06	0.03
MgO	4.03	4.08	4.18	2.87
CaO	0.21	0.03	0.01	0.08
Na ₂ O	0.26	0.08	0.06	0.12
K ₂ O	9.35	11.45	11.36	9.36
Total	97.08	95.11	95.26	94.91
Si	3.537	3.509	3.509	3.414
Ti	0.004	0.002	0.004	0.002
Al	1.896	1.887	1.879	2.107
Cr	0.001	0.000	0.002	0.000
Fe ³⁺	0.000	0.000	0.000	0.000
Fe ²⁺	0.253	0.228	0.233	0.299
Mn	0.005	0.003	0.004	0.002
Mg	0.394	0.412	0.422	0.289
Ca	0.015	0.002	0.001	0.006
Na	0.033	0.011	0.007	0.016
K	0.782	0.991	0.982	0.805
Total	6.919	7.046	7.042	6.941

Table A.3 : Mineral chemistry of the measured paragonites. Mineral formula calculations are based on 11 oxygens.

Paragonite	775	775	775	775	775	775	775	775	775	753A	753A	753A	753A
	16	217	237	238	258	259	262	263	279	38	90	104	109
SiO ₂	47.91	47.41	48.66	48.91	46.71	46.50	49.19	49.03	47.53	47.07	46.27	46.70	46.65
TiO ₂	0.01	0.01	0.03	0.05	0.02	0.04	0.06	0.02	0.05	0.03	0.03	0.03	0.02
Al ₂ O ₃	40.05	38.83	39.96	39.55	40.21	40.17	40.38	39.97	38.87	39.47	40.13	39.41	40.17
Cr ₂ O ₃	0.02	0.01	0.01	0.02	0.07	0.04	0.03	0.01	0.01	0.02	0.02	0.00	0.00
FeO	0.98	0.79	0.31	0.43	0.27	0.19	0.13	0.28	0.45	0.81	0.62	0.55	0.30
MnO	0.06	0.01	0.02	0.00	0.02	0.01	0.02	0.00	0.01	0.02	0.02	0.04	0.00
MgO	0.16	0.24	0.11	0.10	0.03	0.02	0.05	0.14	0.23	0.25	0.14	0.14	0.14
CaO	0.05	0.03	0.05	0.03	0.36	0.38	0.42	0.05	0.04	0.11	0.02	0.04	0.05
Na ₂ O	6.89	7.08	7.36	7.25	7.04	7.12	6.66	6.77	7.47	6.64	6.84	6.20	6.57
K ₂ O	0.88	1.37	0.43	0.64	0.91	0.88	0.51	0.48	0.98	0.86	0.18	0.62	0.26
Total	97.02	95.77	96.93	96.98	95.62	95.35	97.44	96.74	95.64	95.27	94.25	93.73	94.15
Si	3.010	3.027	3.043	3.060	2.975	2.971	3.052	3.062	3.031	3.008	2.975	3.017	2.995
Ti	0.001	0.001	0.002	0.002	0.001	0.002	0.003	0.001	0.003	0.002	0.001	0.002	0.001
Al	2.966	2.922	2.945	2.917	3.019	3.024	2.952	2.942	2.922	2.972	3.042	3.001	3.038
Cr	0.001	0.000	0.001	0.001	0.003	0.002	0.002	0.000	0.000	0.001	0.001	0.000	0.000
Fe ³⁺	0.000	0.000	0.000	0.000	0.000	0.000	0.000	0.000	0.000	0.000	0.000	0.000	0.000
Fe ²⁺	0.052	0.042	0.016	0.022	0.014	0.010	0.007	0.014	0.024	0.043	0.033	0.029	0.016
Mn	0.003	0.000	0.001	0.000	0.001	0.001	0.001	0.000	0.000	0.001	0.001	0.002	0.000
Mg	0.015	0.022	0.010	0.010	0.003	0.002	0.005	0.013	0.022	0.024	0.014	0.014	0.013
Ca	0.004	0.002	0.004	0.002	0.024	0.026	0.028	0.003	0.003	0.007	0.001	0.003	0.003
Na	0.839	0.877	0.893	0.879	0.869	0.881	0.800	0.820	0.923	0.823	0.852	0.777	0.817
K	0.070	0.112	0.034	0.051	0.074	0.072	0.040	0.038	0.080	0.070	0.014	0.051	0.021
Total	6.960	7.005	6.947	6.944	6.984	6.991	6.889	6.894	7.007	6.951	6.935	6.895	6.905

Table A.3 (continued): Mineral chemistry of the measured paragonites. Mineral formula calculations are based on 11 oxygens.

Paragonite	178	178	178	178	178	392	392	392	392	392	392	392
	26	38	44	51	99	4	7	10	13	25	38	39
SiO ₂	47.02	46.77	46.90	46.86	46.81	47.69	47.94	49.91	47.65	47.05	47.46	47.23
TiO ₂	0.00	0.00	0.03	0.02	0.00	0.01	0.02	0.00	0.05	0.05	0.03	0.04
Al ₂ O ₃	39.51	39.95	39.55	39.62	40.01	40.69	40.29	37.88	40.22	40.28	40.35	40.48
Cr ₂ O ₃	0.03	0.04	0.02	0.01	0.01							
FeO	0.36	0.42	0.49	0.50	0.31	0.30	0.23	0.26	0.41	0.58	0.35	0.34
MnO	0.00	0.00	0.01	0.00	0.00	0.01	0.01	0.00	0.01	0.00	0.03	0.00
MgO	0.18	0.02	0.11	0.12	0.09	0.05	0.05	0.08	0.16	0.42	0.12	0.10
CaO	0.04	0.04	0.02	0.04	0.05	0.06	0.05	0.05	0.10	0.05	0.05	0.05
Na ₂ O	6.44	6.62	6.47	6.55	7.27	7.41	7.51	8.28	7.07	6.88	7.27	7.34
K ₂ O	0.70	0.32	0.63	0.80	0.41	0.47	0.34	0.50	0.73	1.02	0.41	0.52
Total	94.28	94.17	94.23	94.51	94.96	96.69	96.45	96.95	96.39	96.33	96.07	96.10
Si	3.021	3.004	3.016	3.009	2.992	2.994	3.014	3.128	3.004	2.977	2.998	2.986
Ti	0.000	0.000	0.002	0.001	0.000	0.001	0.001	0.000	0.002	0.002	0.001	0.002
Al	2.992	3.024	2.997	2.998	3.014	3.011	2.985	2.798	2.988	3.004	3.004	3.016
Cr	0.001	0.002	0.001	0.001	0.000	0.000	0.000	0.000	0.000	0.000	0.000	0.000
Fe ³⁺	0.000	0.000	0.000	0.000	0.000	0.000	0.000	0.000	0.000	0.000	0.000	0.000
Fe ²⁺	0.019	0.022	0.026	0.027	0.017	0.016	0.012	0.014	0.021	0.031	0.019	0.018
Mn	0.000	0.000	0.001	0.000	0.000	0.000	0.001	0.000	0.001	0.000	0.002	0.000
Mg	0.017	0.002	0.011	0.011	0.008	0.004	0.004	0.007	0.015	0.039	0.011	0.010
Ca	0.003	0.003	0.002	0.003	0.003	0.004	0.004	0.003	0.007	0.003	0.003	0.003
Na	0.802	0.824	0.806	0.815	0.901	0.902	0.915	1.006	0.864	0.844	0.890	0.900
K	0.057	0.026	0.052	0.065	0.033	0.037	0.027	0.040	0.058	0.082	0.033	0.042
Total	6.913	6.908	6.913	6.931	6.968	6.969	6.964	6.996	6.961	6.982	6.960	6.976

Table A.4 : Mineral chemistry of the measured garnets. Mineral formula calculations are based on 12 oxygens.

Garnet	775	775	775	775	775	775	775	775
	9	18	19	20	21	26	27	206
SiO ₂	36.36	36.01	36.53	36.09	36.52	36.13	36.65	37.00
TiO ₂	0.07	0.11	0.11	0.13	0.04	0.10	0.08	0.11
Al ₂ O ₃	21.70	21.63	21.62	21.70	21.70	21.34	21.56	21.63
Cr ₂ O ₃	0.00	0.02	0.01	0.05	0.00	0.01	0.02	0.03
FeO	13.00	12.34	14.65	12.55	16.87	12.78	15.12	12.12
MnO	25.10	26.25	24.41	25.93	21.85	26.10	21.25	26.84
MgO	0.31	0.34	0.33	0.34	0.33	0.31	0.19	0.28
CaO	3.49	2.50	3.26	3.14	3.12	2.95	5.52	2.66
Na ₂ O	0.02	0.04	0.00	0.02	0.03	0.02	0.05	0.07
K ₂ O	0.00	0.01	0.02	0.04	0.06	0.00	0.05	0.01
Total	100.04	99.24	100.94	99.99	100.53	99.75	100.48	100.74
Si	2.957	2.955	2.954	2.943	2.961	2.958	2.962	2.987
Ti	0.005	0.007	0.006	0.008	0.003	0.006	0.005	0.006
Al	2.080	2.092	2.061	2.085	2.074	2.059	2.054	2.058
Cr	0.000	0.001	0.001	0.003	0.000	0.001	0.001	0.002
Fe ³⁺	0.000	0.000	0.000	0.000	0.000	0.000	0.000	0.000
Fe ²⁺	0.884	0.847	0.991	0.856	1.144	0.875	1.022	0.818
Mn	1.729	1.824	1.672	1.791	1.501	1.810	1.455	1.836
Mg	0.037	0.042	0.039	0.042	0.040	0.038	0.023	0.034
Ca	0.304	0.219	0.283	0.274	0.271	0.259	0.478	0.230
Na	0.003	0.006	0.000	0.003	0.005	0.003	0.007	0.010
K	0.000	0.001	0.002	0.004	0.006	0.000	0.005	0.001
Total	8.000	7.995	8.010	8.009	8.005	8.008	8.012	7.982
X _{Sps}	59	62	56	60	51	61	49	63
X _{Grs}	10	7	9	9	9	9	16	8
X _{Alm}	30	29	33	29	39	29	34	28
X _{Py}	1	1	1	1	1	1	1	1
Tot	100	100	100	100	100	100	100	100

$X_{Sps} = \text{Mn}/(\text{Mn} + \text{Ca} + \text{Fe}^{2+} + \text{Mg})$, $X_{Grs} = \text{Ca}/(\text{Ca} + \text{Mn} + \text{Fe}^{2+} + \text{Mg})$,
 $X_{Alm} = \text{Fe}^{2+}/(\text{Fe}^{2+} + \text{Mn} + \text{Ca} + \text{Mg})$, $X_{Py} = \text{Mg}/(\text{Mg} + \text{Mn} + \text{Ca} + \text{Fe}^{2+})$.

Table A.4 (continued) : Mineral chemistry of the measured garnets. Mineral formula calculations are based on 12 oxygens.

Garnet	775	775	702A	702A	702A	702A	702A	702A
	209	275	34	35	<i>grt1a</i>	<i>grt1b</i>	<i>grt2a</i>	<i>grt2b</i>
SiO ₂	37.28	37.30	37.27	37.14	38.21	38.23	38.21	39.79
TiO ₂	0.14	0.06	0.15	0.19	0.12	0.18	0.08	0.11
Al ₂ O ₃	21.40	21.95	21.31	20.87	21.29	21.24	21.34	21.06
Cr ₂ O ₃	0.00	0.02	0.00	0.00	0.01	0.01	0.00	0.01
FeO	14.78	16.91	25.43	22.12	24.59	21.01	25.26	23.83
MnO	24.15	20.93	1.04	5.06	1.59	6.65	1.36	1.04
MgO	0.28	0.31	0.57	0.45	0.71	0.47	0.69	0.86
CaO	3.50	3.39	13.97	14.11	14.11	12.66	14.00	12.97
Na ₂ O	0.04	0.04	0.04	0.02	0.00	0.00	0.04	0.83
K ₂ O	0.01	0.26	0.01	0.01				
Total	101.58	101.17	99.79	99.96	100.63	100.46	100.98	100.49
Si	2.990	2.990	2.973	2.970	6.020	6.003	6.008	6.210
Ti	0.008	0.004	0.009	0.011	0.014	0.022	0.010	0.012
Al	2.022	2.073	2.003	1.967	3.953	3.931	3.955	3.874
Cr	0.000	0.001	0.000	0.000	0.001	0.002	0.000	0.001
Fe ³⁺	0.000	0.000	0.000	0.000	0.000	0.000	0.000	0.000
Fe ²⁺	0.991	1.133	1.696	1.479	3.240	2.759	3.323	3.110
Mn	1.641	1.421	0.070	0.343	0.212	0.884	0.181	0.137
Mg	0.033	0.037	0.068	0.053	0.167	0.109	0.162	0.200
Ca	0.301	0.291	1.193	1.209	2.382	2.299	2.359	2.169
Na	0.006	0.006	0.006	0.002	0.000	0.001	0.012	0.250
K	0.001	0.027	0.001	0.001	0.000	0.000	0.000	0.000
Total	7.994	7.985	8.020	8.037	15.989	16.010	16.010	15.963
X _{Sps}	55	49	2	11	4	15	3	2
X _{Grs}	10	10	39	39	40	38	39	39
X _{Alm}	33	39	56	48	54	46	55	55
X _{Py}	1	1	2	2	3	2	3	4
Tot	100	100	100	100	100	100	100	100

X_{Sps}= Mn/(Mn+Ca+Fe²⁺+Mg), X_{Grs}= Ca/(Ca+Mn+ Fe²⁺+Mg),
X_{Alm}= Fe²⁺/(Fe²⁺+Mn+Ca+Mg), X_{Py}= Mg/(Mg+Mn+Ca+ Fe²⁺).

Table A.4 (continued) : Mineral chemistry of the measured garnets. Mineral formula calculations are based on 12 oxygens.

Garnet	702A	702A	702A	702A	702A	702A	702A	702A
	<i>grt3a</i>	<i>grt3b</i>	<i>grt4a</i>	<i>grt4b</i>	<i>grt5a</i>	<i>grt5b</i>	<i>grt6a</i>	<i>grt6b</i>
SiO ₂	38.05	37.08	37.79	38.00	38.16	38.44	37.85	38.44
TiO ₂	0.23	0.10	0.21	0.11	0.19	0.14	0.14	0.13
Al ₂ O ₃	21.28	19.65	21.27	21.27	21.29	21.29	21.29	21.49
Cr ₂ O ₃	0.00	0.00	0.00	0.00	0.00	0.00	0.00	0.00
FeO	21.36	24.09	21.36	25.02	20.46	23.93	22.70	25.11
MnO	5.31	1.01	5.51	1.23	6.58	2.48	4.91	1.32
MgO	0.44	2.73	0.49	0.61	0.43	0.56	0.54	0.65
CaO	13.42	12.88	13.96	14.17	13.82	14.09	13.51	12.98
Na ₂ O	0.03	0.09	0.01	0.03	0.01	0.00	0.01	0.00
K ₂ O								
Total	100.12	97.64	100.60	100.44	100.94	100.93	100.94	100.12
Si	5.986	6.012	5.978	6.006	6.010	6.039	5.978	6.024
Ti	0.027	0.013	0.025	0.013	0.022	0.017	0.016	0.016
Al	3.946	3.755	3.965	3.962	3.952	3.942	3.962	3.970
Cr	0.000	0.000	0.000	0.000	0.000	0.000	0.000	0.000
Fe ³⁺	0.000	0.000	0.000	0.000	0.000	0.000	0.000	0.000
Fe ²⁺	2.810	3.267	2.826	3.307	2.694	3.143	2.999	3.291
Mn	0.707	0.139	0.738	0.164	0.877	0.330	0.657	0.176
Mg	0.104	0.660	0.116	0.145	0.102	0.131	0.127	0.151
Ca	2.430	2.238	2.366	2.399	2.331	2.372	2.286	2.348
Na	0.008	0.029	0.002	0.008	0.002	0.001	0.002	0.000
K	0.000	0.000	0.000	0.000	0.000	0.000	0.000	0.000
Total	16.018	16.113	16.016	16.005	15.990	15.974	16.027	15.976
X _{Sps}	12	2	12	3	15	6	11	3
X _{Grs}	40	36	39	40	39	40	38	39
X _{Alm}	46	52	47	55	45	53	49	55
X _{Py}	2	10	2	2	2	2	2	3
Tot	100	100	100	100	100	100	100	100

$X_{Sps} = \text{Mn}/(\text{Mn} + \text{Ca} + \text{Fe}^{2+} + \text{Mg})$, $X_{Grs} = \text{Ca}/(\text{Ca} + \text{Mn} + \text{Fe}^{2+} + \text{Mg})$,
 $X_{Alm} = \text{Fe}^{2+}/(\text{Fe}^{2+} + \text{Mn} + \text{Ca} + \text{Mg})$, $X_{Py} = \text{Mg}/(\text{Mg} + \text{Mn} + \text{Ca} + \text{Fe}^{2+})$.

Table A.4 (continued) : Mineral chemistry of the measured garnets. Mineral formula calculations are based on 12 oxygens.

Garnet	702A	702A	702A	702A
	<i>grt7a</i>	<i>grt7b</i>	<i>grt8a</i>	<i>grt8b</i>
SiO ₂	38.10	50.84	38.20	38.26
TiO ₂	0.18	0.04	0.19	0.14
Al ₂ O ₃	21.25	19.26	21.28	21.27
Cr ₂ O ₃	0.02	0.01	0.01	0.00
FeO	20.41	12.01	21.24	23.67
MnO	6.76	0.68	5.86	2.93
MgO	0.46	0.72	0.49	0.58
CaO	12.95	6.67	13.01	13.21
Na ₂ O	0.01	7.73	0.00	0.01
K ₂ O				
Total	100.14	97.96	100.28	100.07
Si	5.996	7.525	6.001	6.012
Ti	0.022	0.005	0.022	0.016
Al	3.942	3.360	3.940	3.941
Cr	0.002	0.001	0.001	0.000
Fe ³⁺	0.000	0.000	0.000	0.000
Fe ²⁺	2.686	1.486	2.790	3.111
Mn	0.902	0.085	0.780	0.390
Mg	0.108	0.160	0.116	0.137
Ca	2.352	1.058	2.358	2.392
Na	0.002	2.219	0.000	0.003
K	0.000	0.000	0.000	0.000
Total	16.012	15.898	16.008	16.002
X _{Sps}	15	3	13	6
X _{Grs}	39	38	39	40
X _{Alm}	44	53	46	52
X _{Py}	2	6	2	2
Tot	100	100	100	100

$$X_{\text{Sps}} = \text{Mn}/(\text{Mn}+\text{Ca}+\text{Fe}^{2+}+\text{Mg}), X_{\text{Grs}} = \text{Ca}/(\text{Ca}+\text{Mn}+\text{Fe}^{2+}+\text{Mg}), \\ X_{\text{Alm}} = \text{Fe}^{2+}/(\text{Fe}^{2+}+\text{Mn}+\text{Ca}+\text{Mg}), X_{\text{Py}} = \text{Mg}/(\text{Mg}+\text{Mn}+\text{Ca}+\text{Fe}^{2+}).$$

Table A.5 : Mineral chemistry of the measured chloritoids. Mineral formula calculations are based on 12 oxygens.

Chloritoid	775	775	775	775	775	775	775	775
	210	211	212	214	215	274	277	280
SiO ₂	24.45	24.34	24.77	24.38	24.62	24.52	24.59	24.93
TiO ₂	0.02	0.02	0.02	0.03	0.02	0.01	0.00	0.04
Al ₂ O ₃	41.15	40.82	40.27	41.10	40.93	41.25	41.42	41.47
Cr ₂ O ₃	0.02	0.05	0.01	0.04	0.04	0.05	0.02	0.04
FeO	24.18	24.39	24.77	24.14	24.56	23.94	23.94	23.75
MnO	2.96	2.54	2.32	2.71	2.57	3.32	2.72	2.25
MgO	1.24	1.29	1.60	1.27	1.30	1.11	1.18	1.66
CaO	0.02	0.01	0.01	0.01	0.02	0.01	0.01	0.00
Na ₂ O	0.01	0.00	0.01	0.01	0.03	0.00	0.00	0.00
K ₂ O	0.00	0.01	0.02	0.03	0.03	0.03	0.04	0.03
Total	94.04	93.45	93.80	93.73	94.12	94.24	93.92	94.18
Si	2.005	2.009	2.038	2.005	2.018	2.008	2.013	2.028
Ti	0.001	0.001	0.001	0.002	0.001	0.001	0.000	0.003
Al	3.978	3.970	3.905	3.983	3.954	3.981	3.998	3.975
Cr	0.001	0.003	0.001	0.003	0.003	0.003	0.001	0.003
Fe ³⁺	0.000	0.000	0.000	0.000	0.000	0.000	0.000	0.000
Fe ²⁺	1.659	1.683	1.704	1.660	1.683	1.639	1.639	1.615
Mn	0.205	0.177	0.162	0.189	0.179	0.230	0.189	0.155
Mg	0.152	0.158	0.196	0.155	0.158	0.135	0.144	0.201
Ca	0.001	0.001	0.001	0.001	0.001	0.001	0.001	0.000
Na	0.002	0.000	0.001	0.002	0.005	0.000	0.000	0.000
K	0.000	0.001	0.003	0.003	0.003	0.003	0.004	0.003
Total	8.005	8.004	8.010	8.003	8.006	8.001	7.989	7.982
X _{Mn}	10	9	8	9	9	11	10	8
X _{Mg}	8	8	10	8	8	7	7	10
X _{Fe}	82	83	83	83	83	82	83	82
Tot	100	100	100	100	100	100	100	100

$X_{Mn} = Mn / (Mn + Fe^{2+} + Mg)$, $X_{Mg} = Mg / (Mg + Mn + Fe^{2+})$, $X_{Fe} = Fe^{2+} / (Fe^{2+} + Mn + Mg)$.

Table A.5 (continued) : Mineral chemistry of the measured chloritoids. Mineral formula calculations are based on 12 oxygens.

Chloritoid	775	775	775	775	775	753A	753A	753A
	14	15	28	29	30	70	71	72
SiO ₂	24.20	24.04	24.10	23.94	23.96	24.34	24.47	24.49
TiO ₂	0.02	0.01	0.74	0.00	0.00	0.02	0.08	0.05
Al ₂ O ₃	41.52	40.88	41.37	41.50	41.82	41.88	41.82	41.85
Cr ₂ O ₃	0.02	0.04	0.03	0.03	0.04	0.01	0.06	0.02
FeO	23.45	24.06	23.57	23.41	22.61	23.89	24.49	24.37
MnO	2.33	2.95	2.79	2.99	2.60	3.42	2.79	2.30
MgO	1.54	1.38	1.22	1.26	1.40	1.25	1.35	1.62
CaO	0.01	0.04	0.01	0.00	0.01	0.02	0.03	0.01
Na ₂ O	0.00	0.02	0.01	0.02	0.01	0.00	0.01	0.00
K ₂ O	0.02	0.07	0.01	0.01	0.02	0.00	0.01	0.00
Total	93.10	93.47	93.84	93.16	92.47	94.84	95.12	94.71
Si	1.993	1.987	1.976	1.977	1.981	1.980	1.984	1.988
Ti	0.001	0.000	0.045	0.000	0.000	0.001	0.005	0.003
Al	4.029	3.982	3.996	4.040	4.075	4.015	3.997	4.004
Cr	0.001	0.002	0.002	0.002	0.002	0.001	0.004	0.001
Fe ³⁺	0.000	0.000	0.000	0.000	0.000	0.000	0.000	0.000
Fe ²⁺	1.615	1.663	1.616	1.617	1.563	1.625	1.661	1.655
Mn	0.162	0.206	0.194	0.209	0.182	0.236	0.192	0.158
Mg	0.188	0.171	0.149	0.155	0.173	0.151	0.163	0.196
Ca	0.001	0.003	0.001	0.000	0.001	0.002	0.003	0.001
Na	0.000	0.004	0.001	0.004	0.002	0.000	0.002	0.000
K	0.002	0.007	0.001	0.001	0.002	0.000	0.001	0.000
Total	7.992	8.026	7.981	8.004	7.982	8.011	8.012	8.006
X _{Mn}	8	10	10	11	9	12	10	8
X _{Mg}	10	8	8	8	9	8	8	10
X _{Fe}	82	82	82	82	81	81	82	82
Tot	100	100	100	100	100	100	100	100

$X_{Mn} = Mn / (Mn + Fe^{2+} + Mg)$, $X_{Mg} = Mg / (Mg + Mn + Fe^{2+})$, $X_{Fe} = Fe^{2+} / (Fe^{2+} + Mn + Mg)$.

Table A.5 (continued) : Mineral chemistry of the measured chloritoids. Mineral formula calculations are based on 12 oxygens.

Chloritoid	753A	753A	753A	753A	753A	753A	753A	753A
	73	74	82	128	132	134	135	137
SiO ₂	24.39	24.40	24.61	24.41	24.51	24.16	24.09	24.46
TiO ₂	0.00	0.02	0.02	0.00	0.03	0.02	0.03	0.01
Al ₂ O ₃	41.99	42.27	42.17	41.90	42.33	41.74	41.99	42.03
Cr ₂ O ₃	0.05	0.03	0.00	0.03	0.03	0.00	0.00	0.00
FeO	23.81	23.89	23.93	24.01	24.10	23.93	23.82	23.97
MnO	1.86	1.69	3.00	2.65	2.26	2.60	1.91	2.77
MgO	1.82	1.82	1.48	1.35	1.51	1.24	1.72	1.37
CaO	0.01	0.00	0.01	0.01	0.02	0.01	0.02	0.08
Na ₂ O	0.00	0.01	0.00	0.00	0.00	0.01	0.00	0.00
K ₂ O	0.04	0.04	0.03	0.05	0.01	0.01	0.02	0.01
Total	93.97	94.16	95.24	94.41	94.80	93.71	93.60	94.69
Si	1.987	1.982	1.988	1.988	1.983	1.983	1.972	1.986
Ti	0.000	0.001	0.001	0.000	0.002	0.001	0.002	0.000
Al	4.031	4.046	4.014	4.023	4.037	4.037	4.051	4.023
Cr	0.003	0.002	0.000	0.002	0.002	0.000	0.000	0.000
Fe ³⁺	0.000	0.000	0.000	0.000	0.000	0.000	0.000	0.000
Fe ²⁺	1.622	1.623	1.617	1.636	1.631	1.643	1.630	1.628
Mn	0.129	0.117	0.205	0.183	0.155	0.180	0.132	0.190
Mg	0.221	0.220	0.178	0.164	0.182	0.151	0.210	0.166
Ca	0.001	0.000	0.001	0.001	0.002	0.001	0.002	0.007
Na	0.000	0.001	0.000	0.000	0.000	0.001	0.000	0.000
K	0.004	0.004	0.003	0.005	0.001	0.001	0.002	0.001
Total	7.998	7.995	8.006	8.002	7.996	7.999	8.002	8.002
X _{Mn}	7	6	10	9	8	9	7	10
X _{Mg}	11	11	9	8	9	8	11	8
X _{Fe}	82	83	81	82	83	83	83	82
Tot	100	100	100	100	100	100	100	100

$X_{Mn} = Mn / (Mn + Fe^{2+} + Mg)$, $X_{Mg} = Mg / (Mg + Mn + Fe^{2+})$, $X_{Fe} = Fe^{2+} / (Fe^{2+} + Mn + Mg)$.

Table A.5 (continued) : Mineral chemistry of the measured chloritoids. Mineral formula calculations are based on 12 oxygens.

Chloritoid	753A	753A	753A	753A	178	178	178	178
	<i>138</i>	<i>140</i>	<i>141</i>	<i>142</i>	<i>19</i>	<i>20</i>	<i>28</i>	<i>31</i>
SiO ₂	24.48	24.28	24.53	24.30	24.63	24.68	24.59	24.76
TiO ₂	0.00	0.01	0.00	0.00	0.00	0.02	0.01	0.02
Al ₂ O ₃	42.15	41.75	41.64	41.85	42.59	42.23	42.50	42.48
Cr ₂ O ₃	0.00	0.02	0.05	0.04	0.04	0.02	0.01	0.00
FeO	24.11	23.32	22.88	24.26	24.43	25.61	24.30	24.31
MnO	2.44	2.86	2.92	2.26	0.57	0.80	0.57	0.53
MgO	1.50	1.31	1.38	1.56	2.73	1.65	2.59	2.70
CaO	0.01	0.02	0.01	0.02	0.00	0.00	0.01	0.00
Na ₂ O	0.01	0.00	0.00	0.00	0.00	0.00	0.02	0.00
K ₂ O	0.01	0.00	0.02	0.04	0.01	0.03	0.03	0.02
Total	94.70	93.57	93.42	94.33	94.99	95.05	94.63	94.81
Si	1.985	1.991	2.011	1.981	1.976	1.992	1.980	1.988
Ti	0.000	0.000	0.000	0.000	0.000	0.001	0.000	0.001
Al	4.029	4.036	4.022	4.021	4.026	4.018	4.032	4.020
Cr	0.000	0.001	0.003	0.003	0.002	0.001	0.001	0.000
Fe ³⁺	0.000	0.000	0.000	0.000	0.000	0.000	0.000	0.000
Fe ²⁺	1.635	1.600	1.568	1.654	1.639	1.729	1.636	1.632
Mn	0.168	0.199	0.202	0.156	0.039	0.055	0.039	0.036
Mg	0.181	0.161	0.168	0.189	0.326	0.199	0.310	0.323
Ca	0.001	0.001	0.001	0.001	0.000	0.000	0.001	0.000
Na	0.001	0.000	0.000	0.000	0.000	0.000	0.003	0.000
K	0.001	0.000	0.002	0.004	0.001	0.003	0.003	0.002
Total	8.001	7.990	7.978	8.009	8.010	7.999	8.006	8.002
X _{Mn}	8	10	10	8	2	3	2	2
X _{Mg}	9	8	9	9	16	10	16	16
X _{Fe}	82	82	81	83	82	87	82	82
Tot	100	100	100	100	100	100	100	100

X_{Mn}= Mn/(Mn+Fe²⁺+Mg), X_{Mg}= Mg/(Mg+Mn+ Fe²⁺), X_{Fe}= Fe²⁺/(Fe²⁺+Mn+Mg).

Table A.5 (continued) : Mineral chemistry of the measured chloritoids. Mineral formula calculations are based on 12 oxygens.

Chloritoid	178	178	178	178	178	178	178	178
	32	34	35	36	39	40	41	48
SiO ₂	24.71	24.41	24.40	24.13	24.64	24.95	24.90	24.42
TiO ₂	0.06	0.00	0.01	0.03	0.02	0.00	0.02	0.10
Al ₂ O ₃	42.21	42.37	41.91	41.73	42.15	42.53	42.77	41.70
Cr ₂ O ₃	0.00	0.03	0.03	0.04	0.07	0.02	0.06	0.04
FeO	25.71	25.72	25.29	25.21	25.44	24.64	24.33	25.89
MnO	0.80	0.47	0.78	0.87	0.73	0.56	0.56	0.78
MgO	1.72	1.86	1.91	1.75	1.70	2.61	2.71	1.65
CaO	0.01	0.00	0.01	0.01	0.00	0.00	0.00	0.01
Na ₂ O	0.00	0.00	0.01	0.00	0.01	0.01	0.00	0.03
K ₂ O	0.04	0.02	0.01	0.01	0.04	0.01	0.01	0.04
Total	95.25	94.87	94.36	93.76	94.79	95.34	95.36	94.64
Si	1.992	1.973	1.984	1.976	1.993	1.995	1.987	1.985
Ti	0.003	0.000	0.000	0.002	0.001	0.000	0.001	0.006
Al	4.009	4.036	4.015	4.027	4.018	4.007	4.022	3.997
Cr	0.000	0.002	0.002	0.003	0.004	0.001	0.004	0.003
Fe ³⁺	0.000	0.000	0.000	0.000	0.000	0.000	0.000	0.000
Fe ²⁺	1.733	1.739	1.719	1.726	1.721	1.647	1.624	1.761
Mn	0.055	0.032	0.054	0.060	0.050	0.038	0.038	0.053
Mg	0.206	0.224	0.232	0.213	0.205	0.311	0.322	0.200
Ca	0.001	0.000	0.001	0.001	0.000	0.000	0.000	0.001
Na	0.000	0.000	0.001	0.000	0.001	0.001	0.000	0.004
K	0.004	0.002	0.001	0.001	0.004	0.001	0.001	0.004
Total	8.002	8.009	8.008	8.008	7.997	8.002	8.000	8.013
X _{Mn}	3	2	3	3	3	2	2	3
X _{Mg}	10	11	12	11	10	16	16	10
X _{Fe}	87	87	86	86	87	83	82	87
Tot	100	100	100	100	100	100	100	100

$X_{Mn} = Mn / (Mn + Fe^{2+} + Mg)$, $X_{Mg} = Mg / (Mg + Mn + Fe^{2+})$, $X_{Fe} = Fe^{2+} / (Fe^{2+} + Mn + Mg)$.

Table A.5 (continued) : Mineral chemistry of the measured chloritoids. Mineral formula calculations are based on 12 oxygens.

Chloritoid	178	178	178	178	178	178	178	178
	49	50	54	55	96	97	98	178-75
SiO ₂	24.53	24.76	24.31	24.44	23.96	23.48	23.94	25.42
TiO ₂	0.05	0.00	0.01	0.00	0.08	0.07	0.01	0.00
Al ₂ O ₃	42.71	42.57	42.32	42.36	41.41	40.23	41.76	40.49
Cr ₂ O ₃	0.03	0.00	0.04	0.02	0.06	0.05	0.06	
FeO	24.54	24.52	25.62	24.76	24.88	25.02	25.06	24.27
MnO	0.54	0.57	0.82	0.59	0.80	0.88	0.46	0.56
MgO	2.65	2.60	1.69	2.40	1.93	1.62	2.11	2.64
CaO	0.01	0.00	0.00	0.01	0.01	0.02	0.01	0.02
Na ₂ O	0.01	0.01	0.00	0.00	0.03	0.00	0.03	0.03
K ₂ O	0.02	0.01	0.03	0.01	0.05	0.03	0.04	0.00
Total	95.11	95.04	94.85	94.58	93.20	91.40	93.48	93.43
Si	1.967	1.985	1.969	1.974	1.973	1.979	1.963	2.073
Ti	0.003	0.000	0.001	0.000	0.005	0.004	0.000	0.000
Al	4.036	4.023	4.040	4.032	4.019	3.996	4.035	3.891
Cr	0.002	0.000	0.003	0.001	0.004	0.003	0.004	0.000
Fe ³⁺	0.000	0.000	0.000	0.000	0.000	0.000	0.000	0.000
Fe ²⁺	1.646	1.644	1.735	1.672	1.713	1.764	1.719	1.655
Mn	0.037	0.039	0.056	0.040	0.056	0.063	0.032	0.039
Mg	0.317	0.311	0.204	0.289	0.236	0.203	0.258	0.321
Ca	0.001	0.000	0.000	0.000	0.001	0.001	0.000	0.002
Na	0.002	0.001	0.001	0.000	0.005	0.000	0.004	0.005
K	0.002	0.001	0.003	0.001	0.005	0.003	0.004	0.000
Total	8.013	8.004	8.011	8.010	8.016	8.018	8.021	7.984
X _{Mn}	2	2	3	2	3	3	2	2
X _{Mg}	16	16	10	14	12	10	13	16
X _{Fe}	82	82	87	84	85	87	86	82
Tot	100	100	100	100	100	100	100	100

$X_{Mn} = Mn / (Mn + Fe^{2+} + Mg)$, $X_{Mg} = Mg / (Mg + Mn + Fe^{2+})$, $X_{Fe} = Fe^{2+} / (Fe^{2+} + Mn + Mg)$.

Table A.5 (continued) : Mineral chemistry of the measured chloritoids. Mineral formula calculations are based on 12 oxygens.

Chloritoid	178	178	178	178	178	178	178	178
	<i>178-76</i>	<i>178-77</i>	<i>178-78</i>	<i>178-79</i>	<i>178-83</i>	<i>178-84</i>	<i>178-85</i>	<i>178-86</i>
SiO ₂	25.49	25.43	25.37	25.13	25.31	25.17	25.18	25.20
TiO ₂	0.01	0.04	0.00	0.00	0.02	0.03	0.04	0.03
Al ₂ O ₃	40.03	40.56	40.50	40.45	40.18	40.26	39.47	40.06
Cr ₂ O ₃								
FeO	25.26	23.97	23.92	24.11	25.52	25.44	25.32	25.22
MnO	0.50	0.53	0.56	0.64	0.80	0.76	0.66	0.66
MgO	2.13	2.77	2.75	2.57	1.76	1.99	1.96	2.01
CaO	0.01	0.02	0.02	0.01	0.00	0.01	0.01	0.00
Na ₂ O	0.00	0.01	0.01	0.00	0.02	0.00	0.02	0.04
K ₂ O	0.02	0.04	0.02	0.05	0.00	0.01	0.08	0.00
Total	93.45	93.37	93.16	92.96	93.61	93.67	92.74	93.21
Si	2.088	2.072	2.071	2.061	2.075	2.062	2.085	2.072
Ti	0.001	0.002	0.000	0.000	0.001	0.002	0.003	0.002
Al	3.864	3.894	3.897	3.909	3.883	3.888	3.851	3.882
Cr	0.000	0.000	0.000	0.000	0.000	0.000	0.000	0.000
Fe ³⁺	0.000	0.000	0.000	0.000	0.000	0.000	0.000	0.000
Fe ²⁺	1.730	1.633	1.633	1.653	1.750	1.743	1.753	1.734
Mn	0.035	0.037	0.039	0.045	0.055	0.053	0.047	0.046
Mg	0.260	0.336	0.335	0.314	0.215	0.243	0.242	0.246
Ca	0.001	0.002	0.002	0.001	0.000	0.000	0.001	0.000
Na	0.000	0.002	0.002	0.000	0.002	0.000	0.003	0.006
K	0.002	0.004	0.002	0.005	0.000	0.001	0.009	0.000
Total	7.980	7.982	7.982	7.988	7.983	7.992	7.993	7.988
X _{Mn}	2	2	2	2	3	3	2	2
X _{Mg}	13	17	17	16	11	12	12	12
X _{Fe}	85	81	81	82	87	85	86	86
Tot	100	100	100	100	100	100	100	100

X_{Mn}= Mn/(Mn+Fe²⁺+Mg), X_{Mg}= Mg/(Mg+Mn+ Fe²⁺), X_{Fe}= Fe²⁺/(Fe²⁺+Mn+Mg).

Table A.5 (continued) : Mineral chemistry of the measured chloritoids. Mineral formula calculations are based on 12 oxygens.

Chloritoid	178	178	178	178	178	178	178	178
	<i>178-87</i>	<i>178-88</i>	<i>178-89</i>	<i>178-90</i>	<i>178-91</i>	<i>178-92</i>	<i>178-93</i>	<i>178-94</i>
SiO ₂	25.51	25.12	25.36	25.24	25.53	25.34	25.10	25.11
TiO ₂	0.00	0.00	0.00	0.01	0.03	0.02	0.00	0.00
Al ₂ O ₃	40.33	40.14	40.00	40.15	40.28	40.11	40.09	39.98
Cr ₂ O ₃								
FeO	25.17	25.43	25.36	25.14	25.68	25.31	25.57	25.34
MnO	0.59	0.75	0.89	0.81	0.93	0.79	0.80	0.89
MgO	2.12	1.93	1.94	2.00	1.73	2.16	1.95	1.71
CaO	0.00	0.00	0.00	0.01	0.01	0.00	0.01	0.01
Na ₂ O	0.02	0.00	0.00	0.00	0.00	0.02	0.01	0.00
K ₂ O	0.02	0.00	0.03	0.02	0.00	0.02	0.00	0.06
Total	93.76	93.38	93.58	93.38	94.19	93.77	93.53	93.09
Si	2.082	2.065	2.080	2.072	2.082	2.073	2.062	2.072
Ti	0.000	0.000	0.000	0.001	0.002	0.002	0.000	0.000
Al	3.879	3.889	3.867	3.884	3.871	3.867	3.882	3.888
Cr	0.000	0.000	0.000	0.000	0.000	0.000	0.000	0.000
Fe ³⁺	0.000	0.000	0.000	0.000	0.000	0.000	0.000	0.000
Fe ²⁺	1.718	1.748	1.739	1.726	1.751	1.731	1.757	1.749
Mn	0.041	0.052	0.062	0.057	0.064	0.055	0.056	0.062
Mg	0.258	0.237	0.237	0.245	0.210	0.263	0.239	0.210
Ca	0.000	0.000	0.000	0.001	0.001	0.000	0.001	0.001
Na	0.003	0.001	0.000	0.000	0.000	0.002	0.001	0.000
K	0.002	0.000	0.003	0.002	0.000	0.002	0.000	0.006
Total	7.981	7.991	7.989	7.986	7.981	7.995	7.998	7.987
X _{Mn}	2	3	3	3	3	3	3	3
X _{Mg}	13	12	12	12	10	13	12	10
X _{Fe}	85	86	85	85	86	84	86	87
Tot	100	100	100	100	100	100	100	100

$X_{Mn} = Mn / (Mn + Fe^{2+} + Mg)$, $X_{Mg} = Mg / (Mg + Mn + Fe^{2+})$, $X_{Fe} = Fe^{2+} / (Fe^{2+} + Mn + Mg)$.

Table A.5 (continued) : Mineral chemistry of the measured chloritoids. Mineral formula calculations are based on 12 oxygens.

Chloritoid	178	178	178	178	178	178	178	178
	<i>178-95</i>	<i>178-96</i>	<i>178-97</i>	<i>178-98</i>	<i>178-99</i>	<i>178-100</i>	<i>178-101</i>	<i>178-102</i>
SiO ₂	25.32	25.53	25.45	25.46	25.56	25.35	25.31	25.31
TiO ₂	0.04	0.01	0.00	0.07	0.01	0.00	0.04	0.03
Al ₂ O ₃	39.76	39.86	39.82	39.32	40.02	40.34	40.05	40.04
Cr ₂ O ₃								
FeO	25.04	25.50	25.90	25.39	25.37	25.10	25.57	24.99
MnO	0.79	0.74	0.60	0.65	0.89	0.76	0.91	0.73
MgO	2.18	2.01	1.99	1.90	2.01	2.24	1.67	2.04
CaO	0.01	0.02	0.01	0.01	0.02	0.01	0.00	0.00
Na ₂ O	0.04	0.00	0.00	0.04	0.00	0.00	0.00	0.00
K ₂ O	0.03	0.03	0.04	0.30	0.02	0.02	0.01	0.05
Total	93.21	93.70	93.81	93.13	93.89	93.83	93.57	93.19
Si	2.082	2.091	2.085	2.101	2.088	2.069	2.078	2.080
Ti	0.003	0.001	0.000	0.004	0.000	0.000	0.003	0.002
Al	3.854	3.847	3.845	3.825	3.854	3.880	3.876	3.877
Cr	0.000	0.000	0.000	0.000	0.000	0.000	0.000	0.000
Fe ³⁺	0.000	0.000	0.000	0.000	0.000	0.000	0.000	0.000
Fe ²⁺	1.722	1.746	1.775	1.753	1.733	1.713	1.756	1.717
Mn	0.055	0.051	0.042	0.045	0.062	0.053	0.064	0.051
Mg	0.267	0.245	0.243	0.234	0.245	0.273	0.204	0.250
Ca	0.001	0.002	0.001	0.000	0.001	0.001	0.000	0.000
Na	0.006	0.000	0.000	0.007	0.000	0.000	0.000	0.000
K	0.003	0.003	0.004	0.032	0.002	0.002	0.001	0.005
Total	7.993	7.987	7.995	8.001	7.985	7.992	7.982	7.982
X _{Mn}	3	2	2	2	3	3	3	3
X _{Mg}	13	12	12	12	12	13	10	12
X _{Fe}	84	85	86	86	85	84	87	85
Tot	100	100	100	100	100	100	100	100

$X_{Mn} = Mn / (Mn + Fe^{2+} + Mg)$, $X_{Mg} = Mg / (Mg + Mn + Fe^{2+})$, $X_{Fe} = Fe^{2+} / (Fe^{2+} + Mn + Mg)$.

Table A.5 (continued) : Mineral chemistry of the measured chloritoids. Mineral formula calculations are based on 12 oxygens.

Chloritoid	178	178	178
	<i>178-103</i>	<i>178-104</i>	<i>178-105</i>
SiO ₂	25.34	25.44	25.41
TiO ₂	0.04	0.02	0.07
Al ₂ O ₃	39.51	40.54	39.83
Cr ₂ O ₃			
FeO	25.52	24.59	25.00
MnO	1.01	0.59	0.75
MgO	1.72	2.48	2.17
CaO	0.00	0.01	0.01
Na ₂ O	0.02	0.00	0.02
K ₂ O	0.02	0.03	0.05
Total	93.19	93.70	93.30
Si	2.091	2.072	2.086
Ti	0.002	0.001	0.004
Al	3.843	3.891	3.854
Cr	0.000	0.000	0.000
Fe ³⁺	0.000	0.000	0.000
Fe ²⁺	1.762	1.675	1.716
Mn	0.071	0.040	0.052
Mg	0.212	0.301	0.266
Ca	0.000	0.001	0.001
Na	0.004	0.000	0.003
K	0.002	0.003	0.005
Total	7.987	7.984	7.987
X _{Mn}	3	2	3
X _{Mg}	10	15	13
X _{Fe}	86	83	84
Tot	100	100	100

$X_{Mn} = Mn / (Mn + Fe^{2+} + Mg)$, $X_{Mg} = Mg / (Mg + Mn + Fe^{2+})$, $X_{Fe} = Fe^{2+} / (Fe^{2+} + Mn + Mg)$.

Table A.6 : Mineral chemistry of the measured lawsonites. Mineral formula calculations are based on eight oxygens.

Lawsonite	128	128	128	128	128
	<i>155</i>	<i>157</i>	<i>161</i>	<i>170</i>	<i>185</i>
SiO ₂	38.65	38.19	41.83	38.50	38.49
TiO ₂	0.40	0.24	0.07	0.04	0.37
Al ₂ O ₃	31.46	31.08	29.51	31.89	31.17
Cr ₂ O ₃	0.02	0.01	0.00	0.02	0.00
FeO	0.59	0.98	0.71	0.83	0.60
MnO	0.06	0.01	0.00	0.00	0.00
MgO	0.03	0.00	0.00	0.01	0.00
CaO	16.85	17.45	16.18	16.95	17.05
Na ₂ O	0.01	0.00	0.03	0.01	0.00
K ₂ O	0.01	0.01	0.01	0.01	0.01
Total	88.07	87.97	88.35	88.25	87.71
Si	2.031	2.020	2.174	2.022	2.033
Ti	0.016	0.010	0.003	0.002	0.015
Al	1.949	1.938	1.808	1.974	1.941
Cr	0.001	0.001	0.000	0.001	0.000
Fe ³⁺	0.000	0.000	0.000	0.000	0.000
Fe ²⁺	0.026	0.043	0.031	0.036	0.026
Mn	0.002	0.000	0.000	0.000	0.000
Mg	0.003	0.000	0.000	0.000	0.000
Ca	0.949	0.989	0.901	0.954	0.965
Na	0.001	0.000	0.003	0.001	0.000
K	0.001	0.001	0.001	0.000	0.001
Total	4.979	5.001	4.921	4.990	4.982

Table A.7 : Mineral chemistry of the measured sodic-pyroxenes. Mineral formula calculations are based on four cations.

Sodic-pyroxene	128	128	128	128	128	128	128	211B	211B	211B
	<i>140</i>	<i>141</i>	<i>142</i>	<i>147</i>	<i>149</i>	<i>172</i>	<i>203</i>	<i>289</i>	<i>318</i>	<i>321</i>
SiO ₂	53.88	55.02	53.52	55.43	54.14	54.30	54.85	51.82	51.58	52.02
TiO ₂	0.00	0.08	0.01	0.08	0.02	0.01	0.03	0.03	0.09	0.08
Al ₂ O ₃	2.80	8.71	2.20	9.17	2.34	4.62	6.53	1.49	1.73	2.55
Cr ₂ O ₃	0.00	0.01	0.01	0.00	0.00	0.01	0.02	0.00	0.00	0.02
FeO	13.43	12.11	13.10	12.08	12.67	11.81	13.42	20.07	19.47	15.99
MnO	0.61	0.33	0.58	0.27	0.61	0.89	0.29	0.24	0.21	0.22
MgO	8.44	5.20	9.26	5.13	9.44	8.19	5.96	5.56	5.83	7.25
CaO	15.12	9.61	16.34	9.41	16.44	14.68	11.02	12.83	12.34	13.11
Na ₂ O	5.50	8.96	4.94	9.03	4.88	5.66	8.14	5.84	5.93	5.33
K ₂ O	0.01	0.01	0.02	0.01	0.01	0.02	0.01	0.02	0.02	0.04
Total	99.77	100.03	99.96	100.60	100.55	100.20	100.28	97.90	97.19	96.63
Si	1.989	1.979	1.973	1.982	1.983	1.987	1.985	1.994	1.992	2.002
Ti	0.000	0.002	0.000	0.002	0.000	0.000	0.001	0.001	0.002	0.002
Al	0.122	0.369	0.095	0.386	0.101	0.199	0.278	0.068	0.079	0.116
Cr	0.000	0.000	0.000	0.000	0.000	0.000	0.000	0.000	0.000	0.001
Fe ³⁺	0.294	0.293	0.311	0.271	0.278	0.229	0.322	0.380	0.378	0.274
Fe ²⁺	0.120	0.071	0.093	0.090	0.110	0.132	0.085	0.266	0.251	0.240
Mn	0.019	0.010	0.018	0.008	0.019	0.028	0.009	0.008	0.007	0.007
Mg	0.464	0.279	0.509	0.274	0.516	0.447	0.322	0.319	0.336	0.416
Ca	0.598	0.371	0.646	0.360	0.645	0.576	0.427	0.529	0.510	0.541
Na	0.393	0.625	0.353	0.626	0.346	0.402	0.571	0.435	0.444	0.398
K	0.000	0.000	0.001	0.000	0.000	0.001	0.001	0.001	0.001	0.002
Total	4.000	4.000	4.000	4.000	4.000	4.000	4.000	4.000	4.000	4.000
Aegerine	30	29	31	28	28	23	32	39	40	29
Jadeite	10	33	4	36	7	18	25	6	7	13
Diopside	60	37	65	37	65	59	43	55	53	58
Total	100	100	100	100	100	100	100	100	100	100

Table A.8 : Mineral chemistry of the measured epidotes. Mineral formula calculations are based on 12.5 oxygens.

Epidote	702A	702A	702A	702A	702A	702A	702A	702A	702A	702A	702A	702A	702A
	4	6	8	12	14	15	16	17	19	20	21	22	24
SiO ₂	38.98	39.23	39.65	40.16	40.53	39.96	40.11	40.93	40.43	40.31	39.64	40.24	39.74
TiO ₂	0.09	0.08	0.06	0.06	0.07	0.08	0.04	0.06	0.06	0.08	0.03	0.07	0.08
Al ₂ O ₃	23.01	29.20	24.90	30.27	30.38	26.26	24.96	32.25	30.62	29.88	26.00	30.43	26.28
Cr ₂ O ₃													
FeO	19.04	5.32	10.18	3.13	3.65	7.97	9.52	2.39	2.38	4.33	8.57	3.77	8.14
MnO	2.71	0.09	0.22	0.26	0.16	0.09	0.03	0.01	0.04	0.02	0.05	0.15	0.07
MgO	0.41	0.65	0.03	0.68	0.02	0.03	0.13	0.04	0.00	0.12	0.03	0.03	0.29
CaO	14.14	22.65	23.05	22.60	23.82	23.58	22.68	21.95	24.12	23.85	23.53	23.92	22.94
Na ₂ O	0.00	0.00	0.00	0.00	0.03	0.00	0.00	0.19	0.00	0.00	0.02	0.00	0.01
K ₂ O	0.00	0.00	0.01	0.03	0.01	0.05	0.49	0.74	0.00	0.00	0.03	0.00	0.03
Total	98.39	97.23	98.09	97.19	98.66	98.02	97.98	98.57	97.66	98.58	97.89	98.62	97.59
Si	3.032	3.023	3.076	3.074	3.067	3.086	3.110	3.078	3.083	3.059	3.071	3.050	3.078
Ti	0.005	0.005	0.004	0.003	0.004	0.005	0.003	0.004	0.004	0.004	0.002	0.004	0.005
Al	2.109	2.652	2.277	2.731	2.710	2.390	2.281	2.859	2.752	2.672	2.374	2.718	2.399
Cr	0.000	0.000	0.000	0.000	0.000	0.000	0.000	0.000	0.000	0.000	0.000	0.000	0.000
Fe ³⁺	1.238	0.343	0.661	0.200	0.231	0.515	0.617	0.150	0.152	0.275	0.555	0.239	0.527
Fe ²⁺	0.000	0.000	0.000	0.000	0.000	0.000	0.000	0.000	0.000	0.000	0.000	0.000	0.000
Mn	0.179	0.006	0.014	0.017	0.010	0.006	0.002	0.001	0.002	0.001	0.003	0.010	0.005
Mg	0.048	0.075	0.003	0.078	0.002	0.003	0.015	0.004	0.000	0.013	0.003	0.003	0.034
Ca	1.178	1.870	1.916	1.853	1.932	1.951	1.884	1.769	1.970	1.939	1.953	1.943	1.904
Na	0.000	0.000	0.000	0.000	0.004	0.000	0.000	0.028	0.000	0.000	0.003	0.000	0.002
K	0.000	0.000	0.001	0.003	0.001	0.005	0.048	0.071	0.000	0.000	0.003	0.000	0.003
Total	7.789	7.975	7.952	7.959	7.961	7.960	7.962	7.963	7.962	7.963	7.966	7.967	7.956
Fe ³⁺ /(Fe ³⁺ +Al)	0.37	0.11	0.22	0.07	0.08	0.18	0.21	0.05	0.05	0.09	0.19	0.08	0.18

Table A.8 (continued) : Mineral chemistry of the measured epidotes. Mineral formula calculations are based on 12.5 oxygens.

Epidote	702A	702A	702A	702A	702A	702A	702A	702A	702A	702A	702A	702A	702A
	<i>31</i>	<i>32</i>	<i>49</i>	<i>50</i>	<i>69</i>	<i>82</i>	<i>93</i>	<i>97</i>	<i>102</i>	<i>104</i>	<i>111</i>	<i>119</i>	<i>130</i>
SiO ₂	38.96	38.10	39.10	38.37	39.08	38.30	38.59	38.29	39.08	38.76	38.37	38.97	39.53
TiO ₂	0.08	0.17	0.04	0.07	0.04	0.06	0.06	0.08	0.07	0.06	0.07	0.06	0.06
Al ₂ O ₃	31.11	25.96	32.00	26.22	29.35	25.93	25.57	26.37	26.36	30.04	26.07	30.78	31.26
Cr ₂ O ₃	0.03	0.00	0.00	0.02	0.01	0.01	0.04	0.01	0.01	0.01	0.00	0.00	0.00
FeO	3.46	9.63	3.06	9.30	5.67	9.86	10.39	9.46	8.88	4.65	10.04	4.44	3.54
MnO	0.02	0.03	0.08	0.03	0.09	0.11	0.06	0.05	0.06	0.07	0.32	0.07	0.07
MgO	0.00	0.00	0.02	0.01	0.01	0.02	0.00	0.01	0.28	0.02	0.03	0.20	0.03
CaO	24.20	23.35	24.12	23.35	23.80	23.26	23.38	23.37	23.33	24.13	22.91	23.66	23.87
Na ₂ O	0.04	0.02	0.02	0.00	0.01	0.03	0.00	0.02	0.07	0.01	0.00	0.02	0.00
K ₂ O	0.01	0.01	0.00	0.00	0.00	0.00	0.03	0.01	0.01	0.04	0.00	0.01	0.03
Total	97.90	97.26	98.44	97.37	98.05	97.57	98.12	97.65	98.15	97.80	97.80	98.19	98.39
Si	2.981	2.986	2.969	2.999	3.000	2.993	3.002	2.986	3.024	2.981	2.990	2.975	3.003
Ti	0.005	0.010	0.003	0.004	0.002	0.003	0.003	0.004	0.004	0.003	0.004	0.003	0.004
Al	2.805	2.398	2.863	2.415	2.656	2.388	2.344	2.424	2.404	2.723	2.395	2.769	2.799
Cr	0.002	0.000	0.000	0.001	0.001	0.000	0.003	0.000	0.001	0.001	0.000	0.000	0.000
Fe ³⁺	0.221	0.631	0.194	0.608	0.364	0.644	0.676	0.617	0.575	0.299	0.655	0.284	0.225
Fe ²⁺	0.000	0.000	0.000	0.000	0.000	0.000	0.000	0.000	0.000	0.000	0.000	0.000	0.000
Mn	0.001	0.002	0.005	0.002	0.006	0.007	0.004	0.003	0.004	0.005	0.021	0.004	0.004
Mg	0.000	0.000	0.002	0.002	0.001	0.002	0.000	0.001	0.032	0.002	0.003	0.022	0.003
Ca	1.983	1.961	1.962	1.955	1.958	1.947	1.949	1.952	1.934	1.988	1.913	1.935	1.943
Na	0.006	0.004	0.004	0.000	0.001	0.005	0.000	0.003	0.011	0.001	0.000	0.003	0.000
K	0.001	0.000	0.000	0.000	0.000	0.000	0.003	0.001	0.001	0.004	0.000	0.001	0.003
Total	8.005	7.992	8.002	7.985	7.988	7.990	7.984	7.991	7.989	8.007	7.981	7.997	7.984
Fe ³⁺ /(Fe ³⁺ +Al)	0.07	0.21	0.06	0.20	0.12	0.21	0.22	0.20	0.19	0.10	0.21	0.09	0.07

Table A.8 (continued) : Mineral chemistry of the measured epidotes. Mineral formula calculations are based on 12.5 oxygens.

Epidote	128	128	128	128	128	211B	211B	211B	211B	211B	211B
	<i>156</i>	<i>158</i>	<i>164</i>	<i>184</i>	<i>197</i>	<i>240</i>	<i>241</i>	<i>247</i>	<i>248</i>	<i>251</i>	<i>264</i>
SiO ₂	37.92	39.33	37.54	39.51	38.40	38.13	37.28	37.42	37.30	38.22	37.80
TiO ₂	0.06	0.06	0.16	0.05	0.03	0.13	0.04	0.07	0.09	0.04	0.16
Al ₂ O ₃	24.11	30.58	21.53	32.71	25.13	28.55	22.69	22.43	23.00	22.91	25.76
Cr ₂ O ₃	0.01	0.00	0.01	0.00	0.00	0.00	0.01	0.00	0.01	0.01	0.01
FeO	12.25	4.39	15.03	1.17	10.80	6.74	13.91	14.18	13.50	13.39	10.84
MnO	0.41	0.20	0.05	0.12	0.12	0.15	0.13	0.25	0.18	0.18	0.48
MgO	0.02	0.00	0.01	0.01	0.02	0.02	0.00	0.00	0.01	0.00	0.05
CaO	22.70	24.05	22.93	23.96	23.60	23.06	22.40	22.27	22.50	22.15	22.17
Na ₂ O	0.00	0.01	0.00	0.01	0.00	0.02	0.00	0.01	0.00	0.02	0.00
K ₂ O	0.00	0.05	0.01	0.00	0.01	0.01	0.01	0.00	0.01	0.01	0.01
Total	97.48	98.66	97.25	97.55	98.09	96.79	96.47	96.62	96.60	96.93	97.29
Si	2.988	2.992	2.992	3.008	2.996	2.974	2.981	2.990	2.977	3.029	2.967
Ti	0.004	0.004	0.010	0.003	0.002	0.008	0.002	0.004	0.006	0.003	0.010
Al	2.239	2.742	2.022	2.935	2.310	2.624	2.139	2.112	2.163	2.140	2.383
Cr	0.000	0.000	0.000	0.000	0.000	0.000	0.000	0.000	0.001	0.001	0.001
Fe ³⁺	0.807	0.279	1.000	0.075	0.704	0.439	0.930	0.947	0.901	0.887	0.712
Fe ²⁺	0.000	0.000	0.000	0.000	0.000	0.000	0.000	0.000	0.000	0.000	0.000
Mn	0.027	0.013	0.003	0.008	0.008	0.010	0.009	0.017	0.012	0.012	0.032
Mg	0.003	0.000	0.001	0.001	0.003	0.002	0.000	0.000	0.001	0.000	0.006
Ca	1.916	1.960	1.957	1.954	1.972	1.927	1.919	1.906	1.924	1.881	1.865
Na	0.000	0.002	0.000	0.002	0.000	0.002	0.000	0.001	0.000	0.002	0.000
K	0.000	0.005	0.001	0.000	0.001	0.001	0.001	0.000	0.001	0.001	0.001
Total	7.985	7.997	7.986	7.986	7.996	7.988	7.982	7.977	7.985	7.956	7.976
Fe ³⁺ /(Fe ³⁺ +Al)	0.26	0.09	0.33	0.02	0.23	0.14	0.30	0.31	0.29	0.29	0.23

Table A.8 (continued) : Mineral chemistry of the measured epidotes. Mineral formula calculations are based on 12.5 oxygens.

Epidote	211B	211B	211B	211B	211B	211B	211B	211B	211B	211B	211B
	265	266	287	294	296	303	304	306	307	308	314
SiO ₂	38.62	37.42	38.30	37.94	39.20	37.32	36.63	37.40	37.74	37.31	37.31
TiO ₂	0.05	0.04	0.05	0.02	0.05	0.16	0.04	0.08	0.05	0.01	0.04
Al ₂ O ₃	28.23	22.72	22.69	22.76	27.50	20.79	20.43	25.17	24.75	22.73	22.75
Cr ₂ O ₃	0.00	0.00	0.01	0.00	0.01	0.01	0.00	0.00	0.02	0.00	0.04
FeO	7.31	14.03	13.28	13.55	7.87	16.23	16.22	11.08	10.94	13.82	13.39
MnO	0.12	0.20	0.15	0.10	0.16	0.10	0.26	0.12	0.10	0.17	0.16
MgO	0.01	0.00	0.00	0.01	0.02	0.01	0.00	0.05	0.02	0.00	0.12
CaO	23.20	22.47	21.74	22.40	22.40	22.34	21.79	22.79	22.75	22.46	22.44
Na ₂ O	0.01	0.02	0.18	0.09	0.32	0.01	0.00	0.01	0.00	0.02	0.01
K ₂ O	0.01	0.00	0.00	0.00	0.00	0.00	0.01	0.01	0.00	0.01	0.00
Total	97.56	96.89	96.40	96.87	97.53	96.96	95.38	96.71	96.37	96.52	96.27
Si	2.991	2.981	3.048	3.015	3.035	2.990	2.986	2.960	2.994	2.982	2.987
Ti	0.003	0.002	0.003	0.001	0.003	0.010	0.003	0.005	0.003	0.001	0.003
Al	2.577	2.133	2.128	2.131	2.509	1.963	1.962	2.348	2.314	2.142	2.147
Cr	0.000	0.000	0.000	0.000	0.000	0.001	0.000	0.000	0.001	0.000	0.003
Fe ³⁺	0.474	0.935	0.884	0.900	0.509	1.087	1.106	0.734	0.726	0.924	0.897
Fe ²⁺	0.000	0.000	0.000	0.000	0.000	0.000	0.000	0.000	0.000	0.000	0.000
Mn	0.008	0.013	0.010	0.007	0.011	0.007	0.018	0.008	0.007	0.011	0.011
Mg	0.002	0.000	0.000	0.001	0.002	0.001	0.000	0.006	0.003	0.000	0.015
Ca	1.925	1.918	1.854	1.906	1.858	1.918	1.903	1.933	1.934	1.924	1.925
Na	0.001	0.002	0.028	0.014	0.048	0.001	0.000	0.002	0.000	0.003	0.001
K	0.001	0.000	0.000	0.000	0.000	0.000	0.001	0.001	0.000	0.001	0.000
Total	7.982	7.984	7.957	7.976	7.977	7.976	7.978	7.995	7.982	7.987	7.988
Fe ³⁺ /(Fe ³⁺ +Al)	0.16	0.30	0.29	0.30	0.17	0.36	0.36	0.24	0.24	0.30	0.29

Table A.8 (continued) : Mineral chemistry of the measured epidotes. Mineral formula calculations are based on 12.5 oxygens.

Epidote	775	775	775	775	775	775	753A	753A	753A
	12	25	236	242	253	254	37	41	42
SiO ₂	38.95	37.93	39.30	39.35	38.07	39.28	38.42	37.90	38.40
TiO ₂	0.35	0.14	0.04	0.28	1.76	0.06	0.10	0.13	0.08
Al ₂ O ₃	30.38	28.09	31.42	30.75	30.39	31.22	28.87	27.31	28.34
Cr ₂ O ₃	0.02	0.01	0.00	0.00	0.05	0.00	0.03	0.00	0.00
FeO	5.49	7.55	3.41	4.14	3.92	3.45	6.67	8.46	7.38
MnO	0.41	0.53	0.34	0.43	0.55	0.62	0.58	0.66	0.47
MgO	0.01	0.01	0.00	0.01	0.00	0.01	0.01	0.00	0.03
CaO	22.12	22.30	23.39	23.45	22.78	23.00	22.50	22.04	22.73
Na ₂ O	0.13	0.01	0.01	0.09	0.00	0.00	0.00	0.01	0.01
K ₂ O	0.22	0.09	0.10	0.07	0.04	0.03	0.02	0.05	0.03
Total	98.09	96.65	98.01	98.58	97.54	97.66	97.19	96.56	97.48
Si	2.980	2.970	2.998	2.993	2.931	3.006	2.982	2.978	2.979
Ti	0.020	0.008	0.002	0.016	0.102	0.003	0.006	0.008	0.005
Al	2.739	2.592	2.824	2.757	2.757	2.816	2.641	2.529	2.591
Cr	0.001	0.001	0.000	0.000	0.003	0.000	0.002	0.000	0.000
Fe ³⁺	0.351	0.494	0.217	0.264	0.252	0.221	0.433	0.556	0.479
Fe ²⁺	0.000	0.000	0.000	0.000	0.000	0.000			
Mn	0.027	0.035	0.022	0.028	0.036	0.040	0.038	0.044	0.031
Mg	0.001	0.001	0.000	0.001	0.000	0.001	0.001	0.000	0.004
Ca	1.813	1.871	1.911	1.911	1.879	1.885	1.871	1.855	1.890
Na	0.019	0.002	0.002	0.014	0.000	0.000	0.000	0.001	0.001
K	0.021	0.009	0.010	0.007	0.004	0.003	0.002	0.005	0.003
Total	7.974	7.984	7.986	7.991	7.963	7.974	7.975	7.975	7.983
Fe ³⁺ /(Fe ³⁺ +Al)	0.11	0.16	0.07	0.09	0.08	0.07	0.14	0.18	0.16

Table A.9 : Mineral chemistry of the measured chlorites. Mineral formula calculations are based on 14 oxygens.

Chlorite	702A	702A	702A	702A	702A	702A	702A	702A	702A	702A	702A	702A	702A	702A
	<i>1</i>	<i>7</i>	<i>9</i>	<i>11</i>	<i>23</i>	<i>25</i>	<i>29</i>	<i>47</i>	<i>68</i>	<i>73</i>	<i>88</i>	<i>113</i>	<i>129</i>	<i>132</i>
SiO ₂	28.99	27.87	30.03	27.97	28.59	28.18	26.69	26.84	26.74	27.57	28.05	29.81	27.56	30.21
TiO ₂	0.04	0.00	0.10	0.03	0.05	0.05	0.02	0.02	0.01	0.05	0.03	0.06	0.05	0.01
Al ₂ O ₃	17.47	18.85	18.33	17.81	17.85	20.05	19.43	19.82	19.81	18.09	17.61	16.94	19.12	16.17
Cr ₂ O ₃							0.03	0.00	0.01	0.05	0.25	0.00	0.01	0.42
FeO	28.17	25.61	23.80	27.69	26.20	24.81	27.08	26.48	26.92	25.94	25.28	27.68	26.01	23.32
MnO	0.81	0.23	0.57	0.41	0.40	0.40	0.14	0.16	0.13	0.11	0.07	0.33	0.07	0.16
MgO	12.01	15.27	11.25	13.95	15.25	12.06	14.16	14.51	14.31	15.63	16.56	13.08	15.64	16.98
CaO	1.96	0.16	5.09	0.22	0.20	2.94	0.03	0.07	0.10	0.05	0.21	0.42	0.04	0.93
Na ₂ O	0.03	0.04	0.07	0.02	0.03	0.00	0.04	0.04	0.10	0.00	0.02	0.06	0.03	0.18
K ₂ O	0.04	0.02	0.03	0.00	0.00	0.28	0.08	0.05	0.04	0.01	0.04	0.19	0.04	0.02
Total	89.52	88.06	89.28	88.10	88.57	88.77	87.69	87.98	88.16	87.50	88.12	88.58	88.56	88.38
Si	3.046	2.919	3.107	2.966	2.986	2.938	2.836	2.829	2.821	2.916	2.936	3.132	2.874	3.118
Ti	0.003	0.000	0.008	0.002	0.004	0.004	0.002	0.002	0.001	0.004	0.003	0.005	0.004	0.001
Al	2.164	2.327	2.235	2.226	2.197	2.464	2.432	2.462	2.463	2.254	2.173	2.099	2.351	1.967
Cr	0.000	0.000	0.000	0.000	0.000	0.000	0.002	0.000	0.001	0.004	0.021	0.000	0.001	0.034
Fe ³⁺	0.000	0.000	0.000	0.000	0.000	0.000	0.000	0.000	0.000	0.000	0.000	0.000	0.000	0.000
Fe ²⁺	2.476	2.243	2.059	2.456	2.289	2.163	2.406	2.334	2.375	2.294	2.214	2.433	2.269	2.013
Mn	0.072	0.021	0.050	0.036	0.035	0.035	0.012	0.014	0.011	0.010	0.006	0.029	0.006	0.014
Mg	1.881	2.384	1.735	2.205	2.375	1.874	2.243	2.280	2.250	2.465	2.584	2.049	2.432	2.613
Ca	0.221	0.018	0.564	0.025	0.022	0.328	0.004	0.008	0.011	0.005	0.024	0.048	0.004	0.103
Na	0.006	0.008	0.013	0.003	0.006	0.000	0.007	0.008	0.021	0.000	0.003	0.013	0.006	0.036
K	0.005	0.003	0.004	0.001	0.001	0.037	0.011	0.006	0.006	0.002	0.005	0.025	0.005	0.003
Total	9.874	9.923	9.776	9.921	9.914	9.844	9.954	9.945	9.960	9.953	9.968	9.832	9.952	9.900
Mg/(Mg+Fe ²⁺)	0.43	0.52	0.46	0.47	0.51	0.46	0.48	0.49	0.49	0.52	0.54	0.46	0.52	0.56

Table A.9 (continued) : Mineral chemistry of the measured chlorites. Mineral formula calculations are based on 14 oxygens.

Chlorite	211B	211B	211B	211B	211B	211B	211B	211B	128	128
	242	245	267	268	276	281	292	315	139	153
SiO ₂	25.83	27.22	29.92	26.67	26.02	27.11	27.08	27.05	28.19	29.08
TiO ₂	0.05	0.00	0.04	0.05	0.48	0.01	0.01	0.00	0.01	0.03
Al ₂ O ₃	19.06	18.15	16.13	19.39	20.27	17.62	17.42	18.87	18.87	19.67
Cr ₂ O ₃	0.00	0.00	0.00	0.00	0.00	0.01	0.00	0.02	0.02	0.01
FeO	28.14	25.89	23.00	26.35	27.01	27.11	27.77	26.41	23.94	23.51
MnO	0.50	0.35	0.29	0.33	0.43	0.43	0.38	0.36	0.36	0.36
MgO	13.88	16.00	17.24	15.26	14.40	15.93	15.64	15.14	15.47	15.13
CaO	0.10	0.06	0.23	0.13	0.36	0.08	0.10	0.05	0.31	0.12
Na ₂ O	0.03	0.03	0.03	0.03	0.04	0.04	0.02	0.05	0.16	0.16
K ₂ O	0.01	0.02	0.48	0.02	0.03	0.02	0.02	0.07	0.07	0.17
Total	87.60	87.73	87.35	88.22	89.04	88.35	88.44	88.02	87.40	88.24
Si	2.777	2.877	3.122	2.809	2.730	2.868	2.873	2.856	2.952	2.995
Ti	0.004	0.000	0.003	0.004	0.038	0.001	0.001	0.000	0.001	0.002
Al	2.415	2.261	1.984	2.406	2.506	2.198	2.178	2.348	2.329	2.389
Cr	0.000	0.000	0.000	0.000	0.000	0.001	0.000	0.002	0.001	0.001
Fe ³⁺	0.000	0.000	0.000	0.000	0.000	0.000	0.000	0.000	0.000	0.000
Fe ²⁺	2.530	2.289	2.007	2.320	2.370	2.399	2.464	2.332	2.097	2.026
Mn	0.046	0.031	0.025	0.029	0.038	0.038	0.034	0.033	0.032	0.031
Mg	2.224	2.522	2.681	2.396	2.251	2.513	2.473	2.384	2.415	2.323
Ca	0.012	0.006	0.025	0.015	0.040	0.009	0.012	0.006	0.034	0.013
Na	0.007	0.007	0.006	0.006	0.007	0.007	0.003	0.009	0.033	0.033
K	0.001	0.003	0.064	0.003	0.004	0.002	0.003	0.009	0.009	0.023
Total	10.015	9.997	9.918	9.988	9.985	10.036	10.041	9.979	9.903	9.836
Mg/(Mg+Fe ²⁺)	0.47	0.52	0.57	0.51	0.49	0.51	0.50	0.51	0.54	0.53

Table A.9 (continued) : Mineral chemistry of the measured chlorites. Mineral formula calculations are based on 14 oxygens.

Chlorite	775	775	775	775	775	753A	753A	753A	753A	753A	753A	753A	753A	753A
	220	223	241	245	268	45	80	84	85	86	95	97	99	101
SiO ₂	26.35	26.57	25.26	31.92	25.09	24.35	24.60	25.07	29.38	27.59	26.68	30.69	25.66	25.06
TiO ₂	0.06	0.14	0.05	0.09	0.07	0.03	0.04	0.03	0.17	0.03	0.00	0.00	0.05	0.08
Al ₂ O ₃	21.42	21.58	21.06	22.36	20.98	22.55	21.78	21.59	20.41	21.00	21.43	20.53	21.92	21.95
Cr ₂ O ₃	0.00	0.00	0.04	0.01	0.00	0.01	0.04	0.02	0.00	0.04	0.04	0.00	0.02	0.00
FeO	28.67	28.52	32.40	23.78	33.36	30.20	31.46	30.98	25.91	28.55	26.97	25.52	27.91	27.92
MnO	1.05	1.08	1.01	1.39	1.08	1.34	1.21	1.34	0.81	1.21	1.16	1.06	1.20	1.14
MgO	11.18	10.72	9.61	6.74	8.73	10.61	9.78	10.27	12.43	10.46	12.18	11.67	11.71	11.58
CaO	0.04	0.07	0.03	0.57	0.01	0.05	0.02	0.03	0.02	0.02	0.01	0.03	0.02	0.03
Na ₂ O	0.02	0.10	0.00	0.20	0.08	0.01	0.01	0.01	0.01	0.07	0.02	0.00	0.00	0.00
K ₂ O	0.09	0.16	0.04	0.85	0.04	0.00	0.04	0.01	0.02	0.01	0.02	0.03	0.09	0.03
Total	88.87	88.95	89.51	87.92	89.43	89.16	88.97	89.33	89.15	88.97	88.50	89.55	88.59	87.77
Si	2.789	2.807	2.715	3.286	2.716	2.604	2.654	2.684	3.023	2.905	2.808	3.128	2.720	2.685
Ti	0.004	0.011	0.004	0.007	0.006	0.002	0.003	0.003	0.013	0.002	0.000	0.000	0.004	0.006
Al	2.672	2.687	2.669	2.714	2.677	2.842	2.769	2.724	2.476	2.606	2.658	2.466	2.739	2.772
Cr	0.000	0.000	0.003	0.000	0.000	0.001	0.003	0.001	0.000	0.004	0.004	0.000	0.002	0.000
Fe ³⁺	0.000	0.000	0.000	0.000	0.000	0.000	0.000	0.000	0.000	0.000	0.000	0.000	0.000	0.000
Fe ²⁺	2.537	2.520	2.914	2.048	3.020	2.701	2.839	2.774	2.230	2.513	2.374	2.175	2.475	2.502
Mn	0.094	0.097	0.092	0.121	0.099	0.122	0.110	0.122	0.070	0.108	0.103	0.091	0.108	0.103
Mg	1.763	1.688	1.540	1.034	1.409	1.692	1.573	1.639	1.907	1.641	1.911	1.773	1.851	1.850
Ca	0.005	0.008	0.004	0.063	0.002	0.006	0.002	0.003	0.002	0.002	0.001	0.003	0.002	0.003
Na	0.004	0.020	0.000	0.041	0.016	0.002	0.002	0.002	0.003	0.013	0.004	0.000	0.001	0.000
K	0.012	0.022	0.005	0.111	0.006	0.000	0.005	0.001	0.002	0.001	0.002	0.004	0.012	0.004
Total	9.879	9.859	9.947	9.426	9.951	9.973	9.961	9.952	9.728	9.795	9.864	9.641	9.912	9.925
Mg/(Mg+Fe ²⁺)	0.41	0.40	0.35	0.34	0.32	0.39	0.36	0.37	0.46	0.39	0.45	0.45	0.43	0.43

Table A.9 (continued) : Mineral chemistry of the measured chlorites. Mineral formula calculations are based on 14 oxygens.

Chlorite	753A	753A	753A	753A	753A	753A	753A	753A	753A	753A	753A	753A	753A	753A
	<i>103</i>	<i>105</i>	<i>106</i>	<i>107</i>	<i>111</i>	<i>114</i>	<i>116</i>	<i>117</i>	<i>118</i>	<i>119</i>	<i>121</i>	<i>122</i>	<i>124</i>	<i>125</i>
SiO ₂	26.51	24.90	25.67	25.08	28.70	25.73	25.97	24.91	24.54	24.69	27.19	24.58	25.05	25.47
TiO ₂	0.11	0.04	0.05	0.05	0.01	0.04	0.02	0.02	0.05	0.06	0.06	0.03	0.05	0.02
Al ₂ O ₃	21.44	21.48	22.06	21.45	20.95	21.92	22.12	21.25	21.44	21.71	21.22	21.91	21.35	21.21
Cr ₂ O ₃	0.04	0.00	0.00	0.00	0.01	0.03	0.02	0.01	0.00	0.00	0.00	0.01	0.03	0.01
FeO	27.88	30.80	26.57	31.41	26.85	27.09	27.52	31.85	31.57	31.66	28.02	30.97	31.67	30.07
MnO	1.17	1.31	1.12	1.10	1.14	1.12	1.18	1.12	1.13	1.26	1.21	1.21	1.02	1.10
MgO	11.95	10.12	13.43	9.95	11.55	12.33	11.67	9.63	9.58	9.59	11.11	10.03	9.86	10.96
CaO	0.02	0.04	0.01	0.04	0.01	0.01	0.01	0.02	0.01	0.01	0.01	0.01	0.01	0.02
Na ₂ O	0.00	0.02	0.01	0.01	0.02	0.00	0.01	0.00	0.00	0.01	0.00	0.00	0.01	0.00
K ₂ O	0.02	0.01	0.00	0.02	0.01	0.05	0.02	0.02	0.01	0.01	0.01	0.03	0.01	0.02
Total	89.13	88.72	88.91	89.10	89.24	88.32	88.53	88.83	88.32	88.99	88.82	88.77	89.07	88.89
Si	2.784	2.684	2.690	2.696	2.974	2.722	2.743	2.695	2.669	2.665	2.862	2.650	2.697	2.723
Ti	0.009	0.003	0.004	0.004	0.001	0.003	0.002	0.002	0.004	0.005	0.005	0.002	0.004	0.002
Al	2.654	2.729	2.724	2.717	2.557	2.733	2.754	2.709	2.749	2.761	2.632	2.784	2.709	2.673
Cr	0.003	0.000	0.000	0.000	0.001	0.002	0.002	0.001	0.000	0.000	0.000	0.001	0.002	0.001
Fe ³⁺	0.000	0.000	0.000	0.000	0.000	0.000	0.000	0.000	0.000	0.000	0.000	0.000	0.000	0.000
Fe ²⁺	2.449	2.777	2.328	2.824	2.326	2.397	2.431	2.882	2.872	2.858	2.466	2.792	2.852	2.688
Mn	0.104	0.120	0.100	0.100	0.100	0.101	0.105	0.103	0.104	0.115	0.108	0.111	0.093	0.100
Mg	1.872	1.627	2.098	1.594	1.784	1.944	1.838	1.553	1.553	1.542	1.743	1.612	1.582	1.747
Ca	0.003	0.004	0.001	0.005	0.001	0.001	0.001	0.003	0.001	0.001	0.001	0.001	0.001	0.003
Na	0.000	0.005	0.001	0.003	0.004	0.000	0.001	0.000	0.000	0.002	0.000	0.000	0.002	0.001
K	0.002	0.002	0.000	0.002	0.001	0.006	0.002	0.003	0.001	0.001	0.001	0.004	0.001	0.003
Total	9.880	9.951	9.945	9.944	9.749	9.910	9.879	9.950	9.953	9.951	9.818	9.957	9.945	9.940
Mg/(Mg+Fe ²⁺)	0.43	0.37	0.47	0.36	0.43	0.45	0.43	0.35	0.35	0.35	0.41	0.37	0.36	0.39

Table A.9 (continued) : Mineral chemistry of the measured chlorites. Mineral formula calculations are based on 14 oxygens.

Chlorite	753A	753A	753A	753A	178	178	178	178	178	178
	<i>126</i>	<i>144</i>	<i>145</i>	<i>149</i>	<i>27</i>	<i>59</i>	<i>60</i>	<i>61</i>	<i>63</i>	<i>65</i>
SiO ₂	24.95	24.61	24.74	24.71	24.79	23.85	24.15	27.94	24.37	24.92
TiO ₂	0.05	0.00	0.03	0.04	0.05	0.06	0.06	0.01	0.03	0.00
Al ₂ O ₃	21.51	22.53	21.62	22.18	21.74	23.15	21.56	21.53	22.16	22.10
Cr ₂ O ₃	0.04	0.04	0.00	0.02	0.04	0.02	0.01	0.00	0.00	0.00
FeO	31.16	30.04	31.54	31.03	33.37	32.49	32.76	30.43	31.45	31.96
MnO	1.35	1.30	1.44	1.29	0.38	0.39	0.38	0.38	0.36	0.35
MgO	9.73	9.73	9.22	9.60	8.88	9.05	9.36	9.06	9.09	9.18
CaO	0.02	0.02	0.01	0.02	0.02	0.00	0.02	0.04	0.01	0.03
Na ₂ O	0.02	0.01	0.03	0.05	0.04	0.01	0.00	0.03	0.00	0.02
K ₂ O	0.01	0.08	0.03	0.07	0.04	0.02	0.02	0.26	0.00	0.05
Total	88.83	88.35	88.66	89.01	89.34	89.02	88.31	89.69	87.47	88.62
Si	2.692	2.652	2.682	2.657	2.677	2.574	2.636	2.930	2.663	2.690
Ti	0.004	0.000	0.003	0.003	0.004	0.005	0.005	0.001	0.003	0.000
Al	2.734	2.862	2.762	2.812	2.766	2.944	2.775	2.662	2.854	2.811
Cr	0.003	0.003	0.000	0.001	0.003	0.001	0.001	0.000	0.000	0.000
Fe ³⁺	0.000	0.000	0.000	0.000	0.000	0.000	0.000	0.000	0.000	0.000
Fe ²⁺	2.811	2.708	2.860	2.791	3.013	2.932	2.992	2.669	2.874	2.885
Mn	0.123	0.118	0.132	0.117	0.034	0.035	0.035	0.034	0.033	0.032
Mg	1.565	1.563	1.490	1.539	1.429	1.456	1.523	1.417	1.480	1.476
Ca	0.002	0.002	0.002	0.002	0.003	0.000	0.003	0.005	0.001	0.004
Na	0.004	0.001	0.006	0.009	0.008	0.001	0.000	0.006	0.000	0.005
K	0.001	0.011	0.003	0.010	0.006	0.002	0.003	0.035	0.000	0.006
Total	9.939	9.922	9.939	9.943	9.942	9.950	9.972	9.759	9.908	9.910
Mg/(Mg+Fe ²⁺)	0.36	0.37	0.34	0.36	0.32	0.33	0.34	0.35	0.34	0.34

Table A.9 (continued) : Mineral chemistry of the measured chlorites. Mineral formula calculations are based on 14 oxygens.

Chlorite	392	392	392	392	392	392	392	392	392	392
	<i>12</i>	<i>16</i>	<i>17</i>	<i>19</i>	<i>22</i>	<i>28</i>	<i>30</i>	<i>31</i>	<i>42</i>	<i>45</i>
SiO ₂	25.51	25.76	25.83	25.44	25.73	26.01	25.46	25.62	25.97	25.81
TiO ₂	0.03	0.02	0.03	0.02	0.03	0.04	0.05	0.03	0.05	0.07
Al ₂ O ₃	22.46	22.68	22.99	22.92	22.63	22.71	22.40	22.81	22.05	20.27
Cr ₂ O ₃										
FeO	30.50	30.54	29.51	31.64	29.97	29.96	31.29	29.74	29.53	31.77
MnO	0.18	0.16	0.15	0.17	0.19	0.14	0.19	0.20	0.33	0.23
MgO	9.84	9.75	10.31	10.06	9.47	9.68	9.45	9.50	10.29	10.01
CaO	0.03	0.01	0.03	0.03	0.05	0.05	0.01	0.02	0.02	0.04
Na ₂ O	0.01	0.02	0.00	0.01	0.07	0.04	0.01	0.05	0.00	0.04
K ₂ O	0.03	0.01	0.06	0.07	0.06	0.13	0.04	0.04	0.02	0.04
Total	88.58	88.95	88.93	90.38	88.21	88.76	88.90	88.02	88.26	88.29
Si	2.723	2.734	2.727	2.675	2.750	2.759	2.720	2.740	2.768	2.793
Ti	0.002	0.002	0.002	0.002	0.003	0.003	0.004	0.002	0.004	0.006
Al	2.826	2.837	2.861	2.841	2.850	2.839	2.820	2.875	2.770	2.586
Cr	0.000	0.000	0.000	0.000	0.000	0.000	0.000	0.000	0.000	0.000
Fe ³⁺	0.000	0.000	0.000	0.000	0.000	0.000	0.000	0.000	0.000	0.000
Fe ²⁺	2.723	2.711	2.606	2.783	2.678	2.657	2.795	2.660	2.632	2.876
Mn	0.016	0.014	0.013	0.015	0.017	0.013	0.017	0.019	0.030	0.021
Mg	1.566	1.543	1.623	1.577	1.509	1.531	1.505	1.515	1.635	1.615
Ca	0.003	0.001	0.004	0.003	0.005	0.006	0.001	0.003	0.002	0.005
Na	0.002	0.003	0.000	0.002	0.015	0.007	0.002	0.009	0.000	0.008
K	0.004	0.001	0.008	0.010	0.008	0.018	0.005	0.005	0.003	0.005
Total	9.865	9.847	9.844	9.908	9.834	9.832	9.869	9.828	9.844	9.914
Mg/(Mg+Fe ²⁺)	0.37	0.36	0.38	0.36	0.36	0.37	0.35	0.36	0.38	0.36

Table A.10 : Mineral chemistry of the measured plagioclases. Mineral formula calculations are based on eight oxygens.

Plagioclase	702A	702A	702A	702A	702A	702A	702A	702A	128	128	128
	48	57	67	76	98	100	103	127	154	187	190
SiO ₂	68.47	68.55	68.76	68.91	68.59	67.84	67.54	67.56	68.35	69.21	69.06
TiO ₂	0.00	0.00	0.01	0.02	0.02	0.02	0.03	0.03	0.02	0.00	0.00
Al ₂ O ₃	19.71	19.48	19.39	19.44	19.52	19.38	20.14	18.10	20.42	19.46	19.47
Cr ₂ O ₃	0.00	0.00	0.00	0.00	0.00	0.00	0.00	0.00	0.01	0.00	0.00
FeO	0.51	0.17	0.31	0.13	0.18	0.18	0.26	0.98	0.22	0.15	0.13
MnO	0.00	0.01	0.00	0.00	0.00	0.00	0.00	0.00	0.00	0.02	0.00
MgO	0.11	0.00	0.00	0.00	0.00	0.01	0.02	1.11	0.00	0.01	0.00
CaO	0.45	0.13	0.13	0.03	0.18	0.27	0.95	1.27	1.08	0.14	0.08
Na ₂ O	11.41	11.83	11.70	12.04	11.69	11.36	11.12	11.32	11.15	11.86	11.98
K ₂ O	0.04	0.02	0.02	0.02	0.06	0.04	0.05	0.05	0.04	0.03	0.02
Total	100.70	100.19	100.32	100.60	100.24	99.11	100.10	100.42	101.29	100.89	100.73
Si	2.978	2.992	2.997	2.995	2.992	2.991	2.956	2.970	2.955	2.999	2.997
Ti	0.000	0.000	0.000	0.001	0.001	0.001	0.001	0.001	0.001	0.000	0.000
Al	1.010	1.002	0.996	0.996	1.003	1.007	1.039	0.938	1.041	0.993	0.996
Cr	0.000	0.000	0.000	0.000	0.000	0.000	0.000	0.000	0.000	0.000	0.000
Fe ³⁺	0.000	0.000	0.000	0.000	0.000	0.000	0.000	0.000	0.000	0.000	0.000
Fe ²⁺	0.019	0.006	0.011	0.005	0.006	0.007	0.009	0.036	0.008	0.005	0.005
Mn	0.000	0.000	0.000	0.000	0.000	0.000	0.000	0.000	0.000	0.001	0.000
Mg	0.007	0.000	0.000	0.000	0.000	0.001	0.001	0.073	0.000	0.001	0.000
Ca	0.021	0.006	0.006	0.002	0.008	0.013	0.044	0.060	0.050	0.007	0.004
Na	0.962	1.001	0.989	1.014	0.989	0.971	0.944	0.965	0.935	0.996	1.008
K	0.002	0.001	0.001	0.001	0.003	0.002	0.003	0.003	0.002	0.002	0.001
Total	4.999	5.008	5.000	5.014	5.002	4.992	4.997	5.045	4.992	5.004	5.010
X _{An} (Ca/(Ca+Na))	0.02	0.01	0.01	0.00	0.01	0.01	0.04	0.06	0.05	0.01	0.00

Table A.10 (continued) : Mineral chemistry of the measured plagioclases. Mineral formula calculations are based on eight oxygens.

Plagioclase	211B	211B	211B	211B	211B	211B	211B	775	775	753A
	238	246	250	256	263	290	305	24	227	87
SiO ₂	68.00	68.19	67.91	67.43	68.00	68.49	67.51	67.12	67.17	72.73
TiO ₂	0.02	0.01	0.00	0.02	0.00	0.00	0.02	0.06	0.04	0.09
Al ₂ O ₃	20.08	20.20	20.11	20.25	20.25	19.83	19.91	20.33	20.08	17.26
Cr ₂ O ₃	0.00	0.00	0.00	0.00	0.00	0.00	0.00	0.01	0.01	0.00
FeO	0.10	0.29	0.33	0.68	0.36	0.31	0.18	0.11	0.18	0.39
MnO	0.00	0.01	0.00	0.02	0.00	0.00	0.00	0.00	0.01	0.04
MgO	0.00	0.00	0.01	0.01	0.00	0.01	0.00	0.01	0.01	0.05
CaO	0.16	0.20	0.27	0.02	0.01	0.07	0.06	0.44	0.86	0.37
Na ₂ O	10.12	10.11	10.51	10.56	10.58	10.53	10.18	11.53	11.12	8.70
K ₂ O	0.04	0.04	0.06	0.02	0.03	0.03	0.04	0.09	0.09	0.03
Total	98.53	99.04	99.20	99.00	99.23	99.27	97.90	99.69	99.57	99.64
Si	2.995	2.991	2.982	2.971	2.982	3.000	2.995	2.949	2.955	3.139
Ti	0.001	0.000	0.000	0.001	0.000	0.000	0.001	0.002	0.001	0.003
Al	1.043	1.044	1.041	1.051	1.047	1.024	1.041	1.053	1.041	0.878
Cr	0.000	0.000	0.000	0.000	0.000	0.000	0.000	0.000	0.000	0.000
Fe ³⁺	0.000	0.000	0.000	0.000	0.000	0.000	0.000	0.000	0.000	0.000
Fe ²⁺	0.004	0.011	0.012	0.025	0.013	0.011	0.007	0.004	0.007	0.014
Mn	0.000	0.000	0.000	0.001	0.000	0.000	0.000	0.000	0.001	0.001
Mg	0.000	0.000	0.001	0.001	0.000	0.001	0.000	0.001	0.001	0.003
Ca	0.007	0.009	0.013	0.001	0.001	0.003	0.003	0.021	0.040	0.017
Na	0.865	0.860	0.894	0.902	0.900	0.895	0.875	0.982	0.948	0.728
K	0.002	0.002	0.003	0.001	0.001	0.002	0.002	0.005	0.005	0.002
Total	4.916	4.918	4.946	4.954	4.945	4.936	4.923	5.016	5.000	4.784
X _{An} (Ca/(Ca+Na))	0.01	0.01	0.01	0.00	0.00	0.00	0.00	0.02	0.04	0.02

Table A.10 (continued) : Mineral chemistry of the measured plagioclases. Mineral formula calculations are based on eight oxygens.

Plagioclase	178	178	178	178	178	178	392
	53	81	82	91	92	101	1
SiO ₂	68.49	68.30	68.07	67.02	66.19	66.68	67.41
TiO ₂	0.00	0.00	0.01	0.24	0.04	0.07	0.00
Al ₂ O ₃	20.13	19.14	19.53	19.75	19.53	20.63	20.56
Cr ₂ O ₃	0.00			0.00	0.00	0.00	
FeO	0.21	0.05	0.14	0.10	0.04	0.31	0.02
MnO	0.00	0.00	0.00	0.01	0.00	0.00	0.00
MgO	0.00	0.00	0.07	0.00	0.00	0.12	0.00
CaO	0.05	0.07	0.08	0.10	0.09	0.05	0.06
Na ₂ O	10.47	11.66	11.42	11.61	11.30	10.91	11.96
K ₂ O	0.05	0.04	0.36	0.04	0.06	0.81	0.04
Total	99.39	99.27	99.68	98.87	97.25	99.57	100.05
Si	2.995	3.004	2.987	2.965	2.973	2.939	2.949
Ti	0.000	0.000	0.000	0.008	0.001	0.002	0.000
Al	1.037	0.992	1.010	1.030	1.034	1.071	1.060
Cr	0.000	0.000	0.000	0.000	0.000	0.000	0.000
Fe ³⁺	0.000	0.000	0.000	0.000	0.000	0.000	0.000
Fe ²⁺	0.008	0.002	0.005	0.004	0.001	0.011	0.001
Mn	0.000	0.000	0.000	0.000	0.000	0.000	0.000
Mg	0.000	0.000	0.004	0.000	0.000	0.008	0.000
Ca	0.002	0.003	0.004	0.005	0.004	0.002	0.003
Na	0.887	0.994	0.972	0.996	0.984	0.932	1.014
K	0.003	0.002	0.020	0.002	0.003	0.045	0.002
Total	4.932	4.998	5.003	5.011	5.002	5.012	5.029
X _{An} (Ca/(Ca+Na))	0.00	0.00	0.00	0.00	0.00	0.00	0.00

Table A.11 : Bulk rock compositions and calculated element mol percentages used in the pseudosection calculations.

	128	702A	775	753A	178
<i>Oxide (w.t. %)</i>					
SiO ₂	50.21	46.39	62.71	56.11	62.07
TiO ₂	1.56	2.01	0.70	0.70	0.81
Al ₂ O ₃	14.91	14.25	17.41	19.30	18.20
Fe ₂ O ₃	11.99	13.71	6.95	10.04	6.92
MnO	0.17	0.23	0.45	0.49	0.14
MgO	5.28	6.51	1.98	2.77	1.52
CaO	6.09	8.98	0.34	0.47	0.22
Na ₂ O	4.40	2.85	0.66	0.79	1.06
K ₂ O	0.66	0.57	3.61	3.36	3.45
P ₂ O ₅	0.16	0.24	0.12	0.31	0.12
LOI	4.38	3.95	4.89	5.36	5.21
Total	99.80	99.70	99.82	99.70	99.72
<i>Element (mol%)</i>					
Si	22.23	22.28	28.96	25.67	28.90
Al	7.89	7.42	8.98	9.33	9.41
Ti		1.21			
Fe	8.39	9.59	4.86	6.40	2.54
Mg	3.18	3.93	1.19	1.67	0.92
Ca	3.18	6.52	0.16		
Na	3.26	2.11	0.49	0.59	0.79
K	0.55	0.47	3.00	2.79	2.86
H ₂ O	<i>Saturated</i>	<i>Saturated</i>	<i>Saturated</i>	<i>Saturated</i>	<i>Saturated</i>

Table A.12 : UTM coordinates (European 1979 datum) of the metapelitic samples of the Esenler Unit that were analyzed by Raman Spectroscopy.

Sample	x	y
31	36T 05 86007	45 61629
230	36T 05 88842	45 74615
850	36T 05 89035	45 73738
844	36T 05 87373	45 72916
879	36T 05 88350	45 63831
871	36T 05 87976	45 68095
876	36T 05 85922	45 65761
874	36T 05 85489	45 67304
841	36T 05 84538	45 69821
847	36T 05 88172	45 71385
851	36T 05 90262	45 74020
853	36T 05 86097	45 76405
1126	36T 05 83817	45 77178
859	36T 05 83350	45 77637
861	36T 05 82426	45 79377

Table A.13 : $^{40}\text{Ar}/^{39}\text{Ar}$ analytical data of the dated samples.

Laser output	$^{40}\text{Ar}/^{39}\text{Ar}$		$^{37}\text{Ar}/^{39}\text{Ar}$		$^{36}\text{Ar}/^{39}\text{Ar}$		K/Ca	$^{40}\text{Ar}^*$	^{39}ArK	$^{40}\text{Ar}^*/^{39}\text{ArK}$		Age(Ma)	$\pm 1\sigma$	
					($\times 10^{-3}$)			(%)	fraction (%)					
Sample 31, Laboratory ID: C13038 Neutron Irradiation ID: PP-3														
<i>J= 0.00241</i>														
1.2%	92.61	± 4.00	0.028	± 0.001	254.25	± 75.12	21.39	18.88	2.21	17.49	± 22.14	74.47	± 92.37	
1.4%	29.14	± 1.29	0.047	± 0.002	28.19	± 20.15	12.65	71.42	13.10	20.81	± 6.03	88.28	± 24.96	
1.6%	30.56	± 0.28	0.011	± 0.000	19.54	± 4.36	52.33	81.11	54.28	24.79	± 1.31	104.69	± 5.40	
1.8%	33.58	± 1.09	0.025	± 0.001	42.89	± 9.60	23.98	62.27	24.89	20.91	± 2.90	88.71	± 11.99	
2.0%	37.26	± 3.17	0.137	± 0.011	29.16	± 41.44	4.28	76.90	4.45	28.65	± 12.48	120.46	± 50.78	
2.2%	49.24	± 8.50	0.057	± 0.009	615.16	± 240.11	10.31	-269.15	1.07	-132.54	± -68.38	-694.22	± -436.83	
												Plateau age (Plateau: steps from 1.4% to 1.8%) :	101.50	± 4.80
												Total gas age :	91.70	± 6.90

Table A.13 (continued) : $^{40}\text{Ar}/^{39}\text{Ar}$ analytical data of the dated samples.

Laser output	$^{40}\text{Ar}/^{39}\text{Ar}$		$^{37}\text{Ar}/^{39}\text{Ar}$		$^{36}\text{Ar}/^{39}\text{Ar}$		K/Ca	$^{40}\text{Ar}^*$	^{39}ArK	$^{40}\text{Ar}^*/^{39}\text{ArK}$		Age(Ma)	$\pm 1\sigma$					
					($\times 10^{-3}$)			(%)	fraction (%)									
<i>Sample 230, Laboratory ID: C13039</i>		<i>Neutron Irradiation ID: PP-3</i>																
<i>J=0.002402</i>																		
1.2%	1078.74	±	37.86	0.017	±	0.001	3916.51	±	193.88	34.14	-7.28	0.56	-78.59	±	-40.65	-377.41	±	-217.15
1.4%	66.18	±	2.03	0.020	±	0.001	174.16	±	11.23	29.40	22.24	4.84	14.72	±	2.97	62.68	±	12.43
1.5%	40.77	±	0.65	0.016	±	0.000	59.30	±	7.44	37.39	57.02	6.15	23.25	±	2.22	98.04	±	9.11
1.6%	31.50	±	0.71	0.016	±	0.000	43.34	±	6.32	37.70	59.35	6.21	18.70	±	1.91	79.26	±	7.91
1.7%	28.63	±	0.50	0.010	±	0.000	21.85	±	4.40	61.52	77.44	10.14	22.17	±	1.35	93.60	±	5.58
1.8%	27.43	±	0.35	0.008	±	0.000	14.23	±	2.88	77.61	84.67	12.81	23.22	±	0.90	97.92	±	3.72
1.9%	27.92	±	0.36	0.006	±	0.000	14.99	±	2.17	95.37	84.13	15.75	23.49	±	0.72	99.01	±	2.96
2.0%	27.52	±	0.58	0.009	±	0.000	7.31	±	4.19	63.75	92.15	10.54	25.36	±	1.35	106.67	±	5.53
2.1%	27.51	±	0.51	0.007	±	0.000	10.22	±	2.93	84.37	89.02	13.96	24.49	±	0.98	103.11	±	4.01
2.2%	26.66	±	0.41	0.018	±	0.000	10.44	±	8.41	31.90	88.43	5.28	23.58	±	2.51	99.37	±	10.31
2.4%	26.14	±	0.65	0.010	±	0.000	12.59	±	5.15	56.33	85.77	9.33	22.42	±	1.62	94.63	±	6.67
2.8%	33.14	±	0.70	0.022	±	0.000	29.28	±	9.04	26.70	73.89	4.43	24.49	±	2.72	103.10	±	11.13
												<i>Plateau age (Plateau: steps from 1.7% to 2.8%) :</i>		99.60	±	1.70		
												<i>Total gas age :</i>		94.1	±	2.1		

Table A.13 (continued) : $^{40}\text{Ar}/^{39}\text{Ar}$ analytical data of the dated samples.

Laser output	$^{40}\text{Ar}/^{39}\text{Ar}$		$^{37}\text{Ar}/^{39}\text{Ar}$		$^{36}\text{Ar}/^{39}\text{Ar}$		K/Ca	$^{40}\text{Ar}^*$	^{39}ArK	$^{40}\text{Ar}^*/^{39}\text{ArK}$		Age(Ma)	$\pm 1\sigma$					
					($\times 10^{-3}$)			(%)	fraction (%)									
<i>Sample 392, Laboratory ID: C13040</i>		<i>Neutron Irradiation ID: PP-3</i>																
<i>J= 0.002455</i>																		
1.2%	555.83	±	39.49	0.124	±	0.009	2082.87	±	162.84	4.74	-10.73	0.58	-59.65	±	-20.75	-285.66	±	-107.69
1.4%	60.10	±	1.82	0.022	±	0.001	135.05	±	13.21	27.33	33.60	3.32	20.19	±	3.80	87.29	±	16.02
1.6%	31.72	±	0.32	0.039	±	0.000	23.97	±	1.85	15.00	77.68	18.24	24.64	±	0.60	105.98	±	2.54
1.7%	27.89	±	0.38	0.041	±	0.001	16.21	±	1.23	14.31	82.83	17.41	23.10	±	0.48	99.51	±	2.04
1.8%	25.03	±	0.21	0.030	±	0.000	7.72	±	1.49	19.74	90.90	24.03	22.75	±	0.48	98.06	±	2.06
1.9%	23.54	±	0.18	0.042	±	0.000	7.47	±	1.56	13.87	90.63	16.91	21.33	±	0.49	92.09	±	2.09
2.0%	22.63	±	0.32	0.082	±	0.001	4.02	±	2.80	7.21	94.77	8.79	21.45	±	0.88	92.59	±	3.72
2.2%	22.41	±	0.28	0.010	±	0.000	9.23	±	3.82	60.00	87.83	7.33	19.68	±	1.16	85.12	±	4.89
2.4%	22.87	±	0.53	0.021	±	0.000	9.98	±	8.58	27.75	87.11	3.39	19.92	±	2.58	86.16	±	10.89
												<i>Plateau age (Plateau: steps from 1.6% to 1.8%) :</i>		100.60	±	1.30		
												<i>Total gas age :</i>		94.60	±	1.30		

Table A.13 (continued) : $^{40}\text{Ar}/^{39}\text{Ar}$ analytical data of the dated samples.

Laser output	$^{40}\text{Ar}/^{39}\text{Ar}$		$^{37}\text{Ar}/^{39}\text{Ar}$		$^{36}\text{Ar}/^{39}\text{Ar}$		K/Ca	$^{40}\text{Ar}^*$	^{39}ArK	$^{40}\text{Ar}^*/^{39}\text{ArK}$	Age(Ma)	$\pm 1\sigma$						
					($\times 10^{-3}$)			(%)	fraction (%)									
<i>Sample 753A, Laboratory ID: C13054</i>																		
<i>Neutron Irradiation ID: PP-3</i>																		
<i>J= 0.002459</i>																		
1.6%	92.30	±	40.92	0.280	±	0.122	89.53	±	1489.41	2.10	71.36	0.03	65.88	±	441.06	270.85	±	1683.88
1.8%	23.88	±	1.42	0.002	±	0.000	5.26	±	12.91	235.63	93.49	2.93	22.32	±	4.05	96.40	±	17.02
2.0%	20.05	±	0.59	0.009	±	0.000	0.29	±	5.25	64.34	99.57	8.02	19.97	±	1.66	86.47	±	7.03
2.2%	20.67	±	0.96	0.012	±	0.001	0.87	±	13.14	50.88	98.76	6.34	20.41	±	4.00	88.35	±	16.89
2.4%	20.85	±	0.59	0.006	±	0.000	0.19	±	3.06	98.56	99.74	12.47	20.80	±	1.08	89.98	±	4.56
2.6%	22.36	±	1.09	0.079	±	0.004	0.25	±	3.50	7.43	99.70	9.41	22.29	±	1.50	96.28	±	6.31
2.8%	20.85	±	0.60	0.088	±	0.002	0.28	±	3.75	6.71	99.64	8.49	20.78	±	1.26	89.89	±	5.32
3.0%	21.30	±	0.62	0.064	±	0.002	0.20	±	3.15	9.24	99.75	11.70	21.24	±	1.12	91.86	±	4.74
3.2%	21.02	±	0.79	0.055	±	0.002	0.17	±	1.81	10.76	99.78	13.64	20.97	±	0.96	90.73	±	4.05
3.4%	22.71	±	1.27	0.010	±	0.001	0.32	±	3.65	58.05	99.59	7.36	22.62	±	1.66	97.65	±	6.99
3.6%	21.85	±	0.75	0.010	±	0.000	0.31	±	4.29	59.46	99.58	7.55	21.76	±	1.47	94.04	±	6.20
3.8%	22.07	±	0.98	0.014	±	0.001	0.45	±	4.90	41.05	99.40	5.21	21.94	±	1.75	94.78	±	7.36
4.2%	18.37	±	1.08	0.020	±	0.001	0.63	±	6.20	29.33	99.00	3.73	18.18	±	2.12	78.91	±	9.02
4.6%	19.11	±	1.92	0.043	±	0.003	1.34	±	14.98	13.73	97.95	1.75	18.72	±	4.81	81.18	±	20.42
5.0%	22.25	±	1.98	0.054	±	0.004	1.70	±	21.01	10.83	97.76	1.38	21.75	±	6.50	94.01	±	27.39
											<i>Plateau age (Plateau: steps from 2.0% to 3.8%) :</i>		91.80	±	1.80			
											<i>Total gas age :</i>		91.40	±	2.20			

Table A.13 (continued) : $^{40}\text{Ar}/^{39}\text{Ar}$ analytical data of the dated samples.

Laser output	$^{40}\text{Ar}/^{39}\text{Ar}$			$^{37}\text{Ar}/^{39}\text{Ar}$			$^{36}\text{Ar}/^{39}\text{Ar}$ ($\times 10^{-3}$)			K/Ca	$^{40}\text{Ar}^*$ (%)	^{39}ArK fraction (%)	$^{40}\text{Ar}^*/^{39}\text{ArK}$		Age(Ma)		$\pm 1\sigma$		
<i>Sample 626A, Laboratory ID: C13041</i>		<i>Neutron Irradiation ID: PP-3</i>																	
<i>J= 0.002457</i>																			
1.2%	221.34	±	22.64	0.566	±	0.057	658.86	±	207.72	1.04	12.06	0.12	26.71	±	58.27	114.67	±	242.40	
1.4%	36.95	±	1.15	0.072	±	0.002	30.26	±	16.58	8.20	75.82	0.97	28.02	±	4.99	120.11	±	20.68	
1.6%	38.92	±	0.32	0.037	±	0.000	3.38	±	1.08	16.02	97.44	18.91	37.92	±	0.45	160.71	±	1.91	
1.7%	38.69	±	0.37	0.030	±	0.000	3.02	±	0.92	19.84	97.70	23.45	37.80	±	0.46	160.20	±	1.95	
1.8%	38.22	±	0.38	0.038	±	0.000	3.06	±	1.43	15.49	97.64	18.31	37.32	±	0.56	158.27	±	2.36	
1.9%	39.42	±	0.41	0.008	±	0.000	0.54	±	2.96	77.41	99.60	9.16	39.26	±	0.96	166.15	±	3.95	
2.0%	37.53	±	0.91	0.010	±	0.000	4.62	±	3.03	60.91	96.36	7.21	36.16	±	1.25	153.57	±	5.13	
2.2%	38.02	±	0.32	0.049	±	0.000	3.96	±	1.48	11.94	96.93	14.15	36.85	±	0.54	156.38	±	2.26	
2.4%	38.23	±	1.01	0.090	±	0.002	3.07	±	2.42	6.51	97.65	7.72	37.33	±	1.22	158.33	±	4.97	
															<i>Plateau age (Plateau: steps from 1.6% to 2.4%) :</i>		159.30	±	1.00
															<i>Total gas age :</i>		158.90	±	1.10

Table A.13 (continued) : $^{40}\text{Ar}/^{39}\text{Ar}$ analytical data of the dated samples.

Laser output	$^{40}\text{Ar}/^{39}\text{Ar}$			$^{37}\text{Ar}/^{39}\text{Ar}$			$^{36}\text{Ar}/^{39}\text{Ar}$			K/Ca	$^{40}\text{Ar}^*$	^{39}ArK	$^{40}\text{Ar}^*/^{39}\text{ArK}$		Age(Ma)		$\pm 1\sigma$		
							($\times 10^{-3}$)				(%)	fraction (%)							
Sample 1290, Laboratory ID: C14088		Neutron Irradiation ID: PO-2																	
<i>J= 0.000968</i>																			
1.4%	57.63	±	0.89	0.211	±	0.021	78.29	±	1.98	2.79	59.88	4.80	34.51	±	0.71	59.29	±	1.23	
1.6%	72.18	±	0.56	0.111	±	0.008	7.34	±	0.87	5.32	97.01	8.15	70.02	±	0.60	118.31	±	1.09	
1.8%	99.79	±	0.67	0.048	±	0.002	30.80	±	3.41	12.24	90.88	33.01	90.69	±	1.18	151.81	±	1.99	
2.0%	97.23	±	0.26	0.076	±	0.005	2.09	±	0.49	7.70	99.37	21.46	96.63	±	0.30	161.31	±	0.77	
2.2%	81.53	±	0.54	0.169	±	0.018	5.66	±	1.53	3.48	97.96	7.64	79.88	±	0.69	134.37	±	1.24	
2.4%	62.72	±	0.64	0.222	±	0.021	6.42	±	2.15	2.65	97.00	5.18	60.85	±	0.89	103.26	±	1.52	
2.5%	60.96	±	0.39	0.303	±	0.035	13.00	±	3.34	1.94	93.73	3.50	57.15	±	1.05	97.14	±	1.78	
2.7%	61.49	±	0.19	0.383	±	0.027	10.02	±	1.69	1.53	95.24	5.09	58.58	±	0.53	99.51	±	0.96	
3.0%	64.75	±	1.31	0.351	±	0.032	9.85	±	4.67	1.67	95.55	5.19	61.88	±	1.88	104.95	±	3.13	
3.4%	66.14	±	0.41	0.251	±	0.014	18.61	±	1.79	2.34	91.71	6.00	60.67	±	0.65	102.95	±	1.14	
															Weighted average age (steps from 2.4% to 3.4%) :		101.00	±	0.60
															Total gas age :		133.10	±	0.70

Table A.13 (continued) : $^{40}\text{Ar}/^{39}\text{Ar}$ analytical data of the dated samples.

Laser output	$^{40}\text{Ar}/^{39}\text{Ar}$		$^{37}\text{Ar}/^{39}\text{Ar}$		$^{36}\text{Ar}/^{39}\text{Ar}$ ($\times 10^{-3}$)		K/Ca	$^{40}\text{Ar}^*$ (%)	$^{39}\text{Ar}_K$ fraction(%)	$^{40}\text{Ar}^*/^{39}\text{Ar}_K$		Age (Ma)	$\pm 1\sigma$					
<i>Sample 1214, Laboratory ID: C14043</i>		<i>Neutron Irradiation ID: PO-1</i>																
<i>J = 0.001001</i>																		
1.4%	65.62	±	0.53	0.038	±	0.098	168.78	±	3.31	15.41	24.00	5.38	15.75	±	0.92	28.22	±	1.64
1.6%	41.35	±	0.45	0.081	±	0.039	32.69	±	1.39	7.26	76.66	13.69	31.71	±	0.55	56.37	±	0.99
1.8%	41.47	±	0.30	0.029	±	0.031	9.05	±	1.06	20.44	93.56	15.88	38.80	±	0.43	68.75	±	0.79
2.0%	41.40	±	0.38	0.008	±	0.027	5.64	±	0.97	73.08	95.98	15.20	39.74	±	0.47	70.37	±	0.86
2.2%	42.33	±	0.47	0.005	±	0.020	6.47	±	0.93	125.55	95.49	13.89	40.42	±	0.53	71.55	±	0.96
2.4%	42.45	±	0.44	0.133	±	0.032	8.85	±	1.24	4.42	93.86	11.24	39.85	±	0.56	70.57	±	1.01
2.6%	41.26	±	0.47	0.061	±	0.026	7.39	±	0.79	9.61	94.72	12.91	39.08	±	0.50	69.23	±	0.92
2.8%	43.18	±	0.14	0.151	±	0.044	14.85	±	1.72	3.89	89.86	7.44	38.81	±	0.52	68.75	±	0.95
3.0%	48.26	±	1.30	0.228	±	0.100	21.03	±	4.12	2.58	87.16	2.74	42.07	±	1.66	74.41	±	2.89
3.4%	73.51	±	1.92	0.584	±	0.206	124.94	±	8.43	1.01	49.84	1.41	36.65	±	2.50	65.00	±	4.37
4.2%	568.28	±	53.54	1.801	±	1.563	1678.28	±	163.67	0.33	12.76	0.21	72.60	±	14.52	126.57	±	24.45
												Plateau age (Plateau: steps from 1.8% to 3.4%) :		69.86	±	0.37		
												Total gas age :		66.03	±	0.34		

CURRICULUM VITAE

Name Surname: Mesut Aygöl

Place and Date of Birth: İstanbul, 23.10.1982

Address: İTUAyazağa Kampüsü, Avrasya Yer Bilimleri Enstitüsü, 34469
Maslak/İstanbul Turkey

E-Mail: aygulm@itu.edu.tr, mesutaygul@ymail.com

B.Sc.: İstanbul Technical University, Faculty of Mine, Department of Geological Engineering

M.Sc.: İstanbul Technical University, Eurasia Institute of Earth Sciences

Professional Experience and Rewards:

2007-2015: Research Assistant, İTU Eurasia Institute of Earth Sciences

List of Publications and Patents:

Articles

Okay, A.I., Sunal, G., Sherlock, S., Altın, D., Tüysüz, T., Kylander-Clark, A.R.C., **Aygöl, M.**, 2013. Early Cretaceous sedimentation and orogeny on the active margin of Eurasia: southern Central Pontides, Turkey. *Tectonics*, 32, 1247–1271.

Aygöl, M., Topuz, G., Okay, A.I., Satır, M., Meyer, H.P., 2012. The Kemer Metamorphic Complex (NW Turkey): a subducted continental margin of the Sakarya Zone. *Turkish Journal of Earth Sciences*, 21, 19–35.

Conference abstracts

Aygöl, M., Okay, A.I., 2011. Possible Paleozoic magmatism in the western Sakarya Zone, Biga Peninsula, NW Turkey. EGU General Assembly, Vienna.

Aygöl, M., Topuz, G., Satır, M., 2010. The Kemer metamorphics (NW Turkey): subducted passive margin of the Sakarya Zone. EGU General Assembly, Vienna.

Aygöl, M., Topuz, G., Satır, M., 2009. Metamorphic evolution of the high-pressure metamorphic rocks from the Kemer area (Biga Peninsula, NW Turkey): implications for the accretionary continental growth and closure of the Intra-Pontide Ocean. EGU General Assembly, Vienna.

Aygül, M., Topuz, G., Satır, M., 2009. Late Cretaceous high-pressure metamorphism in northern Biga Peninsula (NW Turkey): implications for the evolution of the Intra-Pontide Ocean. Geological Congress of Turkey, Ankara.

PUBLICATIONS/PRESENTATIONS ON THE THESIS

Articles

Aygül, M., Okay, A.I., Oberhänsli, R., Schmidt, A., Sudo, M., 2015. Late Cretaceous infant intra-oceanic arc volcanism, the Central Pontides, Turkey: petrogenetic and tectonic implications. *Journal of Asian Earth Sciences*, 111, 312–327.

Aygül, M., Okay, A.I., Oberhänsli, R., Ziemann, M.A., 2015. Thermal structure of low-grade accreted Lower Cretaceous distal turbidites, the Central Pontides, Turkey: insights for tectonic thickening of an accretionary wedge. *Turkish Journal of Earth Sciences*, 24, 461–474.

Aygül, M., Okay, A.I., Oberhänsli, R., Sudo, M., 2015. Pre-collisional accretionary growth of the southern Laurasian margin, Central Pontides, Turkey. *Tectonophysics*, submitted for publication.

Conference Abstracts

Aygül, M., Okay, A.I., Oberhänsli, R., 2015. Petrology of HP/LT metapelitic rocks of an accretionary wedge, the Central Pontides, Turkey: evidence for tectonic stacking and syn-subduction exhumation. EGU General Assembly, Vienna.

Aygül, M., Okay, A.I., Oberhänsli, R., Schmidt, A., Sudo, M., 2015. Late Cretaceous infant intra-oceanic arc volcanism, the Central Pontides, Turkey. EGU General Assembly, Vienna.

Aygül, M., Okay, A.I., Oberhänsli, R., Sudo, M., 2014. Cretaceous high-pressure metamorphic belts of the Central Pontides (northern Turkey): pre-collisional Pacific-type accretionary continental growth of Laurasian Margin. EGU General Assembly, Vienna.

Aygül, M., Okay, A.I., Oberhänsli, R., Sudo, M., 2014. Blueschist-facies metamorphic rocks of the Central Pontides (northern Turkey): a case of pre-collisional accretionary continental growth. Geological Congress of Turkey, Ankara.

Aygül, M., Okay, A.I., Oberhänsli, R., 2013. Blueschist-facies metamorphic rocks of the Central Pontides (northern Turkey): their petrology and implications for the accretionary continental growth. 10th International Eclogite Conference, Courmayeur, Italy.

Aygül, M., Okay, A.I., 2012. Blueschist-facies metamorphic rocks in the Central Pontides, northern Turkey. EGU General Assembly, Vienna.

Aygül, M., Okay, A.I., 2012. Geology of Kastamonu-Tosya transect, Central Pontides. Geological Congress of Turkey, Ankara.